ANALYSIS AND DESIGN OF PHOTOVOLTAIC AND FUEL CELL BASED CONVERTER SYSTEMS

A THESIS
Submitted in the partial fulfilment
of the requirements for the award of the degree
of
DOCTOR OF PHILOSOPHY
in
ELECTRICAL ENGINEERING

by
GITANJALI MEHTA

DEPARTMENT OF ELECTRICAL ENGINEERING
INDIAN INSTITUTE OF TECHNOLOGY ROORKEE
ROORKEE-247667 (INDIA)
JULY, 2014

INDIAN INSTITUTE OF TECHNOLOGY ROORKEE
ROORKEE

CANDIDATE'S DECLARATION

I hereby certify that the work which is being presented in the thesis entitled "**ANALYSIS AND DESIGN OF PHOTOVOLTAIC AND FUEL CELL BASED CONVERTER SYSTEMS"** in partial fulfilment of the requirements for the award of the **Degree of Doctor of Philosophy** and submitted in the **Department of Electrical Engineering** of the Indian Institute of Technology Roorkee, Roorkee is an authentic record of my own work carried out during a period from July, 2009 to July, 2014 under the supervision of Dr. S. P. Singh, Professor, Department of Electrical Engineering, Indian Institute of Technology Roorkee, Roorkee.

The matter presented in this thesis has not been submitted by me for the award of any other degree of this or any other Institute.

(GITANJALI MEHTA)

This is to certify that the above statement made by the candidate is correct to the best of my knowledge.

Date: (S. P. Singh)

Supervisor

The Ph. D Viva-Voce Examination of **Ms. Gitanjali Mehta**, Research Scholar, has been held on…………………………………………………………………………………..

Signature of Supervisor Chairman, SRC Signature of External Examiner

Head of Department/Chairman, ODC

ABSTRACT (Comment [1])

The steadily increasing energy consumption, the soaring cost, the exhaustible nature of fossil fuels, and the intensifying concerns over the global environment have created much interest in alternative energy sources such as solar, wind, fuel cell etc. as future energy solution. Alternative energy sources integrated at distribution level is termed as Distributed Generation (DG). Photovoltaic (PV) and Fuel Cells (FC) are the best environmental friendly technologies for DGs and hence receiving increased attention.

The two-stage Power Conditioning Unit (PCU) including the DC-DC boost converter with the Pulse Width Modulated Voltage Source Inverter (VSI) is the state-of-art technology used nowadays worldwide for grid interfacing of the FC. However, it has reduced power conversion efficiency because of the two-stage configuration. Further, it has reduced reliability because of more no of components used in this configuration.

The author has proposed a FC based DG system with a single-stage power conditioning unit. The system is analysed by modelling various units of FCDG system, performing mathematical analysis and simulation studies. The Proton Exchange Membrane Fuel Cell (PEMFC) model used for the simulation studies is based on physical processes inside the PEMFC stack and is modeled using the experimental data obtained from Avista Labs SR-12 0.5 kW PEMFC stack. The inverter controller is designed to control the active power fed to the grid, the reactive power transfer between the inverter and the grid, the DC-link voltage, the quality of the injected power and grid synchronization. The designed control scheme of the inverter consists of a cascade of two independent controllers, where the external voltage controller generates the reference current that is tracked by the inner current controller which generates the pulses for the inverter switches.

Another facet of work done is with respect to solar PV as source of electricity. The conventional grid-interfaced PV systems use a DC-DC converter with Maximum Power Point Tracking (MPPT) control and a DC-AC inverter for grid interfacing. The proposed PV system uses one power conversion stage, thus simplifying the system topology. The single-diode PV circuit model used in the PV system simulation studies is modelled using the experimental values of Kyocera KC200GT 0.2 kW PV module. The MPPT, grid synchronisation, reactive power compensation, output current harmonic reduction is included simultaneously in the control circuit of the VSI connecting the PV to the grid. Due to the utilization of only one energy conversion stage, the single-stage grid-connected PV system proves to be simpler, more efficient and economical than its two-stage counterpart. However, the complexity of the control scheme is somewhat increased.

The increased use of power electronic devices in various loads results in many power quality problems in the power system network. Shunt Active Power Filters (SAPFs) are extensively used to compensate the load current harmonics, reactive power and load unbalance at distribution level. The

principle of operation of the SAPF is to supply the undesired harmonics and reactive power to the load, so that the mains current is of improved quality. However, its implementation results in additional hardware cost.

With the objective of reducing the cost and increasing the efficiency, grid-interactive FC system have been proposed which includes the functionality of SAPF. A control algorithm is developed such that the features of SAPF have been incorporated in the conventional inverter interfacing the FC to the grid without any additional hardware cost. Thus the grid-interfacing inverter is effectively utilised to perform the following functions: control of active power from the FC source to the grid, load reactive power demand support, current harmonic compensation and current imbalance compensation at PCC. With appropriate control of grid-interfacing inverter all the four objectives can be accomplished either individually or simultaneously. This concept, thus, reduces the overall design and cost of the system.

The motivation for the last part of the work is given below. The cost of FC is too high to justify its widespread use. The PV power generation has large variations in its output power during day and night and during varying weather conditions. Hence a PV-FC hybrid system can prove to be better to provide a reliable power source for grid-connected applications than a system comprising any of these single resources. The last part of the work proposes a utility-interactive hybrid DG system consisting of PV and FC to realize a reliable power supply for a grid connected critical load. These sources can be operated independently or in conjunction as per the requirement. The proposed system ensures maximum utilization of the PV array, and necessary utilisation of FC stack resulting in optimum operational costs.

The power circuit topology consists of two DC-DC boost converters, where one of them is fed by a PV array and the other by an FC stack. The Incremental Conductance MPPT control algorithm is implemented in the DC-DC converter connecting the PV array to the DC-link. This ensures extraction of maximum power from the PV array under all conditions. The difference of required power and the PV power is provided by the FC and governed through proper control of DC-DC converter connecting the FC stack to the DC-link. The outputs of the two DC-DC converters are connected to a common DC-link. The power is fed into the grid through an inverter for which the common DC-link acts as the energy source. The inverter control is so designed that apart from feeding active power into the grid, the system can also provide reactive power and harmonic compensation for PCC load.

ACKNOWLEDGEMENT

I bow my head with great reverence to Him who is omnipresent, omnipotent and omniscient and the cause behind every effort.

First of all I am thankful to Indian Institute of Technology, Roorkee for providing me an opportunity to pursue my Ph. D. work and Ministry of Human Resources and Development for providing me the scholarship during the entire program.

I would like to express my indebtness and veneration to Prof. S. P. Singh for giving me an opportunity to work in the emerging area of renewable energy and providing his meticulous supervision, advice and guidance throughout my research work.

I also wish to convey my gratitude to Dr. P. Agarwal, Dr. A. K. Saxena, Dr. M. K. Pathak, Dr. M. J. Nigam, Dr. S. P. Srivastava and Dr. S. P. Dubey for their advice, co-operation and indelible inspiration.

I am thankful to all my friends and colleagues for making my day to day life enjoyable during the course of my research. All these years I have enjoyed technical discussions and cooperation with fellow students and researchers who have been the source of valuable learning and motivation.

I would like to thank Council of Scientific and Industrial Research and Department of Science and Technology, Ministry of Science and Technology for providing me funding to present my papers in conferences in Singapore and Phuket, Thailand respectively.

Words would never be able to fathom the depth of feelings for my reverend parents, Dr. R. C. Mehta and Ms. Pratibha Mehta who have always been a source of inspiration for me.

I want to extend my deepest appreciation and thanks to my parents-in-law Mr. Pradeep Mittra and Ms. Manju Mittra for their meticulous care and support which could make this work a reality.

Special thanks to my brother Dr. Jai Prakash Mehta and my sister-in-law Dr. Sweta Rani Mehta for their moral encouragement and support.

Words alone cannot express the thanks I owe to my husband Mr. Gaurav Mittra and my lovely daughter Ms. Anweshika for their understanding, patience, support, affection and encouragement.

Finally, I would like to thank everyone at Indian Institute of Technology, Roorkee who directly or indirectly helped me during the course of my work.

Gitanjali Mehta

CONTENTS

LIST OF FIGURES

Fig. 3.16 Mode 1 operation: PQ enhancement with FC power injection

Fig. 3.17 Response of the system during start-up in Mode 1

LIST OF TABLES

LIST OF ABBREVIATIONS

Abbreviation	**Stands for**
AC	Alternating Current
ADC	Analog to Digital Converter
AES	Alternative Energy Sources
AFC	Alkaline Fuel Cell
APF	Active Power Filter
CCS	Code Composer Studio
CC-VSI	Current Controlled-Voltage Source Inverter
CHP	Combined Heat and Power
DAC	Digital to Analog Converter
DC	Direct Current
DER	Distributed Energy Resource
DG	Distributed Generation
DMFC	Direct Methanol Fuel Cell
DSP	Digital Signal Processor
et al.	and others
FC	Fuel Cell
FCDG	Fuel Cell Distributed Generation
FF	Fill Factor
FFT	Fast Fourier Transform
GPIO	General-purpose input-output
IC	Incremental Conductance
IDE	Integrated Development Environment
IEEE	Institute of Electrical and Electronics Engineers
IGBT	Insulated-gate Bipolar Transistor
I-V	Current-Voltage
kVAR	Kilo Volt-amperes reactive
kW	Kilo Watt
LPF	Low Pass Filter
MCFC	Molten Carbonate Fuel Cell
mH	Milihenry
MPP	Maximum Power Point
MPPT	Maximum Power Point Tracking
OCV	Open Circuit Voltage

PAFC	Phosphoric Acid Fuel Cell
PCC	Point of Common Coupling
PCU	Power Conditioning Unit
PE	Power Electronics
PEM	Proton Electrolyte Membrane
PEMFC	Proton Exchange Membrane Fuel Cell
PF	Power Factor
P-I	Power-Current
PIL	Processor-in-loop
PLL	Phase Locked Loop
P&O	Perturb and Observe
PQ	Power Quality
P-V	Power-Voltage
PVDG	Photovoltaic Distributed Generation
PWM	Pulse Width Modulation
P-I	Power-Current
P-V	Power-Voltage
RES	Renewable Energy Source
RMS	Root Mean Square
R-C	Resistive –Capacitive
R-L	Resistive-Inductive
S	Second
SAPF	Shunt Active Power Filter
SCC	Short Circuit Current
SOFC	Solid-Oxide Fuel Cell
SPWM	Sinusoidal Pulse Width Modulation
STC	Standard Test Condition
THD	Total Harmonic Distortion
TI	Texas Instrument
UPF	Unity power factor
VAR	Volt-amperes reactive
VSC	Voltage Source Converter
V-I	Voltage-Current
W	Watt
µF	Micro Farad

Chapter-1

INTRODUCTION AND LITERATURE REVIEW

1.1 WHY ALTERNATIVE/RENEWABLE ENERGY

In recent years, alternative energy sources have attracted remarkable attention and investment due to concerns regarding environmental issues, ever-increasing world energy demand, and the exhaustible nature of fossil fuels [1-5]. A variety of renewable energies such as wind power, fuel cells, tidal energy, geothermal energy, biomass energy, and solar cells are being widely utilized and advocated as future sources of energy [3]. The rapid technological advances in the field of power electronics have provided a new opportunity for these alternative energy sources being increasingly connected in distribution systems [6, 7].

Alternative energy source (AES) integrated at distribution level is termed as distributed generation [8]. Distributed Generation [9] is rapidly increasing across the globe because it can meet the increasing power demand while complying with the environmental regulations of low emissions [10, 11]**.** The use of renewable energy is becoming significant due to increasing power demand, instability of the rising oil prices and environmental problems associated with the use of fossil fuels [12].

1.2 DISTRIBUTED GENERATION

Distributed Generation (DG) is the use of small electrical power generation equipment located near consumers or centers of electricity demand [13]. They can provide reliable and uninterrupted supply of power and thus alleviate pressure on the grid. DGs are means to avoid expensive capital projects as both the cost to construct power plants and to erect transmission and distribution lines is enormous [9]. The growing DG market can improve air quality and reduce greenhouse gas emissions if clean and efficient technologies are used. The technology to install and manage both emergency and routine DG for on-site use is easier, more affordable and the technology is improving [13]. DG systems are receiving increased attention today because of their ability to provide combined heat and power, peak power, demand reduction, backup power, improved power quality, and ancillary services to the grid [9, 14-16]**.** DG is referred to small generators in the range of a few kilowatts up to 50 megawatts connected to the utility grid [17, 18]. DG technologies can be categorized into renewable and nonrenewable DGs.

Renewable energy technologies are sustainable and cause little or no environmental damage. They include photovoltaic, wind, geothermal, tidal, biomass and fuel cells. Nonrenewable energy technologies are referred to those that use some type of fossil fuel such as gasoline, diesel, oil, propane, methane, natural gas, or coal as their energy source. They include internal combustion engine, combustion turbine, gas turbine and micro turbine.

1.3 ELECTRICITY GENERATION IN INDIA

The electricity sector in India has an installed generation capacity of 199.87 GW as of March 2012. Thermal power plants constitute 66% of the installed capacity, hydroelectric 20%, nuclear 2% and the rest 12% being a combination of wind, small hydro, biomass, solar etc. constituting the renewable energy [19]. As present, over 300 million Indians have no access to electricity. Of those who have access to electricity, the supply is intermittent and unreliable particularly in rural areas. India currently suffers from a major shortage of electricity and is expected to add about 100 GW of installed capacity between 2012 and 2017. The technologies India adopts to add this electricity generation capacity will make significant impact to global resource and environmental issues. The economic and social drivers for India's push for electricity generation include the goal to provide electricity to all, the need to replace the highly polluting energy sources with cleaner ones, the rapidly growing economy, increasing household incomes and limited reserves of fossil fuels [19, 20].

- **Thermal power -** Thermal power plants convert energy rich fuel into electricity and heat. The thermal power accounts for over 66% of India's generated electricity of which 83% is generated using coal , 16% is generated using gas and 1% is generated using oil.
- **Hydro power -** In hydro power generation, the potential of the water falling under gravitational force is utilized to rotate a turbine which is coupled to a generator, thus leading to generation of electricity. The present installed capacity is approximately 37,367 MW which is 21.53% of total electricity generation in India.
- **Nuclear power -** India has 4.8 GW of installed generation capacity using nuclear fuels which constitutes nearly 2% of the country's total electricity generation. India's share of the nuclear power generation is only 1.2% of the worldwide nuclear power production. $Fig.$ 1.1 shows the installed power generation capacity in India as of March 2012 (in the form of Pie Chart).
- **Renewable energy -** Renewable energy in India is still in its infancy. India has an installed capacity of about 22.4 GW of electricity based on renewable technologies which is about 12% of its total generation capacity. $Fig.$ 1.2 shows the contributions from various renewable energy sources to electricity generation in India.

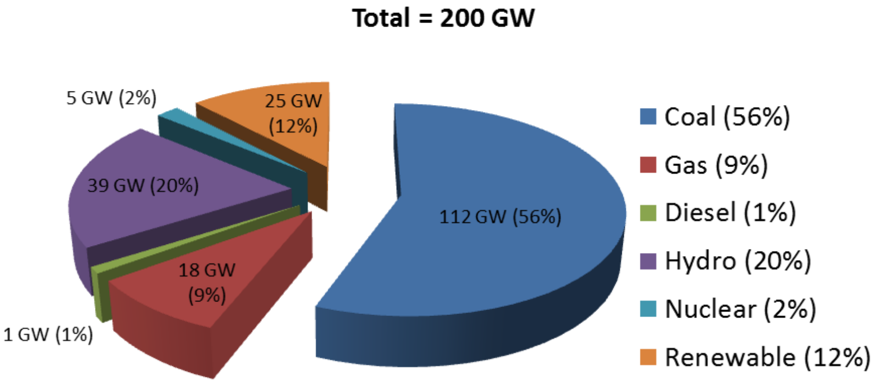

Fig. 1.1 Installed power generation capacity in India (March 2012)

- **Solar energy -** India is endowed with rich solar energy resource. India receives the highest global solar radiation ranging from 4 to 7 kWh/m^2/day across the country. With its growing electricity demand, India has initiated steps to develop its large potential for solar energy based power generation [21].
- **Wind energy -** India has the fifth largest installed wind power capacity in the world [22]. In 2012, the installed capacity of wind power in India was 15.9 GW, spread across several regions [19].
- **Biomass energy -** In this system biomass, bagasse, wood and agricultural wastes are used as fuel to produce electricity. India has been promoting biomass gasifier technologies in its rural areas, to utilize its biomass resources such as rice husk, crop stalks, small wood chips and other agro-wastes [19, 21].
- **Geothermal energy -** India's geothermal energy installed capacity is still in its experimental stage. However, India has potential resources to harvest geothermal energy.
- **Tidal wave energy -** Tidal energy technologies harvest energy from the seas. India is surrounded by sea on three sides thus its potential to harness tidal energy is significant, though still in experimental stage.

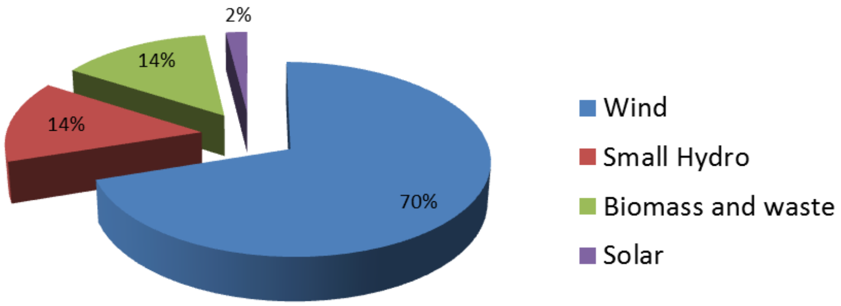

Fig. 1.2 Contributions from various RES to electricity generation in India (March 2012)

- **Fuel Cell energy –** This is a technology for energy conversion from chemical energy directly to electrical energy. Fuel Cell in India is still in its initial stage. Several economic and environmental factors are India to focus on fuel cells. The development of new fuel cell technology that is cost-effective, suited to local needs, and employing region-specific fuels should be commercially successful. The key issues are cost and the availability of fuels for either direct use in fuel cells or reforming to produce pure hydrogen [23].

1.4 FUEL CELL POWER GENERATION

The wind and photovoltaic power generation technologies are widely being used to meet the increasing power demand. The wind power generation although being a clean source of energy requires huge land for free air flow, contributes significantly to noise pollution and can deliver power only when the wind blows. Because of its large size, the wind turbines require more installation time with relatively small addition to capacity. The photovoltaic power generation demands high investment and space as photovoltaic modules are less efficient and can deliver power only when the sun shines [24]. Thus wind and photovoltaic power generation sources cannot be used as primary power source in grid connected operation. In contrast, a Fuel Cell (FC) based generation can provide continuous uninterrupted power supply to the consumers as long as input fuel is supplied. Thus, grid interface of FC is considered as one of the probable area of promising research in the field of distributed generation [25, 26].

Fuel Cells are static energy conversion devices. The stored chemical energy within the hydrogen-rich fuel is directly converted to DC form of electrical energy via an electrochemical reaction, producing water and useful heat as its by-product and operate as long as they are supplied with fuel [4, 7, 12, 27-29]. FCs offer potential efficiency gains compared with conventional thermal generation technologies [27]. FCs are environment friendly as they do not emit the pollutant sulphur and nitrogen compounds released by conventional generation methods and can utilize a variety of conventional and alternative fuels like hydrogen, ethanol, methanol and natural gas [4]. FCs have an essentially modular technology capable of power production from Watts to MegaWatts [30]. It can be placed at any site without geographical limitations unlike other DG sources such as wind and photovoltaic generation [30]. It also has a high efficiency in the range of 40% to 60% and as high as 80% if the waste heat generated by FC is used for cogeneration [25, 31].

The ideal output voltage of single FC is 1.2 V [25, 32]. Under normal operation, a simple FC produces output voltage in the range 0.5-0.9 V [33]. A number of FCs are connected in series so as to obtain a significant output voltage. These strings of series connected FCs are again connected in parallel to increase available output power, thereby constituting a FC stack [7, 25]. Based on the design, FCs can be external-reforming or self-reforming. The external-reforming FCs run on pure hydrogen and hence require an external reformer that is fed with hydrogen-rich fuel [34]. The self-reforming FCs are designed with a built-in catalytic converter and oxidizer, combined together into one single unit thus enabling the fuel to be pumped directly into the FC [35].

1.4.1 Fuel Cell Advantages and Disadvantages

The various advantages and disadvantages of FCs can be summarised as [29, 35]:

Advantages

- Higher efficiency than any other DG technology.
- Reliable source of power.
- Modular and easy installation.
- Portable, site flexibility and require less surface area per unit power produced.
- Zero-emission devices hence environment friendly.
- Suitable for cogeneration because of appreciable amount of useful exhaust heat.
- Zero or negligible noise emission except for occasional vibrations.
- Low operating cost.

Disadvantages

- High initial cost, complicated design and assembly of FC.
- Highly sensitive to fuel contamination, hence fuel reformer required.

1.4.2 Types of Fuel Cells and their Comparison

Fuel cells are generally characterized by the type of electrolyte and fuel used by them. The six major types of FCs available are [30]:

- Proton Exchange Membrane Fuel Cell (PEMFC)
- Alkaline Fuel Cell (AFC)
- Phosphoric Acid Fuel Cell (PAFC)
- Molten Carbonate Fuel Cell (MCFC)
- Solid Oxide Fuel Cell (SOFC)
- Direct Methanol Fuel Cell (DMFC)

Although all FCs are electrochemical energy conversion devices and operate on similar principle, each FC type has different operating characteristics, different materials of construction, different range of operating temperatures, and different applications [36]. Of all kinds of FCs, PEMFCs are being rapidly developed as the primary power source in DG because of its high energy density, solid electrolyte, low working temperature, fast start up, favourable power to weight ratio, firm and simple structure and long stack life [29, 33, 36, 37].

1.4.3 Operation of Proton Exchange Membrane Fuel Cell

Among the available FCs, PEMFCs seems a promising source to be used in residences, industries, and small and large scale DG systems. $Fig.$ 1.3 [38] shows the schematic diagram of PEMFC. Hydrogen and oxygen work as fuel and oxidant. The electrolyte used in PEMFC is proton electrolyte membrane placed between two electrodes that are coated with the platinum catalyst. The proton electrolyte membrane is a specially treated material that allows the conduction of positively charged ions while not allowing electrons to pass through it. The catalyst is made of a platinum powder coated on a carbon paper or cloth. The catalyst is porous to maximize the surface area that can be exposed to hydrogen and oxygen [37, 39].

The hydrogen gas, extracted using reformer from the fuel, is supplied at the anode. Air as source of oxygen is supplied at the cathode. At the anode, the pressurized hydrogen molecules break into electrons and positive ions with the help of a catalyst. The positively charged protons diffuse from the anode through one side of the electrolyte membrane and migrate toward the cathode, while the electrons go from the anode to the cathode through an exterior circuit to recombine with the hydrogen protons and oxygen molecules at the cathode to produce water and provide electric power along the way. [30, 32, 33, 36, 40]. The following reactions take place at the anode and the cathode:

$$\mathrm{H_2 \rightarrow 2H^+ + 2e^-} \qquad \text{(Anode reaction)}$$

$$\mathrm{\frac{1}{2}O_2 + 2H^+ + 2e^- \rightarrow H_2O} \qquad \text{(Cathode reaction)}$$

The overall reaction can be expressed as:

$$\mathrm{H_2 + \frac{1}{2}O_2 \rightarrow H_2O} \qquad \text{(Overall reaction)}$$

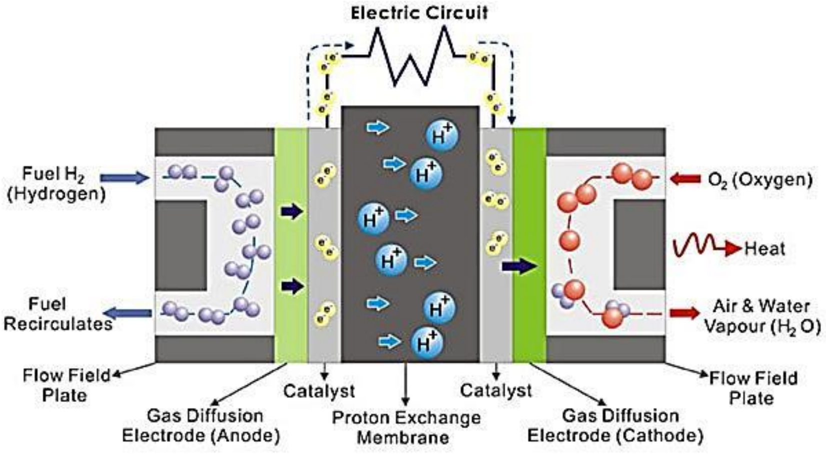

$Fig.$ 1.3 Schematic diagram of PEMFC

At temperature of 25° C and pressure of 1 atm, the theoretic DC voltage of a single PEMFC is 1.23 V theoretic. However, the open circuit voltage of a single PEMFC is approximately 0.7 V in practice because of irreversible voltage losses. PEMFCs have become an important choice for development of

FC based DG systems, and for other emerging applications of FCs [40]. However, there are a number of problems that need to be overcome to make PEMFCs a universal choice. The platinum used in catalyst is expensive. The use of impure hydrogen causes deterioration of electrolyte and catalyst materials which lead to replacement of entire FC after limited operation. Hence, an important issue is development of safe hydrogen, distribution and storage systems.

1.4.4 Electrical Characteristic of Fuel Cell

The operation of a FC is similar to that of a battery in that a FC employs two electrodes and produces DC voltage. One key advantage that FC has over battery is the unlimited amount of power that can be produced as long as fuel is supplied. However, as the amount of current is increased, the voltage drop is increased. The major factors that contribute to this voltage drop are activation loss, ohmic loss and concentration loss [29, 41]. The performance of the FC is generally characterized by the polarization curve, which is a plot of the FC voltage versus load current as shown in $Fig.$ 1.4. The polarization curve is computed by using the Tafel equation, which subtracts the various voltage losses from the open circuit DC voltage. The main factors which affect the polarization curve are cathode and anode pressures and FC temperature [42].

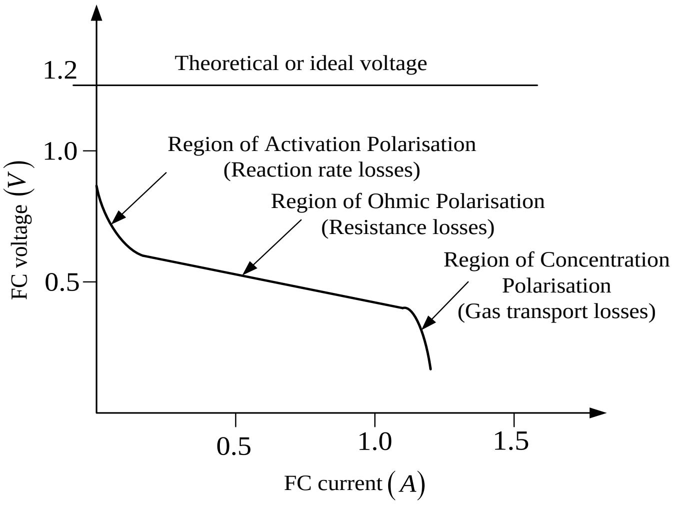

$Fig.$ 1.4 Polarization curve of PEMFC

The voltage drop across the FC associated with low currents is due to the activation loss inside the FC. Activation loss is the sluggish response of the electrochemical reaction of hydrogen and oxygen as a result of electrode kinetics. This creates a highly nonlinear voltage drop. The voltage drop in the middle of the curve is due to the ohmic loss in the FC. Ohmic loss originates from the flow of electrons through the electrolyte and electrodes. Ohmic losses are essentially linear and are directly proportional to the FC current. The output voltage at the end of the curve drops sharply as the load current increases. This is the result of concentration loss. Concentration loss results from the inability of the surrounding material to maintain the initial concentration of the fuel [27, 29, 30, 41].

1.4.5 Modeling of Fuel Cell

Dynamic simulation models of FCs are a powerful tool to investigate FC transient responses when operating conditions change with time and for designing appropriate interfacing circuits and controllers in practical FC power generation systems [33]**.** The FC models reported in literature are chemical, experimental or electrical [33, 41, 43-47]. The chemical models include the electrochemical and thermodynamic phenomenon inside the FC. The experimental models are derived from experimental data and they represent the FC by empirical equations applied to predict the effect of input parameters on the polarization curve of the FC without examining in depth the physical and electrochemical phenomena involved in FC operation. The electrical models represent the FC by electrical circuit elements and do not include the FC thermodynamics. In all approaches of modelling, the model parameters are obtained either empirically or by performing some tests on the real FC. The lack of information about the exact values that should be used for the FC modelling parameters is the major difficulty in obtaining an accurate dynamic model of FC [33, 37, 48].

The experimental based model of FC developed by *Prabha et al.* [49] represents the FC by empirical expressions and does not include the FC thermodynamics. It does not represent the effect of operating parameters such as gas inlet pressures, flow rates, compositions and temperature. *Soltani and Bathee* [44] have reported a semi-empirical dynamic model of PEMFC that can address the effect of changes in fuel pressures and operating temperature. *Al-Baghdadi* [29] have presented a mathematical model to study the performance of PEMFC at different operating parameters and compared with the available experimental results. *Yu et al.* [41] have developed a chemical model which includes complex chemical and thermodynamic phenomena such as mass transport, heat transfer and gas diffusion processes inside the FC. *Wang et al.* [50] have used equivalent electrical circuits to represent the electrochemical and thermodynamic phenomena inside the PEMFC. The dynamic model of SOFC developed by *Sedghisigarchi and Feliachi* [51] based on electrochemical and thermal equations, accounts for temperature dynamics and output voltage losses. *Souleman et al.* [48] have proposed an FC model which is generic and able to represent the behaviour of most FCs fed with hydrogen and air. The proposed model which requires a few variables from FC manufacturer's datasheet is validated with datasheet curve and with experimental results from a real FC stack. *Puranik et al.* [36] have worked on neural network modeling of PEMFC. The nonlinear dynamics of the PEMFC is effectively modeled using two-layer recurrent neural network.

1.4.6 Converter Interface to Grid-Connected FC System

The commercially available FC stack generates voltage in the range of 25-50 V. The power electronic interface plays an important role to convert the FC stack low output DC voltage into suitable form for grid-interfacing. This is achieved by using a combination of DC-DC converter in series with DC-AC inverter forming multistage conversion [41]. The efficiency of the system depends upon conduction and switching losses and cost of the system depends upon the total component count. Thus the selection of suitable topology, switching frequency and controller determines the overall performance and cost of the FC grid-interfaced system [45]. Various review works on FC technologies and power electronic interface is available in literature [12, 25, 41, 52, 53].

With the requirement of low cost and efficient power interface for FC applications, different DC-DC converter topologies and DC-AC inverter topologies have been proposed by different authors. The non-isolated DC-DC boost converter is preferred to step up DC voltage from one level to another due to its high efficiency and lower component count. The isolated DC-DC converter topologies like push pull, half bridge, and full bridge converters have benefits of high boosting ratio and protective feature [4, 12, 25, 28, 54]. However, the problem associated with push pull converter is that the half portion of the transformer cannot be symmetrically wound, resulting in transformer saturation under full load conditions [4]. This makes its use restricted to low and medium power applications. Alternatively, the half bridge converter with large transformation ratio can be used for high power applications. The full bridge converter although requires more number of switches yet it offers advantages in terms of reduced device current ratings, transformer turns ratio and alleviated voltage and current stress across switching devices. The full bridge converter is thus suitable for high power applications [24, 25, 54]. While in DC-AC inverter, the conventional pulse width modulated inverter gives better performance due to higher efficiency and simplicity in control, the Z source and LLCC inverter can be used if there is no electrical isolation required between FC and load [25].

1.4.7 Literature Review on FC Systems

Different works have been carried out on various aspects of grid-interfaced FC system and reported in literature. In [55] *Hatziadoniu et al.* have presented a simplified dynamic model of a grid-connected FC power plant. *El-Sharkh* [34] have proposed an integrated dynamic model for a FC power plant which includes a FC model, a gas reformer model and a power conditioning unit block to control the active and reactive power output from FC plant for standalone application. *Sedghisigarchi and Feliachi* [56] have analyzed the stability of power distribution systems containing SOFCs as DGs. *Wang et al.* [28] have presented the modeling and control of PEMFC DG system with focus on the active and reactive power control from the FC system to the utility grid. An overall evaluation of FC power plant in terms of stack modeling, power flow control and power quality has been carried out by *Tanrioven and Alam* [42]. *Nehrir et al.* [30] have reported a grid-side converter control consisting of two cascaded loops, a fast internal current loop to regulate the grid current, and an external voltage loop to control the DC-link voltage. *Dai et al.* [57] have addressed power flow control problem of a grid-connected inverter in DG applications. *Park et al.* [58] have studied the active and reactive power flow control for Solid-Oxide FCDG system. *Kirubakaran et al.* [25] have presented a DSP-controlled single-stage power electronic interface for FC based generation for grid-connected applications. The real time control in dq reference frame developed in MATLAB is interfaced with DSP TMS320F2812 to generate pulses for the inverter. *Jain et al.* [24] have presented the modelling, design, simulation and experimental investigations of a single-stage power electronic interface for PEMFC for standalone application as well as for grid interface with control scheme implementation in dq reference frame with an objective of reducing the component count resulting in increased reliability and low losses. The main focus in recent years has been on single-stage power conversion for FCDG system and further work is required for the same.

1.5 PHOTOVOLTAIC POWER GENERATION

With increasing advancements in Photovoltaic (PV) technology and its growing popularity as an alternative to conventional energy, PV based systems are being increasingly employed for both stand-alone and grid-connected applications [59]. Despite issues related to high penetration levels with grid-connected systems, they have attracted tremendous efforts from researchers owing to the advantages that they offer in terms of no emission electricity generation and high utilisation [1, 60, 61].

Photovoltaic cell is a non-polluting energy source of electricity that uses no fuel other than sunlight, gives off no waste and has no moving part when it operates. Thus, it reduces emission of polluting gases which are generated from conventional fuel burning power plants thus decreasing the impact of energy generation on the environment [3]. With the modular characteristic, it can be constructed of any size depending upon the requirement. Moreover, it requires minimal maintenance and has a life span of more than 30 years with stable efficiency [16, 59, 62].

1.5.1 Solar Energy

Solar energy is one of the most abundant of all the renewable energy resources. The electromagnetic waves from the sun are referred to as the solar radiation. The amount of sunlight received on the earth depends on several factors including geographical location, time of the day, season, local landscape and local weather. The range of wavelength of light that reaches the earth varies between 300 nm to 400 nm approximately. The density of power radiated from the sun at the outer atmosphere is 1.373 kW/m^2. A part of this energy is absorbed and scattered by the earth's atmosphere. The sunlight incident on earth's surface has a peak density of 1 kW/m^2 at noon in the tropics. The PV technology is essentially concerned with the conversion of this energy into usable electrical form [31, 63, 64].

1.5.2 Solar or Photovoltaic Cell

A PV cell is basically a semiconductor diode whose $p-n$ junction is exposed to light. PV cells are made of several types of semiconductors using different manufacturing processes. Silicon PV cells are composed of a thin silicon film connected to electric terminals. One of the sides of the silicon layer is doped to form the $p-n$ junction. A thin metallic grid is placed on the Sun-facing surface of the semiconductor. $Fig.$ 1.5 [65] shows the cross-section of a PV cell. The incidence of light on the PV cell generates charges when the energy of the incident photon is sufficient to detach the covalent electrons of the semiconductor. This phenomenon depends on the semiconductor material and on the wavelength of the incident light. These generated charge carriers originate an electric current if the cell is short-circuited. Thus the PV phenomenon can be described as the absorption of solar radiation, the generation and of free carriers at the $p-n$ junction and the collection of these electric charges at the PV device terminals [66].

The rate of generation of electric carriers depends on the flux of incident light and the capacity of absorption of the semiconductor. The absorption capacity depends mainly on the semiconductor bandgap, the reflectance of the cell surface, the intrinsic concentration of carriers of the semiconductor, the electronic mobility, the recombination rate, the temperature, and several other factors. The solar radiation is composed of photons of different energies. The photons with energies lower than the bandgap of the PV cell are useless and generate no voltage or electric current. Photons with energy superior to the bandgap generate electricity, but only the energy corresponding to the bandgap is used and the remainder of energy is dissipated as heat in the body of the PV cell. Silicon is not the only and probably not the best semiconductor material for PV cells, but it is the only one whose fabrication process is economically feasible in large scale. Other materials can achieve better conversion efficiency, but at higher and unfeasible cost [63, 67].

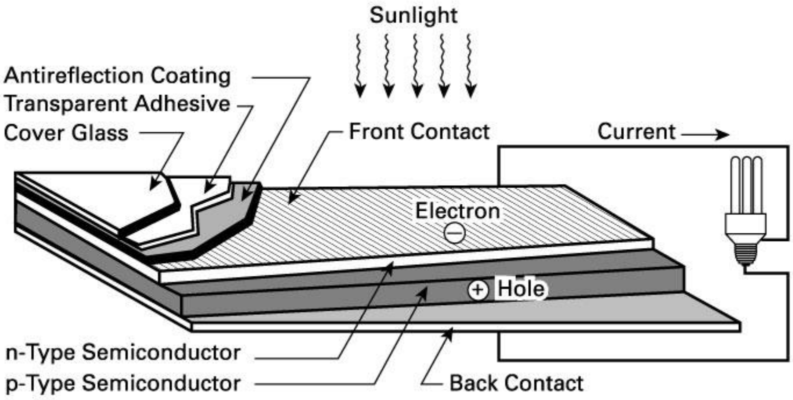

$Fig.$ 1.5 Structure of a Photovoltaic Cell

1.5.3 Photovoltaic Module, Panel and Array

In order to obtain the appropriate voltage and output for different applications, PV cells are interconnected in series for larger voltage and in parallel for larger current to form the PV module. Thus PV module is the smallest complete environmentally protected assembly of interconnected PV cells. In a series connection the same current flows through all the cells and the voltage at the module terminals is the sum of the individual voltages of each cell. When modules are connected in parallel the current is the sum of the individual cell currents and the output voltage is that of a single cell [68]. PV panel is a group of modules fastened together, pre-assembled and wired, designed to serve as an installable unit in an array. PV array is a mechanically integrated assembly of a number of PV panels or modules, mounted on the same plane with electrical connections to provide enough electrical power for a given application. The connection of PV panels in an array is similar to the connection of PV cells in a PV module. To increase the voltage, the PV panels are connected in series and to increase the current they are connected in parallel [63].

1.5.4 Current-Voltage Curve of a Photovoltaic Array

$Fig.$ 1.6 shows the $I-V$ characteristic of a PV array for a certain irradiance G and a certain temperature T. The PV array can be operated at any point along its $I-V$ curve. Two important points on this curve are the open circuit voltage V_{oc} and short circuit current I_{sc}. V_{oc} is the maximum voltage at zero current, whereas I_{sc} is the maximum current at zero voltage. For a silicon PV cell at standard test conditions of irradiance and temperature, V_{oc} is approximately 0.6-0.7 V and I_{sc} is around 20-40 mA for every square cm of PV cell area. I_{sc} is proportional to the irradiance G whereas V_{oc} is proportional to the logarithm of irradiance. I_{sc} increases linearly with temperature T whereas V_{oc} decrease with temperature. Thus the $I-V$ curve changes as the temperature and insolation levels change [69]. The $I-V$ curve of the PV array shows that there is a unique point on the $I-V$ curve at which the PV cell generates maximum power. This point is termed as maximum power point denoted by ($V_{mp,}\ I_{mp}$) on the $I-V$ curve. Thus a PV cell can be characterized by the following fundamental parameters: $V_{oc,}\ I_{sc,}\ V_{mp,}\ I_{mp}$. Fill factor is a term describing how square the $I-V$ curve is and given as:

$$FF = \frac{P_{mp}}{V_{oc} I_{sc}} = \frac{V_{mp} I_{mp}}{V_{oc} I_{sc}}$$

To maximise the output power of the PV cell, steps are taken during fabrication to maximise the three basic cell parameters: V_{oc}, I_{sc} and the FF.

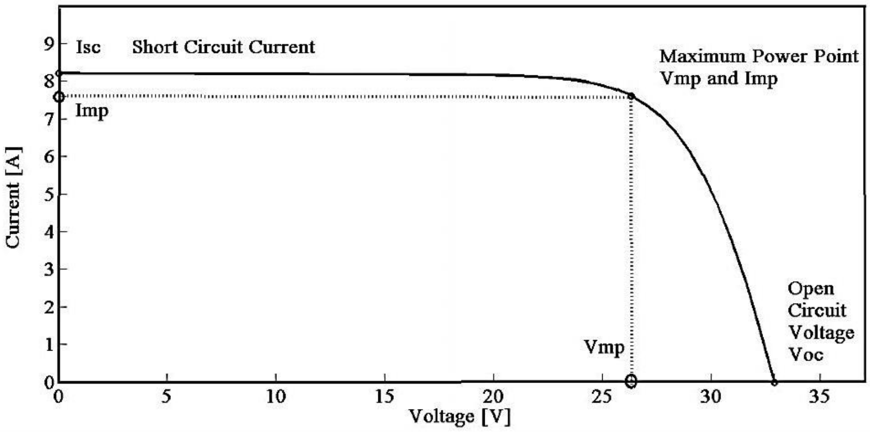

$Fig.$ 1.6 Current-Voltage curve of a PV array

1.5.5 Photovoltaic Array Modeling

Different PV array models have been reported in the literature. The single-diode circuit model of PV accounts for the photo-generated current and the physics of the $p-n$ junction. The two-diode circuit model of PV also includes the effects of recombination of carriers, which are dominant at low voltage and low irradiance [70-72]. A three-diode circuit model of PV further includes the effect of large leakage current through peripheries [67, 73]. The single-diode circuit is the most commonly used model for simulation studies, since it offers a reasonably good trade-off between simplicity and accuracy [68, 74, 75].

1.5.6 Converter Interface to Grid-Connected PV System

The rapid growth of the solar industry over the past several years has expanded the importance of PV system design and application for more reliable and efficient operation, both in stand-alone and grid-connected mode. For a PV system, the voltage output is a constant DC whose magnitude depends on the configuration in which the PV cells/modules are connected. On the other hand, the current output from the PV system primarily depends on the available solar irradiance. The main requirement of power electronic interfaces for the PV systems is to convert the generated DC voltage into a suitable AC for consumer use and utility connection. Generally, the DC voltage magnitude of the PV array is required to be boosted to a higher value by using DC-DC converters before converting them to the utility compatible AC [76]. The DC-AC inverters are then utilized to convert the voltage to 50 Hz AC. The process of controlling the voltage and current output of the array must be optimized based on the weather conditions. Specialized control algorithms have been developed called Maximum Power Point Tracking (MPPT) to constantly extract the maximum amount of power from the array under varying conditions [5, 77-79]. The MPPT control process and the voltage boosting are usually implemented in the DC-DC converter, whereas the DC-AC inverter is used for grid-current control [80].

1.5.7 Photovoltaic System Configuration

PV systems can be structured into several operational configurations. Fig 1.7 (a) shows the configuration where a centralized inverter is used. PV modules are connected in series and/or parallel and connected to a centralized DC-AC converter. The primary advantage of this design is that this system has the lowest design cost because of the presence of only one inverter. Fig 1.7 (b) shows the configuration of a string-array PV system. The series of PV panels are strung together in series and interconnected to the utility with one inverter per string. This is especially useful when multiple strings are mounted on fixed surfaces in different orientations. The disadvantage to this configuration is the increased cost due to additional inverters.

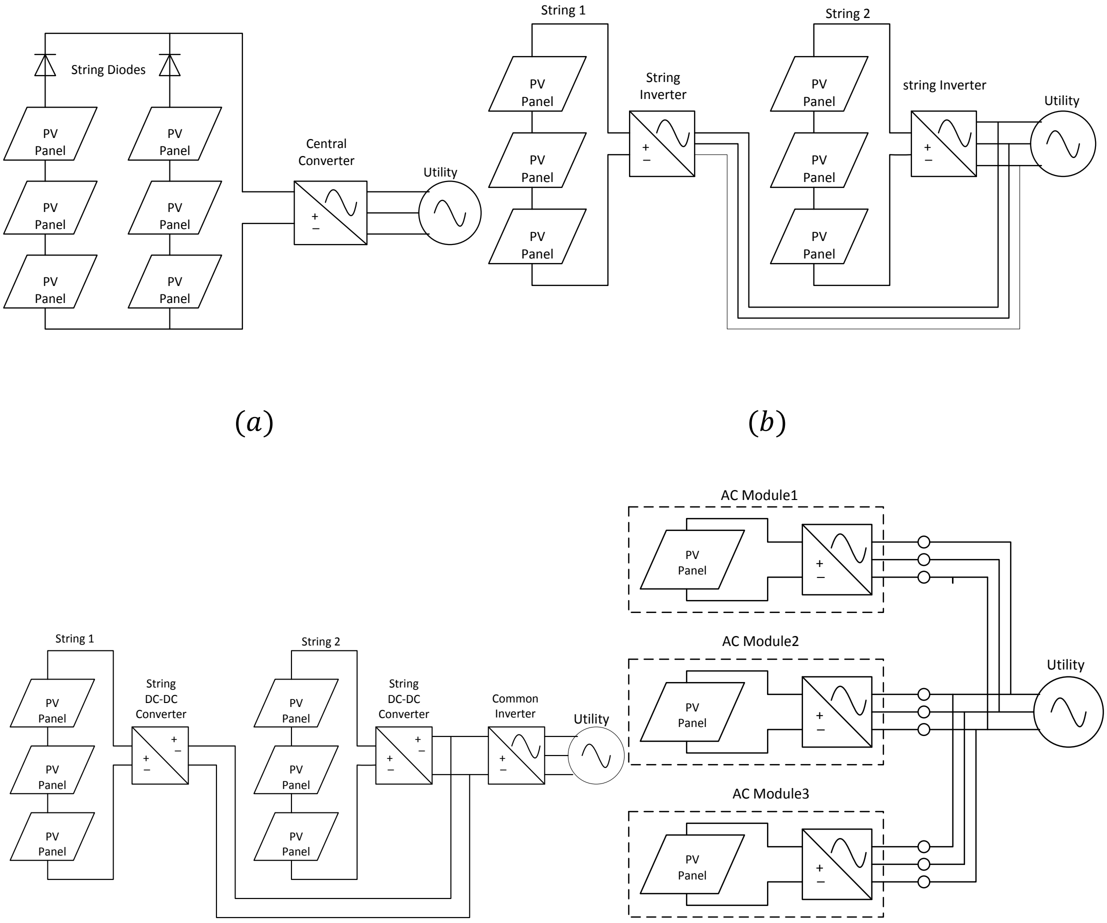

(a) (b)

(c) (d)

$Fig.$ 1.7 Photovoltaic Configurations (a) Centralized PV Configuration (b) PV panels in strings with individual inverters (c) PV panels in a multi-string configuration (d) AC-Module PV configuration

Multi-string inverter configuration shown in $Fig. 1.7\ (c)$ has several strings that are interfaced with their own DC-DC converter for voltage boosting and are then connected to a common DC bus. A common DC-AC inverter is then used for utility interfacing. $Fig. 1.7\ (d)$ shows a configuration where each PV module has its own inverter. This design is also known as an AC-module. Advantage of this type of system is that it is easy to add modules because each module has its own DC-AC inverter and the connection to the utility is made by connecting the inverter AC field wirings together [16, 81-83].

1.5.8 Maximum Power Point Tracking

The position of the maximum power points on the PV module characteristic depends strongly on the solar radiation and the cell temperature. Tracking the Maximum Power Point (MPP) of a PV array is usually an essential part of a PV system. Over the years, many MPPT methods have been developed and implemented. These techniques can be classified as either direct or indirect methods. The problem considered by MPPT techniques is to automatically find the voltage V_{mp} or current I_{mp} at which the PV array should operate to obtain the maximum power output P_{max} under a given temperature and solar irradiation and thus continuously tune the PV energy system so that it draws maximum power from the solar array regardless of weather or load conditions [84]. The Perturb and Observe method and the Incremental Conductance method [85] , as well as variants of those techniques are the most widely used. *Esram and Chapman* [84] and *Hohm and Ropp* [86] have analysed several MPPT techniques taken from literature such as hill climbing, perturb and observe, incremental conductance, fractional open-circuit voltage, fractional short-circuit current, fuzzy logic control, neural network control and ripple correlation control. These MPPT methods vary in complexity, required sensors, convergence speed, cost, range of effectiveness, implementation hardware, popularity, etc [16, 84, 87].

Perturb and Observe Method - In Perturb and Observe (P&O) method, periodic incremental or decremental perturbations are imposed on the PV system output voltage and the resulting power output is compared with the value in the last perturbation cycle. If the operating voltage of the PV array is perturbed in a given direction and if the power drawn from the PV array increases, the operating voltage must be further perturbed in the same direction; if the power drawn from the PV array decreases, the direction of the operating voltage perturbation must be reversed [68, 84, 86, 88-90]. The P&O method is known for its simple implementation and low cost, but at steady state the operating point deviates from and oscillates around the MPP giving rise to the waste of some amount of available energy. Further, the P&O method oscillates close to the MPP when atmospheric conditions are constant or slowly changing. However, the P&O method fails to track the MPP effectively with rapidly changing atmospheric conditions [88, 90].

Incremental Conductance - The Incremental Conductance (IC) method has good accuracy and efficiency. This method tracks the MPP of the PV module by comparing incremental conductance with instantaneous conductance. As a result, under rapidly changing atmospheric conditions, this method performs well, but the response time for finding the MPP is increased due to the relatively complex computations required by the control algorithm. Its implementation is expensive. Therefore, it loses cost efficiency for small-scaled PV applications [68, 84, 88-92].

Short circuit current method - The MPP tracking method using the short circuit current (SCC) of the PV module exploits the fact that the operating current at the MPP of the solar array is linearly proportional to its SCC. Under rapidly changing atmospheric conditions, this method has a relatively fast response time for tracking the MPP. However, the control circuit is complicated and both the conduction loss and the cost of the MPPT converter are relatively high [84, 90, 93].

Open circuit voltage method - Open circuit voltage (OCV) of the PV module method employs the fact that the operating voltage of the PV module at the MPP is linearly proportional to its OCV. Although the method is cost effective, its application results in considerable errors in MPP tracking and consequent energy losses [84, 90, 93].

1.5.9 Literature Review on PV Systems

Many of the recent works have investigated different aspects of PV systems. *Villalva et al.* [67] have developed a mathematical model of PV array by using the following information from PV array datasheet: open circuit voltage, short circuit current, maximum output power, voltage at the MPP, current at the MPP, current/temperature coefficient and voltage/temperature coefficient. *Jain and Agarwal* [94] have presented a comparison of various MPPT techniques applied to single-phase grid-connected PV systems using buck-boost topology inverter. The MPPT techniques are compared on the basis of the time taken to track the MPP, operating point oscillations near MPP, dependence of the algorithms on PV array configuration and on the basis of the energy extracted from the PV source. *Casadei et al.* [95] have developed an MPPT algorithm to allow an array of PV modules to be connected to the single-phase grid by using a single-stage converter by exploiting the current and voltage oscillations caused by the pulsations of the instantaneous power, which are inherent in single-phase systems. This simple structure yields higher efficiency and reliability when compared with standard solutions based on double-stage converter configurations. *Libo et. al.* [96] have presented a single-stage three-phase grid connected PV system with modified Incremental conductance MPPT method so as to improve system stability during rapidly changing solar insolation. Reactive power compensation based on the instantaneous reactive power theory is simultaneously realised in the PV system to compensate the reactive power of the local load. *Yazdani and Dash* [97] have proposed a control strategy for a three-phase PV system connected to distribution network which is based on an inner current control loop and an outer DC-link voltage control loop. The outer DC-link voltage control loop enables control and maximisation of the real power output. The current control loop makes the PV system protected against external faults [98]. *Ropp and Gonzalez* [99] have worked on single-phase grid connected PV system with Perturb and Observe MPPT implemented in the inverter system. *Kim et al.* [75] have presented a two-loop controller in dq reference frame for a grid-connected PV system inverter and analysed the PVDG system for power control dynamics, harmonics, anti-islanding performance and response to grid faults. *Ghoddami and Yazdani* [1] have proposed a single-stage three-phase PV system with improved energy yield under partial shading conditions. *Yazdani et al.* [68] have presented modelling guidelines for power system simulation studies for grid-connected single-stage three-phase PV system. Most of the recent works have laid emphasis on single-stage conversion and further work is required to investigate the various aspects of single-stage grid-interfaced photovoltaic system.

1.6 CONTROL STRUCTURES OF GRID-INTERFACING VSIs

The control strategy applied to the grid-side converter consists mainly of two cascaded loops. There is a fast internal current loop which regulates the grid current, and an external voltage loop which controls the DC-link voltage. The control is implemented using either stationary reference frame or synchronous reference frame. When hysteresis current control is used, the choice of reference frame is of no practical significance. The advantage associated with hysteresis controller is the simplicity of implementation and its robustness while a number of disadvantages exist. The current is not strictly limited within the hysteresis band, the switching frequency is not fixed and the inverter output current contains sub-harmonic and inter-harmonic components.

The problem of the variable switching frequency can be overcome using the proportional-integral (PI) control scheme where the output of the PI controllers act as reference signals and compared to the triangular carrier to determine the inverter switching. Thus inverter switching frequency is fixed and the harmonics in the inverter output current appear as sidebands centered around switching frequency and its multiples. However, when the PI control scheme is adopted, the stationary reference frame is not preferred, because of the steady-state amplitude and phase errors introduced by the PI regulators. In contrast, when currents are transformed to the synchronous reference frame, the PI regulators achieve zero steady state error. Thus the control strategies can be classified with respect to the reference frame in which they are implemented [16, 100]:

1.6.1 Synchronous dq Reference Frame Control

Synchronous reference frame control or dq control, uses $abc \rightarrow dq$ transformation to transform the grid current and voltage into dq reference frame that rotates synchronously with the grid voltage. Thus the control variables become DC values making filtering and controlling easy. A schematic of the dq control is shown in $Fig. 1.8\,(a)$. In this structure, the DC-link voltage is controlled in accordance to the necessary output power. The output of the DC-link controller is the reference for the active current controller. The reactive power is controlled according to the reactive power reference imposed to the system. The output of the reactive power controller is the reference for the reactive current controller. If the reactive power control is not allowed, the reference for the reactive current is set to zero. The dq control structure is normally associated with PI controllers since they provide satisfactory behaviour when regulating DC variables.

Cross-coupling terms and voltage feed-forward are usually used for improving the performance of PI controllers. However, with all these improvements, the compensation capability of the low-order harmonics in the case of PI controllers is very poor. If the current controller has to be immune to the grid voltage harmonic distortion, harmonic compensator for each harmonic order should be designed. Thus, the complexity and computational burden of the control scheme makes the implementation very difficult [16, 100]. The phase angle used by the $abc \rightarrow dq$ transformation module is extracted from the grid voltages. Filtering of the grid voltage and using arctangent function to extract the phase angle is one method. However, the phase-locked loop (PLL) [101] technique is the state of the art in extracting the phase angle of the grid voltages in the case of DG systems [102].

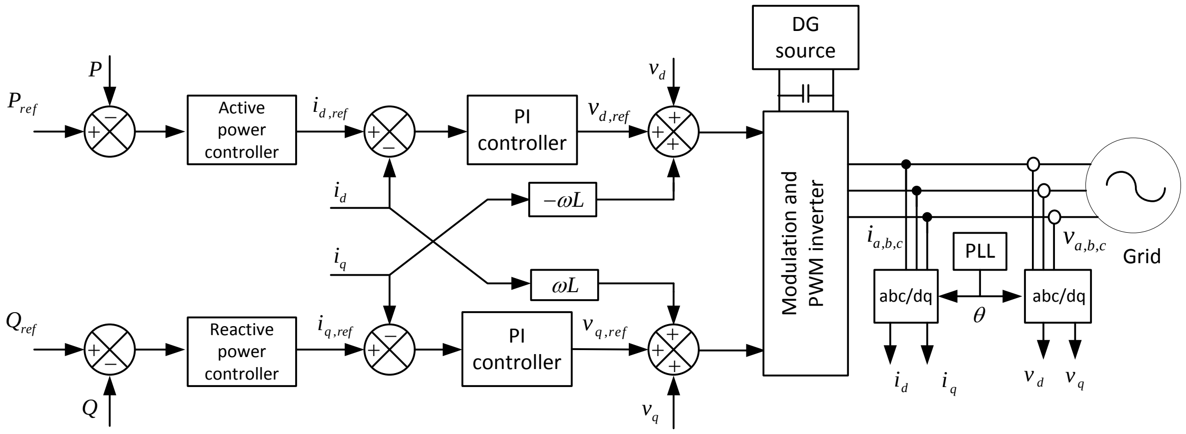

$Fig. 1.8\,(a)$ Synchronous dq reference frame control strategy

1.6.2 Stationary abc Reference Frame Control

In abc reference frame control there is an individual controller for each grid current. Non-linear controllers like hysteresis or dead beat are preferred due to their high dynamics. The performance of these controllers is proportional to the sampling frequency. Digital systems such as digital signal processors and field-programmable gate array provide easy implementation for such systems. A possible implementation of abc control is depicted in $Fig.1.8\ (b)$. Using the $dq \rightarrow abc$ transformation, three current references are created. Each of them is compared with the corresponding measured current, and the error goes into the controller. If hysteresis or dead-beat controllers are employed in the current loop, the modulator is not required. The output of these controllers is the switching states for the converter switches.

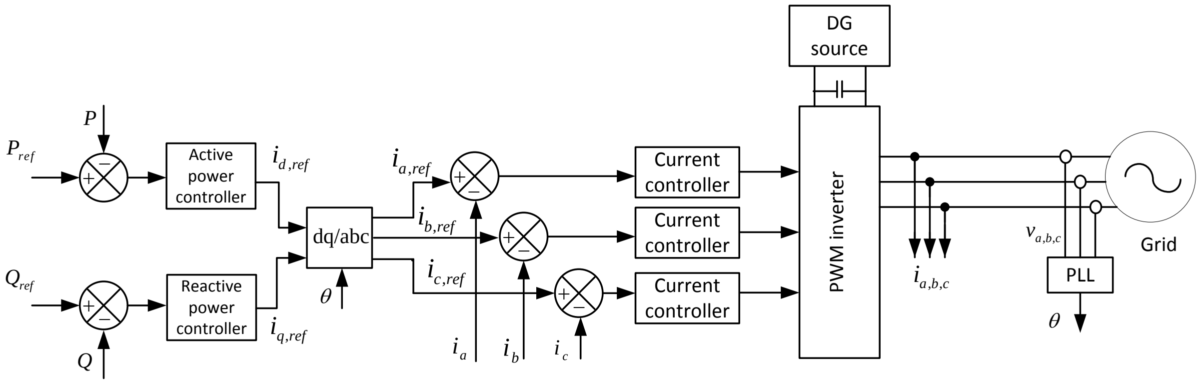

$Fig.1.8\ (b)$ Stationary abc reference frame control

1.7 POWER QUALITY PROBLEMS

With the increase in energy conversion systems utilizing power electronic devices, we have seen the emergence of Power Quality (PQ) as a major area of research. The power electronic technology has played a major role in creating power quality problems and simple control algorithm modifications to this same technology can often play an equally dominant role in enhancing overall quality of electrical energy available to end-users [63]. Power quality issues include all possible situations in which the waveform of supply voltage and load current deviate from the sinusoidal waveform along with variation of base frequency and amplitude beyond the permissible limit. The power quality disturbances cover sudden, short duration deviations e.g. impulsive and oscillatory transients, voltage dips, short interruptions. Another type of power quality problem is distortion of the voltage/current waveforms from the normal sinusoidal wave shape which are known as the harmonic distortions. Applications such as switched-mode power supplies, DC arc furnaces, electronic fluorescent lamp ballasts, adjustable speed drives, and flexible AC transmission components are always a cause of concern. These power quality problems can lead to operational and life expectancy problems for other equipment. The power quality problems can be divided into following categories [63]:

- Steady-state voltage magnitude and frequency,
- Voltage sags,

- Harmonics,
- Voltage fluctuations and flicker, and
- Transients

1.8 HARMONICS

Harmonics are the additional frequency components present in the mains voltage or current which are integer multiples of the mains frequency. Harmonic distortion originates due to the nonlinear characteristics of the devices and loads on the power system. These harmonic distortions create problems to both utility and customers and are considered one of the most significant reasons for power quality problems [103, 104]. While switching converters produce harmonics because of the non-linear relationship between the voltage and current across the switching device, harmonics are also produced by a large variety of conventional equipment including power generation equipment, induction motors, transformers, magnetic-ballast fluorescent lamps and AC electric arc furnaces [105]. All these devices cause harmonic currents to flow and some devices, actually, directly produce voltage harmonics. Any AC current flowing through any circuit at any frequency will produce a voltage drop at that same frequency.

Harmonic currents, which are produced by power electronic loads, will produce voltage drops in the power supply impedance at those same harmonic frequencies [106]. Because of this inter-relationship between current flow and voltage drop, harmonic currents created at any location will distort the voltage in the entire supply circuit [107]. Harmonics, thus, increases power system losses, damage sensitive loads, cause excessive heating in rotating machinery, create significant interference with communication systems, generate noise on regulating devices and control systems, etc. [108, 109]. Therefore, harmonic and reactive current compensation has become a major concern.

1.9 ACTIVE POWER FILTER

In recent years with the development of power semiconductor technology, power electronics based devices such as static VAR compensators, adjustable speed drives and uninterruptible power supplies are widely employed in various applications. Because of their nonlinear $V - I$ characteristics these devices draw current with harmonic content and reactive power from AC mains. Current harmonics drawn by nonlinear loads disturb the waveform of the voltage at the Point of Common Coupling (PCC) and lead to the voltage harmonics that the other linear loads and sensitive electronic equipments have to deal with [110, 111]. Conventionally, to reduce harmonics passive LC filters and to improve power factor of the AC loads capacitor banks were used [112]. However these solutions have the demerits of large size and weight, fixed compensation design, increased operating losses and risk of resonance occurrence [105, 106]. Power system and power electronics engineers made an effort to develop dynamic and adjustable solution to these power quality problems and a concept of Active Power Filter (APF) was introduced a couple of decade ago [113].

Nowadays active power filters are used to provide compensation for harmonics in current, reactive power, voltage distortions, sag/swell in voltage at PCC, unbalance in current, voltage flicker and terminal voltage regulation separately or simultaneously [110]. Various types of APFs have been reported in literature, and are classified based on converter types, configuration, objectives and their installations in power networks. APFs are categorized either shunt or series based on circuit configurations with load to be compensated and called shunt and series active power filters, respectively. In some applications, the combinations of several types of filters called hybrid filter is adopted to achieve greater benefits [106, 109, 111].

APFs are seen as a viable alternative over classical passive filter and reactive power compensation of non-linear loads. In general the APF are Pulse Width Modulated (PWM) inverters with capacitor or inductor on its DC-side. The PWM inverter switches are controlled such that it supplies a compensating current and cancels current harmonic on the AC-side by generating harmonics opposite to the load harmonics. This makes the source current almost sinusoidal. The design can cater to the requirements of either both harmonic and reactive power compensation or only harmonic compensation. In addition to the harmonics and reactive power compensation, APFs are also used to eliminate voltage harmonics, load balancing, regulation of the terminal voltage, suppression of voltage flicker etc. These wide ranges of objectives are achieved either individually or in combination depending on the requirements of control strategy and configuration.

Shunt Active Power Filter (SAPF) is the most viable solution for solving current harmonic, reactive power compensation, and load unbalancing problems widely presented in electrical distribution systems [114]. The SAPF operates as an active compensation device to mitigate the above mentioned power quality problems by drawing or supplying suitable compensating current from or to the utility, so that supply current can be maintained sinusoidal [115-117]. Three major areas are to be considered for SAPFs: estimating the compensating current, looking for possible converter topologies that may be used and exploring pulse modulation techniques that may actually generate and track the corresponding reference currents [104, 118].

1.10 ESTIMATION OF COMPENSATING SIGNALS FOR SAPF

One important aspect of compensation is the designing of a control algorithm for SAPFs to generate the required reference current [119]. Any inaccuracy in phase and magnitude of the reference currents result in incorrect compensation thus resulting in performance degradation. The control algorithm should be robust, simple, accurate and should give its best performance not only in ideal but also in distorted and/or unbalanced supply voltage conditions [115, 120]. The literature presents different solutions to compute the harmonic extraction for APFs. The methods are classified as direct and indirect methods [114]. The direct methods include the Fourier transform method [121], the instantaneous reactive power (IRP) theory [63] and the synchronous reference frame (SRF) theory [63]. On the other hand, the indirect methods include the use of enhanced phase-locked loop scheme or a controller such as PI to find the reference current. Among these solutions, the IRP and the SRF theories are the most addressed ones in the literature [104, 120, 122, 123].

1.10.1 Instantaneous Reactive Power Theory

According to this theory, the instantaneous source voltage and current signals in abc coordinates are transformed into two-phase $\alpha\beta$ orthogonal co-ordinates using Clark's transformation as follows:

$$\begin{bmatrix} v_{s\alpha} \\ v_{s\beta} \end{bmatrix} = \sqrt{\frac{2}{3}} \begin{bmatrix} 1 & -\frac{1}{2} & -\frac{1}{2} \\ 0 & \frac{\sqrt{3}}{2} & -\frac{\sqrt{3}}{2} \end{bmatrix} \begin{bmatrix} v_{sa} \\ v_{sb} \\ v_{sc} \end{bmatrix}, \quad \begin{bmatrix} v_{L\alpha} \\ v_{L\beta} \end{bmatrix} = \sqrt{\frac{2}{3}} \begin{bmatrix} 1 & -\frac{1}{2} & -\frac{1}{2} \\ 0 & \frac{\sqrt{3}}{2} & -\frac{\sqrt{3}}{2} \end{bmatrix} \begin{bmatrix} v_{La} \\ v_{Lb} \\ v_{Lc} \end{bmatrix}$$

The instantaneous reactive power p and the instantaneous reactive power are defined as:

$$p = v_{s\alpha} i_{L\alpha} + v_{s\beta} i_{L\beta}$$

$$q = v_{s\alpha} i_{L\beta} - v_{s\beta} i_{L\alpha}$$

Hence
$$\begin{bmatrix} p \\ q \end{bmatrix} = \begin{bmatrix} v_{s\alpha} & v_{s\beta} \\ -v_{s\beta} & v_{s\alpha} \end{bmatrix} \begin{bmatrix} i_{L\alpha} \\ i_{L\beta} \end{bmatrix}$$

The instantaneous active and reactive power contains DC as well as AC components due to fundamental and harmonic currents of load respectively. The active and reactive powers are filtered using high pass filters. The output of the high pass filters is extracted as harmonic active power $\tilde{p}$ and harmonic reactive power $\tilde{q}$. The reference compensating current i_c^* is calculated in such a way that it supplies the instantaneous reactive power q and the harmonic component of the instantaneous active power $\tilde{p}$. The reference compensating current i_c^* is obtained as:

$$\begin{bmatrix} i_{c\alpha}^* \\ i_{c\beta}^* \end{bmatrix} = \frac{1}{v_{s\alpha}^2 + v_{s\beta}^2} \begin{bmatrix} v_{s\alpha} & -v_{s\beta} \\ v_{s\beta} & v_{s\alpha} \end{bmatrix} \begin{bmatrix} \tilde{p} \\ \tilde{q} \end{bmatrix}$$

The reference compensating current in $\alpha\beta$ frame is transferred to abc frame using inverse Clark's transformation as:

$$\begin{bmatrix} i_{ca}^* \\ i_{cb}^* \\ i_{cc}^* \end{bmatrix} = \sqrt{\frac{2}{3}} \begin{bmatrix} 1 & 0 \\ -\frac{1}{2} & \frac{\sqrt{3}}{2} \\ -\frac{1}{2} & -\frac{\sqrt{3}}{2} \end{bmatrix} \begin{bmatrix} i_{c\alpha}^* \\ i_{c\beta}^* \end{bmatrix}$$

This method does not take into account the zero sequence components and hence the effect of unbalanced voltages and currents. The instantaneous reactive power theory is widely used for balanced non-linear loads such as rectifiers [114, 124].

1.10.2 Synchronous Reference Frame Theory

The control algorithm based on synchronous reference frame theory relies on Clarke's and Park's transformation. In this method, the load current signals are first transformed into stationary reference $\alpha\beta$ frame using Clarke's transformation and then to synchronously rotating reference dq frame using Park's transformation. The positive sequence component of load current is transformed to dq axes by generating positive sequence phase information using PLL. The DC quantity in the positive sequence waveform is the fundamental component of load current and the AC quantity include all the harmonic components. The negative sequence component of the load current is also transformed to dq axes by generating negative sequence phase information from the PLL. The negative sequence components of the load currents are subtracted from the positive sequence components of the load current, and the difference is transformed into abc co-ordinates using reverse Clarke's transformation. This method is suitable under balanced and unbalanced distorted source voltage and load conditions and hence considered better than the instantaneous pq theory. However it is complex to implement because of more number of transformations [124].

1.11 DISTRIBUTED GENERATION WITH ACTIVE POWER FILTER

In order to solve the above power quality problems, many APFs have been proposed in the recent years because the conventional passive filters used because of their low cost and high efficiency have demerits of fixed compensation, large size and resonance. The SAPF presents a dynamic solution best suited for the compensation necessities. The SAPF can compensate the unwanted reactive, unbalanced and harmonic load current components under non-sinusoidal supply voltage. The principle of operation of the SAPF is to supply the undesired harmonics and reactive power to the load, so that the mains current is of improved quality. But the installation of the SAPF requires additional costs. The cost of installing DG system is also large. Thus, the function of SAPF can be implemented with the DG system thus reducing the overall cost [8, 125].

With the objective of reducing the cost and increasing the efficiency, research is going on to utilise the grid-interactive DG system inverter also for active power filtering purpose. The function of APF is added in the existing inverter of DG system by making the necessary modification in the control circuit [8]. Various works on PV inverter with APF functionality in single-phase system and in three-phase system has been carried out. *Patel and Agarwal* [60] have investigated PV-APFs based on string-inverter, multi-string inverter and centralised inverter configurations for three-phase four-wire distribution systems. The control schemes of various inverter configurations are studied and their performance in meeting the reactive, harmonic and imbalance needs created by the linear/non-linear/unbalanced loads is evaluated under uniform and non-uniform radiation conditions. *Singh et al.*

[8] have proposed a novel control strategy where the grid interfacing inverter is utilised to inject real power generated from renewable energy source to the grid and/or operate as shunt active power filter. *Wu et al.* [126] have proposed a single-phase two-wire inverter system for photovoltaic power injection that can fully or partially perform APF functionality, process PV power, eliminate harmonic currents and improve power factor. *Mastromauro et al.* [127] have presented a single-phase photovoltaic inverter system that provides compensation of harmonic distortion at PCC using Incremental Conductance MPPT control algorithm. *Sung et al.* [128] and *Schonardie and Martin* [129] proposed dq based control of a three-phase grid-connected PV system with APF functions. *Gajanayake et al.* [130] and *Jung and Keyhani* [7] have presented a Z-source inverter based DG system for grid power quality improvement. *Cavalkanti et al.* [80] have proposed a system that provides photovoltaic generation as well as the functions of a unified power quality conditioner. The system is controlled for current harmonics and reactive power compensation simultaneously by using a converter operating as shunt active filter. The other converter is used as series active filter and it compensates voltage harmonics, sags and swells. Using only an inverter in photovoltaic energy conversion process, the system presents increased efficiency when compared to the conventional systems. The synchronous reference frame method is used to control the three-phase converters. *Tao et al.* [131] have proposed a line-interactive FC powered uninterrupted power supply system that can operate in both standalone and grid-connected modes in which the system injects constant power into the grid and also compensates for the reactive and harmonic current demanded by local loads. *Kuo et al.* [77] have proposed a single-stage PV energy conversion system with a novel fast tracking MPPT controller, which provides solar generation when insolation is adequate and active power line conditioning when solar insolation is inadequate. *Park et al.* [132] have applied the concept of pq theory to simulate a hybrid system with active filter functions. A novel concept of optimal utilization of a PV solar farms as a STATCOM during nightime in a PV-Wind hybrid system has been proposed by *Varma et al.* [133] and validated through MATLAB/Simulink simulations. *Bojoi et al.* [120] have proposed a DG system using H-bridge inverter providing harmonic and reactive power compensation for grid-connected operation employing current reference generator based on sinusoidal signal integrator and instantaneous reactive power theory with a repetitive current controller.

Most of these control schemes require various transformations and are difficult to implement hence the need for a simple control scheme for grid-interfacing inverter in distributed generation system that can compensate for customer as well as utility generated harmonics under unbalanced and varying load conditions along with active power transfer from DG to the grid and load reactive power demand support. Moreover, not much work has been presented for FCDG inverter being used as an APF which includes the control of FC active power requirement and hence a probable area of research.

1.12 PHOTOVOLTAIC – FUEL CELL HYBRID DG SYSTEM

When different types of energy sources are integrated into a DG system, it is called a hybrid DG system [134]. Several hybrid systems have been reported in literature [55, 135, 136]. The PV array does not incur any running or maintenance cost and has long life, hence an attractive energy source. However, there are some drawbacks associated with the PV power generation. The PV $V-I$ curve follows a non-linear relationship. Hence it is required to operate the PV array at its maximum power point to ensure maximum utilisation of its capacity. Further variation in solar insolation causes variation in PV generated power thus causing disturbance to the utility. No power generation during night time is another major drawback. The above mentioned drawbacks can be reduced if the PV source is coupled with a suitable auxiliary energy source. Various auxiliary energy sources such as FCs, battery, wind turbine, diesel generators etc. can be used in conjunction with the PV array. Batteries can provide only a short-term solution. Wind energy, though clean and renewable source, cannot provide a reliable solution. The diesel generator has the advantage of compact size and high energy density. However it is not environment friendly and has a high running cost.

In *Rahman and Tam* [137] have made a feasibility study of PV-FC hybrid energy system. Since then many works on PV-FC hybrid systems have been carried out [138-143]. *Tam and Rahman* [138] have proposed a PV-FC HDGS in which the two energy sources are connected to two inverters and a single multi-winding transformer for interfacing to the grid. However, it suffers from following drawbacks. It requires two inverters operated in parallel. It uses a low frequency multi-winding transformer which is heavy and costly. Further, individual contribution of each source cannot be controlled. The PV inverter control also does not have MPPT capability. *Ro and Rahman* [139] have reported a PV-FC system which also uses a two inverter topology in which an independent control of active and reactive power is achieved without any constraints. Further Neural network based MPPT has been incorporated in the PV inverter. Unlike the previous approaches where the PV and FC sources were connected to the common grid through separate inverters, *Ready and Agarwal* [140] have proposed a hybrid system where a single inverter is used to interconnect the PV and FC energy sources. This scheme has several advantages such as low cost and easy implementation. The PV and FC are first connected to a common DC-link and then to grid through a single inverter. *Khanh et al.* [141] have presented an efficient power management strategy for grid-connected PV-PEMFC hybrid system wherein the PV-FC source is connected to the main grid at the PCC to deliver uninterrupted power to the load at PCC. The proposed system can be operated in two control modes. In the unit-power control mode, the variations of load demand are picked up by the main grid because the PV-FC power is regulated to a reference value. In the other control mode the extra load demand is picked up by the PV-FC source. *Shahnia et al.* [142] have proposed a HDGS where power sharing algorithm is used to control its power management and one of the distributed generators in the microgrid is used as a power quality compensator for the unbalanced and harmonic load at PCC. The current reference generation for power quality improvement takes into account the active and reactive power to be supplied by the DG source which is connected to the compensator. However, there is still a need for an optimal design of PV-FC hybrid system which can provide maximum utilisation of PV system and optimal utilisation of FC system to provide clean energy to the PCC load and the grid and also provide reactive and harmonic compensation if the load connected at the PCC is non-linear thus providing maximum benefit from the hybrid system.

1.13 CONTRIBUTIONS FROM THE PRESENT WORK (Comment [2] [3])

Main contributions of the author are summarized below.

- *Design and analysis of a single-stage PEMFC based distributed generation system with active and reactive power flow control, thus simplifying the system topology. The grid-interfacing inverter control is designed to provide independent control of real and reactive power delivered from FC to the grid, the DC-link voltage control, grid synchronization and injected power quality control. An attempt has been made to address the following key challenges to make the technology viable:*
    - *Development of single-stage DC-AC conversion with low component count,*
    - *Regulation of active and reactive power from FC to the grid,*
    - *Harmonic control in inverter output voltage, and*
    - *Grid Synchronisation.*

  The load following analysis and fault analysis of the FCDG system is also performed to determine the system stability.
- *Design and analysis of FCDG system with active power flow control and reactive and harmonic compensation of linear/non-linear PCC load. The active power filtering capability is embedded in the control circuit of the inverter interfacing the FC to the grid. The grid-interfacing inverter is effectively utilized to perform the following functions:*
    - *Transfer of FC active power to the PCC,*
    - *Load reactive power demand support,*
    - *Current harmonic compensation at PCC,*
    - *Load current unbalance, and*
    - *Utility generated harmonic compensation.*

  All these objectives can be accomplished either individually or simultaneously. The control scheme has been designed for two different modes of operation:
    - *Simultaneous power quality enhancement and FC power injection, and*
    - *Only power quality enhancement.*

  The design works properly under non-sinusoidal voltage and compensates customer as well as utility generated harmonics under unbalanced and varying load conditions.

- *Design and analysis of single-stage grid-connected PV system. A two-loop control scheme is designed to control the power delivered from the PV system to the utility grid. The maximum power point tracking, grid synchronization, reactive power compensation, output current harmonic reduction is included simultaneously in the inverter control, thus simplifying the converter topology.*
- *Design and analysis of utility-interactive hybrid DG system consisting of PV and FC to realize a reliable power supply for a grid connected critical load so as to ensure maximum utilization of the PV array and necessary utilization of FC stack and also providing reactive and harmonic compensation at PCC. The author's main contributions to this work are:*
    - *Designing DC-DC converter for PV array with Incremental conductance MPPT thus extracting maximum power from PV array.*
    - *Designing DC-DC converter for FC stack for voltage boosting and extracting necessary power from FC.*
    - *Designing the inverter control to satisfy the grid active power requirement and also providing reactive and harmonic compensation of PCC non-linear load.*

1.14 ORGANIZATION OF THE THESIS

The thesis is organized in seven chapters and the content of each chapter is briefly outlined. The first part of the **Chapter 2** gives an overview of the FC technology and the FC stack modelling. The second part of the chapter presents a dynamic circuit model for a Proton Exchange Membrane FC based on its electrochemical and thermodynamic phenomena including the voltage losses and the double-layer charging effect.

Chapter 3 deals with analysis and design of a single-stage Fuel Cell grid-interfaced system with active and reactive power flow control. A Proton Exchange Membrane Fuel Cell based distributed generation system is analyzed by modeling various units of the FCDG system, performing mathematical analyses and simulation studies. Simulation in MATLAB and Processor-in-Loop simulation using Digital Signal Processor (DSP) TMS320F2812 is carried out and results presented to verify the operation and the control principle.

Chapter 4 deals with design and analysis of FCDG system with active power filtering capability embedded in control circuit of the inverter interfacing the FC to the grid for single-phase and three-phase systems. The aim is to control the active power supplied by the FCDG system while compensating harmonics and reactive currents caused by the nonlinear loads using SAPF. The designed controller either regulates the power flow between the FC and the grid or works as an APF or performs both the functions simultaneously. Simulation in MATLAB/Simulink environment and Processor-in-Loop simulation using DSP TMS320F2812 and experimentation is carried out and results presented for different modes of operation to verify the operation and the control principle.

The first part of **Chapter 5** gives an overview of the PV technology for converting solar energy into electrical energy and the modelling of PV array required for PVDG simulation studies. The second half of this chapter presents the modeling and design of a single-stage three-phase PVDG system with MPPT and reactive power control. The MPPT control, the output current control and the reactive power control is realized simultaneously in one power conversion stage thus simplifying the system topology. Simulation in MATLAB/Simulink environment is carried out to verify the operation and the control principle.

Chapter 6 proposes a utility-interactive hybrid distributed generation system consisting of PV and FC to realize a reliable power supply for a grid connected critical load where both the sources can be operated independently or in conjunction as per requirement. The proposed system ensures maximum utilization of the PV array and necessary utilisation of FC resulting in optimum operational costs. The power conditioning unit consists of two DC-DC boost converters where one of them is fed by a PV array and the other by an FC stack, and then connected to a common inverter interfacing the grid. The power circuit description, the control circuit for the PV DC-DC converter which extracts maximum power from the PV array, the control circuits for the FC DC-DC converter which regulates the required FC power, the control circuit for the DC-AC converter which apart from feeding active power to the grid also provides reactive power and harmonic compensation of PCC load, the algorithm implementation of MPPT in PV, and MATLAB simulation results are presented.

Chapter 7 summarizes the author’s work and gives the scope for future research work.

Appendix A gives the modelling of grid-interfacing voltage source inverter.

Appendix B gives the design of active power filter parameters.

Appendix C gives the design of DC-DC boost converter.

Appendix D gives the details of *experimentation (Comment [5])*.

Appendix E gives the MPPT control algorithms.

Chapter-2

GRID-INTERFACED FUEL CELL SYSTEM WITH ACTIVE AND REACTIVE POWER FLOW CONTROL

The first half of this chapter presents a dynamic circuit model for a Proton Exchange Membrane FC based on its electrochemical and thermodynamic phenomena. The second half of this chapter deals with the design of a single-stage grid-interfaced FC system with power flow control. A PEMFC based DG system is analyzed by modeling various units of the FCDG system, performing mathematical analysis and simulation studies.

2.1 FUEL CELL STACK MODELING

Dynamic model of PEMFC is required to understand the FC operation, investigate FC transient responses when operating conditions change with time and for designing appropriate interfacing circuits and controllers for practical FC systems [29, 33, 36, 37, 44, 46, 48, 64, 144]. The anode and cathode pressures and the operating temperature are known to affect the performance of PEMFCs. The presented dynamic model of a 0.5 kW PEMFC based on Avista Labs SR-12 500 Watt PEMFC stack models the open-circuit output voltage of the PEMFC, irreversible voltage losses in the PEMFC, formation of a charge double-layer in the PEMFC along with a mass balance and thermodynamic energy balance [50, 145]. The $V-I$ characteristics and $P-I$ characteristics of the PEMFC are obtained for different values of anode and cathode channel pressures. *Table 2.1* gives the nomenclature for PEMFC modeling.

2.2 PEMFC DYNAMIC MODEL DEVELOPMENT

Table 2.1 **Nomenclature for PEMFC Modeling**

A	Electron transfer coefficient
ϵ	Electrical permittivity
ΔH	Change in enthalpy
a, b	Constants in Tafel equation (V/K)
a_0	Constants in Tafel equation (V)
A_s	Area of each cell (m^2)
C	Capacitance due to charge double layer (F)
C_{FC}	Overall specific heat capacity of FC stack(J/mol-K)
C_i	Specific heat capacity of species I (J/mol-K)
$D_{i,j}$	Effective binary diffusivity of i-j pair of species (m^2/s)

dl	Distance between two charged layers (m)
E_n	Reversible potential of each cell (V)
$E_{0,cell}$	Reference cell potential (V)
$E_{0,cell}^0$	Standard reference cell potential at standard state (298 K temperature, 1atm pressure) (V)
F	Faraday constant, 96487 C/mol
h_s	Convective heat transfer coefficient (W/m^{2}K)
H_v	Heat of vaporisation of water (J/mol)
I_{fc}	FC stack current (A)
I_0	Exchange current (A)
I_d	Current density (A/m^2)
I_{lim}	FC Limitation current (A)
k_{RI}	Empirical constant in calculating R_{ohm} (Ω/A)
k_{RT}	Empirical constant in calculating R_{ohm} (Ω/K)
l_a	Distance from anode to reaction site (m)
l_c	Distance from cathode to reaction site (m)
$m_{H_2,in/out/net}$	Input/output/net mole flow rate of H_2 (mol/s)
$m_{O_2,in/out/net}$	Input/output/net mole flow rate of O_2 (mol/s)
$m_{H_2O,gen}$	Mole flow rate of H_2O (mol/s)
M_{FC}	Total mass of FC stack
M_v	Moles of vapour (mol)
$(m_v)_M$	Vapour transfer rate (mol/s)
N	Number of species in gas mixture
N_i (N_j)	Superficial gas flux of species i (j) (mol/m^{2}s)
n_d	Electro-osmotic coefficient
n_s	Number of cells in the stack
P	Overall pressure of the gas mixture (atm)
P_a (P_c)	Overall gas pressure at anode (cathode) (atm)
p_{H_2} (p_{O_2}) (p_{H_2O})	Partial pressure of H_2 (O_2) (H_2O) (atm)
$p_{H_2O}^a$ $(p_{H_2O}^c)$	Partial pressure of H_2O at anode (cathode) (atm)
$p_{H_2o}^{sat}$	Saturated vapour pressure of H_2O (atm)
q_{net}	Net heat generated inside PEMFC (J)
q_{chem}	Chemical energy (J)
q_{elec}	Electrical energy (J)
q_{sens}	Sensible heat (J)
q_{latent}	Latent heat (J)
q_{loss}	Heat loss (J)
R	Gas constant, 8.3143 (J/mol-K)
R_m	Ohmic resistance of membrane (Ω)
T	Stack temperature (K)
T_r	Room temperature (K)
t_m	Membrane thickness (m)
V_a (V_c)	Volume of anode (cathode) channel (m^3)
V_{fc}	FC stack output voltage (V)
$V_{o,FC}$	Open circuit output voltage of PEMFC stack (V)

$x_i\ (x_j)$	Mole fraction of species i (j)
λ_a	Fuel flow delay at anode (s)
λ_c	Oxidant flow delay at cathode (s)
$\emptyset_a(\emptyset_b)$	Relative humidity at anode (cathode)
ΔG	Gibbs free energy (J/mol)
ΔG_0	Gibbs free energy at standard condition (J/mol)
ΔH	Change in enthalpy (J/mol)
ΔS	Change in entropy(J/(mol/K))
V_c	Voltage across capacitor (V)

2.2.1 Gas Diffusion at Anode and Cathode

In a gas mixture consisting of N species, the diffusion of component i through the porous electrodes can be given by the Stefan-Maxwell equation as [50]:

$$\frac{dx_i}{dx} = \frac{RT}{P}\sum_{j=1}^{N}\frac{x_iN_j - x_jN_i}{D_{i,j}} \tag{2.1}$$

At the anode, the gas stream is a mixture of hydrogen H_2 and water in gas phase H_2O. Assuming one-dimensional transport and taking the molar flux of water normal to anode surface N_{H_2O} equal to zero, the diffusion of H_2O along the x-axis can be expressed as:

$$\frac{dx_{H_2O}}{dx} = \frac{RT}{P_a}\left(\frac{x_{H_2O}N_{H_2} - x_{H_2}N_{H_2O}}{D_{H_2O,H_2}}\right) = \frac{RT}{P_a}\left(\frac{x_{H_2O}N_{H_2}}{D_{H_2O,H_2}}\right) \tag{2.2}$$

The molar flux of H_2 as determined by Faraday's law, can be expressed as:

$$N_{H_2} = \frac{I_d}{2F} \tag{2.3}$$

Substituting the value of N_{H_2} from (2.3) to (2.2) and integrating (2.2) with respect to x from the anode channel to the catalyst surface gives the molar fraction of H_2O at the anode catalyst interface as:

$$x_{H_2O} = x_{H_2O}^{ch}exp\left(\frac{RTI_dl_a}{2FP_aD_{H_2O,H_2}}\right) \tag{2.4}$$

Here 'ch' denotes the conditions at the anode or cathode channel.

At the anode, the molar fraction of H_2 is:

$$x_{H_2} = 1 - x_{H_2O} \tag{2.5}$$

Assuming uniformity of gas distribution along x-axis, the effective partial pressure of H_2 can be expressed as:

$$p_{H_2} = \frac{p_{H_2O}}{x_{H_2O}}\left(1 - x_{H_2O}\right) = p_{H_2O}\left\{\frac{1}{x_{H_2O}^{ch}exp\left(\frac{RTI_dl_a}{2FP_aD_{H_2O,H_2}}\right)} - 1\right\} \tag{2.6}$$

At the cathode, the gas stream is a mixture of oxygen O_2, nitrogen N_2, H_2O and carbon-dioxide CO_2. The diffusion of water along x-axis taking N_{H_2O} equal to zero can be expressed as:

$$\frac{dx_{H_2O}}{dx} = \frac{RT}{P_c}\left(\frac{x_{O_2}N_{H_2O} - x_{H_2O}N_{O_2}}{D_{H_2O,O_2}}\right) = \frac{RT}{P_c}\left(\frac{-x_{H_2O}N_{O_2}}{D_{H_2O,O_2}}\right) \tag{2.7}$$

he molar fraction of H_2O, N_2 and CO_2 at the cathode catalyst interface is derived as:

$$x_{H_2O} = x_{H_2O}^{ch} exp\left(\frac{RTI_d l_c}{4FP_c D_{H_2O,O_2}}\right) \tag{2.8}$$

$$x_{N_2} = x_{N_2}^{ch} exp\left(\frac{RTI_d l_c}{4FP_c D_{N_2,O_2}}\right) \tag{2.9}$$

$$x_{CO_2} = x_{CO_2}^{ch} exp\left(\frac{RTI_d l_c}{4FP_c D_{CO_2,O_2}}\right) \tag{2.10}$$

The molar fraction of O_2 is:

$$x_{O_2} = 1 - x_{H_2O} - x_{N_2} - x_{CO_2} \tag{2.11}$$

The effective partial pressure of O_2 can be expressed as:

$$p_{O_2} = \frac{p_{H_2O}}{x_{H_2O}} x_{O_2} = \frac{p_{H_2O}}{x_{H_2O}}\left(1 - x_{H_2O} - x_{N_2} - x_{CO_2}\right) \tag{2.12}$$

2.2.2 Open Circuit Output Voltage of PEMFC

Nernst voltage E_n, the thermodynamics voltage of the FC depends on the temperature and partial pressures of reactants inside the FC stack and is given as [146]:

$$E_n = E_{0,cell} + \frac{RT}{2F} ln\left(p_{H_2} p_{O_2}{}^{\frac{1}{2}}\right) \tag{2.13}$$

$E_{0,cell}$, the reference potential is a function of temperature represented as:

$$E_{0,cell} = E_{0,cell}^{0} + \left(\frac{-44.43}{2F}\right)(T - 298) \tag{2.14}$$

where $E_{0,cell}^{0}$ is the standard reference potential at standard state of 298 K temperature and 1 atm pressure. Substituting the value of 2.14 in 2.13, we get:

$$E_n = E_{0,cell}^{0} + \left(\frac{-44.43}{2F}\right)(T - 298) + \frac{RT}{2F} ln\left(p_{H_2} p_{O_2}{}^{\frac{1}{2}}\right) \tag{2.15}$$

E_n is the individual open-circuit output voltage of one FC. The parameters of individual cells can be lumped together to form the PEMFC stack [147]. Hence, the open-circuit output voltage of the PEMFC stack $V_{o,fc}$ can be given as:

$$V_{o,fc} = n_s E_n = n_s E_{0,cell}^{0} + n_s\left(\frac{-44.43}{2F}\right)(T - 298) + \frac{n_s RT}{2F} ln\left(p_{H_2} p_{O_2}{}^{\frac{1}{2}}\right) \tag{2.16}$$

where n_s is the number of cells in the stack.

2.2.3 Irreversible Voltage Losses in PEMFC

The actual output voltage of the PEMFC at normal operating conditions is determined by irreversible voltage losses, which exists within the PEMFC [145]. Three types of voltage losses exist: activation losses, ohmic losses, and concentration losses [29, 30, 33, 36, 37, 42, 45].

2.2.3.1 Activation Voltage Loss

The governance of sluggish electrode kinetics by the rate of electrochemical reaction at an electrode surface gives rise to activation losses in the PEMFC. These losses are dominant at low current density [36].

$$V_{act} = \frac{RT}{2\alpha F}\ln\left(\frac{I}{I_0}\right) = a_0 + T.[a + b\ln(I)] = V_{act1} + V_{act2} \tag{2.17}$$

The term $V_{act1} = a_0 + T.a$ represents the temperature-dependent voltage loss, and the term $V_{act2} = T.b.\ln(I)$ represents the activation voltage loss based on both current and temperature. The activation resistance corresponding to the activation voltage loss is [147]:

$$R_{act} = \frac{V_{act2}}{I} = \frac{T.b.\ln(I)}{I} \tag{2.18}$$

2.2.3.2 Ohmic Voltage Loss

The ohmic losses are due to the ohmic resistance of the PEMFC that includes the resistance of the anode and cathode due to imperfections in the electrode manufacturing and the resistance of the proton electrolyte membrane to the movement of ions [145]. The overall ohmic voltage drop can be expressed as:

$$V_{ohm} = V_{ohm,a} + V_{ohm,m} + V_{ohm,c} \tag{2.19}$$

where $V_{ohm,a}$, $V_{ohm,m}$ and $V_{ohm,c}$ are ohmic voltage drops at anode, membrane and cathode respectively. The electrode resistances of the PEMFC depend on the stack current and temperature and hence the ohmic resistance can be given as [145]:

$$R_{ohm} = R_0 + k_{RI}I + k_{RT}T \tag{2.20}$$

where R_0 is constant part of R_{ohm}. k_{RI} and k_{RT} are empirical constants.

2.2.3.3 Concentration Voltage Loss

The concentration losses exist due to the formation of concentration gradients of reactants at the surface of the electrodes. The consumption of more fuel reduces the concentrations of hydrogen and oxygen at various points in the PEMFC gas channels, and increases the concentrations of these reactants at the input of the stack. The concentration losses for a single PEMFC stack can be given as [145]:

$$V_{conc} = -\frac{RT}{2F}\ln\left(1 - \frac{I}{I_{lim}}\right) \tag{2.21}$$

The equivalent concentration loss resistance can therefore be defined as:

$$R_{conc} = -\frac{RT}{2FI}\ln\left(1 - \frac{I}{I_{lim}}\right) \tag{2.22}$$

The limiting current I_{lim} of the PEMFC is determined by the rate of consumption of fuel and rate of fuel supply. Hence, concentration losses grow significant at higher currents, when fuel is consumed at a higher rate [145]. Thus, the actual output voltage of the PEMFC stack at normal operating conditions is given by subtracting the voltage losses from the open-circuit output voltage of the PEMFC as follows [145]:

$$V_{fc} = V_{O,fc} - n_s(V_{act} + V_{ohm} + V_{conc}) \tag{2.23}$$

2.2.4 Mass Balance in PEMFC

The net mole flow rate of oxygen at the cathode is the difference between the mole flow rate of oxygen coming inside the FC and mole flow rate of oxygen going outside the FC [145]. Using ideal gas law, the dynamic equation for the effective partial pressure of H_2 and O_2 in the anode and cathode channel respectively can be written as:

$$\frac{V_a}{RT}\frac{dp_{H_2}}{dt} = m_{H_2,in} - m_{H_2,out} - \frac{I}{2F} = m_{H_2,net} - \frac{I}{2F} \tag{2.27}$$

$$\frac{V_c}{RT}\frac{dp_{O_2}}{dt} = m_{O_2,in} - m_{O_2,out} - \frac{I}{2F} = m_{O_2,net} - \frac{I}{2F} \tag{2.28}$$

At steady state, all partial pressures are considered to be constant [50], hence we can write:

$$\frac{dp_{H_2}}{dt} = \frac{dp_{O_2}}{dt} = 0 \tag{2.29}$$

And hence the net flow rates of H_2 and O_2 become:

$$m_{H_2,net} = 2m_{O_2,net} = \frac{I}{2F} \tag{2.30}$$

The flow of oxygen and hydrogen in the PEMFC cannot follow changes in the load instantly, and there exists a time lag between the change in the load current, and flow of oxygen and hydrogen [145]. The net mole flow rate of H_2 at the anode and O_2 at the cathode can be given as:

$$\frac{dm_{H_2,net}}{dt} = \frac{1}{\lambda_a}\left(\frac{I}{2F} - m_{H_2,net}\right) \tag{2.31}$$

$$\frac{dm_{O_2,net}}{dt} = \frac{1}{\lambda_c}\left(\frac{I}{2F} - m_{O_2,net}\right) \tag{2.32}$$

2.2.5 Thermodynamic Energy Balance in PEMFC

The net heat generation due to the chemical reaction inside the PEMFC can be written as:

$$q_{net} = q_{chem} - q_{elec} - q_{sens} - q_{latent} - q_{loss} \tag{2.33}$$

where q_{net} is the net heat energy, q_{chem} is the chemical energy, q_{elec} is the electrical energy, q_{sens} is the sensible heat, q_{latent} is the latent heat and q_{loss} is the heat loss.

The energy released due to change in enthalpy ΔH of the chemical reaction inside PEMFC can be written as:

$$q_{chem} = m_{H_2,net}\Delta H \tag{2.34}$$

ΔH can be calculated using the Gibbs free energy using equation:

$$\Delta G = \Delta H - T\Delta S \tag{2.35}$$

$$\Delta G = \Delta G_0 - RTln\left(p_{H_2}{p_{O_2}}^{\frac{1}{2}}\right) \tag{2.36}$$

The electrical output energy can be written as:

$$q_{elec} = V_{fc} I_{fc} \tag{2.37}$$

Sensible heat q_{sens} is the heat energy that is transferred by a body that has higher temperature than its surroundings. It is the product of species mole flow rate, its specific heat capacity and the difference in its temperature and room temperature. It can be represented as:

$$q_{sens} = m_{H_2,out}(T - T_r)C_{H_2} + m_{O_2,out}(T - T_r)C_{O_2} + m_{H_2O,gen}(T - T_r)C_{H_2O} \tag{2.38}$$

Latent heat q_{latent} is the heat energy released or absorbed by a substance when changing from one phase to another.

$$q_{latent} = m_{H_2O,gen}\, H_v \tag{2.39}$$

The heat loss q_{loss} by air convection can be expressed as:

$$q_{loss} = h_s(T - T_r)n_s A_s \tag{2.40}$$

At steady state FC operates at constant temperature. Hence, $\dot{q}_{net} = 0$. During transients, FC temperature rises or falls and hence:

$$\dot{q}_{net} = M_{FC} C_{FC} \tag{2.41}$$

where M_{FC} is the total mass of FC stack and C_{FC} is the overall specific heat capacity of the stack.

2.2.6 Formation of Charge Double Layer in PEMFC

In the PEMFC, due to the presence of polymer membrane, electrons from the anode flow towards the cathode via an external circuit, while positive hydrogen ions reach the cathode through the polymer membrane [145]. As a result, two charged layers of opposite polarities are formed at the cathode/electrolyte interface. This charge double-layer is storage of electrical charges and energy, thus it behaves as an electrical capacitor. This effect causes retardation in the dissipation of the electrical charges near the electrolyte/electrode interface. Hence, voltage formed due to this charge double-layer will take certain time to respond to sudden change in the current. [30, 36, 37, 45].

An equivalent electrical circuit to model the FC dynamic behaviour is represented in $Fig. 2.1$ [50]. In the circuit, there is a first-order delay in the activation and the concentration voltage components. This delay is caused by the charge double layer effect [37, 148]. The ohmic voltage drop is not affected by the charge double layer effect as it is directly related to the current. The capacitor is placed in parallel with the activation and concentration voltages to take into account the dynamic effect of these voltage drops. This resulting loop is then connected in a series with the Nernst potential and with the ohmic voltage component [37, 148]. Therefore, in the PEMFC, when the current is increased by sudden increase in the load, the output voltage shows an immediate drop due to the drop across R_{ohm} of the PEMFC, but then the voltage reaches its new value in an exponential manner, due to the capacitance of the charge double-layer [145].

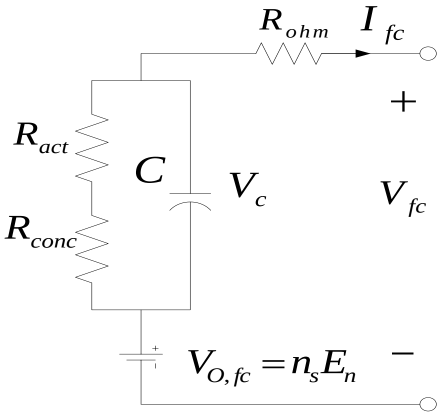

$Fig.$ 2.1 Equivalent circuit of PEMFC showing double-layer charging effect

The capacitance due to the charge double-layer effect is a function of the cell surface area A_s, the separation between the plates dl, and the electrical permittivity ϵ [145]. Its value is usually a few Farads. The value of the capacitance is given as:

$$C = \frac{\epsilon A_s}{dl} \tag{2.42}$$

The dynamic equation of the model presented in Fig. 2.1 is represented by:

$$\frac{dV_C}{dt} = \frac{I}{C} - \frac{V_C}{\tau} \tag{2.43}$$

where V_C represents the dynamic voltage across the equivalent capacitor (associated with V_{act} and V_{conc}), C is the equivalent electrical capacitance and τ is the FC electrical time constant defined as:

$$\tau = C(R_{act} + R_{conc}) = \frac{C}{I}(V_{act} + V_{conc}) \tag{2.44}$$

The resulting FC voltage is then defined as:

$$V_{fc} = V_{O,fc} - V_{ohm} - V_C \tag{2.45}$$

2.3 SIMULATION RESULTS OF THE PEMFC MODEL

The block diagram of MATLAB/Simulink model of PEMFC based on its electrochemical and thermodynamic characteristics is shown in $Fig.$ 2.2 [50]. The inputs are anode pressure, cathode pressure, initial FC temperature and room temperature. The mass diffusion equations (2.1-2.12) are used to calculate the effective partial pressures of hydrogen and oxygen. The Nernst equation (2.13-2.15) and the overall fuel and oxidant delay effect (2.31-2.32) are employed to determine the internal potential of the FC. The activation voltage drop equations (2.17-2.18), ohmic voltage drop equations (2.19-2.20) and concentration voltage drop equations (2.21-2.22) together with the voltage of the equivalent capacitance of double-layer charge effect (2.43-2.44) are applied to determine the output voltage of the FC. Thermodynamic effect is considered using energy balance equations (2.33-2.41).

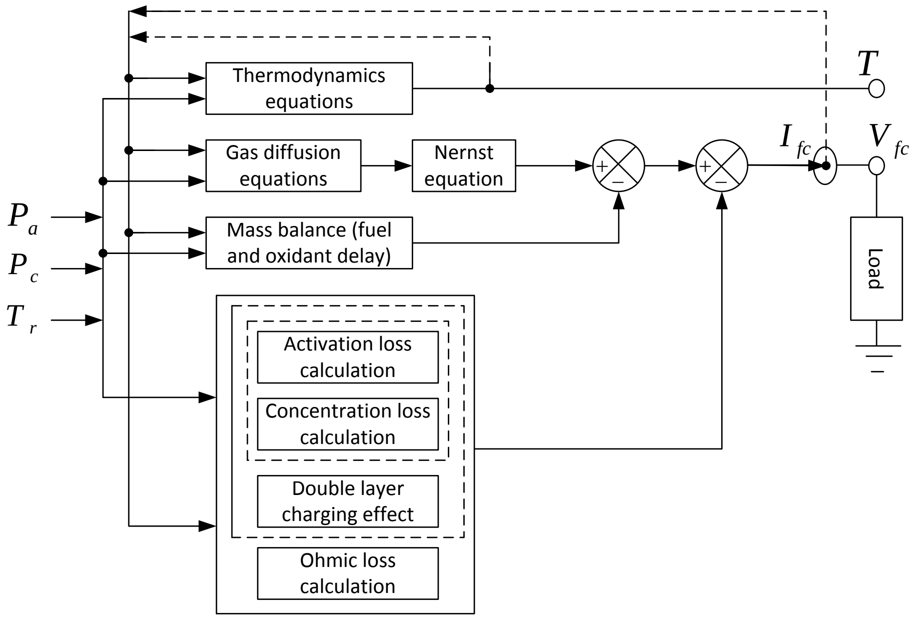

$Fig.$ 2.2 Block diagram for dynamic model of PEMFC

$Fig.$ 2.3 and Fig 2.4 shows the $V\!-\!I$ characteristic and $P-I$ characteristic of the 0.5 kW PEMFC model obtained by simulating the model at anode pressure $P_a = 2$ atm, cathode pressure $P_c = 1$ atm and room temperature $T_r = 308$ K. In $Fig.$ 2.3, the voltage drops at the left end and the right end of the curve are due to activation and concentration losses respectively. The voltage drop at the middle of the curve is due to the ohmic loss in the PEMFC. Thus the 0.5 kW PEMFC model has a rated current of 20 A and output voltage of approximately 25 V.

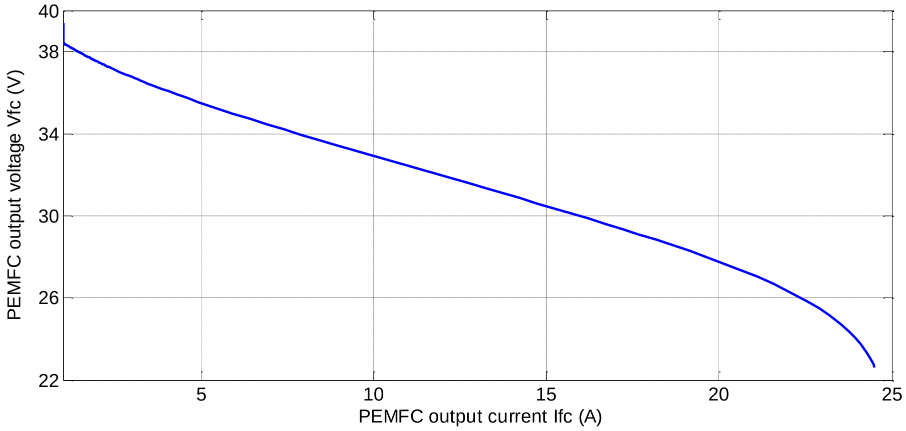

$Fig.$ 2.3 $V-I$ Characteristic of the PEMFC model at $P_a = 2\ atm$, $P_c = 1\ atm$, $T_r = 308\ K$

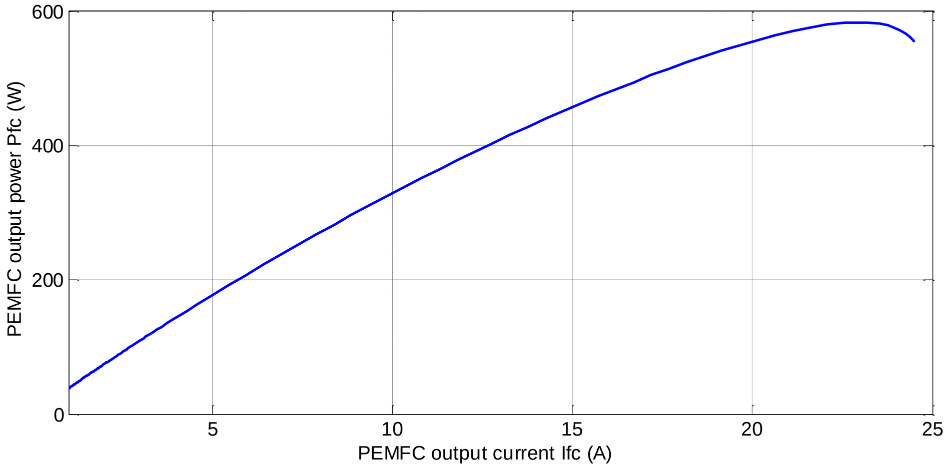

$Fig. 2.4$ $P - I$ Characteristic of the PEMFC model at $P_a = 2\ atm, P_c = 1\ atm, T_r = 308\ K$

2.3.1 Variation in $V - I$ and $P - I$ curve with Input Parameters

The PEMFC model is further subjected to different values of input variables P_a and P_c in order to study their effect on the $V - I$ and $P - I$ characteristics, output voltage of the FC and voltage losses. $Fig. 2.5$ shows the $V - I$ characteristics and $Fig. 2.6$ the $P - I$ characteristics obtained by simulating the model for different values of P_a. The other two input variables P_c and T_r are kept constant at 1 atm and 308 K respectively. It is seen from the figure that as P_a is increased, the output voltage of the PEMFC increases and it reduces the voltage losses in the PEMFC. Hence, it is possible to reduce voltage losses in the PEMFC by operating it at higher values of P_a. $Fig. 2.7$ shows the $V - I$ characteristics and $Fig. 2.8$ the $P - I$ characteristics obtained by simulating the FC model for increasing values of P_c. The other two input variables P_a and T_r are kept constant at 2 atm and 308 K respectively. Again, it can be seen that as P_c is increased, the output voltage of the PEMFC increases which reduces voltage losses in the PEMFC. For the higher values of P_c, voltage losses are smaller.

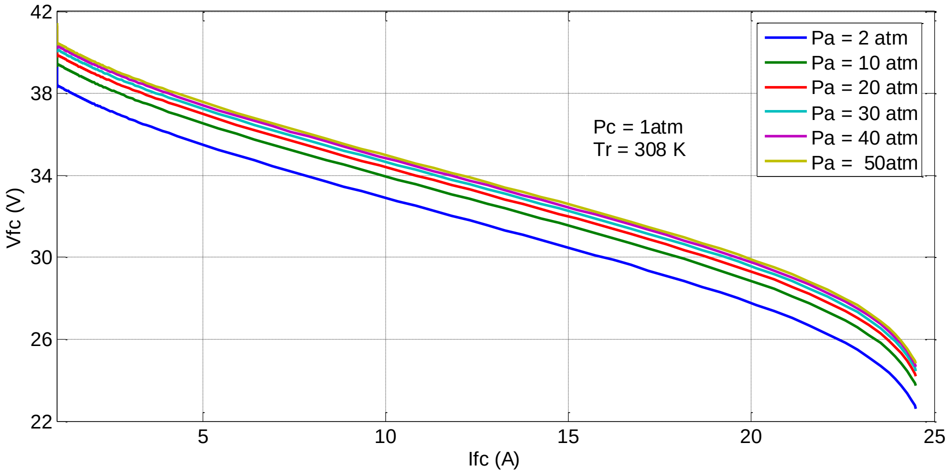

$Fig. 2.5$ $V - I$ Characteristic of the PEMFC model for increasing anode channel pressure P_a

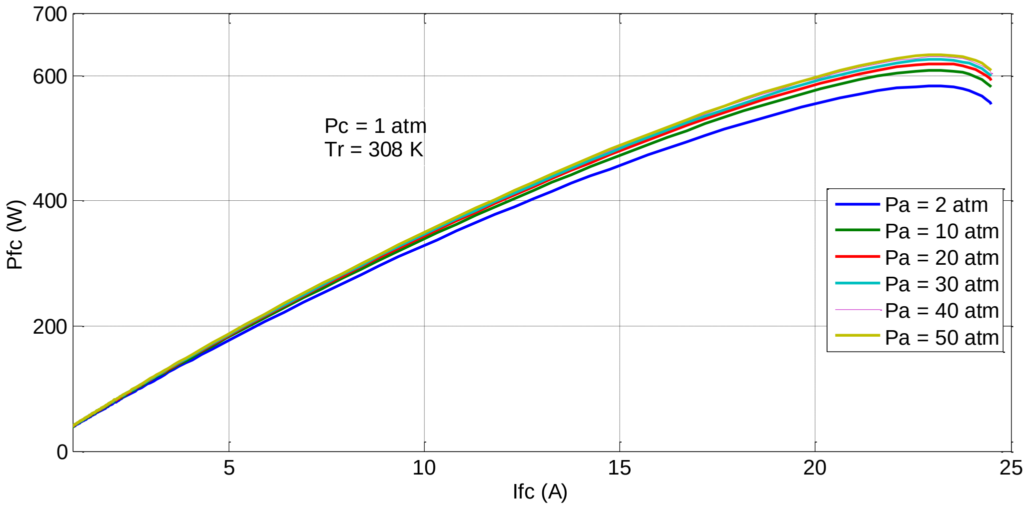

$Fig. 2.6$ $P - I$ characteristic of the PEMFC model for increasing anode channel pressure P_a

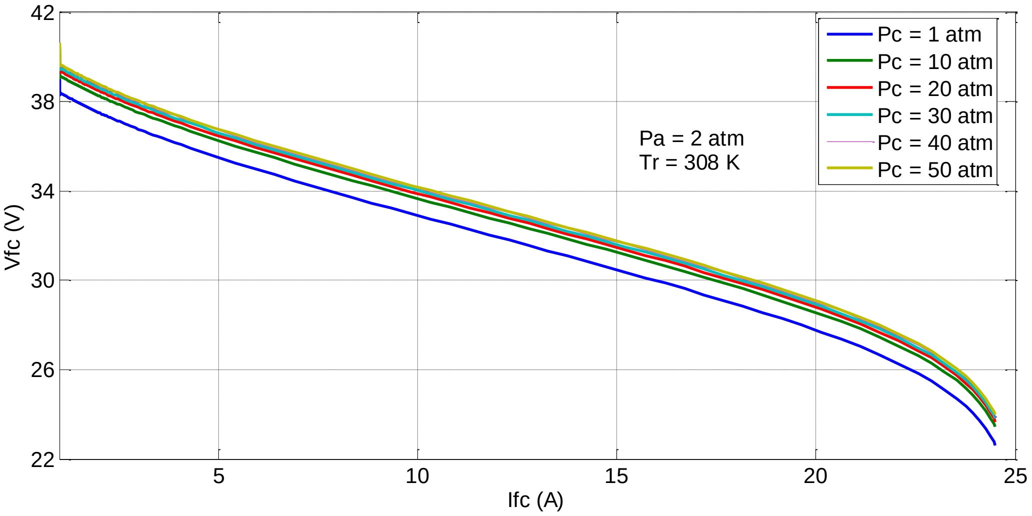

$Fig. 2.7$ $V - I$ Characteristic of the PEMFC model for increasing cathode channel pressure P_c

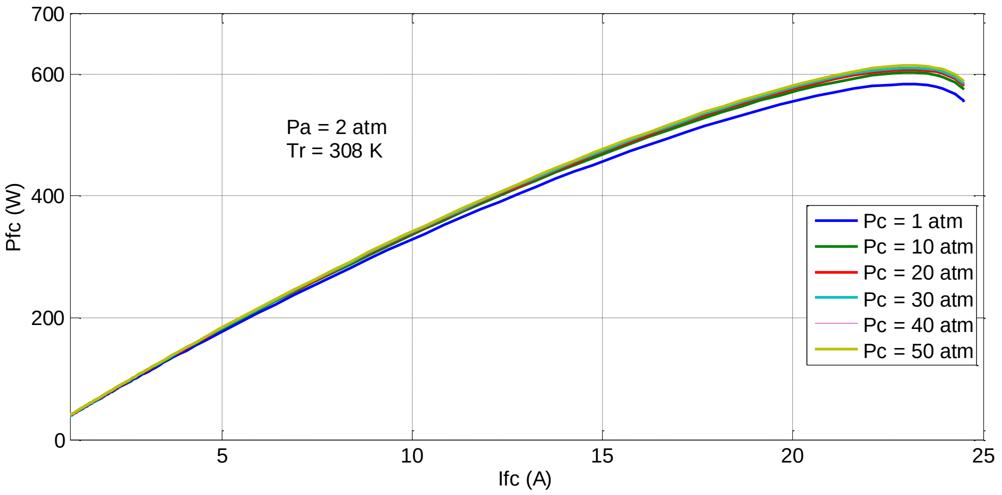

$Fig. 2.8$ $P - I$ Characteristic of the PEMFC model for increasing cathode channel pressure P_c

From $Fig. 2.5$ and $Fig. 2.7$, it can be seen that as P_a and P_c are increased, the output voltage of the PEMFC increases, which reduces voltage losses. For higher values of P_a and P_c, voltage losses are smaller. Hence, it is possible to reduce voltage losses in the PEMFC by operating it at higher values of P_a and P_c.

2.3.2 Formation of PEMFC Array

Each 0.5 kW FC used in the PEMFC stack has a rated current of 25 A. The 6-kW PEMFC array used in single-phase simulations is formulated by combining 2 (series) x 6 (parallel) = 12 0.5 kW FC stacks. $Fig. 2.9$ shows the formulation of the 6 kW PEMFC array from 0.5 kW FC stacks in MATLAB/Simulink. The 6 kW PEMFC array has the rated current of 150 A. The $V - I$ characteristics and the $P - I$ characteristic of the array is shown in $Fig. 2.10$ and $Fig. 2.11$ respectively.

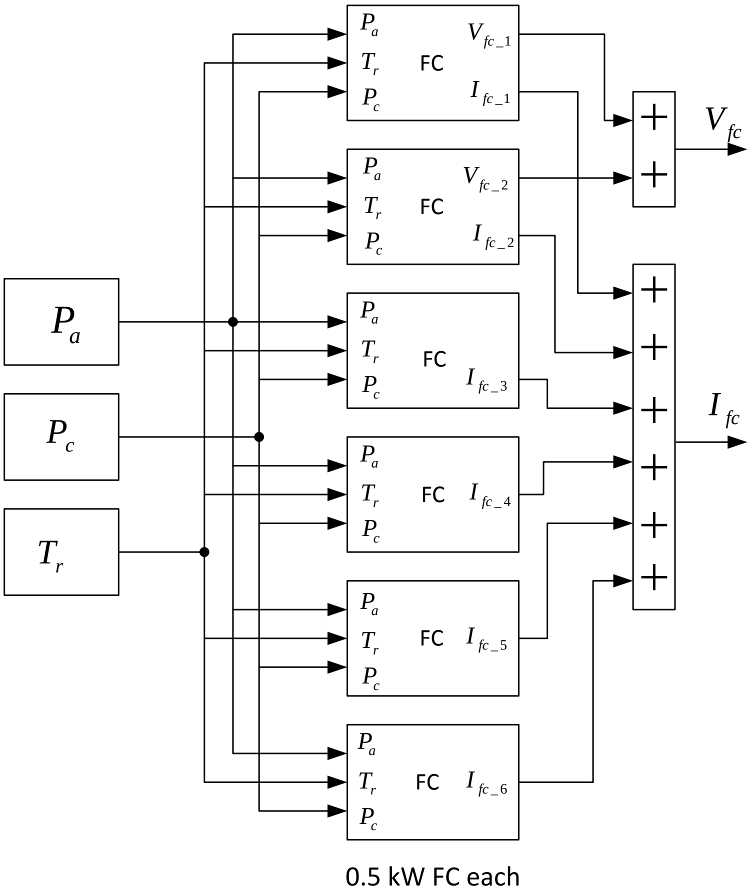

$Fig. 2.9$ Formulation of the 6 kW PEMFC stack from 0.5 kW PEMFC stack model

Similar to model development of 6 kW PEMFC that is used for single-phase simulation studies, 100 kW PEMFC model is developed from series parallel combination of stacks for use in three-phase simulation studies.

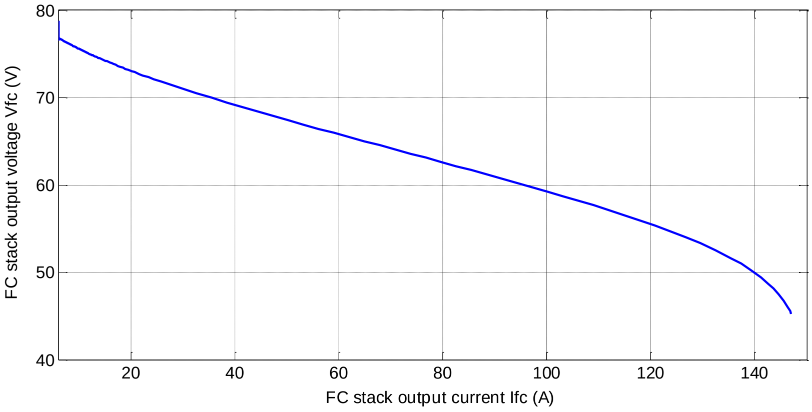

$Fig.$ 2.10 $V-I$ curve of 6 kW PEMFC stack

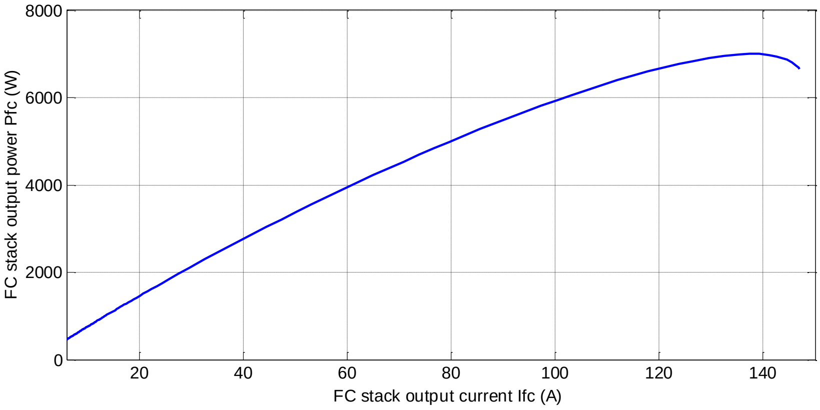

$Fig.$ 2.11 $P-I$ curve of 6 kW PEMFC stack

2.3.3 Transient Response of the PEMFC Model

The dynamic response of the PEMFC depends on the capacitance of double-layer charge effect, fuel and oxidant flow delays and the thermodynamic characteristics of the PEMFC [36, 145]. $Fig.$ 2.12 shows the transient response of the model. The load is varied in steps over a small time period between 1 to 4 s to observe the transient behaviour of the model. It can be seen that as the load is increased or decreased, the output voltage drops or increases simultaneously which is mainly due to the voltage drop across the FC ohmic resistance, which increases with increase in loading of FC and vice-versa. After the instantaneous change, the FC output voltage increases exponentially to its new steady state value when the FC is loaded and decreases exponentially when the FC is unloaded. This is due to the time constant associated with the capacitance of the charge double layer formed on the surface of the cathode. However, in the long time range the transient phenomena is affected by the thermodynamic time constant, as well as due to air and hydrogen flow delays inside the PEMFC. These delays can vary from few seconds to few minutes in the PEMFC.

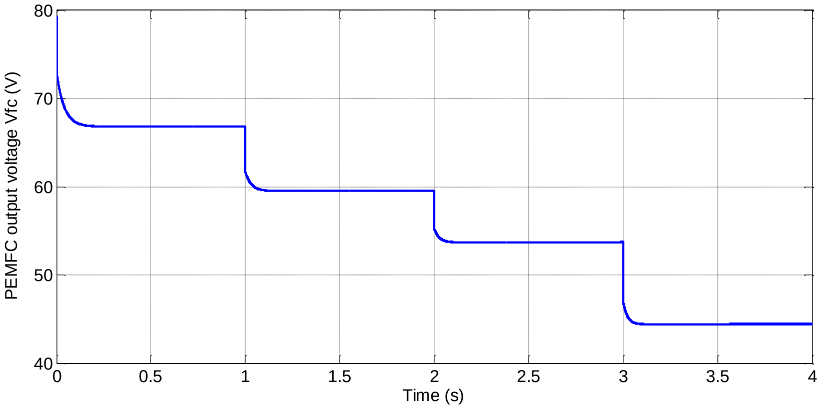

$Fig.$ 2.12 Transient response of the PEMFC model

2.4 FUEL CELL BASED DISTRIBUTED GENERATION SYSTEM

Fuel Cell technology holds promise towards sustainable power generation, it being pollution free and using readily available fuels [27, 29, 33, 37, 144]. Since the FC delivers DC power, it needs to be inverted and stepped up to be able to be used as distributed generation [4, 24]. Further, the FC voltage decreases almost linearly with the increase in load current [42]. Hence, the FC output voltage must be regulated at a desired level. A suitable power electronic interface is required between FC and grid, with the capabilities of FC voltage regulation, output voltage matching and galvanic isolation between FC and grid [25]. The aforementioned task is achieved by connecting a DC-DC converter to the FC followed by a DC-AC inverter [4, 24, 34] .

The block diagram representation of power electronic interface associated with FC systems is shown in $Fig.$ 2.13 [16]. The power electronic interface accepts power from the FC source and converts it to power at the required voltage and frequency. Four major modules for a power electronic interface are depicted in the figure. They include the DC-DC converter module to change the DC voltage level, an inverter module to convert the DC voltage to grid-compatible AC voltage, the output interface module to filter the AC output from the inverter and the controller module [16, 28, 131].

Several DC-DC non-isolating and isolating converters topologies have been researched for FC applications. The non-isolating type of DC-DC converter is generally used when the voltage needs to be stepped up or down by a relatively small ratio and there is no problem with the output and input having no dielectric isolation. The efficiency of the conventional boost converter is always greater than the other DC-DC converter topologies because it has reduced component counts and simplicity in control [25]. However, when isolation and high conversion ratio is required, the flyback converter, forward converter, push-pull converter [4], half bridge converter and full-bridge converter [54] are considered [12]. The output of DC-DC converter is given to DC-AC converter. For single-phase requirement, half-bridge and full-bridge PWM inverter configurations are used. Both designs are simple in nature and have low component count. As compared to half-bridge inverter, the full-bridge inverter has two more switches adding to the cost while doubling the output voltage rating [12, 25].

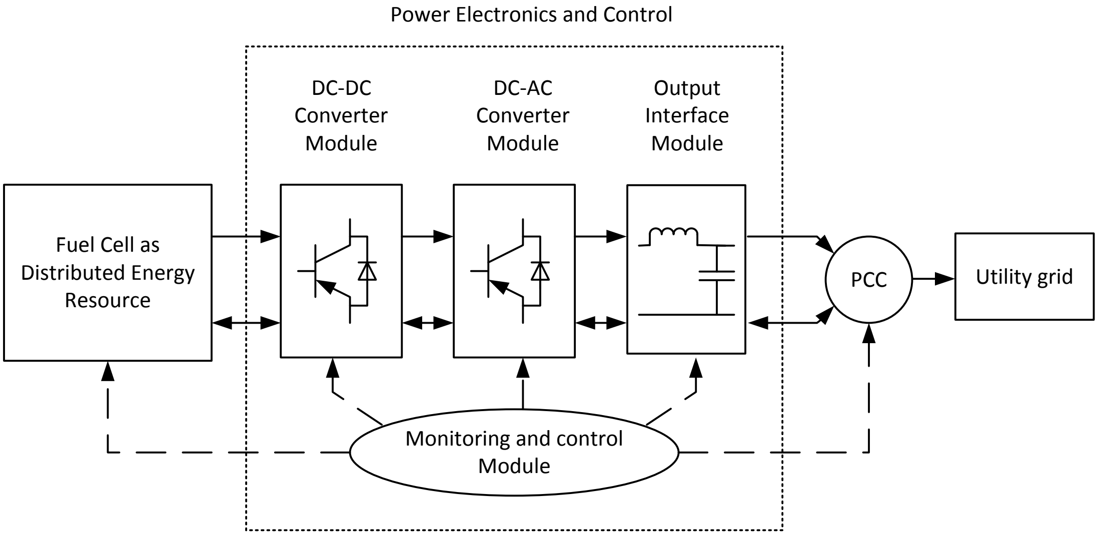

$Fig.$ 2.13 General block diagram of FC power electronic system

For medium and high power applications the conventional three-phase Pulse Width Modulated - Voltage Source Inverter (PWM-VSI) is preferred because of the simplicity in control technique. This converter is simple in nature and with the filter can provide an adequate AC output. The PWM-VSI is the state of the art technology used nowadays worldwide by all manufacturers for interacting with the power system [25, 28, 100]. The use of IGBTs switched typically at 10 to 20 kHz leads to a better power quality performance. The possibility of high switching frequencies combined with proper control makes these converters suitable for grid interface [100].

Power supply reliability and power quality have become important issues for all kind of power electronic systems including FC systems. For interconnecting a FC system with utility, it is necessary that the system should meet the harmonic standard (IEEE Std 929-2000) [149] and the active power supply requirement. The power flow control to the utility, as well as the sinusoidal unity power factor current injection into the utility is obtained by the inverter controller [144]. All these topologies discussed earlier use multiple-stage conversion to deal with the aforementioned challenges, which results in large component count, poor reliability, additional cost and low efficiency [24]. Another possibility is directly connecting an inverter to the FC followed by a step-up transformer.

Direct connection of DC-AC inverter to the FC with AC gain step-up transformer has only one conversion stage [24]. This topology offers the advantages of least component count and low losses. The step-up transformer provides the isolation between FC and grid/load as well [24]. Grid interface of FC using single-stage conversion is one of the probable area of research and complete design, modelling and implementation of control scheme need more focused attention. This chapter presents modeling and simulation of a single-stage power electronic interface between FC and the grid. This model is used to define the active and reactive power reference, which can be supplied by the system to facilitate grid interface. A simulation model of 100 kW PEMFC is considered for the design and study. Control scheme is implemented in dq reference frame and various simulation results are presented in steady state as well as during transients.

2.5 POWER CIRCUIT DESCRIPTION OF SINGLE-STAGE GRID INTERFACED FUEL CELL SYSTEM

The schematic diagram of the proposed FC system is shown in $Fig. 2.14$. Pulse-width modulated voltage source inverter is used to interconnect the FC system to the grid for real and reactive power control purposes. A DC-link capacitor on the DC-side of the VSI acts as an energy buffer and makes a stable DC voltage for the converter in the steady state condition. An LC filter is connected at the output of the inverter to reduce the harmonics introduced by the inverter. A step-up transformer is then used to increase the voltage level before the system is connected to the grid. Thus a single-stage power electronic interface for FC based power system consists of FC stack, DC-AC inverter, filter and a step-up transformer for grid connected applications. In order to meet the requirements for interconnecting the FC system to a grid and control the power flow between them it is necessary to shape and control the inverter output voltage in amplitude, angle and frequency [144]. The controller is required to perform the following functions: control the active power generated to the grid, control the reactive power transfer between the FC and the grid, control the DC-link voltage, ensure high quality of the injected power and grid synchronization.

2.5.1 Low Pass Filter

The FCDG scheme needs to confirm to power quality standards demanded by utility. Hence, an output filter is required to eliminate harmonics injected by FC inverter in the system. The filter attenuates the harmonic components of the VSI AC-side voltage and prevents them from penetrating into the grid [24, 25, 42, 68]. For simplicity and economy, a low-pass LC filter [4, 24, 150] is mostly used. The aim of the LC filter is to keep the harmonic currents injected by the FC system into the grid at reasonably low levels and thus maintain a low voltage distortion at the PCC. The objective is fulfilled by selection of proper values for the filter inductance L and capacitance C. A value between 0.1 to 0.25 per unit is selected for L, to keep the inductor size and cost low [68]. L consists of the parallel connection of grid equivalent inductance plus the interconnection transformer leakage inductance. C is calculated such that the resonant frequency of the LC filter circuit is sufficiently larger than the grid nominal frequency ω_0, but considerably smaller than the VSI switching frequency f_s. A large switching frequency for the VSI allows for smaller filter capacitance [68]. A switching frequency of 10 kHz for PWM inverter operation and a cut-off frequency f_c of 650 Hz is considered here for LC filter design.

2.5.2 Interconnection Transformer

A transformer is included in the grid-connected FC system to adapt the VSI AC-side terminal voltage to the nominal PCC voltage. The transformer has a delta winding connection on low voltage side and a grounded wye winding configuration on the higher voltage side to avoid distortions due to the triple-n harmonics of the magnetizing current. Also, the transformer isolates the FC system from the grid, in terms of zero sequence components of fault currents. In addition to the isolation transformer, utilities require another transformer, called the interconnection transformer, to interface the FC system with the network [68]. The combined effect of the two transformers is referred to as the interconnection transformer in this work. The filtered output voltage is stepped up through a transformer to 230 V rms per phase for interfacing to grid.

2.5.3 Grid Synchronization

Information about the phase angle, amplitude and frequency of the grid voltage is of vital importance for the VSI control system to be able to accurately control the flow of active and reactive power. The purpose of the grid synchronization technique is therefore to identify the information needed by the control system. Although a wide range of synchronization methods have been proposed, the most common and well known synchronization technique for three-phase VSI is the Synchronous Reference Frame Phase Locked Loop [102].

In a PLL, space vector corresponding to the grid voltage $\vec{v}$ is projected on the d and q axes of a dq frame as shown in $Fig. 2.15$ and the q frame is rotated in such a way that v_q becomes zero. This objective is achieved through a closed loop mechanism where any deviation of v_q from zero is processed by a filter $H(s)$, and translated into a higher or lower rotational speed of the dq frame with respect to the power system nominal frequency ω_0.

In a steady state v_q settles to zero, the d axis of the dq frame gets aligned with the grid voltage vector and the dq frame rotational speed becomes equal to the grid angular frequency. As such, the extracted angle ρ becomes equal to the grid voltage angle θ. The frequency response of $H(s)$ is tailored so that grid voltage imbalance and distortion does not affect ρ. PLL also provides a measure of the grid instantaneous frequency $\omega = d\theta/dt$ [68].

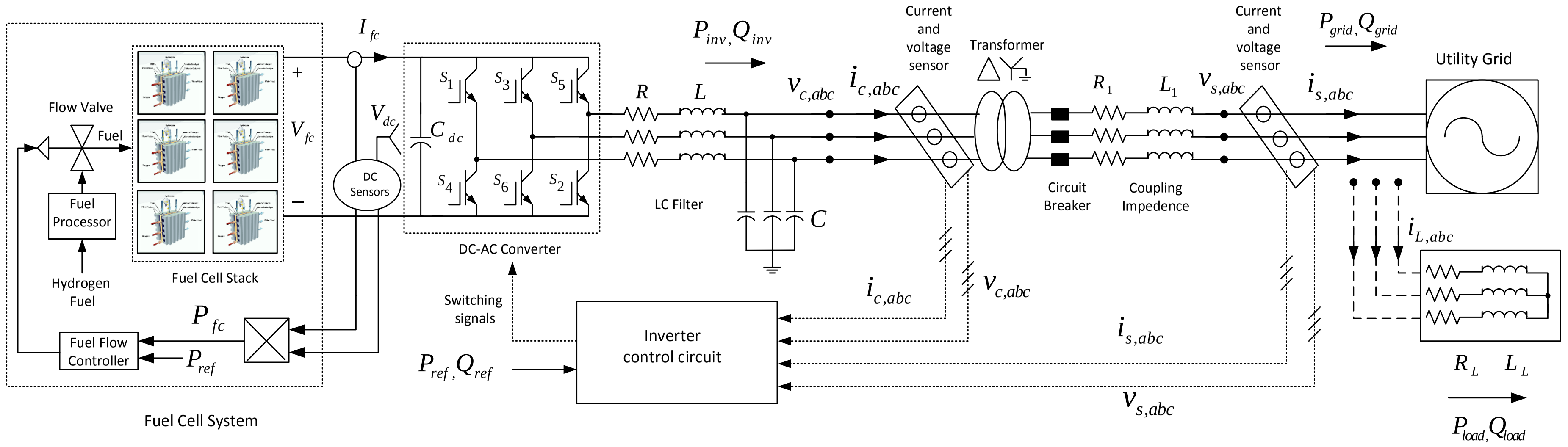

$Fig.$ 2.14 Schematic diagram of Grid-interfaced Fuel Cell System

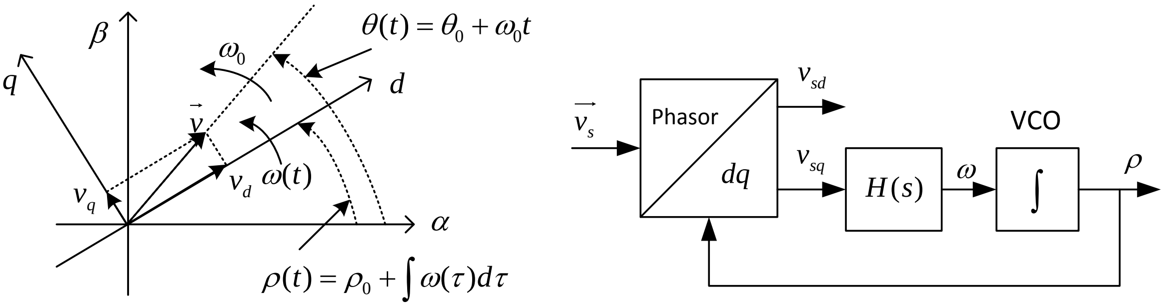

(a) (b)

$Fig.$ 2.15 (a) Vector diagram illustrating the operation principle of Phase-Locked Loop (b) Block diagram of the Phase-Locked Loop

2.6 POWER FLOW CONTROL FROM FC TO THE GRID

In grid-connected mode, the output active power P_{fc} and reactive power Q_{fc} from the FC system to the grid should be regulated to desired values P_{ref} and Q_{ref} respectively. Both P_{ref} and Q_{ref} can be positive or negative, which provides possibility for the FC unit to help with the energy production and stability enhancement of the power system. The power regulation goals are stability, low steady state error, and fast response with low coupling between P_{fc} and Q_{fc}. The current injected into the DC-link by the FC stack I_{fc} can be given as:

$$I_{fc} = \frac{P_{fuel}}{V_{dc}} \tag{2.46}$$

where V_{dc} is the DC-link voltage and P_{fuel} is the power generated from the FC. The current flowing out of the DC-link I_{dc} can be represented as

$$I_{dc} = \frac{P_{in}}{V_{dc}} = \frac{P_{grid}+P_{loss}}{V_{dc}} \tag{2.47}$$

where P_{in}, P_{grid} and P_{loss} are total power available at grid interfacing inverter, active power supplied to the grid and loss power. To regulate the DC-link voltage, conventional PI controllers are used. The loss power i.e. the energy required by the DC-link capacitor to charge from actual voltage V_{dc} to reference voltage $V_{dc,ref}$ can be expressed as:

$$P_{loss} = \frac{1}{2} C_{dc}({V_{dc,ref}}^2 - {V_{dc}}^2) \tag{2.48}$$

where C_{dc} is the DC-link capacitor. $Fig.$ 2.16 shows the single line diagram of FCDG system where the inverter output voltage $V_c\angle\delta_c$ is connected to the PCC $V_s\angle 0$ through impedance $Z_c = R_c + j\mathrm{X}_c$ which includes the filter, transformer, coupling and transmission line impedances. $V_{fc} = V_{dc}$ is the DC-link voltage and I_c is the current flowing from inverter to the PCC. The apparent power transfer from the FC inverter to the grid can be expressed as:

$$\vec{S} = P_{fc} + jQ_{fc} = \overrightarrow{V_s}\overrightarrow{I_c} = \vec{V_s}\left(\frac{\vec{V_c}-\vec{V_s}}{Z_c}\right) \tag{2.49}$$

where P_{fc} is the real power, Q_{fc} is the reactive power flow from FC to the grid.

$$\vec{S} = V_s\left(\frac{V_c cos\delta_c + jV_c sin\delta_c - V_s}{R_c + jX_c}\right) \tag{2.50}$$

Multiplying the numerator and denominator of the above equation by the conjugate of the line impedance $R_c - jX_c$, we get:

$$P_{fc} = V_s\left[\frac{R_c(V_c cos\delta_c - V_s) + X_c V_c sin\delta_c}{{R_c}^2 + {X_c}^2}\right] \tag{2.51}$$

$$Q_{fc} = V_s\left[\frac{X_c(V_c cos\delta_c - V_s) - R_c V_c sin\delta_c}{{R_c}^2 + {X_c}^2}\right] \tag{2.52}$$

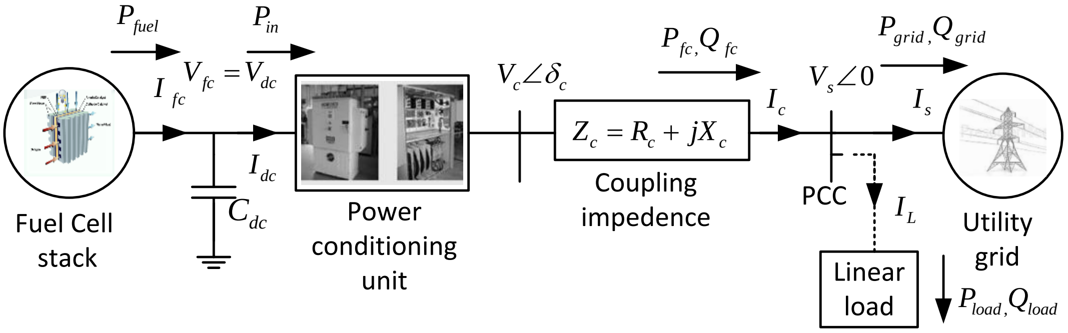

$Fig.$ 2.16 Single line diagram of FCDG system

The Equations (2.51) and (2.52) represent the active and reactive power transfer from FC to the grid. Neglecting the line resistance R_c, assuming the reactance X_c to be large compared to R_c,

$$P_{fc} = \frac{V_s V_c}{X_c} sin\delta_c \tag{2.53}$$

$$Q_{fc} = \frac{V_s}{X_c}(V_c cos\delta_c - V_s) \tag{2.54}$$

From the above equations, it is observed that both P_{fc} and Q_{fc} depend upon V_c and δ_c, which is called coupling between P_{fc} and Q_{fc}. However both V_c and δ_c have different levels of impact upon P_{fc} and Q_{fc} [151]. Taking partial derivatives of P_{fc} and Q_{fc} with respect to V_c and δ_c, we get:

$$\frac{\partial P_{fc}}{\partial \delta_c} = \frac{V_s V_c}{X_c} cos\,\delta_c\,, \frac{\partial P_{fc}}{\partial V_c} = \frac{V_s}{X_c} sin\,\delta_c \tag{2.55}$$

$$\frac{\partial Q_{fc}}{\partial \delta_c} = \frac{V_s V_c}{X_c} sin\,\delta_c\,, \frac{\partial Q_{fc}}{\partial V_c} = \frac{1}{X_c}(V_c - V_s\,cos\,\delta_c) \tag{2.56}$$

When δ_c is small as in large capacity power systems,

$$\frac{\partial P_{fc}}{\partial \delta_c} \approx \frac{V_s V_c}{X_c}, \frac{\partial P_{fc}}{\partial V_c} \approx 0 \tag{2.57}$$

$$\frac{\partial Q_{fc}}{\partial \delta_c} \approx 0\,, \frac{\partial Q_{fc}}{\partial V_c} \approx \frac{1}{X_c}(V_c - V_s) \tag{2.58}$$

Thus P_{fc} is predominantly dependent on the power angle δ_c and Q_{fc} is dependent on the voltage magnitude difference $(V_c - V_s)$. This different levels of sensitivity of P_{fc} and Q_{fc} to V_c and δ_c provides the possibility of controlling P_{fc} and Q_{fc} independently [151]. The inverter output voltage is controlled by the modulation index m_a and phase angle δ_c. Thus if the desired values of real and reactive power P_{ref} and Q_{ref} are known, the values of V_c and δ_c can be determined from Equations (2.53) and (2.54):

$$V_c = \frac{Z_c^2}{V_s^2}\left({P_{ref}}^2 + {Q_{ref}}^2\right) + V_s^2 + 2Q_{ref}Z_c \tag{2.59}$$

$$\delta_c = \frac{\pi}{2} - \cos^{-1}\left(\frac{Z_c P_{ref}}{V_s V_c}\right) \tag{2.60}$$

The Equations (2.53) and (2.54) can also be written as:

$$P_{fc} = \frac{m_a V_s V_{fc}}{X_c} sin\delta_c \tag{2.61}$$

$$Q_{fc} = \frac{V_s}{X_c}\left(m_a V_{fc} cos\delta_c - V_s\right) \tag{2.62}$$

For small phase angle, P_{fc} is predominantly dependent on the power angle δ_c and Q_{fc} is dependent on the voltage magnitude difference $(V_c - V_s)$. As a result, the control of real and reactive power flow is reduced to the control of the power angle and the voltage of the inverter. Although the flow of real and reactive power is not completely decoupled, they are independent to a good extent, the control of one has a very minor impact on the other one [151].

2.7 DESIGN OF CONTROL CIRCUIT FOR GRID INTERFACING VSI

The control strategy applied to the VSI consists of two cascaded loops. There is an inner current loop which regulates the grid current, and an external voltage loop which controls the DC-link voltage or an external power loop that controls the power flow. The current loop is responsible for power quality issues and current protection. The DC-link voltage/power controller is designed for balancing the power flow in the system [28]. The overall control scheme adopted for FC grid-connected inverter is shown in $Fig.$ 2.17. (v_{ca}, v_{cb}, v_{cc}) is the VSI AC output voltage, $\left(i_{ca}, i_{cb,} i_{cc}\right)$ the VSI AC output current and (v_{sa}, v_{sb}, v_{sc}) is the grid voltage. $(v_{cd},\ v_{cq})$ are the dq components of (v_{ca}, v_{cb}, v_{cc}) , $\left(i_{cd}, i_{cq}\right)$ are the dq components of $\left(i_{ca}, i_{cb,} i_{cc}\right)$ and $\left(v_{sd}, v_{sq}\right)$ are the dq components of (v_{sa}, v_{sb}, v_{sc}). The values of voltage V_c and angle δ_c are calculated corresponding to P_{ref} and Q_{ref} using Equation (2.59) and (2.60) respectively. The inverter control variables, voltage and angle are converted to $v_{cd,ref}$ and $v_{cq,ref}$.

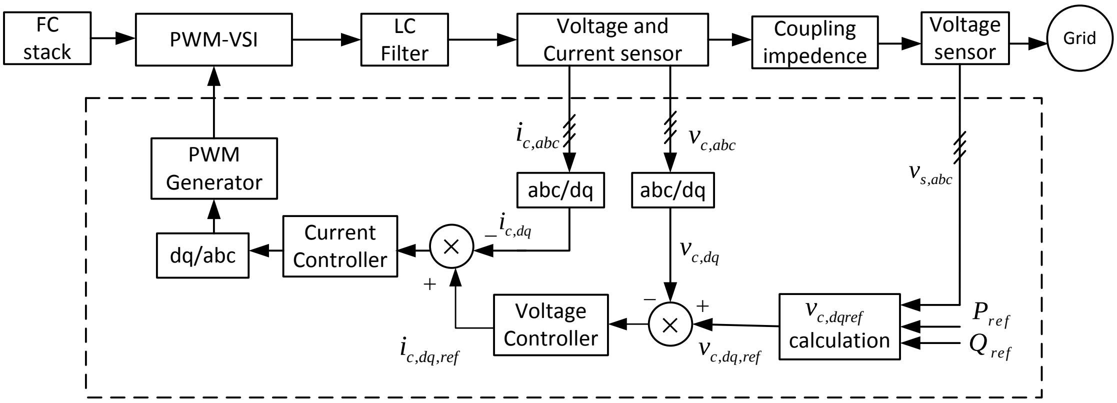

$Fig.$ 2.17 Control Circuit for the FCDG inverter

The error signals between the actual dq output voltages and the dq reference voltages are fed to the PI controller that generates the current reference signals $i_{cd,ref}$ and $i_{cq,ref}$ for the current control loop. The output of the current controller transformed back to stationary reference frame is used to produce the sinusoidal PWM pulses to the inverter switches. The controller parameters are realised by trial and error method. The PLL technique is used for extracting the phase angle of the grid voltage and current.

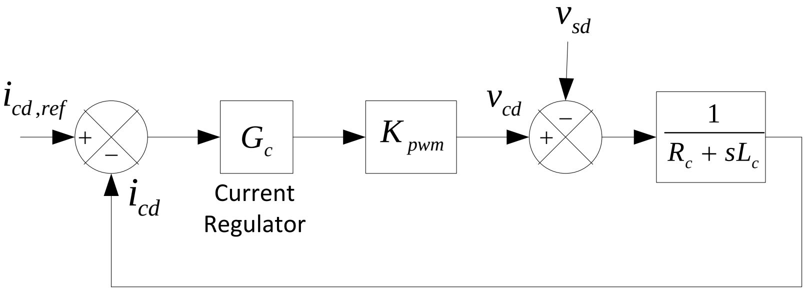

$Fig.$ 2.18 Inner current control loop (d-axis component) of grid-interfacing inverter

$Fig.$ 2.18 shows the d-axis component of the inner current control loop. K_{PWM} is the gain of the pulse width modulator and can be expressed as: $K_{PWM} = \frac{V_{fc}}{2V_{tri}}$ where V_{tri} is the amplitude of the carrier signal. G_c is the current controller which is chosen as a generic PI controller with transfer function:

$$G_c(s) = \frac{k_{cp}s+k_{ci}}{s} = k_{cp}\left(1 + \frac{k_{ci}}{k_{cp}s}\right) \tag{2.63}$$

The expression $1/R_c + L_c s$ is the model of the overall equivalent admittance of the LC filter inductor, transformer, coupling inductor and transmission line. The transfer function of the current control loop can be expressed as:

$$T_c(s) = \frac{i_{cd}(s)}{i_{cd,ref}(s)} = \frac{K_{PWM}\left(\frac{1}{R_c+sL_c}\right)}{1+K_{PWM}\left(\frac{1}{R_c+sL_c}\right)} \tag{2.64}$$

(Comment [8])The transfer function given in (2.64) is used to design the PI current controller as follows:

- *Determine the desired crossover frequency ω_c where the phase angle of $T_c(s)$ is $-180° + \emptyset_m + \emptyset_c$. $\emptyset_m$ is the specified phase margin. $\emptyset_c$ normally, $5°$ is the phase allowance for the angle contributed by the controller $G_c(s)$ at ω_c .*

- *Determine* k_{cp} *so that* $k_{cp}T_c(s)$ *crosses the 0-dB axis at the specified crossover frequency* ω_c.
- *Choose the break frequency* k_{ci}/k_{cp} *of the controller one decade below* ω_c, *i.e.* $k_{ci}/k_{cp} = \omega_c/10$ *to find* k_{ci}.
- *Plot* $G_c(s)T_c(s)$ *to verify that all the specifications are met.*

The parameters used for the design of current control loop and voltage control loop of inverter are given in Table 2.2.

Table 2.2: Parameters used for the design of inverter control

Parameters	***Values***
V_{dc}	*400V*
V_{tri}	*1V*
R_c	*0.001Ω*
L_c	*1 mH*
k_{cp}	*75*
k_{ci}	*0.75*
k_{vp}	*7.5*
k_{vi}	*0.075*

The unit step response of the current control loop is shown in Fig. 2.19. It is noted that the overshoot is 2.5% and the equivalent time constant is about 0.005s. Therefore, the overall current control loop can be approximated by a simple lag as $T_c(s) \cong \frac{1}{1+\tau s}$, *where* $\tau = 0.005\text{s}$ *is the equivalent time constant of the current control loop. This approximated value is used for the design of voltage control loop.*

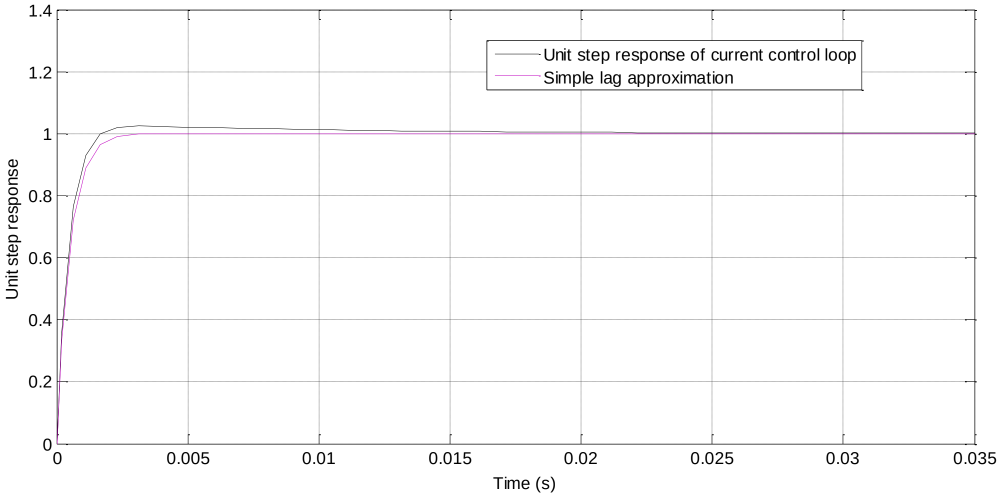

Fig. 2.19 Unit step response of the current control loop and its approximation

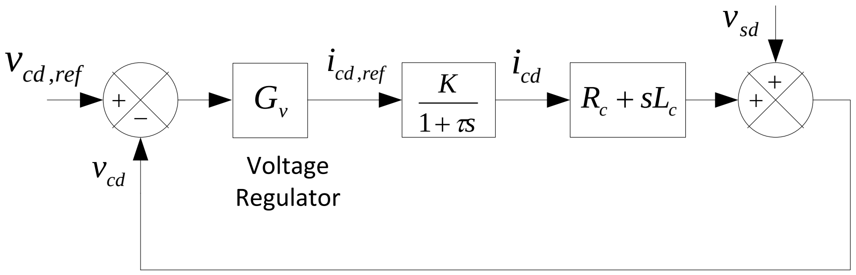

$Fig.$ 2.20 Outer voltage control loop (d-axis component) of grid-interfacing inverter

$Fig.$ 2.20 shows the d-axis component of the outer voltage control loop. G_v is the current controller which is chosen as a generic PI controller with transfer function:

$$G_v(s) = \frac{k_{vp}s + k_{vi}}{s} = k_{vp}\left(1 + \frac{k_{vi}}{k_{vp}s}\right) \tag{2.65}$$

The expression $R_c + L_c s$ is the overall impedance of the transformer, coupling inductor and transmission line. The transfer function of the voltage control loop can be expressed as:

$$T_v(s) = \frac{\left(\frac{1}{1+\tau s}\right)(R_c + L_c s)}{1 + \left(\frac{1}{1+\tau s}\right)(R_c + L_c s)} \tag{2.66}$$

The transfer function given in (2.66) is used to design the PI voltage controller. The voltage controller parameters are determined using the four steps used for determining the current controller parameters.

2.8 PROCESSOR - IN - LOOP SIMULATION, RESULTS AND DISCUSSIONS

Processor-in-Loop (PIL) simulation is a means to run the control algorithm in a fixed point Digital Signal Processor. $Fig.$ 2.21 gives an overview of the PIL simulation. In PIL simulation, the system model runs in Simulink software, while the code generated from the control subsystem runs in the DSP. The Simulink software sends the control signal from the model for one sample interval to the DSP via Code Composer Studio - Integrated Development Environment (CCS-IDE) [25].

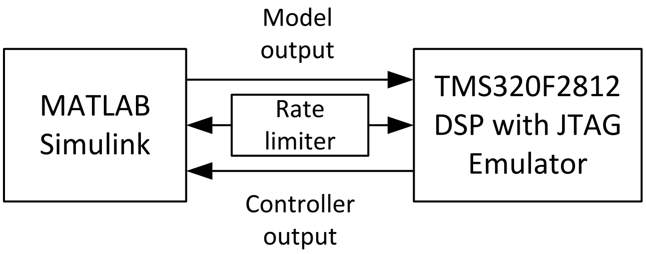

$Fig.$ 2.21 Overview of Processor-in-Loop simulation

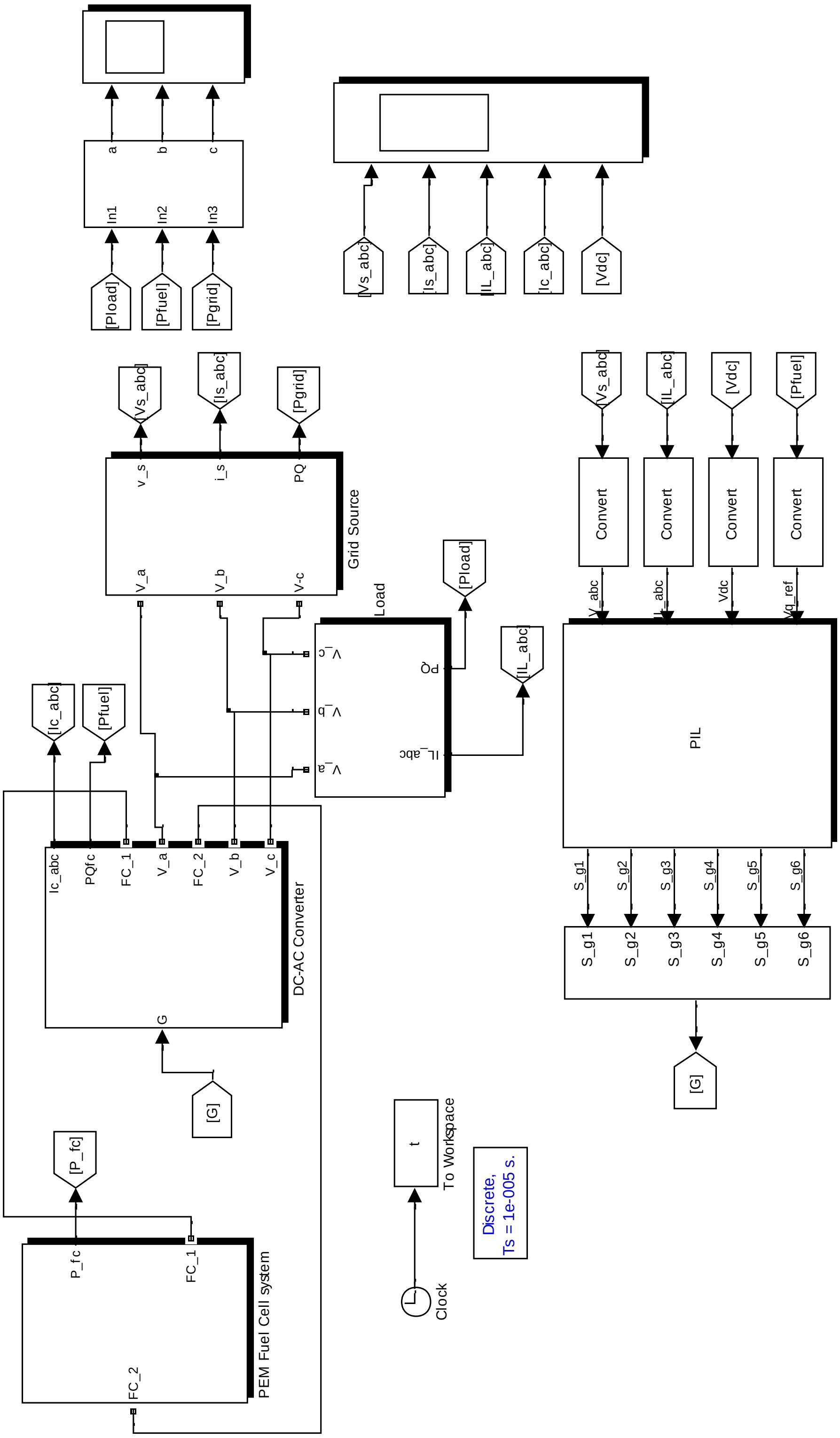

Fig. 2.22 (*a*) Overall PIL simulation model of the proposed FCDG system

Rate limiters and data type converters are used to convert the output signals to DSP compatible signals. On receiving the signals, the processor executes the algorithm for one sample step and returns the output signals to Simulink software via CCS-IDE interface. Thus, one sample cycle of the simulation is completed and the system model proceeds to the next sample interval. The complete process repeats itself and the co-simulation progresses.

The model of proposed FCDG system is simulated in MATLAB/Simulink environment and then co-simulated in TMS320F2812 DSP to validate its performance. The simulation model of the FCDG system developed in Simulink using power system block sets is shown in $Fig. 2.22\ (a)$. The control circuit is developed as per $Fig. 2.22\ (b)$ in Simulink and created in subsystem with TMS320F2812 ezdsp target processor.

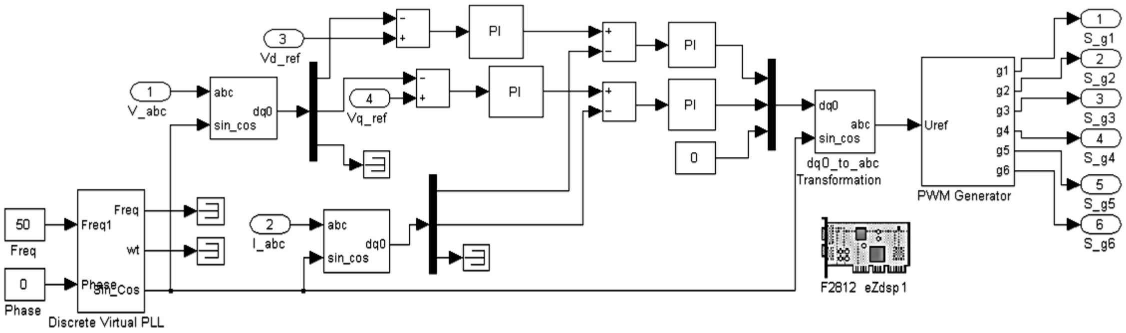

Fig. 2.22 (b) PIL control circuit of proposed FCDG system

$Fig. 2.23$ and $Fig. 2.24$ shows the FCDG system response with the required active and reactive power demand. $Fig. 2.23$ shows the output voltage V_{fc}, output current I_{fc}, and output power P_{fuel} of the FC stack. $Fig. 2.24$ shows the active power P_{fc} delivered from the FC stack to the grid along with the active power reference P_{ref} and the reactive power flow Q_{fc} from FC to the grid along with the reactive power reference Q_{ref}. The initial active power demand from FC is set to 80 kW and the reactive power demand to 50 kVAR.

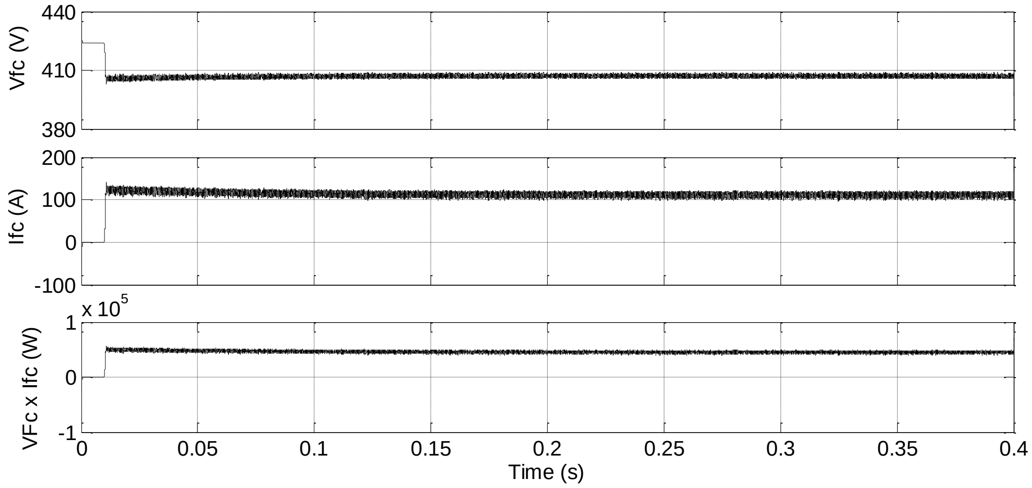

$Fig. 2.23$ Output voltage V_{fc}, output current I_{fc} and output power P_{fuel} $(V_{fc} \times I_{fc})$ of FC stack during start up

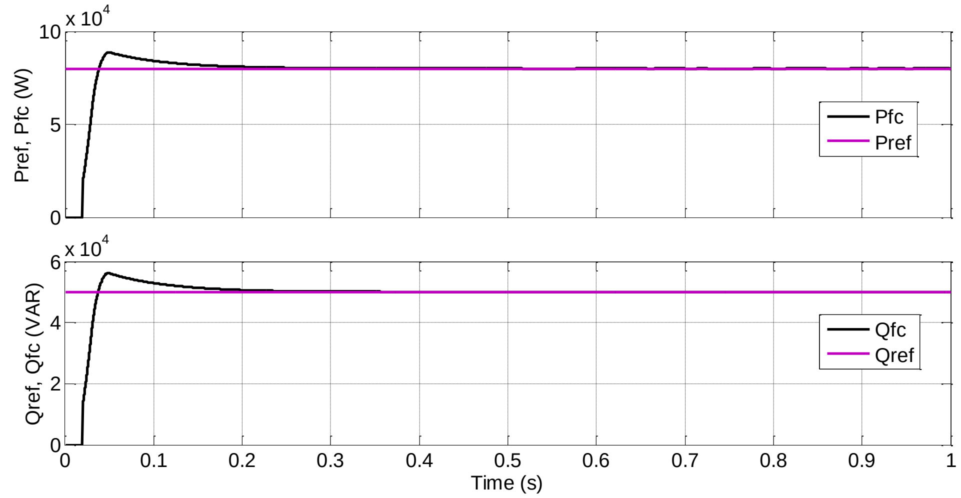

$Fig.$ 2.24 Active power flow P_{fc} from FC to the grid along with active power reference P_{ref}, Reactive power Q_{fc} from FC to grid along with the reactive power reference Q_{ref}

The stability of the FC system is investigated under electrical fault [17]. A three-phase to ground fault is simulated at t = 1.1s and is cleared at t = 1.109s in the FC system. During the fault the power flow changes direction, flowing from the grid towards the fault. $Fig.$ 2.25 shows the change in power flow in the FC system resulting from the three-phase to ground fault. From the figure it is clear that the system remains stable after the fault.

However, the energy drawn from the FC during the fault swings the voltage and current to maximum and minimum during the fault. The effect of this could be detrimental to the FC health and lifetime. Drawing the maximum current from the FC can move its operation into the concentration region [17].

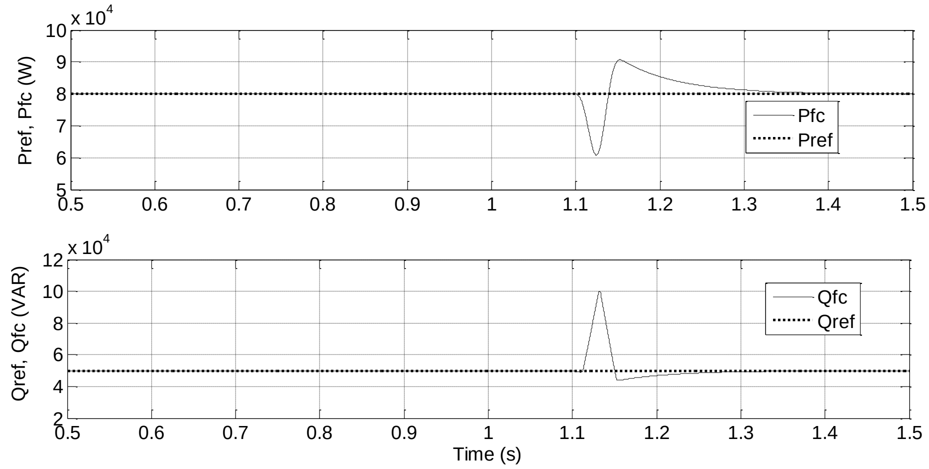

$Fig.$ 2.25 FC system response to three phase to ground fault

The FCDG system circuit has been simulated for load variations in forward interconnected mode as well as reverse interconnected mode. In forward interconnected mode, the FCDG and the grid both supply power to the local loads. In reverse interconnected mode, the FCDG supply power to local loads as per the load requirement and rest of the power is injected to the grid.

$Fig.$ 2.26 shows the performance of FCDG system for active power control in reverse interconnected mode. In reverse interconnected mode, the load active power demand is less than the FCDG capacity i.e. $P_{fc} > P_{load}$ and hence FCDG supply active power to the load as per load requirement and rest of the power is injected to the grid system. The initial load demand is 30 kW. The FC supplies 30 kW power to the load. The rest of the power is injected into the grid. The grid currents are 180° out of phase with respective phase voltages which proves that DG system is injecting extra power into the grid. $Fig.$ 2.26 (a) and (b) shows the response of the system $\left(P_{fc}, P_{load}, \text{ and } P_{grid}\right)$ to increase and decrease in resistive load respectively when $P_{fc} > P_{load}$. $Fig.$ 2.26 (a) shows the response of the system when P_{load} is increased from 30 kW to 60 kW at t = 0.3s. $Fig.$ 2.26 (b) shows the response of the system when P_{load} is decreased from 60 kW to 30 kW at t = 0.3s.

$Fig.$ 2.27 show the performance of FCDG system for active power control in forward interconnected mode. In this case the active power demand of load is more than the FCDG capacity i.e. $P_{fc} < P_{load}$ and hence the grid and FCDG both will supply active power to load. The initial load demand is 150 kW. In all the cases the FC supply constant 100 kW power and the rest of the power is provided by the grid. $Fig.$ 2.27 (a) and (b) shows the response of the system to increase and decrease in resistive load respectively when $P_{fc} < P_{load}$. $Fig.$ 2.27 (a) shows the response of the system when P_{load} is increased from 150 kW to 200 kW at t = 0.4s. $Fig.$ 2.27 (b) shows the response of the system when P_{load} is decreased from 200 kW to 150 kW at t = 0.4s.

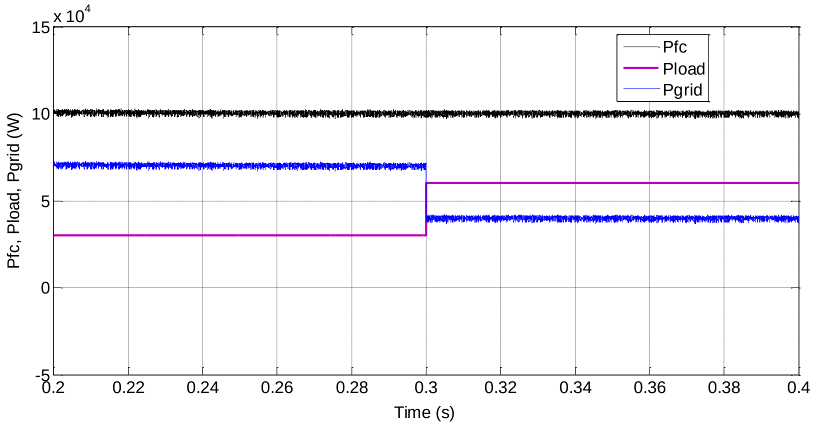

(a)

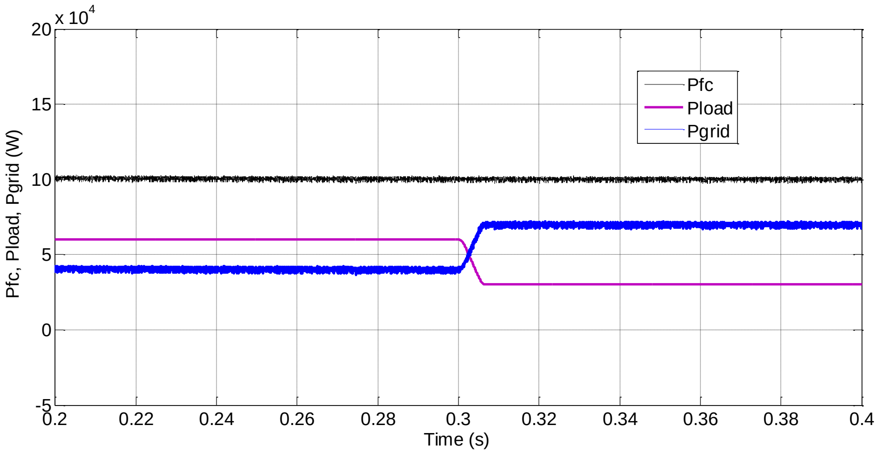

(b)

$Fig.$ 2.26 Response of the system when $P_{fc} > P_{load}$ (a) to increase in resistive load (b) to decrease in resistive load

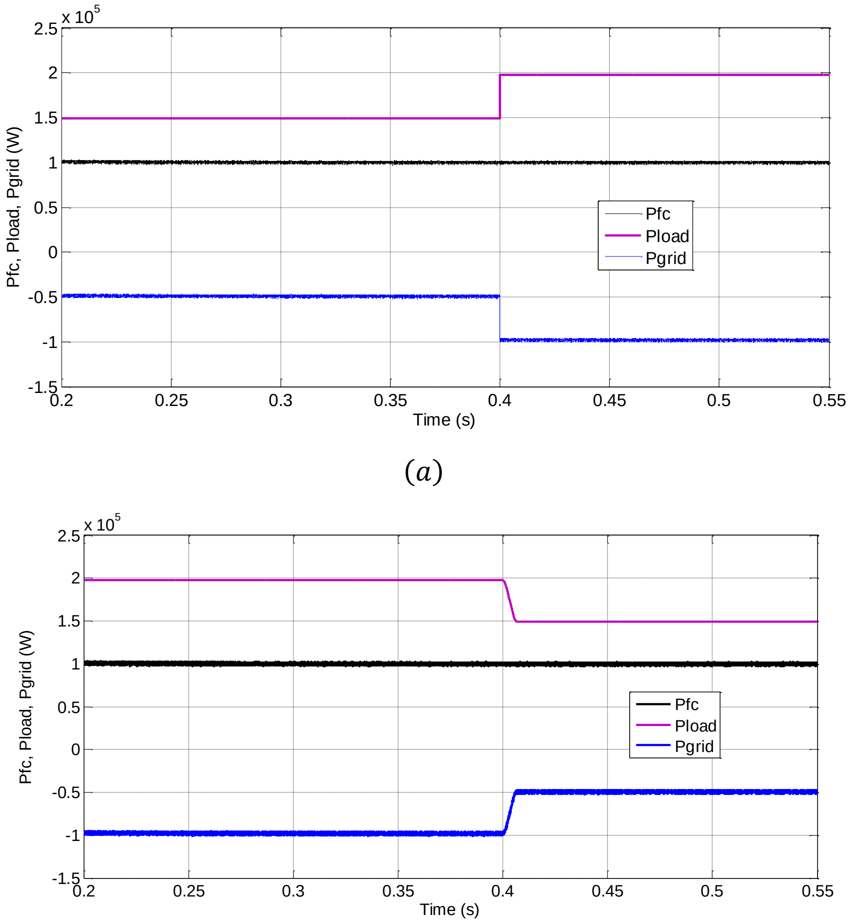

(a)

(b)

$Fig.$ 2.27 Response of the system when $P_{fc} < P_{load}$ (a) to increase in resistive load (b) to decrease in resistive load

2.9 CONCLUSION

In this work, dynamic model of 0.5 kW PEMFC is presented which models an open-circuit output voltage of the PEMFC, voltage losses in the PEMFC, formation of a charge double-layer on the surface of the cathode in the PEMFC, along with a mass balance and thermodynamic energy balance inside the PEMFC. The inputs to the FC model are anode and cathode pressures, initial temperature of the FC and room temperature.

It can be seen that as anode channel pressure and cathode channel pressure are increased, the output voltage of the PEMFC increases, which reduces voltage losses in the PEMFC. For higher values of anode and cathode channel pressures, voltage losses are smaller. Hence, it is possible to reduce voltage losses in the PEMFC by operating the PEMFC at higher values of anode and cathode channel pressures. Simulation results show that the model can predict the electrical response of the PEMFC stack under steady-state as well as transient conditions. Finally a 6kW PEMFC stack is developed from series parallel combination of the 0.5 kW FC stack. This PEMFC stack model is used in further work for designing the interfacing power electronic circuits in FCDG system.

This second half of the chapter presented the modeling and control of a single-stage FC based generation intended for grid-connected applications with real and reactive power control capability. The inverter control is designed to control the flow of active and reactive power from FC to the grid.A dq transformed two-loop control scheme using PI controllers is used to control the real and reactive power delivered from FC to the grid. The external voltage controller generates the reference current to be tracked by the internal current controller, the output of which, transformed back to stationary reference frame is used to produce the sinusoidal PWM pulses to the inverter switches. With the proposed control the active and the reactive power could be controlled independent of each other.

The validity of the proposed control schemes is verified by developing a MATLAB/Simulink model of the proposed FCDG system. The control scheme is then co-simulated in Digital Signal Processor TMS320F2812 through Processor-in-Loop. The results show that the real and reactive power delivered from the FC system to the utility grid can be controlled as desired while the DC-link voltage is maintained constant. The load following analysis and fault analysis of the PEMFC power plant is also performed. The results show that the FCDG system with the proposed two-loop inverter control scheme is capable of load-following and can remain stable under the occurrence of electrical faults.

Chapter-3

REACTIVE POWER AND HARMONIC COMPENSATION OF PCC LOAD IN FCDG SYSTEM USING ACTIVE POWER FILTER

The chapter deals with design and analysis of FC system with active power filtering capability embedded in control circuit of the inverter interfacing the FC to the grid for both single-phase and three-phase systems. Simulation in MATLAB/Simulink environment, Processor-in-Loop simulation using Digital Signal Processor TMS320F2812 and experimentation is carried out and results presented to verify the operation and the control principle.

3.1 INTRODUCTION

The increased use of power semiconductor devices in wide variety of loads have resulted in numerous power problems in the electric networks These Power Quality (PQ) problems are mitigated by installing filters in shunt with nonlinear loads. Earlier, passive filters were used, but owing to drawbacks of large size, resonance and fixed compensation associated with them, the focus has shifted towards Active Power Filters (APFs) [105, 111, 152]**.** APFs can provide harmonic compensation, reactive power compensation, balance supply currents, damping of oscillation in currents and voltage regulation. Since shunt APFs are connected in parallel with the load, they do not burden the source on account of displacement power factor and loading. The non-linear load current harmonics may result in voltage harmonics and can create a serious power quality problem in the power system network. APFs are extensively used to compensate the load current harmonics and load unbalance at distribution level thus resulting in an additional cost [153].

To maintain the accuracy and fast response of APF controller, proper estimation of reference current and the hardware is required both in quality and configuration. Most of the algorithms reported in literature based on two axis transformations are complex in implementation. Some direct and indirect controls of shunt APFs are reported in the literature [106, 154, 155]. The rising uncertainties in AC system and increasing dynamics and nonlinearity of loads have attracted more attention of researchers to evolve improved algorithms. This led to evolution of universal control technique of compensation having substantially improved transient performance under unbalanced load conditions. In addition to above, in most of the industrial environment the distortion in utility voltage is escalating at a very fast rate. It is experienced that the performance of APF has deteriorated under distorted supply voltage conditions [8, 110, 113, 156]. Under distorted supply voltage conditions, the harmonics are generated in the load current, despite the load being a linear load. *Xu and Liu* [156] proposed a method to split out the customer and supply side current harmonic contributions.

Various topologies of APF have been developed in recent years to compensate for harmonics and reactive power of non-linear loads [110, 121, 124, 154, 155, 157-160]. The Shunt Active Power Filter (SAPF) based on Current Controlled Pulse Width Modulated Voltage Source Inverter (CC PWM-VSI) is most effective even for highly non-linear loads. Various frequency-domain methods based on Fourier transform and time-domain methods based on instantaneous reactive power pq theory, synchronous reference frame dq theory, instantaneous active-reactive current $i_d i_q$ theory, have been developed for reference signal estimation [105].

Further large numbers of Alternative Energy Sources (AES) are being integrated at distribution level. The high penetration level of intermittent AES in distribution systems is a matter of great concern as it may pose a threat to network in terms of stability, voltage regulation and power-quality issues. The Distributed Generation (DG) systems are hence required to comply with strict technical and regulatory frameworks to ensure safe, reliable and efficient operation of overall network [8]. With the advancement in power electronics and digital control technology, the DG systems can now be actively controlled to enhance the system operation with improved PQ at Point of Common Coupling (PCC). However, the extensive use of power electronics based equipment and non-linear loads at PCC generate harmonic currents, which may deteriorate the quality of power [161].

As a consequence, there is a need to develop a method which attributes the responsibilities of the customer and utility at the PCC, and controller for APF that works properly under non-sinusoidal voltage and compensates customer as well as utility generated harmonics under unbalanced and varying load conditions. Technological advancement and availability of modern low cost Digital Signal Processors (DSPs) have motivated to develop simple and high performance control techniques. However, the installation of APF is accompanied by additional cost.

Generally, current controlled voltage source inverters are used to interface the intermittent AES in distributed system. Recently, a few control strategies for grid connected inverters incorporating PQ solution have been proposed. In [162], a control strategy for renewable interfacing inverter based on pq theory is proposed. In this strategy both load and inverter current sensing is required to compensate the load current harmonics. The photovoltaic inverter system in [163] can perform both active power filtering and real power injection to the grid. A dq based control of a three-phase grid-connected photovoltaic system with APF functions is proposed [128, 129]. However, these methods of control need large number of transformation, and thus, are complicated to implement. Singh et. al. [8] have presented a novel control of an existing grid interfacing inverter to improve the quality of power at PCC for a three-phase four-wire DG system.

The private sectors and utilities are now concentrating on DGs based on renewable energy sources with accrued benefits on account of higher efficiency, improved power quality, reliability, and environmental friendly nature for grid connected applications. In this scenario, DGs play an important role over fossil fuel generation. Among different DG technologies such as fuel cell, wind power, and solar; the fuel cell based DGs are becoming more popular due to its high efficiency, cleanliness, modularity, and cost effectiveness [25].

Thus features of APF has been incorporated in the conventional inverter interfacing FC with the grid, without any additional hardware cost thus making maximum utilization of inverter rating. The grid-interfacing inverter is effectively utilized to transfer FC active power to the PCC, load reactive power demand support, current harmonics compensation of PCC load and load current unbalance. With adequate control of grid-interfacing inverter, all the four objectives is accomplished either individually or simultaneously. The PQ constraints at the PCC are therefore strictly maintained within the utility standards without additional hardware cost [164].

In the presented work, the output of the FC stack is given to the DC-side of the VSI for interfacing to the grid and the features of APF have been incorporated in the control circuit of the CC-VSI [165] interfacing the FC to the grid. Thus the function of APF is added in the existing inverter of FC system by making the necessary modification in the control circuit. A common inverter is utilized to inject FC power generated to the grid and also to act as SAPF to compensate for load current harmonics and reactive power demand. This chapter is divided into three major parts. The basic principle of compensation of APF is discussed in the first part. The second and third part of the chapter deals with the design and analysis of FC-APF-DG system utilizing a single inverter, for single-phase and three-phase network respectively.

3.2 OPERATING PRINCIPLE OF SHUNT ACTIVE POWER FILTER

$Fig.$ 3.1 shows the basic compensation principle of the shunt active power filter. The supply voltage can be written as:

$$v_s(t) = V_m \, sin\omega t \tag{3.1}$$

where V_m is the peak value of source voltage. The non-linear load will draw current that will have a fundamental component and harmonic components which can be represented as:

$$i_L(t) = \sum_{n=1}^{\infty} I_n \, sin(n\omega t + \varphi_n) = I_1 \, sin(\omega t + \varphi_1) + \sum_{n=2}^{\infty} I_n \, sin(n\omega t + \varphi_n) \tag{3.2}$$

where I_1 and I_n are the peak values of fundamental load current and n$^{\text{th}}$ harmonic load currents respectively. $\emptyset_1$and $\emptyset_\text{n}$ are the phase angles of the fundamental and harmonic component of the load current respectively. The instantaneous power drawn by load can be given as:

$$\begin{aligned} p_L(t) &= v_s(t) * i_L(t) \\ &= V_m I_1 sin^2\omega t * cos\varphi_1 + V_m I_1 \, sin\,\omega t * cos\,\omega t * sin\,\varphi_1 \\ &\quad + V_m \, sin\,\omega t * \sum_{n=2}^{\infty} I_n \, sin(n\omega t + \varphi_n) \\ &= p_a(t) + p_r(t) + p_h(t) \end{aligned} \tag{3.3}$$

The first term is the instantaneous load active power, the second term is the instantaneous load reactive power and the third term is the instantaneous load harmonic power. A SAPF is required to be connected in parallel with the non-linear load to detect its reactive and harmonic current and to inject into the system a compensating current equal to the load reactive and harmonic current [117, 146]. The grid needs to supply only the real power requirement of the load, the reactive and harmonic power is to be provided by the compensator. The SAPF consists of an inductance L_c and a resistance R_c per phase on the AC-side of CC-VSI with a DC-link capacitor C_{dc} [11, 153, 159, 164, 166, 167].

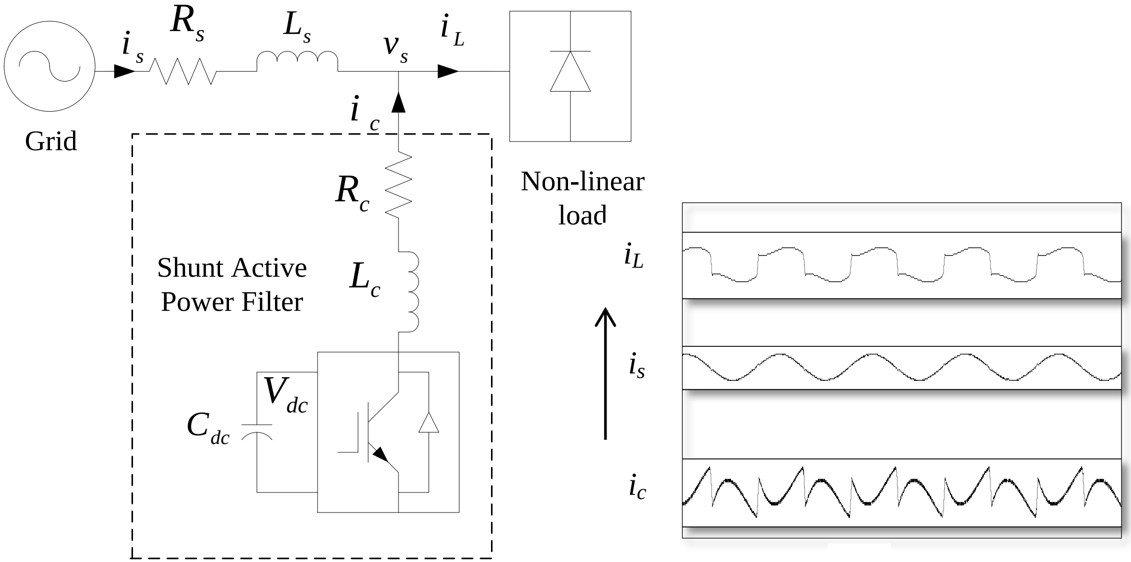

$Fig.$ 3.1 Compensation principle of Shunt Active Power Filter

3.3 SINGLE-PHASE FCDG SYSTEM WITH SAPF

This section presents the modeling and control of single-phase grid-interfaced FC system with embedded active filter functioning.

3.3.1 Power Circuit Description

$Fig.$ 3.2 shows the schematic diagram of single-phase grid-interfaced fuel cell system with non-linear load at PCC The system consists of a 6 kW PEMFC, connected to H-bridge VSI for interfacing to the grid via an energy storage DC-link capacitor C_{dc}. An inductive filter with inductance L_c and a resistance R_c is connected on the AC-side of single-phase IGBT H-bridge VSI. A step-up transformer is used to increase the voltage level before the system is connected to the PCC. An uncontrolled diode rectifier non-linear load is connected at the PCC. The inverter control is designed to compensate the load current harmonics and load power factor and regulate the FC power flow to the PCC. Simulation study in MATLAB/Simulink and experimentation is carried out to verify the proposed system with its control so as to achieve both the objectives of grid interfacing of FC system as well as active filtering.

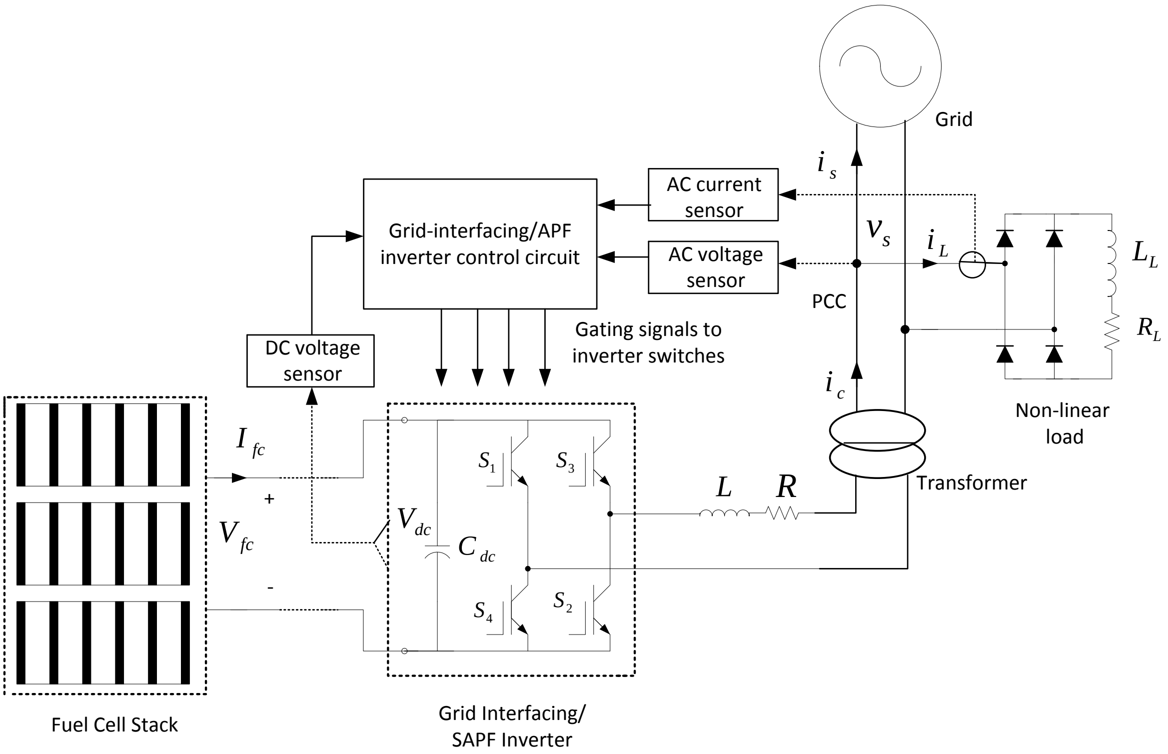

Fig. 3.2 Schematic diagram of single-phase FCDG system with non-linear load at PCC

3.3.2 Grid-Interfacing / SAPF Inverter Control

Pulse-width modulated H-Bridge CC-VSI is used to interconnect the FC system to the utility grid for power flow and power quality control purposes. A DC-link capacitor on the DC-side of the VSI acts as an energy buffer and maintains a stable DC voltage for the converter in the steady state condition. This DC-link capacitor decouples the FC from the grid and also allows independent control of converters on either side of DC-link [146].

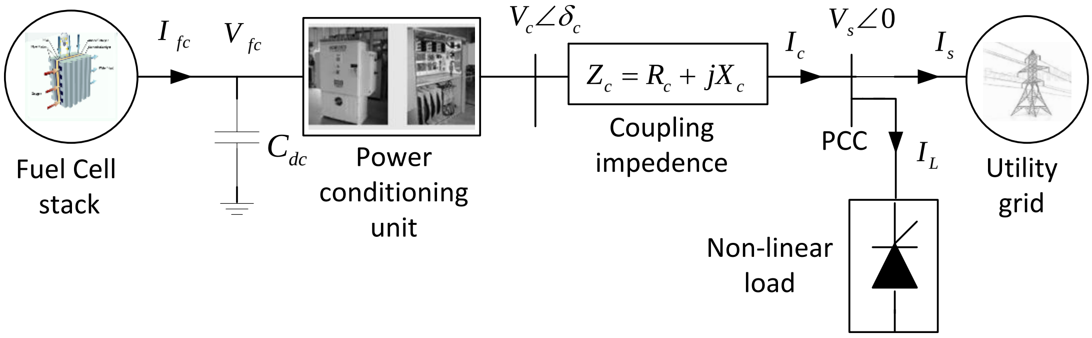

Fig. 3.3 Single line diagram of FCDG-APF system

$Fig.$ 3.3 shows the grid-interfacing inverter $V_c\angle\delta_c$ connected to the PCC $V_s\angle 0$ through a coupling impedance Z_c. The AC-side voltage of the inverter is controlled both in magnitude and phase to control the active and reactive power flow between the FC and the grid.

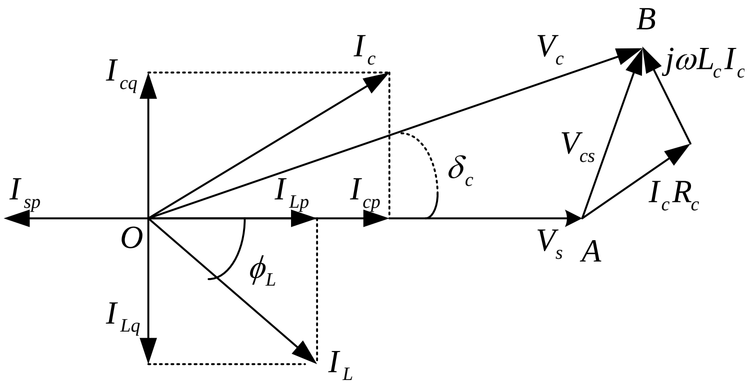

$Fig.$ 3.4 Vector diagram at unity power factor operation mode

$Fig.$ 3.4 represents the vector diagram with unity power factor. In this figure V_s and V_c are the rms voltages at PCC and AC-side of the inverter respectively. I_s, $I_L$and I_c are the rms values of currents to the grid, to load and from the inverter respectively. I_{sp} and I_{sq} are the active and reactive components of grid current I_s, I_{Lp} and I_{Lq} are the active and reactive components of load current I_L while I_{cp} and I_{cq} are the active and reactive components of inverter output current I_c, respectively. $\emptyset_L$ is the load power factor angle. δ_c is the angle between V_c and V_s. Taking R_c very small as compared to $X_c(=\omega L_c)$, current I_c through inductor L_c can be written as

$$I_c = \frac{V_{cs}}{X_c} \tag{3.4}$$

From the vector diagram, we get

$$V_{cs}{}^2 = V_c{}^2 + V_s{}^2 - 2V_c V_s \cos\delta_c \tag{3.5}$$

From Equations (3.4) and (3.5), we get

$$I_c{}^2 = \frac{V_c{}^2 + V_s{}^2 - 2V_c V_s \cos\delta_c}{X_c{}^2} \tag{3.6}$$

The active power P and reactive power Q flow from FC inverter output to the PCC can be given by:

$$P = \frac{V_s V_c}{X_c} sin\,\delta_c = \frac{m_a V_{fc} V_s}{X_c} sin\,\delta_c \tag{3.7}$$

$$Q = \frac{V_s}{X_c}(V_c \cos\delta_c - V_s) = \frac{V_s}{X_c}(m_a V_{fc} \cos\delta_c - V_s) \tag{3.8}$$

where m_a is the inverter modulation index. The grid-interface/SAPF inverter control circuit of proposed grid-interactive FC system is shown in $Fig.$ 3.5. The inverter consumes a small amount of active power to maintain the DC-link voltage and to overcome the losses associated with the inverter. The losses in the inverter are because of the switching loss in the devices, iron and copper losses in the circuit components etc [8, 11, 164, 168]. Proportional–Integral (PI) controller is used to maintain a constant DC-link voltage under varying conditions.

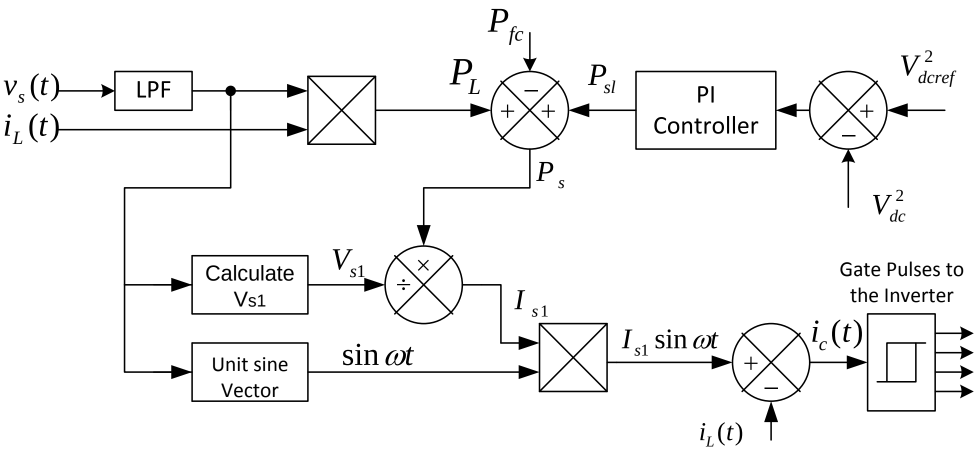

$Fig.$ 3.5 Control circuit of Grid-interfacing/SAPF Inverter

Thus inverter loss power can as expressed as:

$$P_{sl} = K_p\left(V_{dcref}^2 - V_{dc}^2\right) + K_i \int \left(V_{dcref}^2 - V_{dc}^2\right) dt \tag{3.9}$$

The average value of active power supplied by the grid is:

$$P_s = P_L + P_{sl} - P_{fc} \tag{3.10}$$

where P_L is the load active power, P_{sl} is the active loss power of the inverter and P_{fc} is the active power supplied by the FC stack. P_s is positive when both grid and FC supply power to the load. P_s is negative when the FC supply power to the load as per the load requirement and rest of the power is supplied to the grid. The active power supplied by the source can be written as,

$$P_s = \frac{V_{s1} I_{s1} \cos \phi_s}{2} \tag{3.11}$$

V_{s1} and I_{s1} are the peak value of fundamental component of PCC voltage and grid current respectively. The peak value of the desired source currents after compensation can be obtained as:

$$I_{s1} = \frac{2P_s}{V_{s1}} \tag{3.12}$$

where $cos\, \emptyset_s = 1$ for unity power factor operation. The multiplication of peak value of the desired source current with unity grid voltage generates the reference grid current [11]. An LPF is used to filter out the high frequency components in the PCC voltage. The grid synchronising angle obtained from PLL is used to generate unity grid voltage.

$$i_s^*(t) = I_{s1} \sin \omega t \tag{3.13}$$

The reference current is compared with the load current to get the compensating current $i_c(t)$.

$$i_c^*(t) = i_L(t) - i_s^*(t) \tag{3.14}$$

The hysteresis controller generates the switching pulses for the gate drivers of grid-interfacing inverter on the basis of error Δi_{ca} between the actual and reference current of inverter.

$$\Delta i_c = i_c^*(t) - i_c(t) \tag{3.15}$$

If $\Delta i_c > H_b$, where H_b is the width of hysteresis band, then upper switch S_1 is on and lower switch S_4 is off in the phase-a leg of inverter and vice-versa if $\Delta i_c < H_b$ [8].

3.3.3 Controller Design (Comment [9])

The DC-link capacitor is used as the energy storage element for the CC-VSI. There are two major factors that affect the voltage fluctuation of the DC-link capacitor. One is the transient under real power imbalance and other is the reactive power of the load to be compensated. To get the desired compensation the voltage fluctuation on the DC-link capacitor must be avoided. To regulate the DC-link voltage, conventionally PI controllers are used. The dynamic response of conventional PI control during transient is slow. To overcome the disadvantage of conventional PI controller, an energy based discrete PI controller is used here. To regulate the DC-link capacitor voltage at the desired level, an additional real power has been drawn by the APF from source to charge the capacitor. The energy E_{dc} required by the DC-link capacitor to charge the capacitor from actual V_{dc} to the reference voltage V_{dcref} can be expressed as:

$$E_{dc} = \frac{1}{2} C_{dc}\left(V_{dcref}^2 - V_{dc}^2\right) \tag{3.16}$$

On the other hand, the charging energy E_{ac} delivered by the source to the inverter will be:

$$E_{ac} = \frac{V_{s1}}{\sqrt{2}}\frac{I_{sl}}{\sqrt{2}}t = \frac{V_{s1}I_{sl}}{2}t = V_{s1}I_{sl}T_c \tag{3.17}$$

where V_{s1} is the peak value of fundamental component of source voltage, I_{sl} is the peak value of active loss component of source current and t is the charging time to charge the capacitor. In general, the DC-link capacitor voltage has ripples with double frequency, that of the supply frequency, so that t can be defined as $T = 2T_c$, where T is the time period of source voltage and T_c is the time period of DC-link capacitor voltage. According the energy conversion law (3.16) is equal to (3.17)

$$\frac{1}{2} C_{dc}\left(V_{dcref}^2 - V_{dc}^2\right) = V_{s1}I_{sl}T_c \tag{3.18}$$

$$I_{sl} = \frac{C_{dc}\left(V_{dcref}^2 - V_{dc}^2\right)}{2T_c V_{s1}} \tag{3.19}$$

However, due to lack of integral term, there is always some steady-state error while compensating the load. This can be eliminated by introducing the integral term in the (3.19). After introducing the integral term the expression of I_{sl} can be rewritten as:

$$I_{sl} = \frac{K_{pe}\left(V_{dcref}^2 - V_{dc}^2\right) + K_{ie}\int\left(V_{dcref}^2 - V_{dc}^2\right)dt}{V_{s1}} \tag{3.20}$$

where K_{pe} and K_{ie} are the proportional and integral gain of the controller. As energy based controller, its response is faster as compared to conventional PI controller. The value of K_{pe} can be given as:

$$K_{pe} = \frac{C_{dc}}{2T_c} \tag{3.21}$$

The selection of K_{ie} depends upon the trade-off between the transient response and overshoot in the compensated source current. If $K_{ie} \gg K_{pe}$, it will cause too much overshoot in the DC-link capacitor voltage. If $K_{ie} \ll K_{pe}$, it may give a slow response in the controlled variable and compensated currents. Thus we can safely choose the value of K_{ie} in the range of $\left(K_{pe}/5 \text{ to } K_{pe}\right)$.

Therefore, the selection of the gains for the proposed controller is relatively simple and straight forward. If the value of DC-link capacitor is 1500 µF and its voltage ripple period is 0.01 s, then K_{pe} *is computed as 0.075 using (3.21).*

3.3.4 Simulation Results and Discussions

The entire FCDG circuit is simulated in MATLAB/Simulink to validate its performance. The simulation results are presented for two different modes of operation. In the first mode of operation there is no power generation from the FC stack. Thus in this mode of operation, the grid-interfacing inverter is working as a SAPF, thus improving the power quality at PCC. In the second mode of operation, apart from working as a SAPF, the inverter is also injecting active power from FC to the grid. The grid current waveforms have been analysed to obtain their THDs before and after compensation in different modes of operation. The parameters used for FC/APF inverter simulation is given in *Table 3.1*.

3.3.4.1 Mode 1: No supply from FC, active power filtering mode

In this mode of operation, there is no power generation from the FC stack. Thus the grid interfacing inverter is operating as a SAPF. In the SAPF mode of operation, the inverter consumes a small amount of active power from the grid to maintain the DC-link voltage and to overcome the losses associated with the inverter and most of the load reactive power need is provided by inverter effectively.

Case 1(a) *Reactive compensation of linear load under sinusoidal voltage*

In this case a linear load is connected at PCC. Thus both source voltage as well as source current is sinusoidal but not in phase. The APF is required to compensate the reactive power only. At t = 0.1 s, the inverter is switched on. At this instant the inverter starts injecting the compensating current so as to compensate the phase difference between the source voltage and current. $Fig.$ 3.6 (a) shows the waveforms of grid voltage V_s, load current I_L, grid current I_s, APF inverter compensating current I_c and DC-link capacitor voltage V_{dc}. The grid voltage V_s (scaled by a factor 0.2) and grid current I_s is together shown in $Fig.$ 3.6 (b). At time t = 0.1s, when the inverter is switched on, there is a significant improvement in the power factor. Thus the APF compensates the phase difference between the grid voltage and grid current. The DC-link voltage is maintained at 150V. The linear load is changed at time t = 0.4 s and t = 0.8 s. The results confirm the good dynamic performance of the SAPF for a rapid change in the linear load current. The corresponding grid, load and inverter active powers $\left(P_{grid,}P_{load}\text{ and }P_{inv}\right)$ and reactive powers $\left(Q_{grid,}Q_{load}\ and\ Q_{inv}\right)$ is shown in $Fig.$ 3.6 (c).

Table 3.1 **Parameters used for Single-Phase FC/APF Inverter Simulation**

Parameters	**Values**		
Source voltage, frequency	v_s = 230V, 50 Hz		
Source resistance	R_s = 0.1 Ω		
Source inductance	L_s = 0.15 mH		
Filter inductance	L_c = 5 mH		
DC-link capacitance	C_{dc} = 1500 μF		
DC-link voltage	V_{dcref} = 100 V		
Switching frequency	f_{sw} = 10 kHz		
Step-up transformer	V_n=100V/230V, P_n=10 kW		
Load parameters	Mode 1(a)	t < 0.4, t > 0.8	Z = 7.5+j7.85
		0.4 < t < 0.8	Z = (7.5+j7.85)$\parallel$(7.5+j0)
	Mode 1(b)	t < 0.4, t > 0.8	Z_{dc_side}= 7.5+j7.85
		0.4 < t < 0.8	Z_{dc_side}= (7.5+j7.85)$\parallel$(7.5+j0)
	Mode 1(c)	t < 0.4, t > 0.8	Z_{dc_side}= 7.5+j7.85
		0.4 < t < 0.8	Z_{dc_side}= (7.5+j7.85)$\parallel$(7.5+j0)
	Mode 2	t < 0.4, t > 0.8	Z_{dc_side}= 7.5+j7.85
		0.4 < t < 0.8	Z_{dc_side}= (7.5+j7.85)$\parallel$(7.5+j0)

Case 1(b) *Reactive and harmonic compensation of non-linear load under sinusoidal voltage*

The source voltage is sinusoidal and the load current is non-sinusoidal because of the non-linear load connected at PCC. The load in this case is a diode bridge rectifier load followed by an inductor in series with a resistor. $Fig. 3.7\ (a)$ shows the waveforms of grid voltage V_s, load current I_L, grid current I_s, APF inverter compensating current I_c and DC-link capacitor voltage V_{dc}. The APF inverter is switched on at t = 0.1 s. The grid current at t = 0.1 s become pure sinusoidal and in phase with the grid voltage as shown in $Fig. 3.7\ (b)$. The Fast Fourier Transform (FFT) of the grid current before and after compensation is carried out. The current THD is reduced from 30.58% to 2.70% as shown in $Fig. 3.7\ (c)$. The non-linear load is changed at time t = 0.4 s and t = 0.8 s to verify the dynamic performance of APF.

Case 1(c) *Reactive and harmonic compensation in non-linear load under non-sinusoidal voltage*

Most of the developed techniques assume sinusoidal supply voltage when compensating non-linear load currents. Practically, the supply voltage contains harmonics which further affect the shape of supply current with increased THD level. A non-sinusoidal voltage signal of 50.93% voltage THD is generated by adding a 3rd harmonic voltage source of $150H_Z$ in series with the 50 H_Z source. This

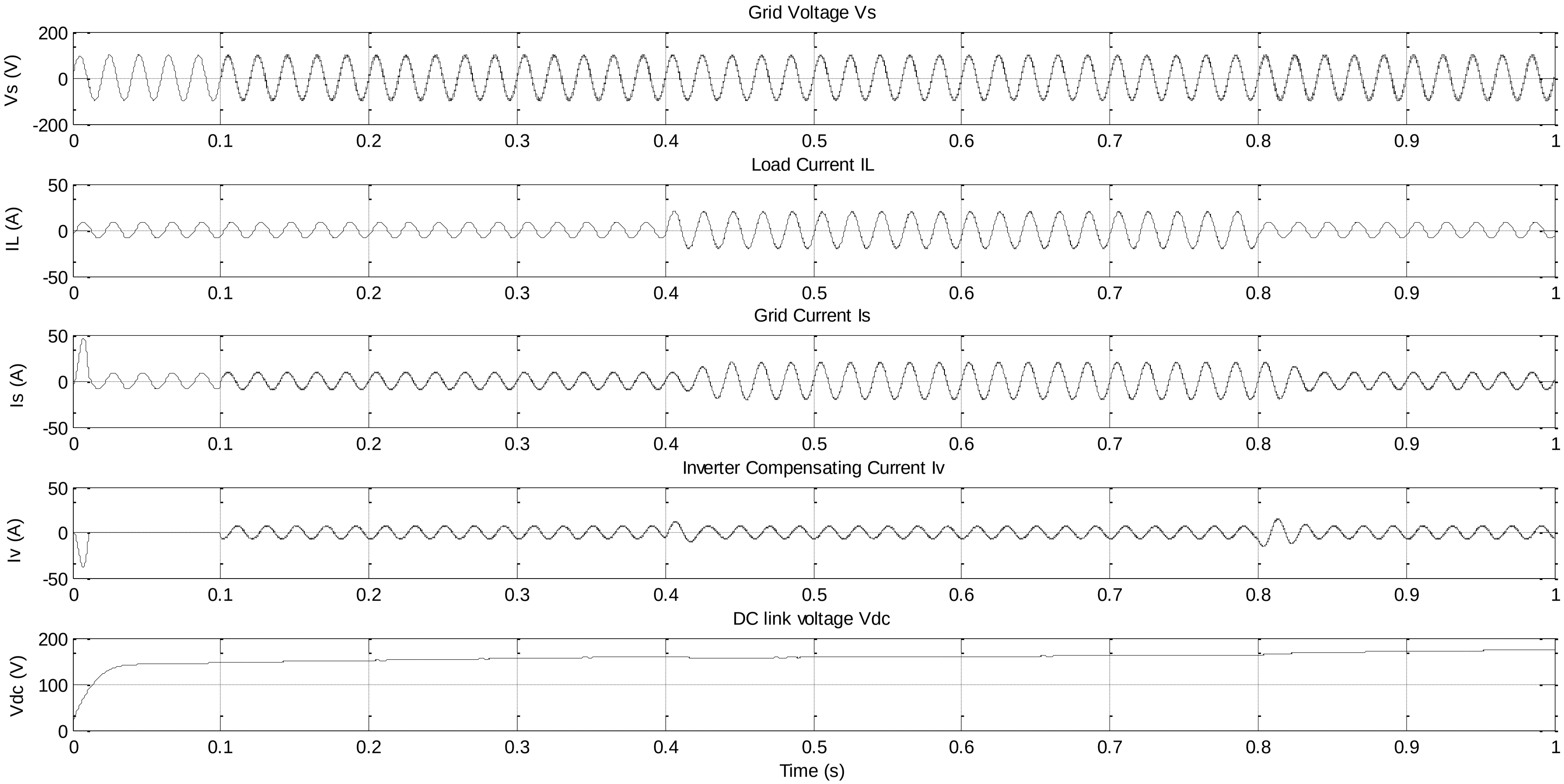

$Fig. 3.6\ (a)$ Grid voltage V_s, load current I_L, grid current I_s, inverter compensating current I_c and DC-link voltage V_{dc} for Case 1(a)

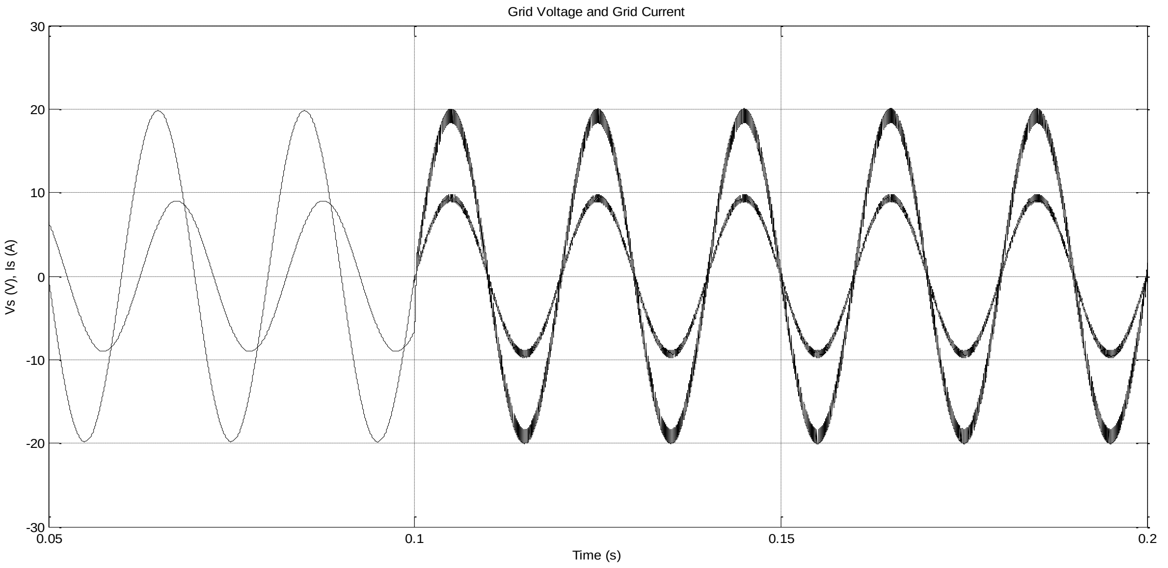

$Fig. 3.6\ (b)$ Grid voltage V_s (scaled by factor 0.2) and current I_s

non-sinusoidal voltage is applied to uncontrolled diode rectifier with series resistive-inductive load to build a non-sinusoidal load current with 43.98% current THD.

$Fig. 3.8\ (a)$ shows the waveforms of grid voltage V_s, load current I_L, grid current I_s, APF inverter compensating current I_c and DC-link capacitor voltage V_{dc}. At the instant the inverter is switched on at t = 0.1 s, it starts injecting the current in a manner so that the grid current profile changes from non-linear to sinusoidal current. $Fig. 3.8\ (b)$ reveals a comparison between grid voltage and grid current before and after compensation. Also the APF maintains its performance during change in load at 0.4 s and 0.8 s as shown. The FFT of the source current before after compensation is carried out. The current THD is trimmed down from 43.98% to 7.79% as shown in $Fig. 3.8\ (c)$. Thus the SAPF compensates for unwanted reactive and harmonic load current components under non-sinusoidal supply voltage condition also.

3.3.4.2 Mode 2: FC feeding power, non-linear load at PCC.

In this mode of operation, the FC is supplying power to the grid and the load. Thus the inverter is also injecting active power from FC to the PCC apart from working as a SAPF. The AC-side voltage of APF inverter is controlled both in phase and magnitude to control the active and reactive power, respectively. The inverter is switched on at t = 0.05 s. Thus at t = 0.05 s the inverter starts injecting active power generated from FC stack. Since the FC power is more than the load active power demand P_{load}, after meeting the load power demand, additional power of the FC flows to the grid. $Fig. 3.9\ (a)$ shows the FC stack output voltage V_{fc} and current I_{fc}. The PCC voltage V_s, load current I_L, grid current I_s and inverter current I_c is shown in $Fig. 3.9\ (b)$. Thus, the grid-connected inverter provides the entire

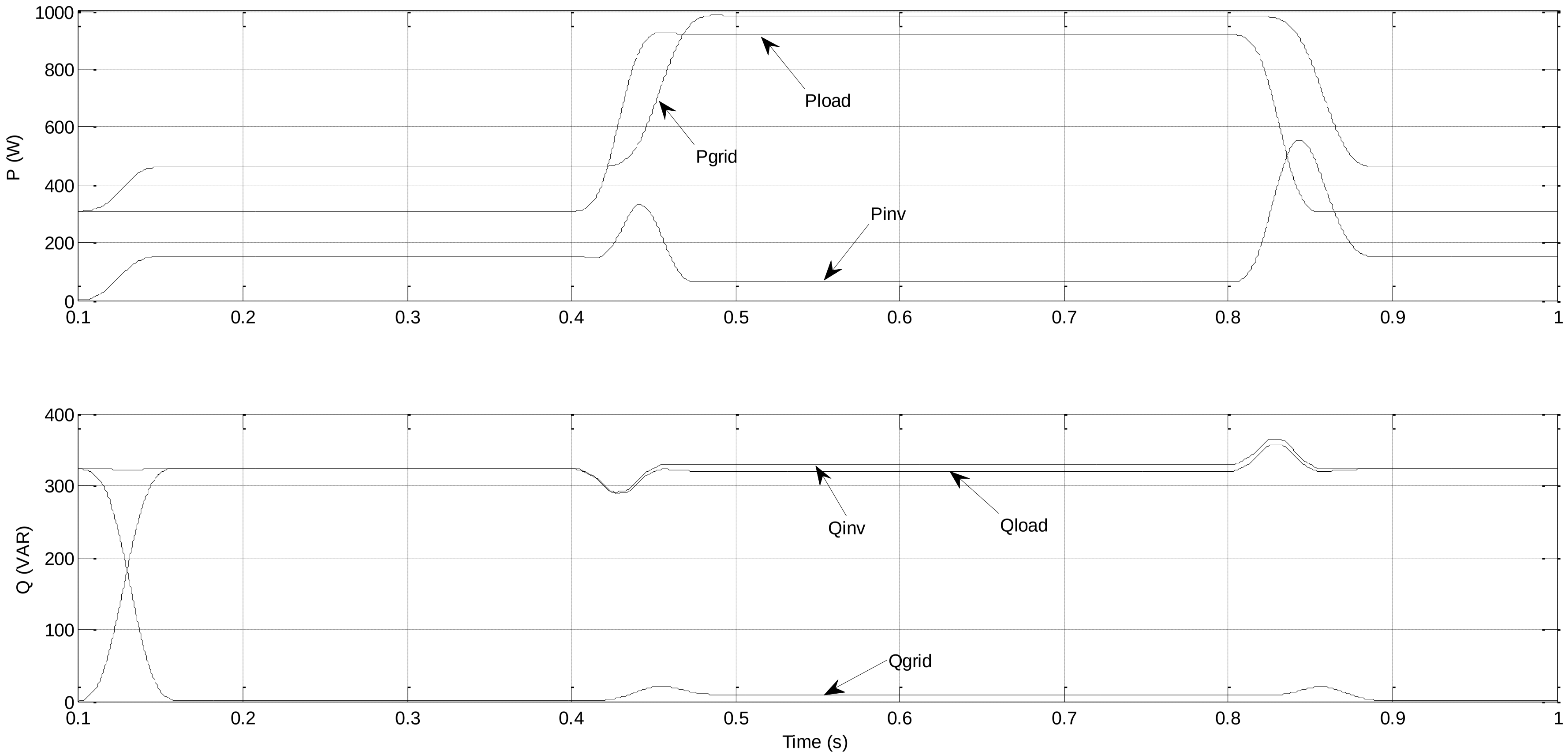

$Fig. 3.6\ (c)$ Grid, load and inverter active powers $(P_{grid,} P_{load}$ and $P_{inv})$ and reactive powers $(Q_{grid,} Q_{load}\ and\ Q_{inv})$

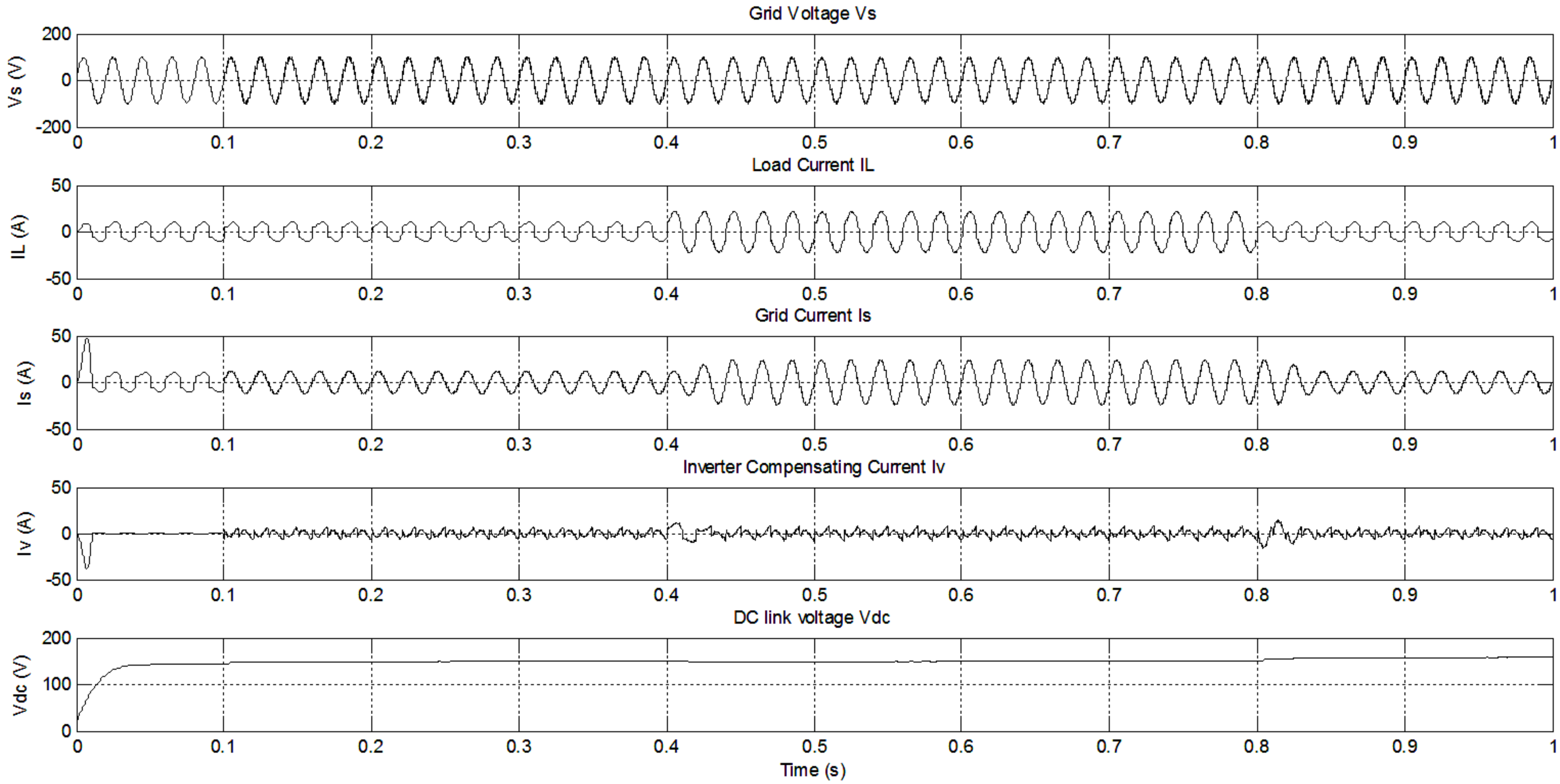

$Fig. 3.7$ (a) Grid voltage V_s, load current I_L, grid current I_s, inverter compensating current I_c and DC-link voltage V_{dc} for Case 1(b)

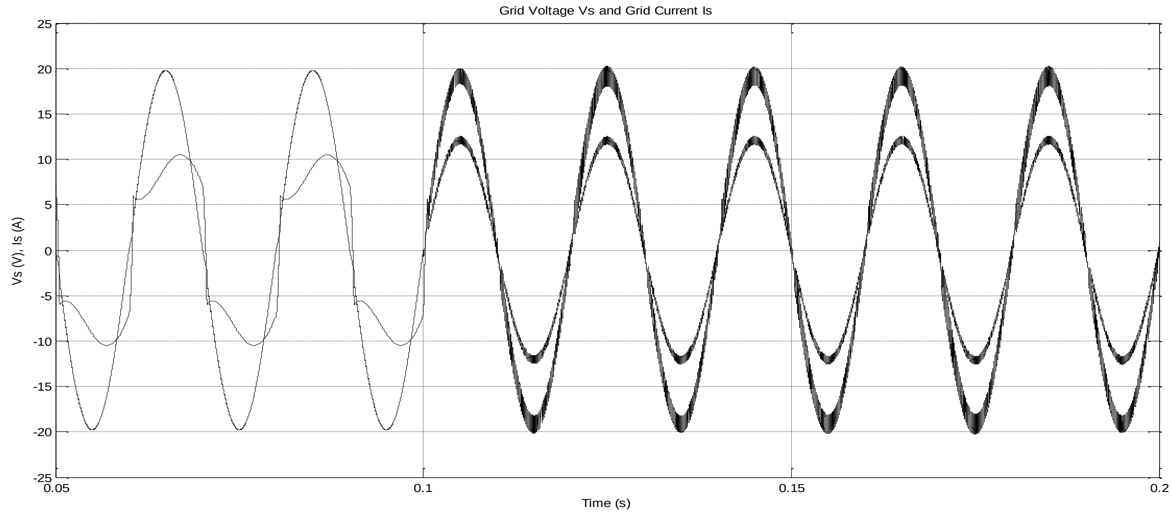

$Fig.$ 3.7 (b) Grid voltage V_s (scaled by factor 0.2) and current I_s

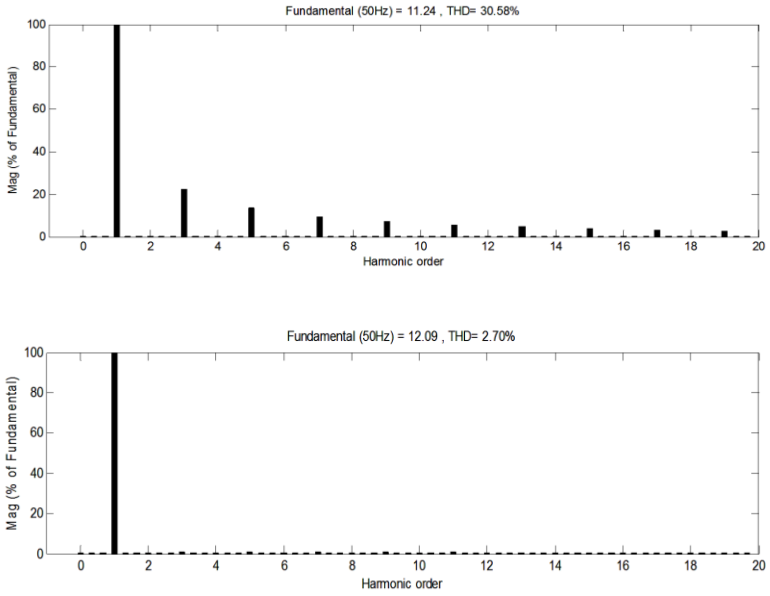

$Fig.$ 3.7 (c) THDs of grid current before and after compensation

load power demand i.e. active reactive and harmonic load power and feeds the additional active power to the grid. The grid current and voltage together is shown in $Fig.$ 3.9 (c). The 180 degree phase shift between the grid voltage and grid current suggests that the additional power is fed to the grid at unity power factor. The exchange of active and reactive powers between grid, load and FC stack is shown in $Fig.$ 3.9 (d). The active powers of grid, load and FC stack are represented as $(P_{grid,} P_{load}$ and $P_{fc})$ and the reactive powers of grid, load and FC stack by $(Q_{grid,} Q_{load}$ and $Q_{fc})$ respectively. Thus in this case the grid interfacing inverter is simultaneously utilised to inject the power generated from FC to PCC and to improve the power quality at PCC. $Fig.$ 3.9 (e) shows the FC power reference $P_{fc,ref}$ and FC power P_{fc} simultaneously with variations in $P_{fc,ref}$.

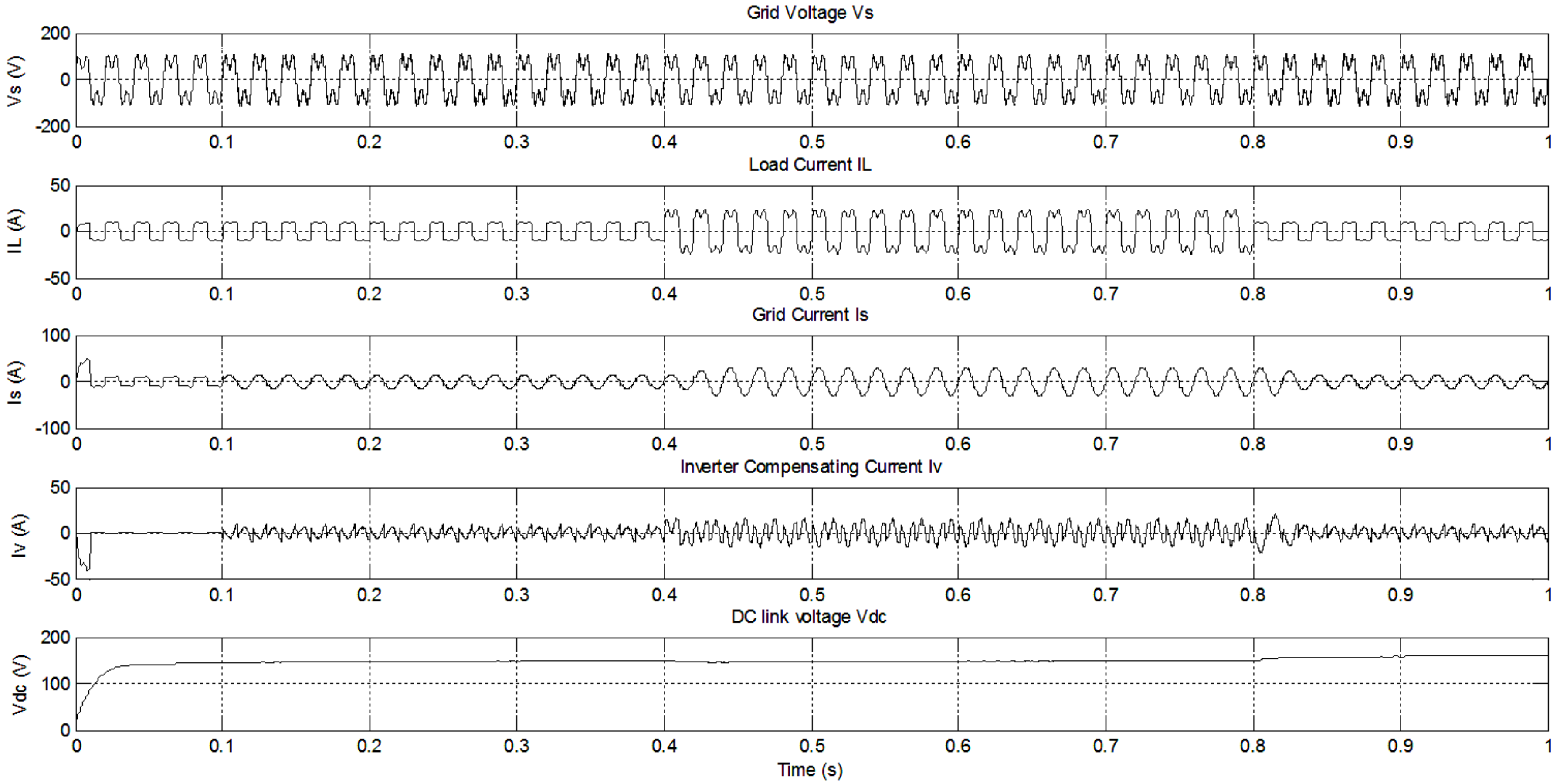

$Fig. 3.8\ (a)$ Grid voltage V_s, load current I_L, grid current I_s, inverter compensating current I_c and DC-link voltage V_{dc} for Case 1(c)

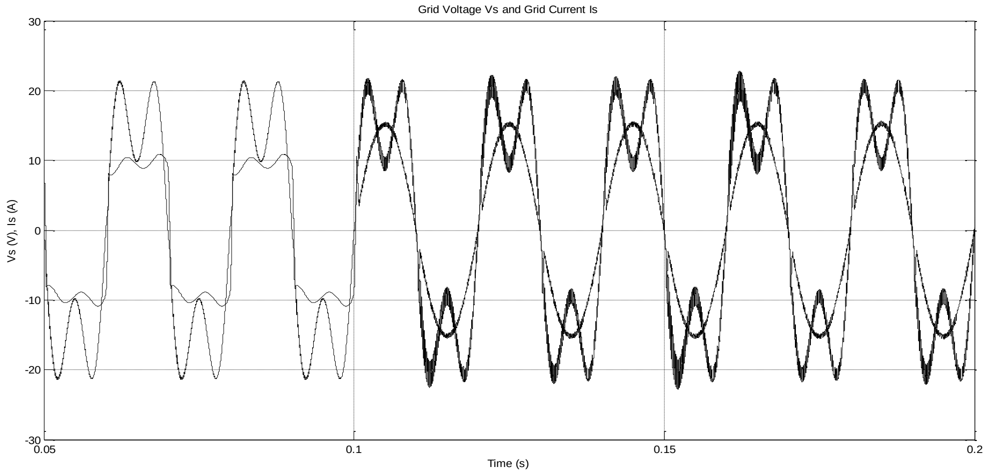

$Fig. 3.8$ (b) Grid voltage V_s (scaled by factor 0.2) and current I_s

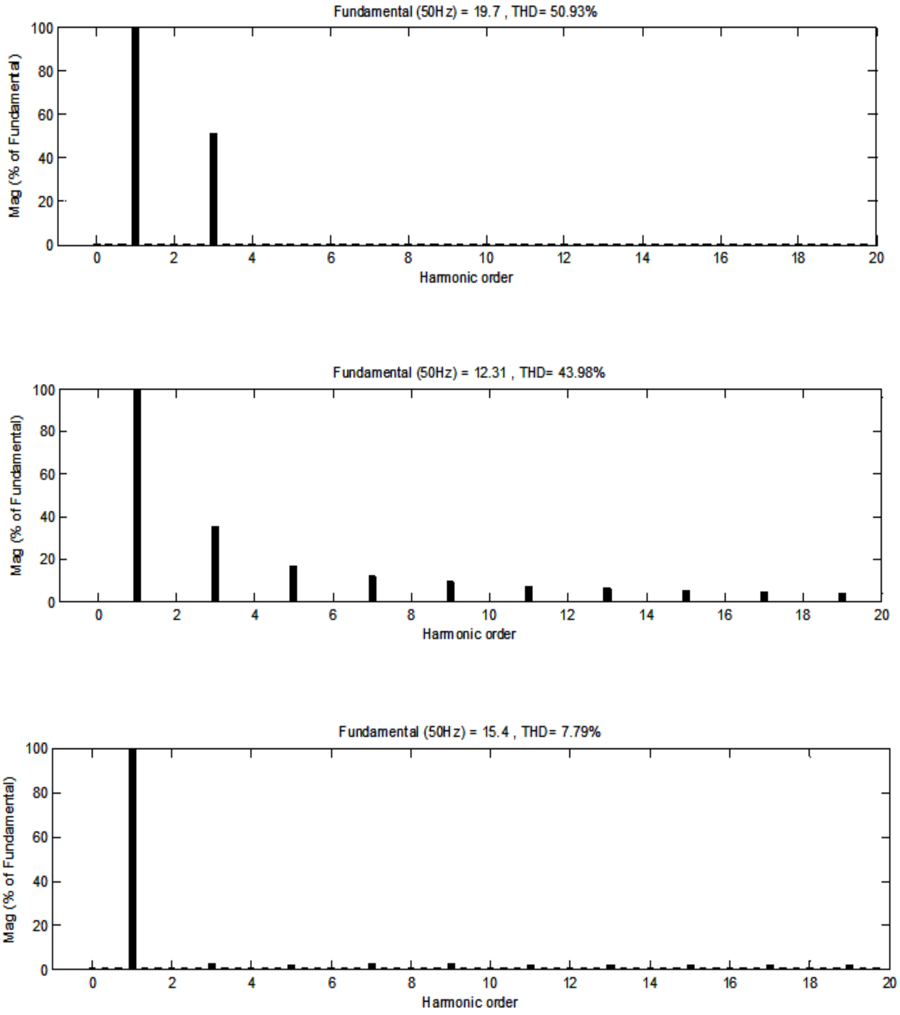

$Fig. 3.8$ (c) THDs of grid voltage, grid current before compensation and grid current after compensation

3.3.5 Experimental Validation

Experimental prototype as shown in $Fig. 3.10$ is developed and results obtained for Mode 1 operation. The TMS320F2812 DSP is used to realize the proposed control scheme. The control algorithm is developed in MATLAB using power system block sets and the TMS320F2812 DSP is connected with MATLAB through a parallel port connector for transferring the real-time generated codes using the software Code Composer Studio. The DC-link voltage is sensed by a DC voltage sensor, load current is sensed by LA25-NP current sensors and PCC voltage by LV25-P voltage sensor. These signals are then applied to the inbuilt analog-to-digital converter of the processor through signal conditioner. The signal conditioner converts these entire signals into unipolar values in the range of 0-3 V compatible with DSP. The DSP generated pulses are applied to the switches through pulse isolation and a driver circuit [152]. The details of *experimentation (Comment [5])* are given in *Appendix-D*. $Fig. 3.11$ shows real-time pulse generation circuit which is an interface between MATLAB and eZdsp. The parameters used for the experimental studies are given in *Table 3.2*.

$Fig. 3.12$ shows the experimental results for active power filtering mode of operation when there is no power generation from the FC stack. $Fig. 3.12\ (a)$ shows the experimental results for reactive compensation in steady-state under sinusoidal voltage and linear load. It is observed that APF compensate the reactive component but current THD in this case after compensation is increased to some extent but within the recommended limits. $Fig. 3.12\ (b)$ shows the experimental results for reactive and harmonic compensation in steady-state under sinusoidal voltage and non-linear load. The source current THD in this case is reduced from 35.87% to 2.62% along with reactive compensation. $Fig. 3.12\ (c)$ shows the experimental results for reactive and harmonic compensation in steady-state under non-sinusoidal voltage (THD 6.4%) and nonlinear load (THD 38.87%). Source current is found in phase with source voltage and sinusoidal which ensures both harmonic and reactive compensation capabilities. The source current THD in this case is reduced from 37.88% to 2.92%.

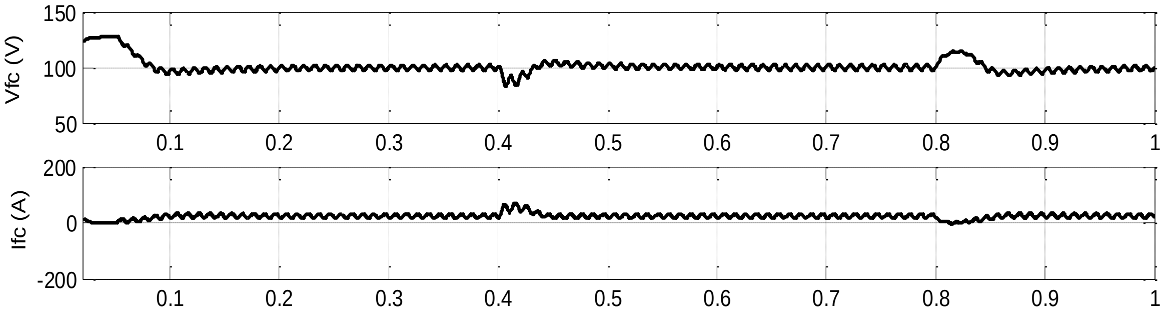

$Fig. 3.9\ (a)$ Fuel cell stack output voltage V_{fc} and current I_{fc}

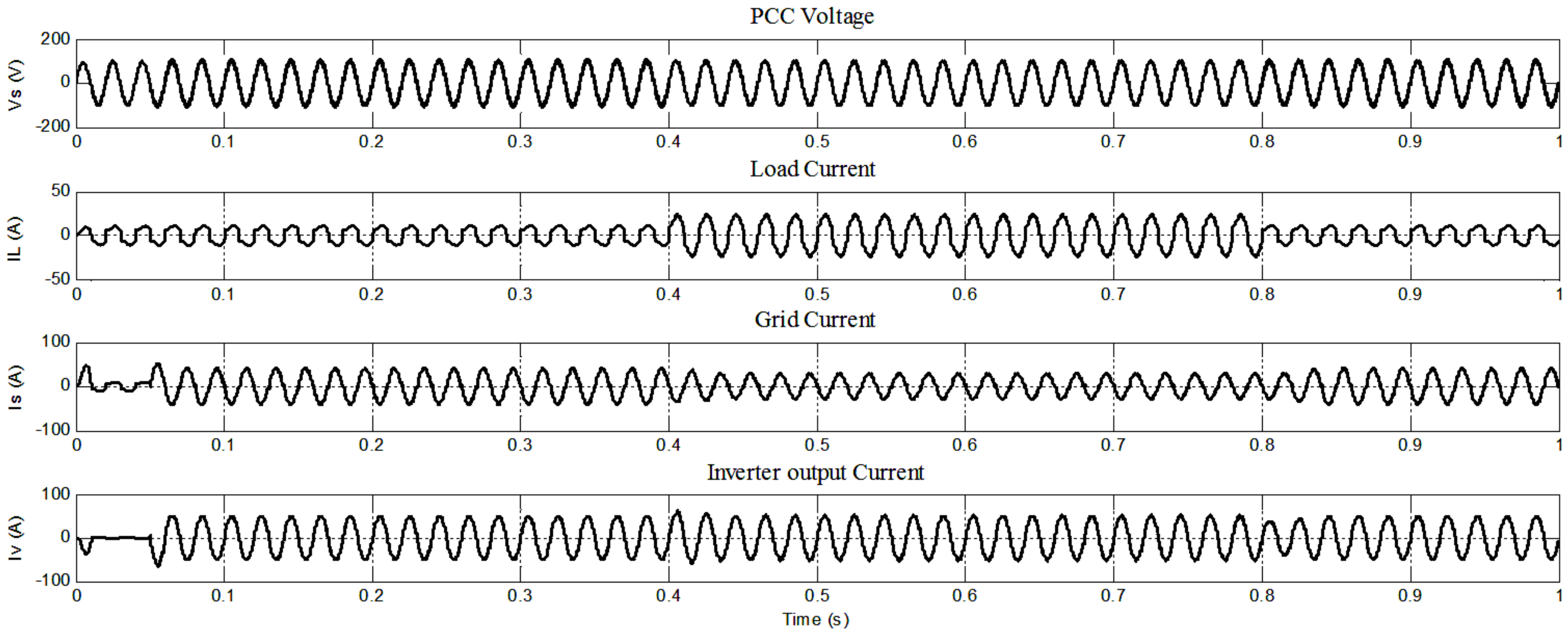

$Fig.3.9\ (b)$ Grid voltage V_s, load current I_L, grid current I_s and inverter output current I_c for Case 2

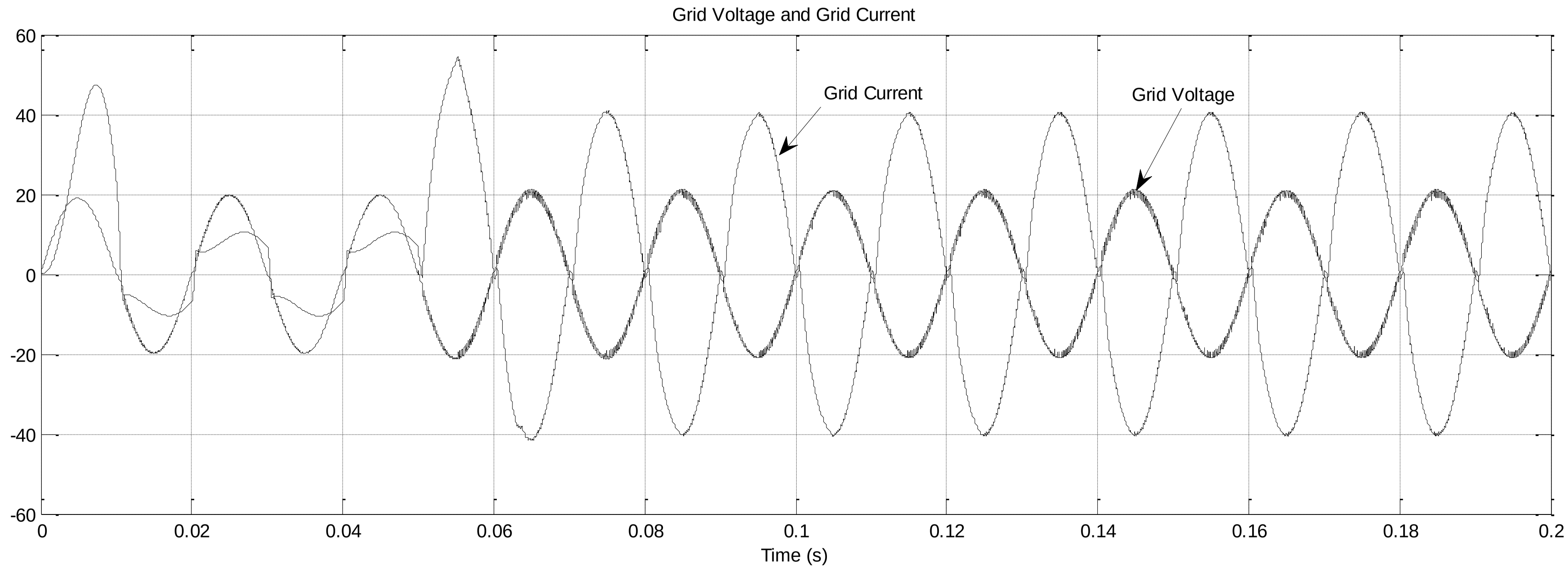

$Fig. 3.9\ (c)$ Grid voltage V_s (scaled by factor 0.2) and current I_s

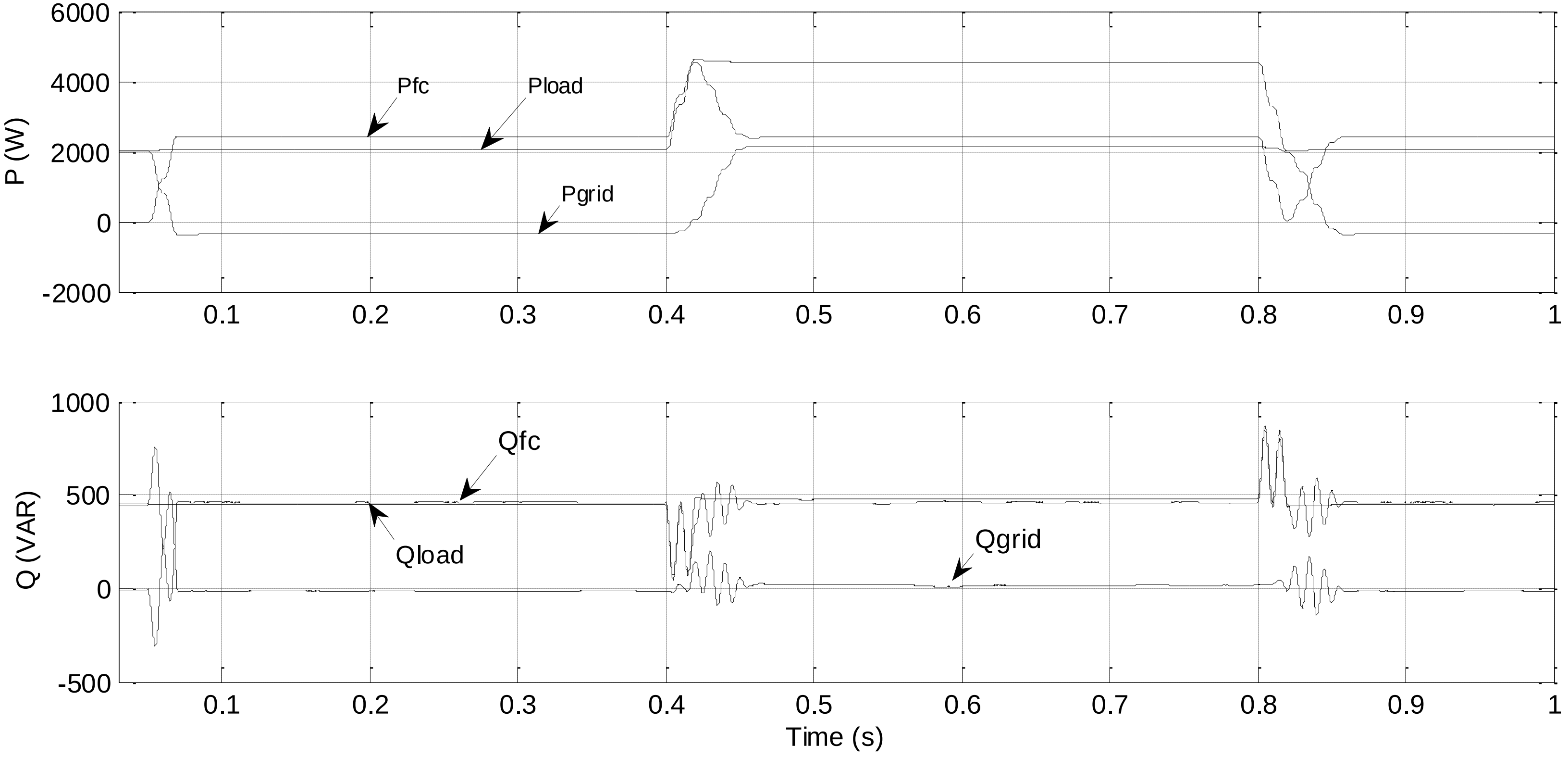

$Fig. 3.9\ (d)$ Grid, load and FC active powers $\left(P_{grid,}P_{load}\text{ and }P_{fc}\right)$ and reactive powers $\left(Q_{grid,}Q_{load}\text{ and }Q_{fc}\right)$

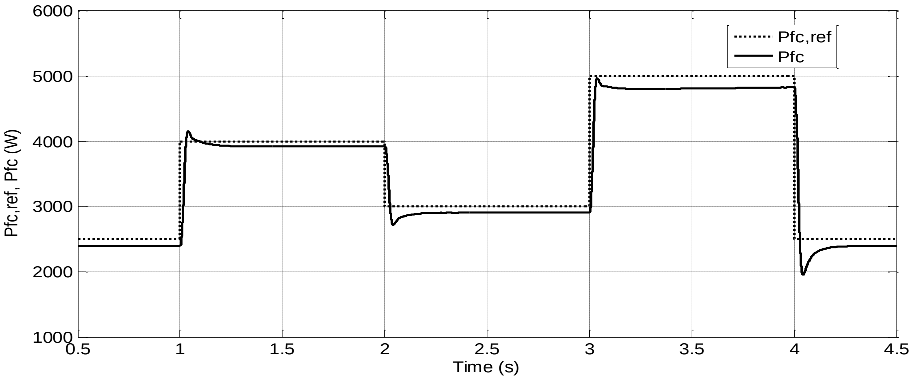

$Fig.$ 3.9 (e) FC power reference $P_{fc,ref}$ and P_{fc} simultaneously

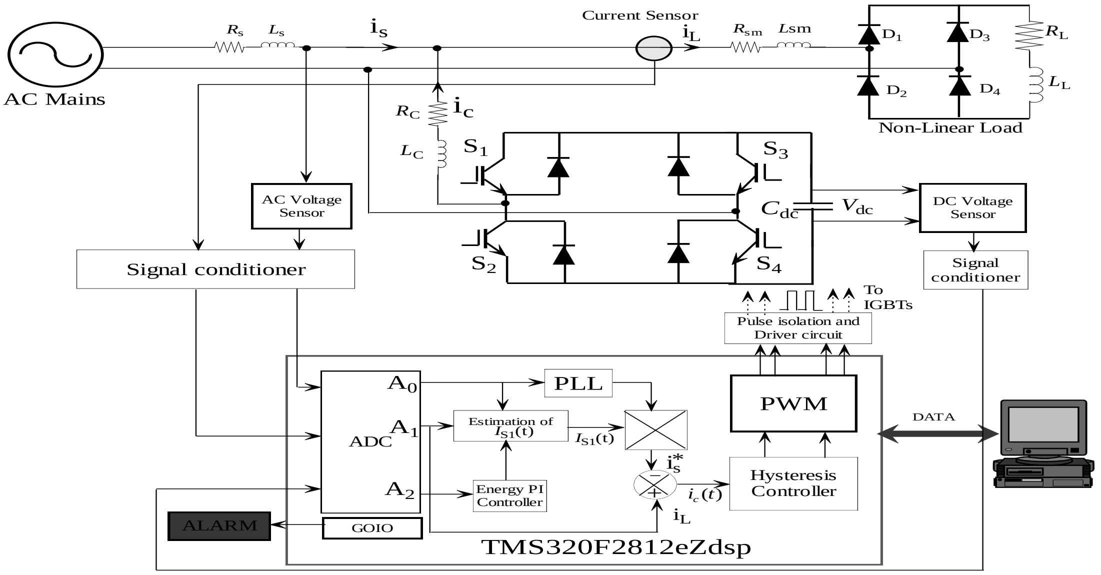

$Fig.$ 3.10 Experimental prototype for active power filtering operation

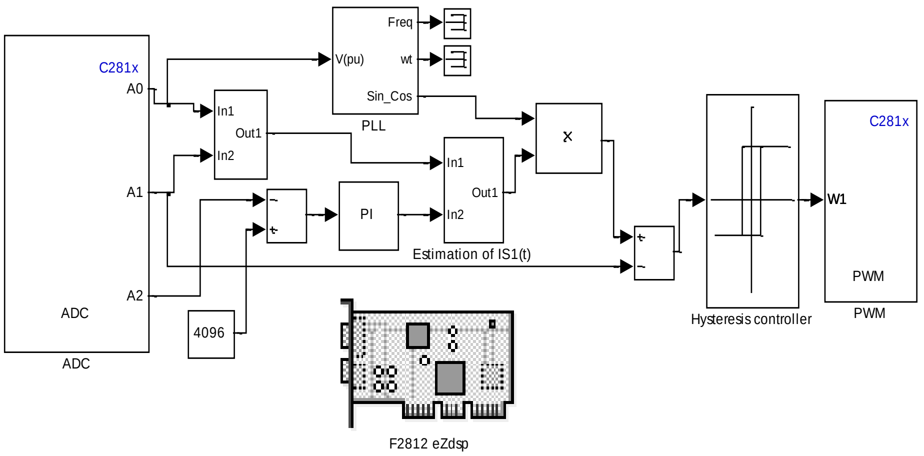

$Fig.$ 3.11 Real-time pulse generation

Photograph showing the experimental set-up

Table 3.2 **Parameters used for Experimentation in Single-Phase**

Parameters	**Values**
Source voltage and frequency	v_s = 30V, 50Hz
Source inductance	L_s = 0.15mH
Filter inductance	L_c = 2.75mH
DC-link capacitance	C_{dc} = 1600 μF
DC-link voltage	V_{dcref} = 75V

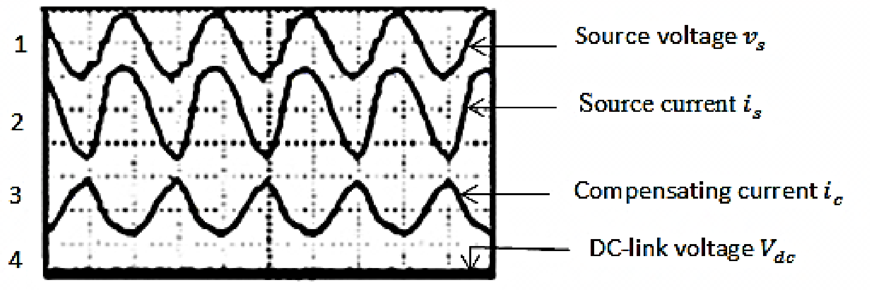

(a)

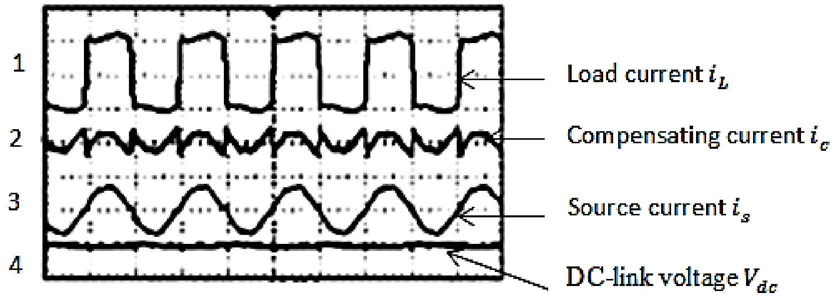

(b)

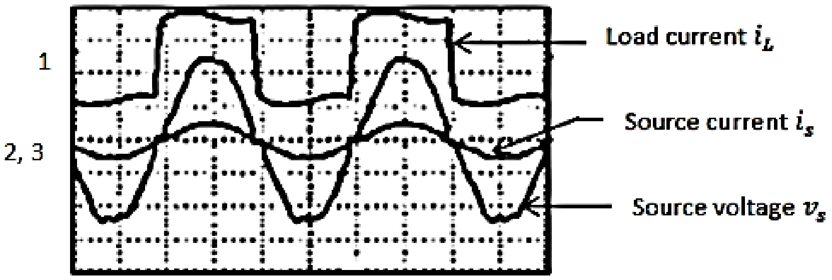

(c)

$Fig.$ 3.12 Experimental results for Case 1

(a) Case 1(a) 1. $(v_s - 30V)$ 2. $(i_s - 1.67A)$ 3. $(i_c - 0.75A)$ 4. $(V_{dc} - 70V)$. (time - 10 ms/div) (b) Case 1(b) 1. $(i_L - 1.8A)$ 2. $(i_c - 0.8A)$ 3. $(i_s - 1.60A)$ 4. $(V_{dc} - 70V)$. (time - 10 ms/div) (c) Case 1(c) 1. $(i_L - 1.8A)$ 2. $(v_s - 28.3V)$ 3. $(i_s - 1.72A)$ (time - 5 ms/div)

3.4 THREE-PHASE FCDG SYSTEM WITH SAPF

This section presents the modeling, control and design analysis of a three-phase FCDG system with active filter functions. The main focus is to control the active power supplied by the FCDG system while compensating harmonics and reactive currents caused by the nonlinear loads using SAPF. The designed controller either regulates the power flow between the FC and the grid or works as an APF or performs both the functions simultaneously. Simulation in MATAB is carried out to verify the operation and the control principle. The results are obtained for different operating conditions with varying load demands to prove the effectiveness of the entire system.

3.4.1 Power Circuit Description

$Fig.$ 3.13 shows the circuit of the proposed grid-interactive FC system that comprises of a 100 kW FC stack connected to a three-phase VSI for interfacing to the grid via an energy storage DC-link capacitor C_{dc}. A three-phase inductive filter is connected on the AC-side of the VSI. A step-up transformer is used to increase the voltage level before the system is connected to the PCC. An uncontrolled diode rectifier balanced/unbalanced non-linear load is connected at the PCC. The inverter control is designed to compensate the load current harmonics, load power factor, load current imbalance with distorted supply voltage and regulate the FC power flow to the PCC.

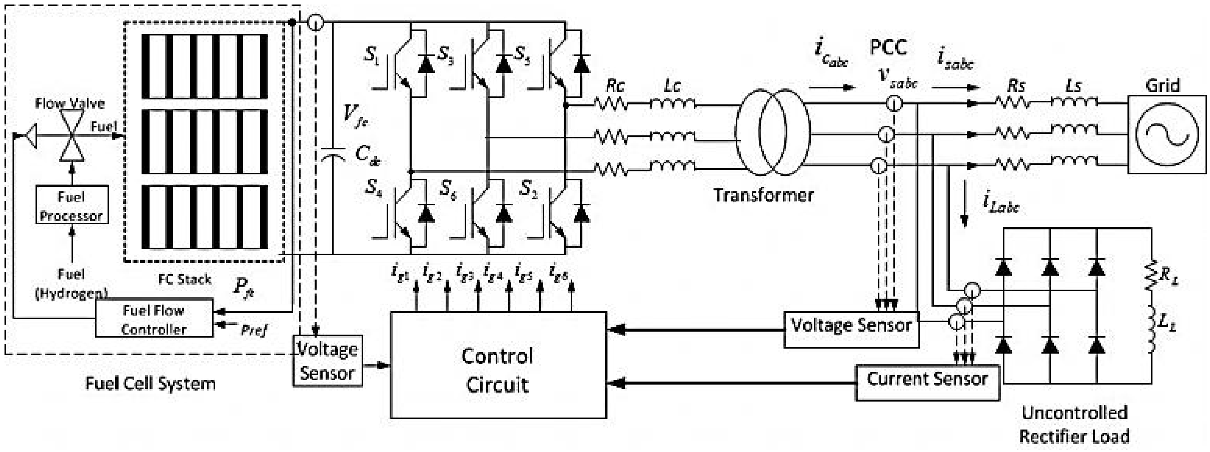

$Fig.$ 3.13 Proposed three-phase FCDG system

3.4.2 Control Circuit Analysis and Design of Grid-Interfacing Inverter

Assuming the PCC voltage and the load current consists of a set of harmonic components n, where $n = \{1, 2 \ldots N\}$, the PCC voltage vector $v_s(t)$ and load current vector $i_L(t)$ can be expressed as:

$$v_s(t) = \begin{bmatrix} v_{sa} \\ v_{sb} \\ v_{sc} \end{bmatrix} = \begin{bmatrix} \sum_{n=1}^{N} V_{sna} sin(n\omega t) \\ \sum_{n=1}^{N} V_{snb} sin(n(\omega t - 120°)) \\ \sum_{n=1}^{N} V_{snc} sin(n(\omega t + 120°)) \end{bmatrix} \tag{3.16}$$

$$i_L(t) = \begin{bmatrix} i_{La} \\ i_{Lb} \\ i_{Lc} \end{bmatrix} = \begin{bmatrix} \sum_{n=1}^{N} I_{Lna}\, sin(n\omega t - \emptyset_{na}) \\ \sum_{n=1}^{N} I_{Lnb}\, sin(n(\omega t - 120°) - \emptyset_{nb}) \\ \sum_{n=1}^{N} I_{Lnc}\, sin(n(\omega t + 120°) - \emptyset_{nc}) \end{bmatrix} \tag{3.17}$$

Here $\left(V_{sna,}V_{snb,}V_{snc}\right)$ are the peak values of PCC voltages, $\left(I_{Lna,}I_{Lnb,}I_{Lnc}\right)$ are the peak values of load currents and $\left(\emptyset_{na,}\emptyset_{nb,}\emptyset_{nc}\right)$ are the phase angles corresponding to n^{th} order harmonics.

The control circuit of grid-interfacing inverter is developed as per $Fig. 3.14$. PCC voltages v_s, grid currents i_s, load currents i_L, DC-link voltage V_{dc} and FC output current I_{fc} are the inputs the control algorithm. PCC voltages and load currents are used to calculate average value of load power. The inverter power loss is obtained by regulating DC-link capacitor voltage. The FC power is subtracted from the sum of active load power and the inverter loss to compute the source active power. Positive sequence component and unit sine template of the source voltages are estimated simultaneously. Optimized peak value of desired source currents is calculated by equating source active power to apparent power supplied by the source, and multiplied with voltage unit templates to compute the desired source currents. The desired source currents are compared with the actual load currents. The differences of the compared signals are, then, applied to hysteresis controllers to switch the devices used in CC-VSI. For compensation at unity power factor, the active power supplied by the source P_s should be equal to the source apparent power as given by:

$$P_s = P_L + P_l - P_{fc} = \frac{3}{2} V_{s1} I_{s1}^{*} \tag{3.18}$$

where P_L is the load active power, P_l is the active loss power of the inverter and P_{fc} is the active power supplied by the FC, V_{s1} is the peak value of the PCC voltages and $I_{s1}^{*}$is the peak value of the desired source currents after compensation. Thus

$$I_{s1}^{*} = \frac{2P_s}{3V_{s1}^{*}} \tag{3.19}$$

The reference instantaneous source currents $(i_{sa,}^{*} i_{sb}^{*}, i_{sc}^{*})$ are computed using the desired peak value and unit current vectors $(u_{sa}, u_{sb}\ and\ u_{sc})$ derived from sensed source voltages using PLL.

$$\begin{aligned} i_{sa}^{*}(t) &= I_{s1}^{*} u_{sa} \\ i_{sb}^{*}(t) &= I_{s1}^{*} u_{sb} \\ i_{sc}^{*}(t) &= I_{s1}^{*} u_{sc} \end{aligned} \tag{3.20}$$

The unit sine vectors are generated by instantaneous source voltage of any one phase using PLL. The unit sine templates are expressed as:

$$\begin{aligned} u_{sa}(t) &= u_1(t) \\ u_{sb}(t) &= -\frac{1}{2} u_1(t) + \frac{\sqrt{3}}{2} u_2(t) \end{aligned} \tag{3.21}$$

$$u_{sc}(t) = -\frac{1}{2}u_1(t) - \frac{\sqrt{3}}{2}u_2(t)$$

where $u_1(t) = sin\ \omega t$ and $u_2(t) = cos\ \omega t$. The reference inverter currents are computed by taking the difference between instantaneous source reference currents and sensed load currents.

$$\begin{aligned} i_{ca}^*(t) &= i_{sa}^*(t) - i_{La}(t) \\ i_{cb}^*(t) &= i_{sb}^*(t) - i_{Lb}(t) \\ i_{cc}^*(t) &= i_{sc}^*(t) - i_{Lc}(t) \end{aligned} \tag{3.22}$$

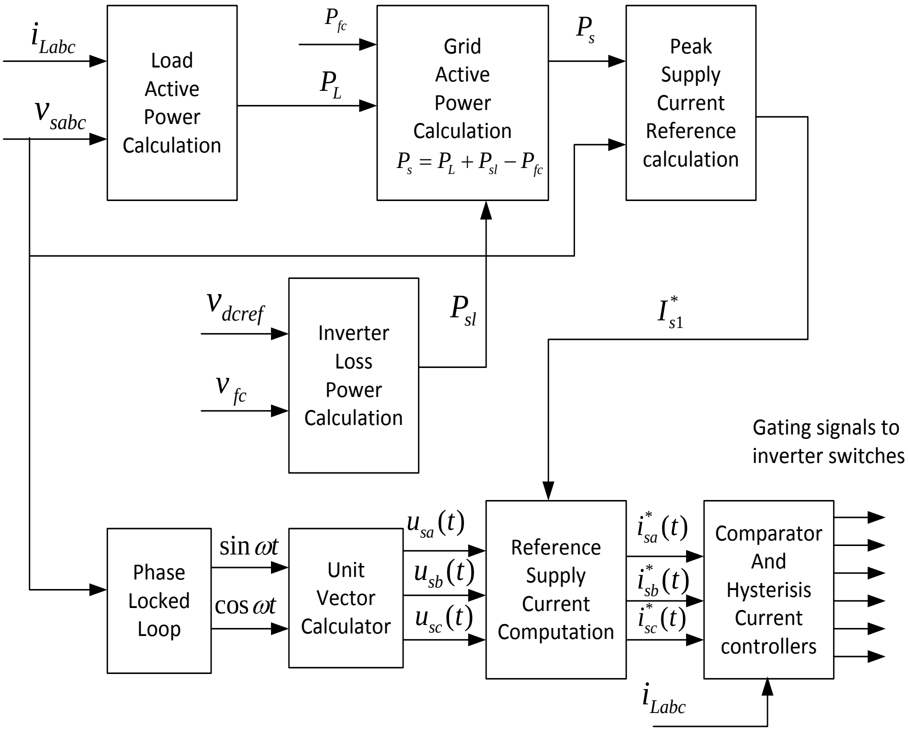

$Fig.$ 3.14 Control circuit of grid-interfacing inverter

The error (Δi_{ca}, Δi_{cb} and Δi_{cc}) between the reference inverter current and the actual inverter current are given to hysteresis current controller which regulates the duty cycle of the PWM inverter.

$$\begin{aligned} \Delta i_{ca} &= i_{ca}^* - i_{ca} \\ \Delta i_{cb} &= i_{cb}^* - i_{cb} \\ \Delta i_{cc} &= i_{cc}^* - i_{cc} \end{aligned} \tag{3.23}$$

The hysteresis controller generates the switching pulses for the gate drives of grid-interfacing inverter on the basis of error between actual and reference current of inverter. If $\Delta i_{ca} > H_b$ then upper switch S_1 is on and lower switch S_4 is off in the phase-a leg of inverter and vice-versa if $\Delta i_{ca} < H_b$. Here H_b is the width of hysteresis band. The switching pulses for the other two legs operate on the same principle.

3.4.3 Simulation Results and Discussions

$Fig.$ 3.15 (a) shows the PIL simulated model of the proposed system. $Fig.$ 3.15 (b) shows the control circuit of the proposed system which is created in PIL subsystem for its real time simulation. The simulation study is carried out in MATLAB/Simulink to verify the proposed control algorithm to achieve multi-objectives of power quality enhancement and FC power injection to the grid. The aim of proposed approach is to regulate the power at PCC in two different modes of operation (1) Simultaneous power quality enhancement and FC power injection $P_{fc} > 0$ and (2) Only power quality enhancement mode P_{fc} = 0. *Table 3.3* shows the parameters used for FC/APF circuit simulation.

3.4.3.1 Mode - 1 operation: Simultaneous Power Quality Enhancement with FC power injection

In this mode of operation, FC is supplying power to the PCC. Thus in this case the grid interfacing inverter is simultaneously utilised to inject the power generated from FC to PCC and to improve the power quality at PCC. An uncontrolled diode-rectifier with series resistive-inductive non-linear load is connected at PCC. The FCDG supply active and reactive power to local loads as per the load requirement and rest of the active power is injected to the grid. The grid voltage is taken as non-sinusoidal with THD of 13.93% generated by adding a 5th harmonic voltage source of 250 Hz in series with 50 Hz source. Thus the harmonics in grid voltage further affect the grid current with increased THD levels.

Table 3.3 **Parameters Used For Three-Phase FC/APF Circuit Simulation**

Parameters	**Values**
FC Stack Capacity	100 kW
Grid voltage and frequency	V_s = 440V (Ph-Ph rms), 50 Hz
Grid resistance	R_s = 0.1 Ω/phase
Grid inductance	L_s = 0.15 mH/phase
Filter inductance	L_c = 5 mH/phase
DC-link capacitance	C_{dc} = 1500 µF
DC-link voltage	V_{dcref} = 380 V
Switching frequency	f_{sw} = 10 kHz

The PCC voltage V_s, grid current I_s, load current I_L and inverter output current I_c is shown in $Fig.$ 3.16 (a). The inverter connecting the FCDG to the grid is switched on at t = 0.1 s. Thus at t = 0.1 s the inverter starts injecting active power generated from FC stack. $Fig.$ 3.16 (b) shows the exchange of active powers between grid, load and FC $\left(P_{grid,} P_{load} \text{ and } P_{fc}\right)$. The grid-connected inverter provides the entire load power demand i.e. active reactive and harmonic load power and feeds the additional active power to the grid. There is a non-linear load variation between time t = 4.0 s to t =

4.2 s and load imbalance in between times t = 4.6 s and t = 4.8 s. $Fig. 3.16\ (c)$ shows the FC stack output voltage V_{fc}, output current I_{fc} and FC stack output power P_{fc}.

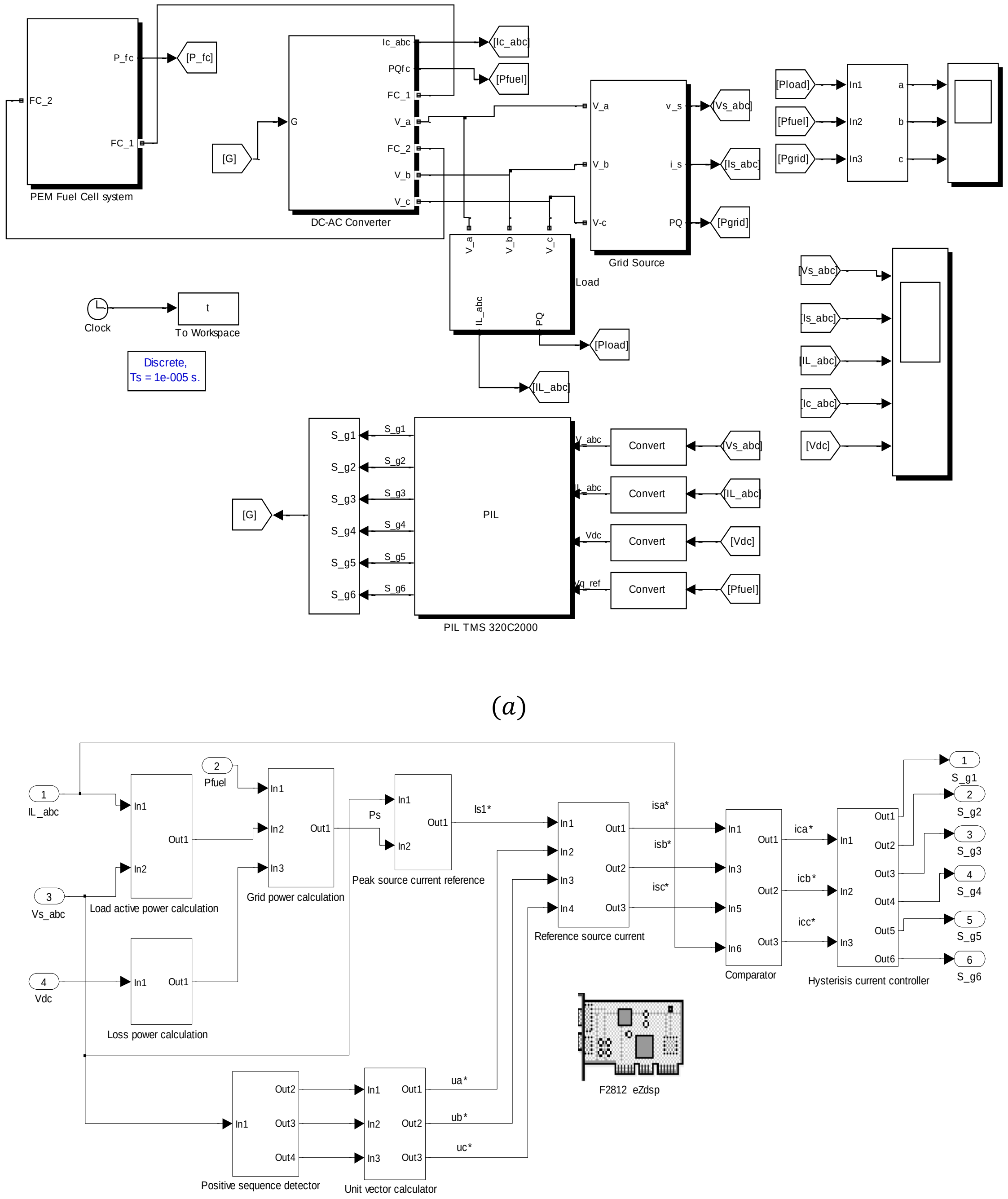

(a)

(b)

$Fig. 3.15\ (a)$ Overall PIL simulation model of the proposed FC-APF system (b) PIL control circuit of proposed system

- **Start-up**

The PCC voltage V_s, grid current I_s, load current I_L and inverter output current I_c for times t = 0 s to t = 0.4 s i.e. during start-up is shown in $Fig. 3.17\ (a)$. From the figure it can be seen that the

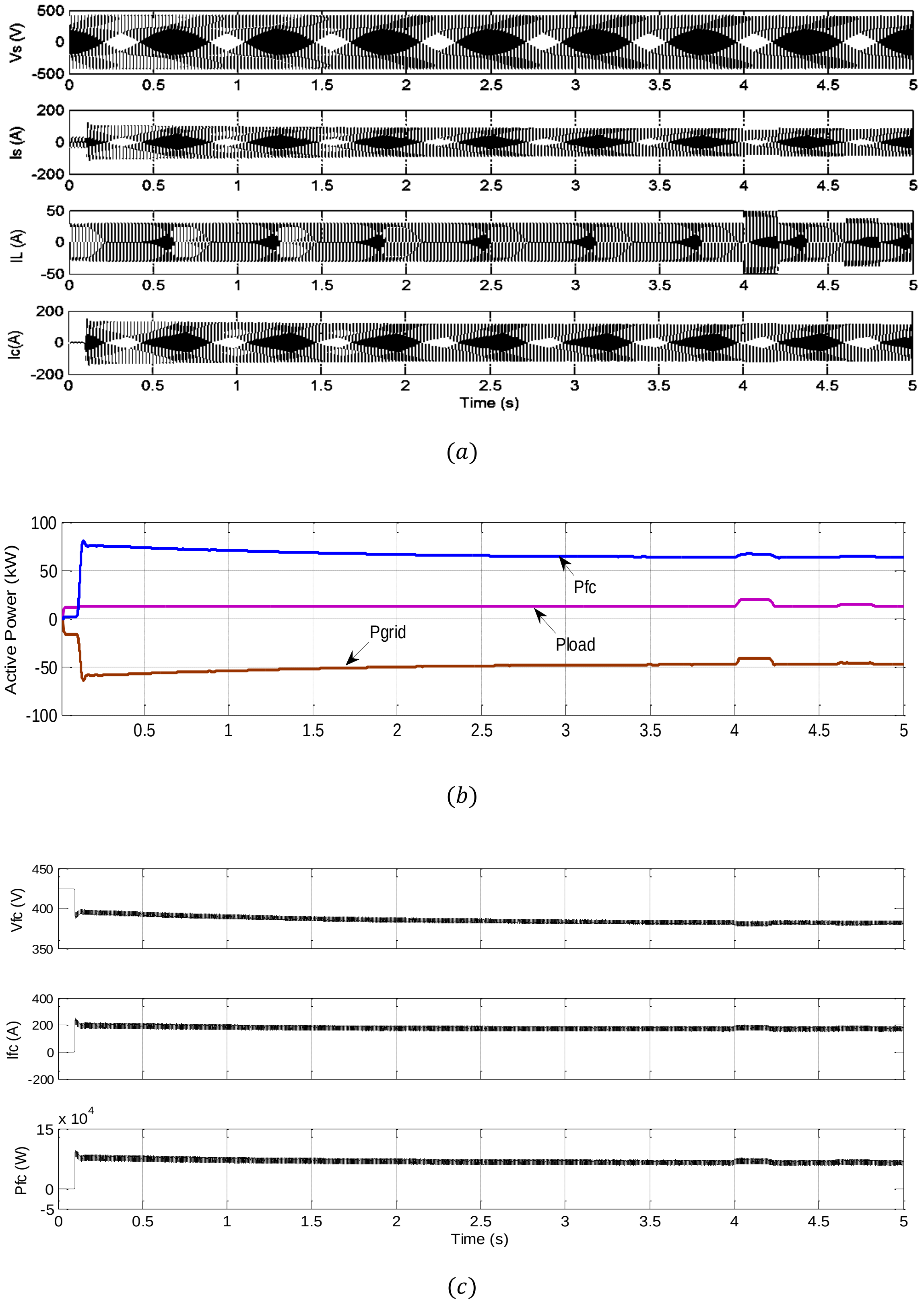

*Fig.*3.16 Mode 1 operation: PQ enhancement with FC power injection (a) PCC voltage V_s, grid current I_s, load current I_L and inverter terminal output current I_c (b) Grid, load and FC active powers $(P_{grid,}\ P_{load}$ and $P_{fc})$ (c) FC stack output voltage V_{fc}, output current I_{fc} and FC output power P_{fc}

PCC voltage is highly distorted with THD of 13.93% and the load current has a THD of 20.87%. $Fig. 3.17\ (b)$ shows the three-phase PCC voltage and grid current simultaneously. Initially the reactive power demand of the load connected at PCC is provided by the grid and hence the PCC voltage and current are not in phase with each other. At t = 0.1s, when the FC is switched on, there is a 180-degree phase shift between the PCC voltage and grid current which suggests that the additional power from FC is fed to the grid at unity power factor. Further, the grid current becomes perfectly sinusoidal in nature. Thus as shown in $Fig. 3.17\ (c)$ with supply voltage distortion of 13.93 %, the grid current has THD of 18.52% before compensation and a THD of 2.91% after compensation with PCC load current THD of 20.87%. The power factor is improved to 0.999 after FC is switched on.

- **Non-linear load variation**

The non-linear loads are time-varying, hence it is required to study the dynamic performance of the system with variation in non-linear load. The load consists of a three-phase diode rectifier followed by inductor L_L = 10 mH in series with a resistor R_L = 20 Ω. Another R-L segment of R = 20 Ω and L = 5 mH is added to the existing load at t = 4.0 s and removed at t = 4.2 s. Thus the non-linear load current increases from 30.76 A to 47.86 A at time t = 4.0 s and decreases from 47.86 A to 30.76 A at t = 4.2 s. The PCC voltage V_s, the supply current I_s, the varying load currents I_L and the compensating current I_c for times t = 3.9 s to t = 4.3 s are shown in $Fig\ 3.18\ (a)$. The results confirm good dynamic performance of the control for rapid change in non-linear load. $Fig. 3.18\ (b)$ shows the THDs of load current and grid current after increase in the load current. Thus with increase in PCC load current, the THD of grid current is reduced from 18.52% before compensation to 6.08% after compensation with load current THD of 13.99% and supply voltage distortion of 13.93 %.

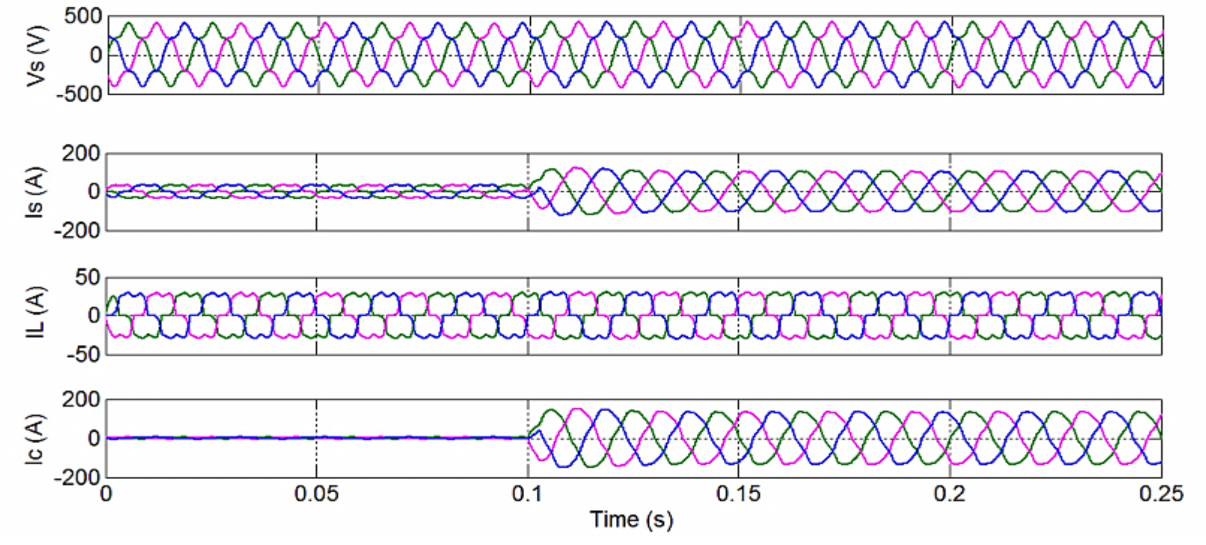

(a)

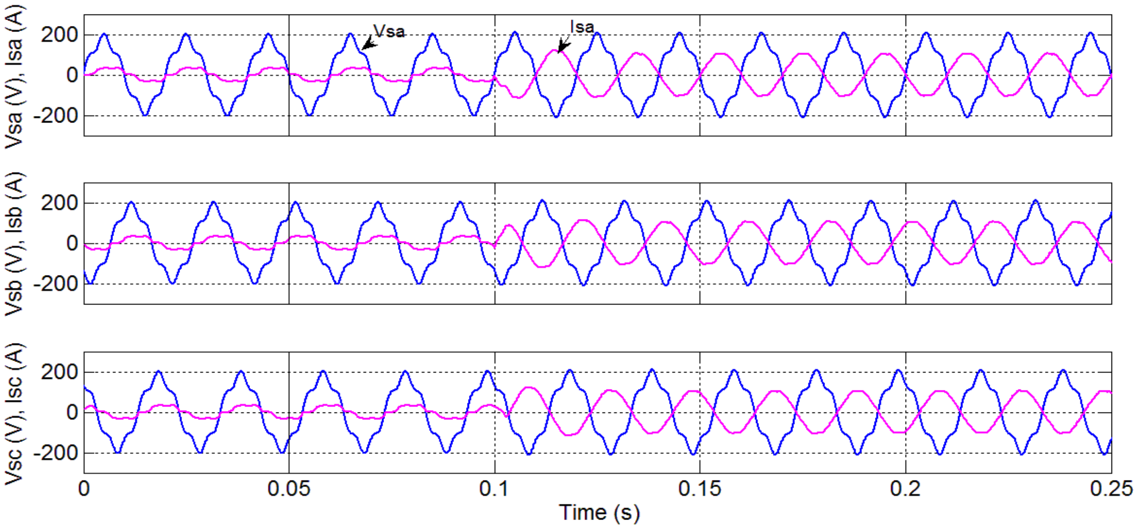

(b)

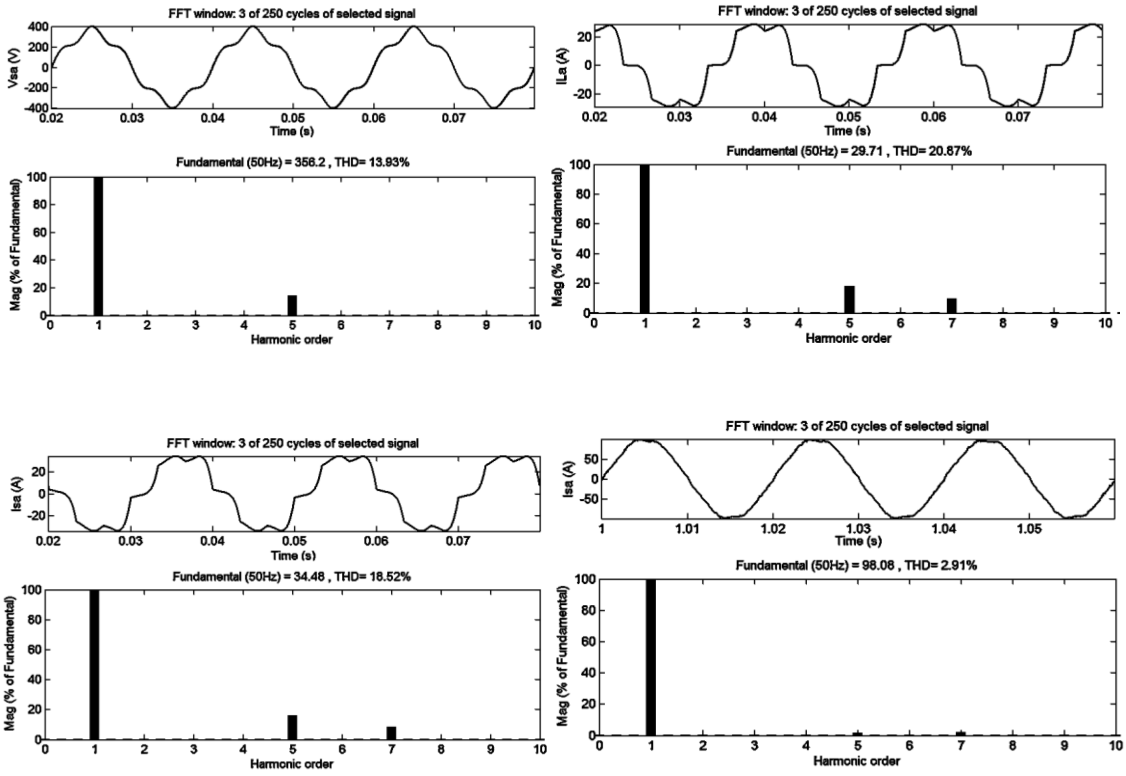

(c)

$Fig.$ 3.17 Response of the system during start-up in Mode 1: (a) PCC voltage V_s, grid current I_s, load current I_L and inverter terminal output current I_c with distorted grid voltage and non-linear load at PCC, the FC inverter switched on at t = 0.1 s (b) Grid current and PCC voltage simultaneously for phase a, b and c (c) THDs of PCC voltage, load current, grid current before the FC is switched on and grid current after the FC is switched on.

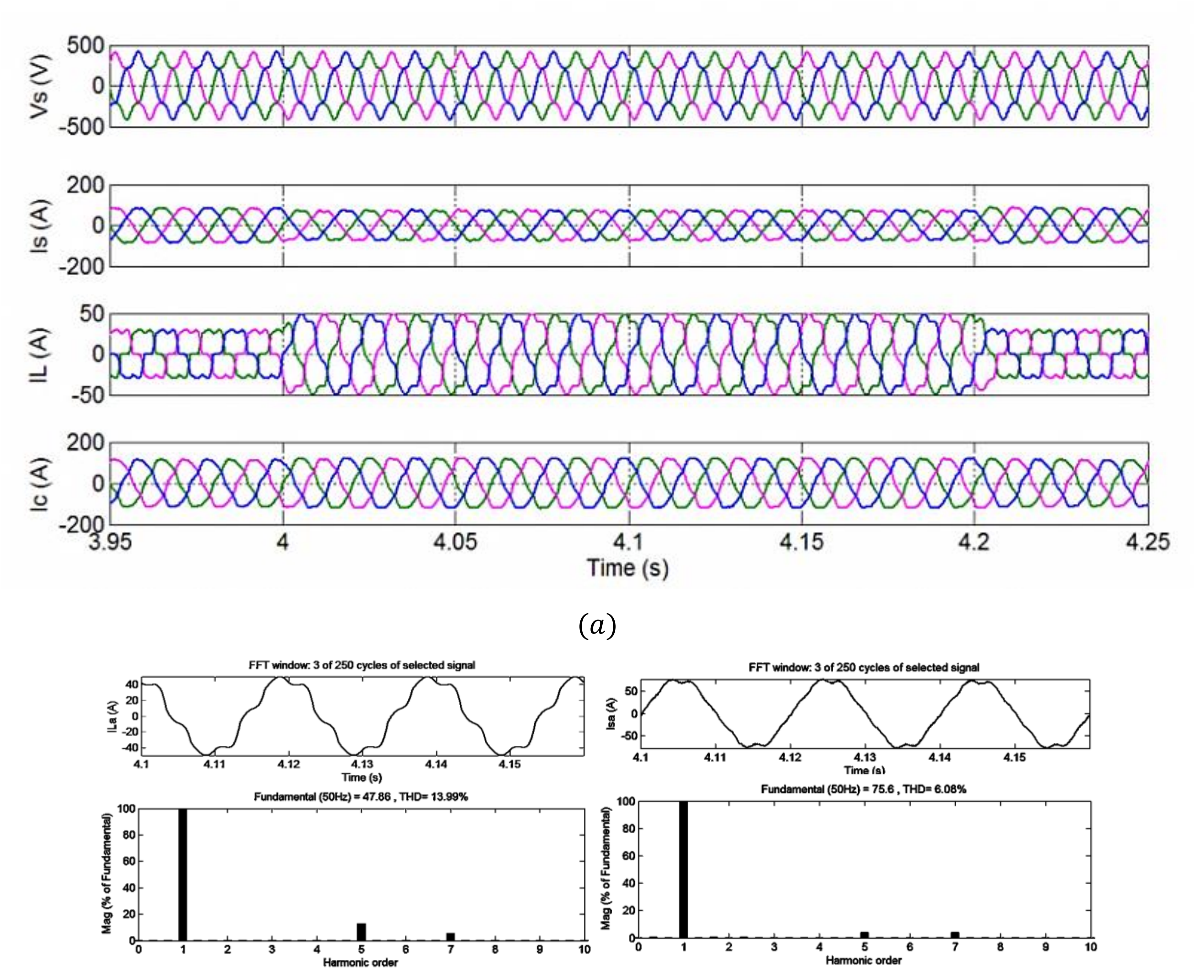

(a)

(b)

$Fig.$ 3.18 (a) Response of the system to non-linear load variation in Mode 1: PCC voltage V_s, grid current I_s, load current I_L and inverter terminal output current I_c with non-linear load variation at the PCC at time t = 4s and t = 4.2s (b) THDs of load current and grid current after increase in the load current.

- **Unbalanced Non-Linear Load**

To verify the compensation of non-active load currents, an unbalanced non-linear load, whose unbalance, harmonics and reactive power need to be compensated is connected at PCC. The load initially consists of a three-phase diode rectifier followed by inductor L_L = 10 mH in series with a resistor R_L = 20 Ω. A single-phase diode rectifier followed by a resistor R = 75 Ω is connected to the PCC between phase a and phase b at time t = 4.6 s and removed at t = 4.8 s. The PCC voltage V_s, the supply current I_s, the unbalanced three-phase load current I_L and the inverter output current I_c is shown in $Fig.$ 3.19 (a). It can be seen that the supply currents are balanced even with unbalanced load at PCC. Thus the proposed control can balance the line currents while simultaneously compensating for reactive and harmonic load current components as shown by the frequency spectrum analysis of load and line currents in $Fig. 3.19$ (b) and $Fig. 3.19$ (c) respectively. The THDs of load current are 19.33%, 17.27% and 21.75% for phase a, b and c while THDs of grid current are 4.77%, 4.71% and 4.63% for phase a, b and c respectively between time t = 4.6 s and t = 4.8 s.

Table 3.4 gives a brief summary of the simulation carried out for Mode 1: the fundamental values and THDs of PCC voltage, load current and supply current, load and source power factors for phase a, b and c for different time intervals t_1, t_2, t_3 and t_4. $Fig. 3.20$ (a) shows the load power factor for phase a, b and c which varies between 0.899 to 0.948. $Fig. 3.20$ (b) shows the source power factor for phase a, b and c which is unity negative after the FC is switched on.

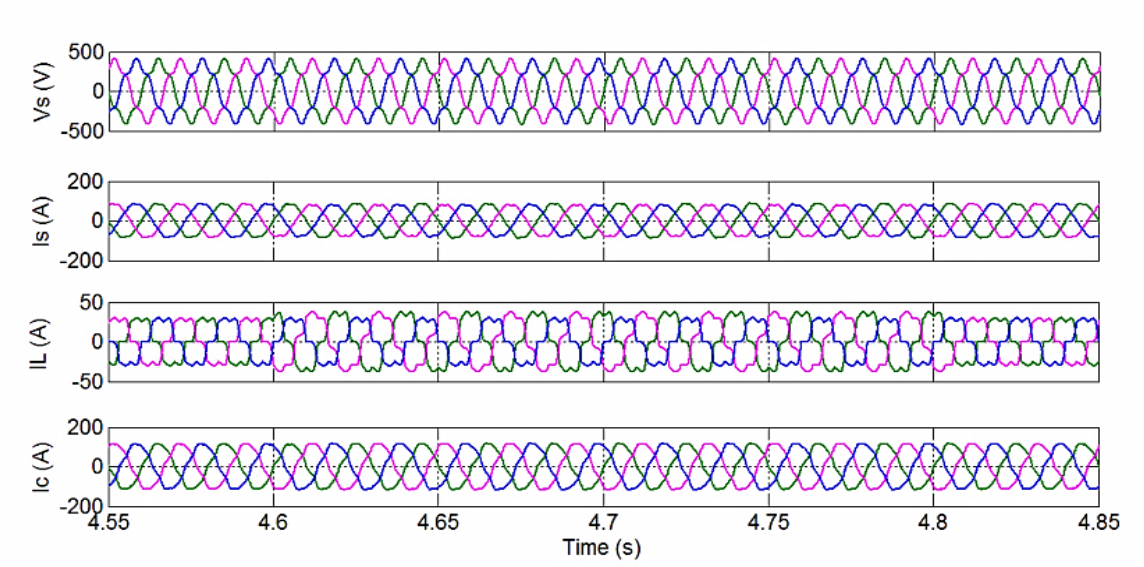

(a)

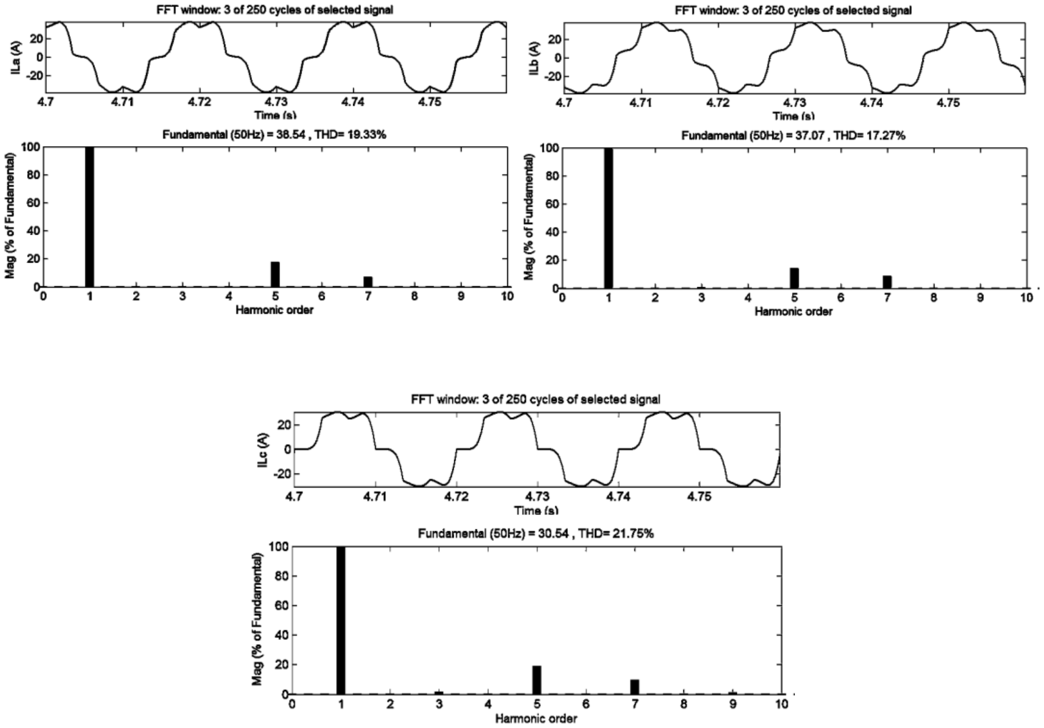

(b)

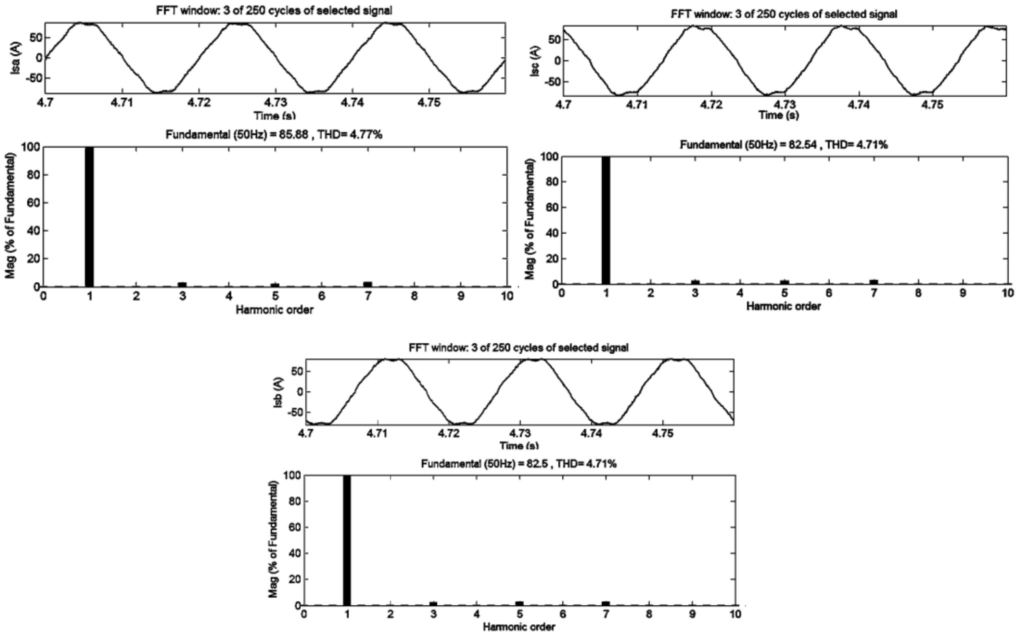

(c)

$Fig.3.19$ (a) Response of the system to load imbalance in Mode 1: PCC voltage V_S, grid current I_S, load current I_L and inverter terminal output current I_C with unbalanced non-linear load at the PCC from time t = 4.6 s to t = 4.8 s (b) THDs of unbalanced load currents (c) THDs of grid currents with unbalanced non-linear load at PCC

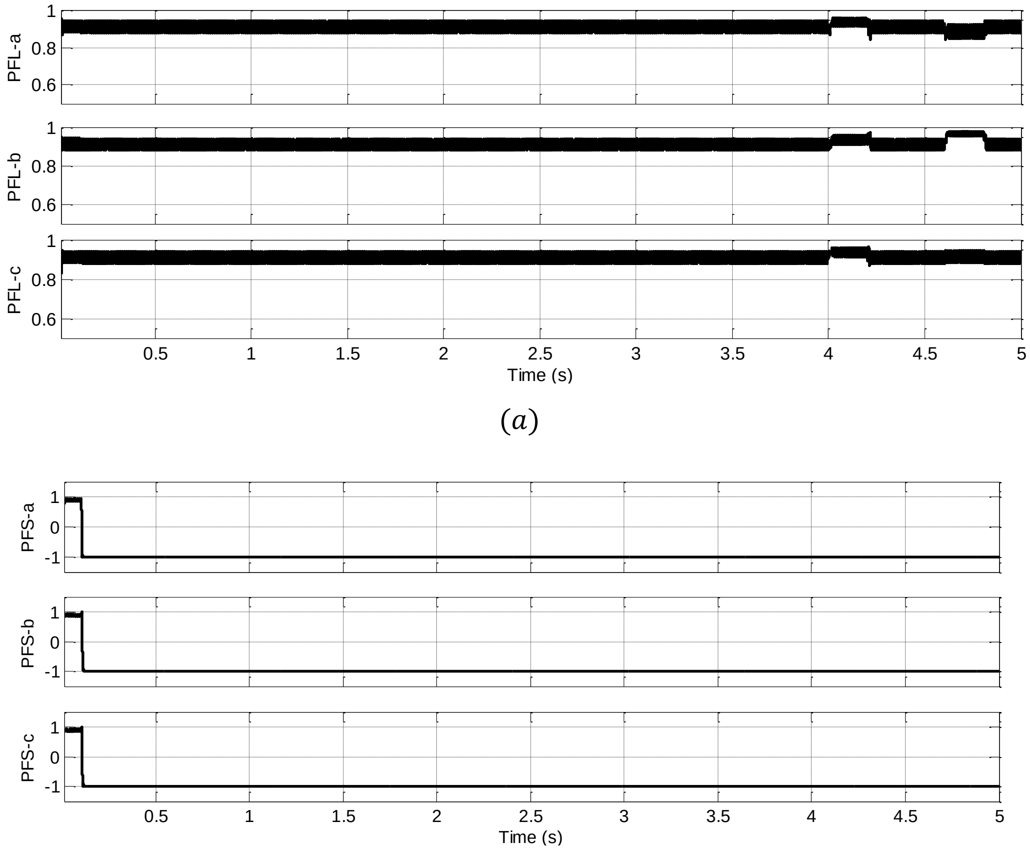

(a)

(b)

$Fig.3.20$ (a) Load power factor for phase a, b and c (b) Source power factor for phase a, b and c

Table 3.4 **Summary of the Simulated Results for Mode 1 Operation**

	Phase	t_1	t_2	t_3	t_4
V_s **(V)**	**a**	356.2	368.3	366.8	367.8
	b	356.2	368.3	366.8	367.5
	c	356.2	368.3	366.8	367.5
I_L **(A)**	**a**	29.71	30.76	47.86	38.54
	b	29.71	30.76	47.86	37.07
	c	29.70	30.75	47.85	30.54
I_s **(A)**	**a**	34.48	90.87	75.6	85.88
	b	34.49	90.91	75.25	82.5
	c	34.49	90.87	75.22	82.56
THD of V_s **(%)**	**a**	13.93	13.54	13.56	13.56
	b	13.93	13.54	13.57	13.56
	c	13.93	13.55	13.56	13.56
THD of I_L **(%)**	**a**	20.87	21.29	13.99	19.33
	b	20.87	21.29	13.98	17.27
	c	20.88	21.30	13.98	21.75
THD of I_s**(%)**	**a**	18.52	3.04	6.08	4.77
	b	18.52	3.12	5.98	4.71
	c	18.52	3.01	6.28	4.63
Load PF	**a**	0.905	0.899	0.926	0.905
	b	0.899	0.899	0.948	0.911
	c	0.904	0.902	0.933	0.901
Source PF	**a**	0.873	0.999	0.999	0.998
	b	0.857	0.999	0.998	0.999
	c	0.880	0.999	0.999	0.999

t_1 : 0 < t < 0.1 s, t_2 : 0.1 s < t < 4 s, 4.2 s < t < 4.6 s, 4.8 s < t < 5 s, t_3 : 4 s < t < 4.2 s, t_4 : 4.6 s < t < 4.8 s

3.4.3.2 Mode - 2 operation: Power quality enhancement (P_{fc} = 0)

In this mode of operation, there is no power generation from the FC stack. Thus the grid interfacing inverter is operating as a SAPF. The inverter is switched on at t = 0.1 s. The PCC voltage V_s, the supply current I_s, the non-linear load current I_L, the compensating current I_c and the DC-link voltage V_{dc} are shown in $Fig.$ 3.21 (a). $Fig.$ 3.21 (b) shows the grid, load and inverter active powers P_{grid}, P_{load} and P_{inv}. The grid-connected inverter provides the entire reactive and harmonic load power and load active power is provided by the grid. There is a non-linear load variation between time t = 1.5 s to t = 1.7 s and load imbalance between times t = 2 s and t = 2.2 s.

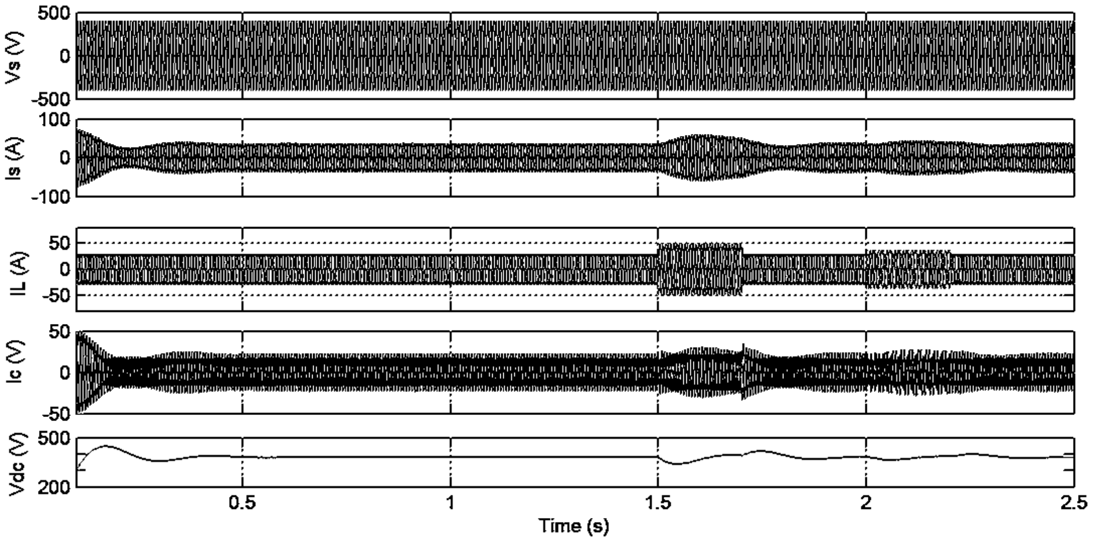

(a)

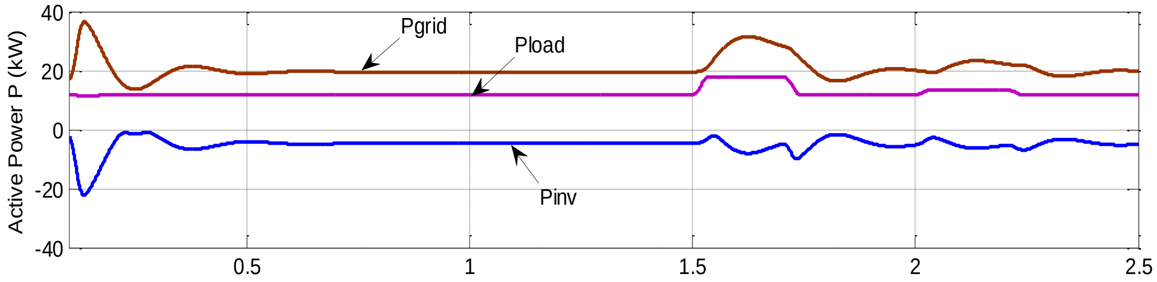

(b)

$Fig.$ 3.21 Mode 2 operation: Power quality enhancement (a) PCC voltage V_s, grid current I_s, load current I_L, inverter compensating current I_c and DC-link voltage $V_{dc.}$ (b) Grid, load and inverter active powers (P_{grid}, P_{load} and P_{inv})

- **During Start-up**

The PCC voltage V_s, grid current I_s, load current I_L, inverter output current I_c and DC-link voltage V_{dc} for time t = 0 to t = 0.4 s is shown in $Fig.$ 3.22 (a). $Fig.$ 3.22 (b) shows the three-phase grid voltage and current simultaneously. Initially the reactive power demand of the load connected at PCC is provided by the grid and hence the grid voltage and current are not in phase with each other. At t = 0.1s, when the inverter is switched on, the PCC voltage and grid current become in phase with each other. Further, the grid current becomes perfectly sinusoidal in nature and the capacitor voltage reaches a steady state value within a few cycles. With supply voltage distortion of 13.93 %, the grid current has THD of 18.52% before compensation and a THD of 0.86% after compensation with PCC load current THD of 20.87%. The input power factor has been improved to 0.999 after compensation.

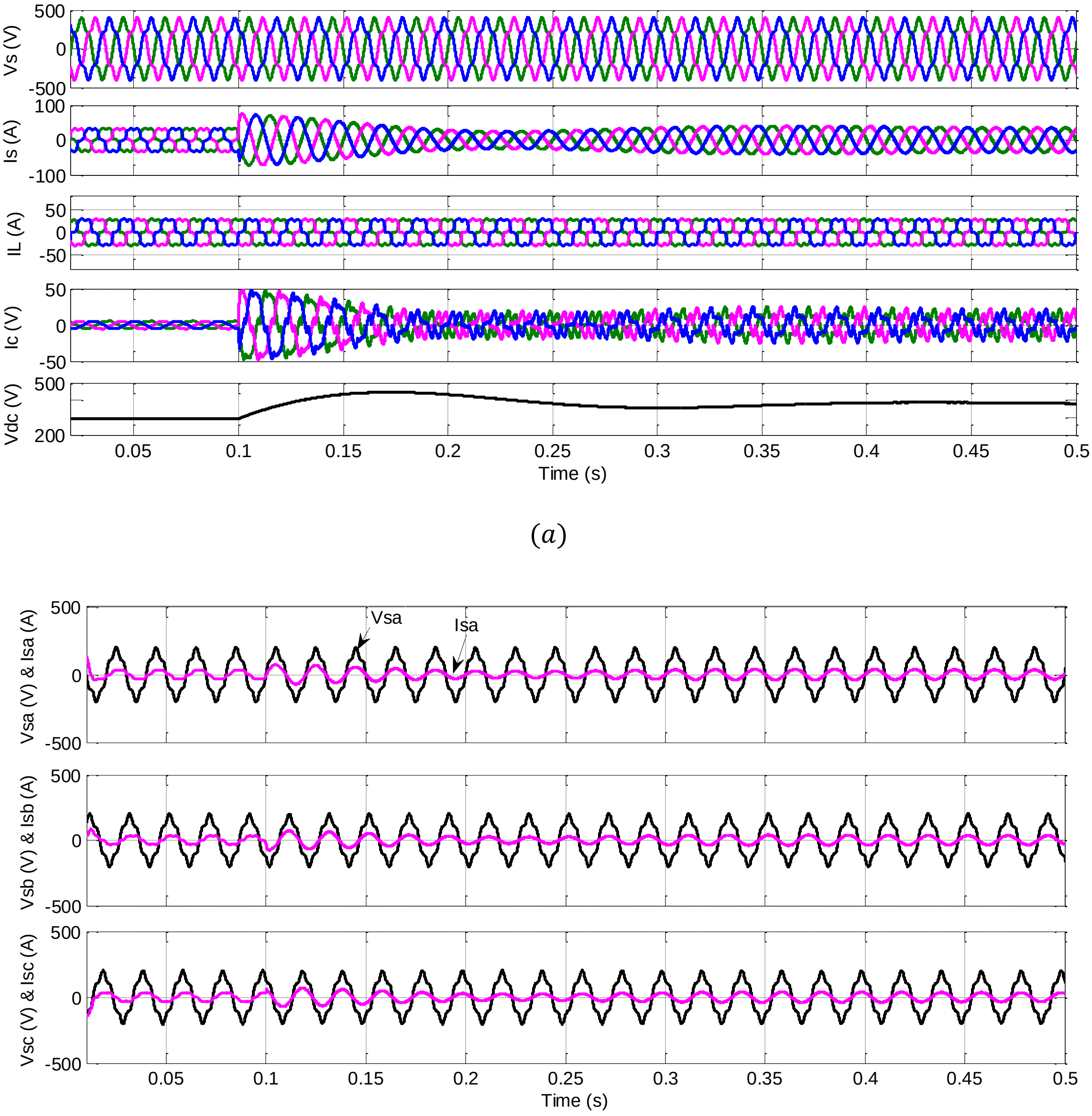

(a)

(b)

$Fig. 3.22\,(a)$ Response of the system: PCC voltage V_s, grid current I_s, load current I_L, inverter compensating current I_c and DC-link voltage V_{dc} with distorted grid voltage and non-linear load at PCC, the inverter switched on at t = 0.1 s (b) Grid current and distorted grid voltage simultaneously for phase a, b and c

- **Non-linear Load Variation**

The PCC voltage V_s, the supply current I_s, the load current I_L, the compensating current I_c and the DC-link voltage V_{dc} are shown in $Fig. 3.23$ for non-linear load variations at times t = 1.5 s and t = 1.7 s. Initially, the load consists of a three-phase diode rectifier followed by inductor L_L = 10 mH in series with a resistor R_L = 20 Ω. Another $R - L$ segment of R = 20 Ω and L = 5 mH is added to the existing load at t = 1.5 s and removed at t = 1.7 s. Thus the non-linear load current increases from 29.66 A to 46.07 A at time t = 1.5 s and decreases from 46.07 A to 29.66 A at t = 1.7 s. The results confirm good dynamic performance of the SAPF for rapid change in non-linear load. With increase or decrease in load current, the capacitor voltage decreases or increases from the reference value to release or absorb energy during the transient period. The steady state condition is reached within a few cycles of the supply. For a change in load current there is smooth change in the grid current. With increase in PCC load current, the THD of grid current is reduced from 18.52% before compensation to 0.59% after compensation with load current THD of 14.16% and supply voltage distortion of 13.93 %.

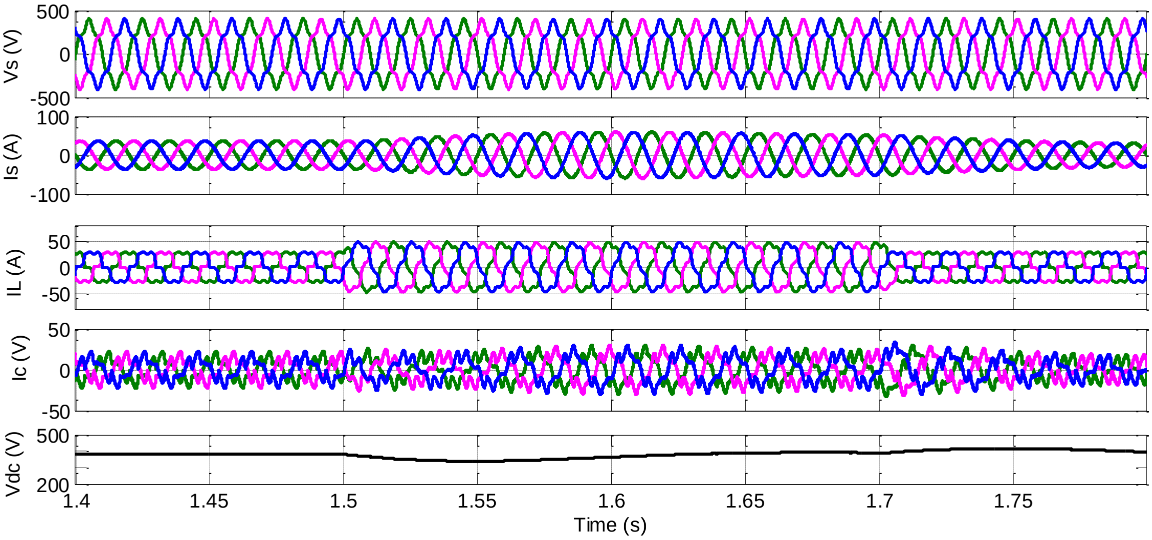

$Fig.3.23$ Response of the system: PCC voltage V_s, grid current I_s, load current I_L, inverter compensating current I_c and DC-link voltage V_{dc} to non-linear load variation at the PCC at times t = 1.5 s and t = 1.7 s

- **Unbalanced Non-linear Load**

The PCC voltage V_s, the supply current I_s, the unbalanced three-phase load current $I_{L,}$ the inverter output current I_c and DC-link voltage V_{dc} is shown in $Fig.3.24$ for load imbalance from time t = 2 s to t = 2.2 s. The non-linear load consists of a three-phase diode rectifier followed by inductor L_L = 10mH in series with a resistor R_L = 20 Ω. A single-phase diode rectifier followed by a resistor R = 75 Ω is connected to the PCC between phase a and phase b at time t = 2 s and removed at t = 2.2 s. It can be seen that the supply currents after compensation are balanced. Thus the proposed control can balance the line currents while simultaneously compensating for reactive and harmonic load current components. The THDs of load current are 19.43%, 17.33% and 21.78% for phase a, b and c while THDs of grid current are 0.75%, 0.78% and 0.77% for phase a, b and c respectively between time t = 2 s and t = 2.2 s.

Table 3.5 gives a brief summary of the simulation carried out for Mode 2: the fundamental values and THDs of PCC voltage, load current and supply current, load and source power factors for phase - a, b and c for different time intervals t_1, t_2, t_3 and t_4. $Fig.$ 3.25 (a) shows the load power factor for phase - a, b and c which varies between 0.880 and 0.968. $Fig.$ 3.25 (b) shows the source power factor for phase - a, b and c which is nearly unity after compensation.

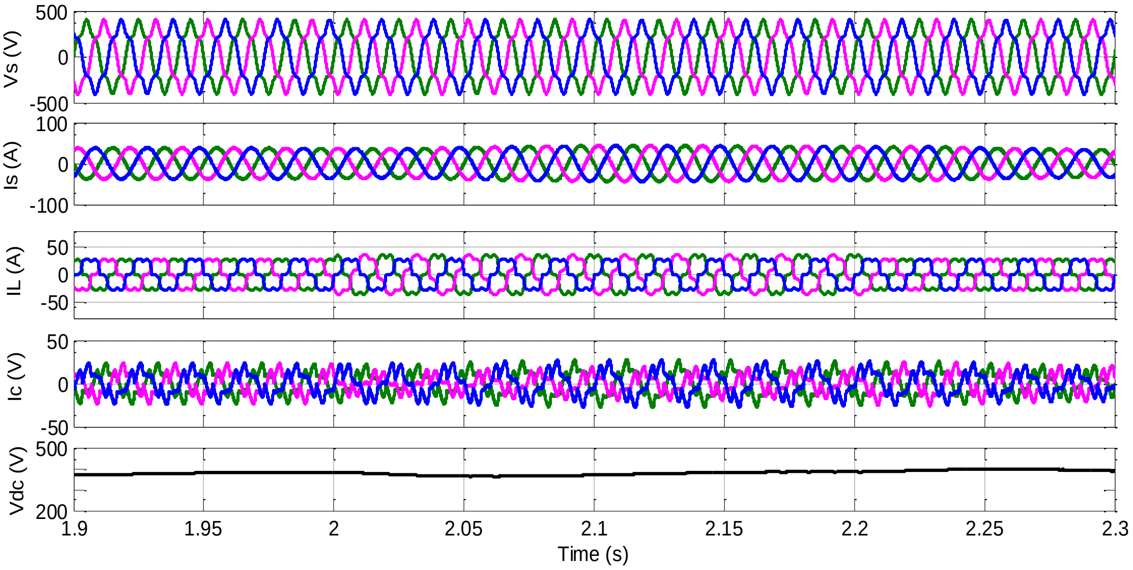

$Fig.$ 3.24 Response of the system: PCC voltage V_s, grid current I_s, load current I_L, inverter compensating current I_c and DC-link voltage V_{dc} to unbalanced non-linear load at the PCC from time t = 2 s to t = 2.2 s

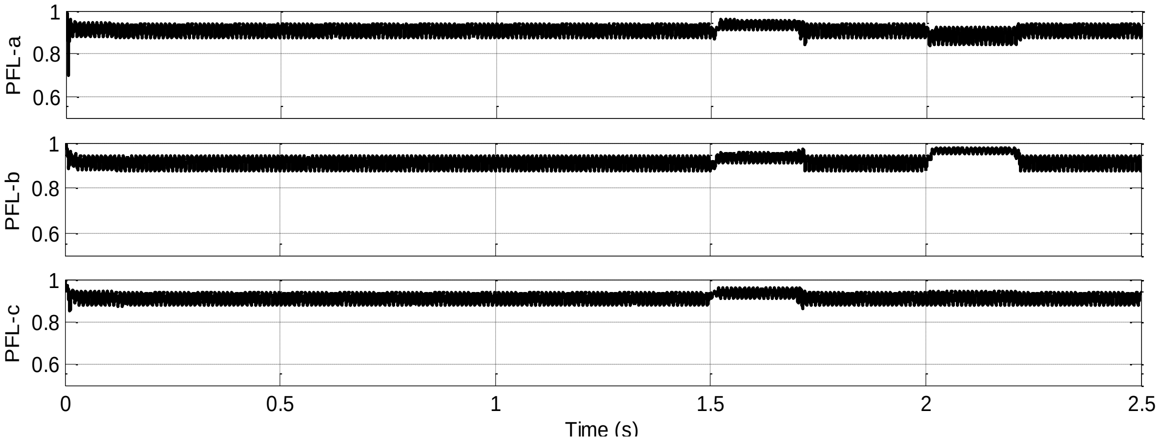

(a)

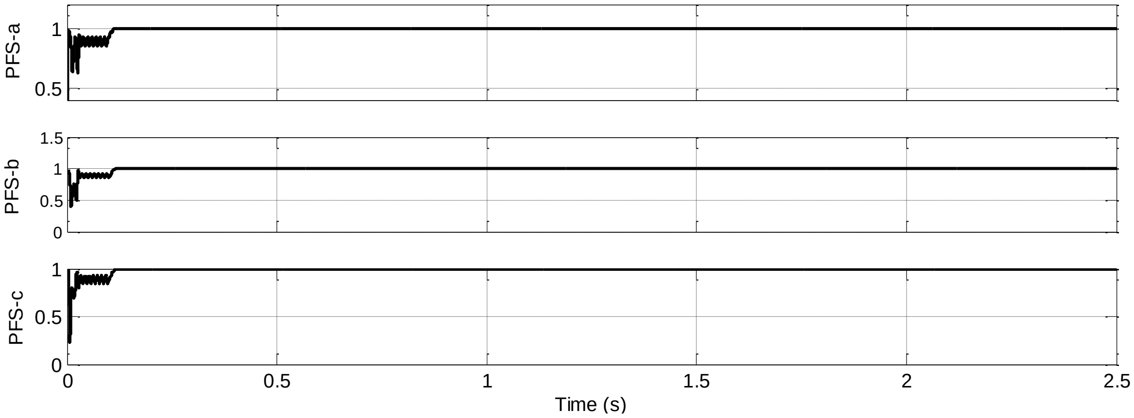

(b)

$Fig.$ 3.25 (a) Load power factor for phase a, b and c (b) Source power factor for phase a, b and c

Table 3.5 **Summary of the Simulated Results for Mode 2 Operation**

	Phase	t_1	t_2	t_3	t_4
V_s **(V)**	**a**	356.2	355.6	353.5	354.9
	b	356.2	355.6	353.5	354.9
	c	356.2	355.6	353.5	354.9
I_L **(A)**	**a**	29.71	29.66	46.07	37.19
	b	29.71	29.66	46.07	35.75
	c	29.70	29.65	46.06	29.43
I_s **(A)**	**a**	34.48	36.44	57.83	43.36
	b	34.49	36.45	57.91	43.39
	c	34.49	36.46	57.71	43.28
THD of V_s **(%)**	**a**	13.93	14.06	14.14	14.09
	b	13.93	14.06	14.14	14.09
	c	13.93	14.06	14.14	14.09
THD of I_L **(%)**	**a**	20.87	21.29	14.16	19.43
	b	20.87	21.29	14.15	17.33
	c	20.88	21.30	14.16	21.78
THD of I_s**(%)**	**a**	18.52	0.86	0.59	0.75
	b	18.52	0.85	0.81	0.78
	c	18.52	0.90	0.80	0.77
Load PF	**a**	0.930	0.931	0.869	0.883
	b	0.922	0.922	0.968	0.957
	c	0.880	0.876	0.893	0.901
Source PF	**a**	0.930	0.999	0.998	0.998
	b	0.921	0.999	0.999	0.999
	c	0.871	0.995	0.999	0.999

t_1 : 0 < t < 0.1 s, t_2 : 0.1 s < t < 1.5 s, 1.7 s < t < 2 s, 2.2 s < t < 2.5 s, t_3 : 1.5 s < t < 1.7 s, t_4 : 2 s < t < 2.2 s

3.4.4 Experimental Validation

Experimental prototype is developed for power quality enhancement mode of operation i.e. when there is no power supply from the FC and the grid interfacing inverter is utilised only as APF in improving the power quality at the PCC. Fixed point DSP TMS320F2812 is used to implement the proposed control algorithm. The processor is interfaced to MATLAB through a parallel port connector using Code Composer Studio. The inputs to the controller are the DC-link voltage, the PCC voltage and the load current. The voltage and current signals sensed by the voltage and current sensors respectively are given to the signal conditioner to convert them into unipolar signals in range of 0-3V and then fed to the eZdsp. The GPIO outputs of the eZdsp are given to the gates of IGBTs of the inverter through the pulse isolation and amplifier circuit. The parameter values used for experimentation are given in $Table3.6$. The experimental results are presented for the following cases:

Table 3.6 **Parameters used for Experimentation in Three-Phase**

Parameters	**Values**
Source voltage and frequency	V_S = 50V rms, 50 Hz
Source inductance	L_S= 0.15 mH
Filter inductance	L_c = 2.75 mH
DC-link capacitance	C_{dc}=1500μF
DC-link voltage reference	V_{dcref} = 150 V

3.4.4.1 Case-1: No supply from FC, sinusoidal source voltage and non-linear load

In this case the source voltage is taken as sinusoidal. Three-phase diode rectifier with a resistive load on its DC-side is taken as the non-linear load. $Fig. 3.26\ (a)$ show the experimental waveforms of the source voltage, load current, source current, and APF compensating current for phase a under steady-state. $Fig. 3.26\ (b)$ shows the source voltage and source current together and the APF-compensating current for phase-a. The compensated source current is in phase with the source voltage which ensures reactive power compensation. The FFTs of the load current, as well as the compensated source current are carried out and shown in $Fig. 3.26\ (c)$. The THDs of the load current and compensated source current are measured as 24.4% and 3.2%, respectively.

3.4.4.2 Case 2: No supply from FC, distorted source voltage and non-linear load

In this case, non-sinusoidal source voltages and non-linear loads are used to validate the performance of the controller. To obtain distorted voltage at the PCC, another non-linear load with

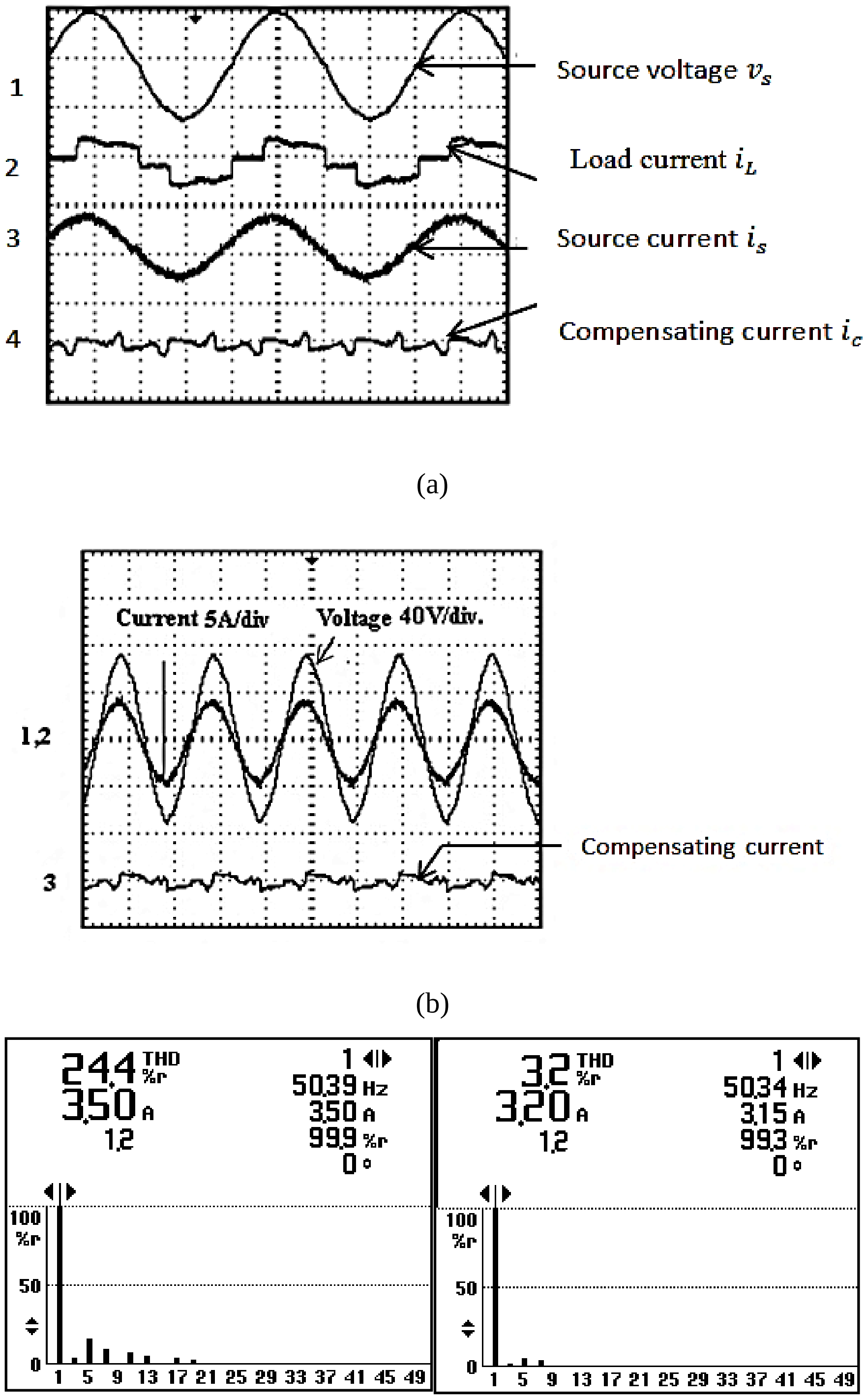

(a)

(b)

(c)

$Fig.$ 3.26 Experimental Results for Case 1: (a) 1 - Source voltage (75 V/div), 2 - Load current (10 A/div), 3-Source current (5 A/div), 4 - Inverter compensating current (5 A/div) (b) 1, 2 - Source voltage and source current together, 3 - Inverter compensating current (c) THDs of load current and compensated source current

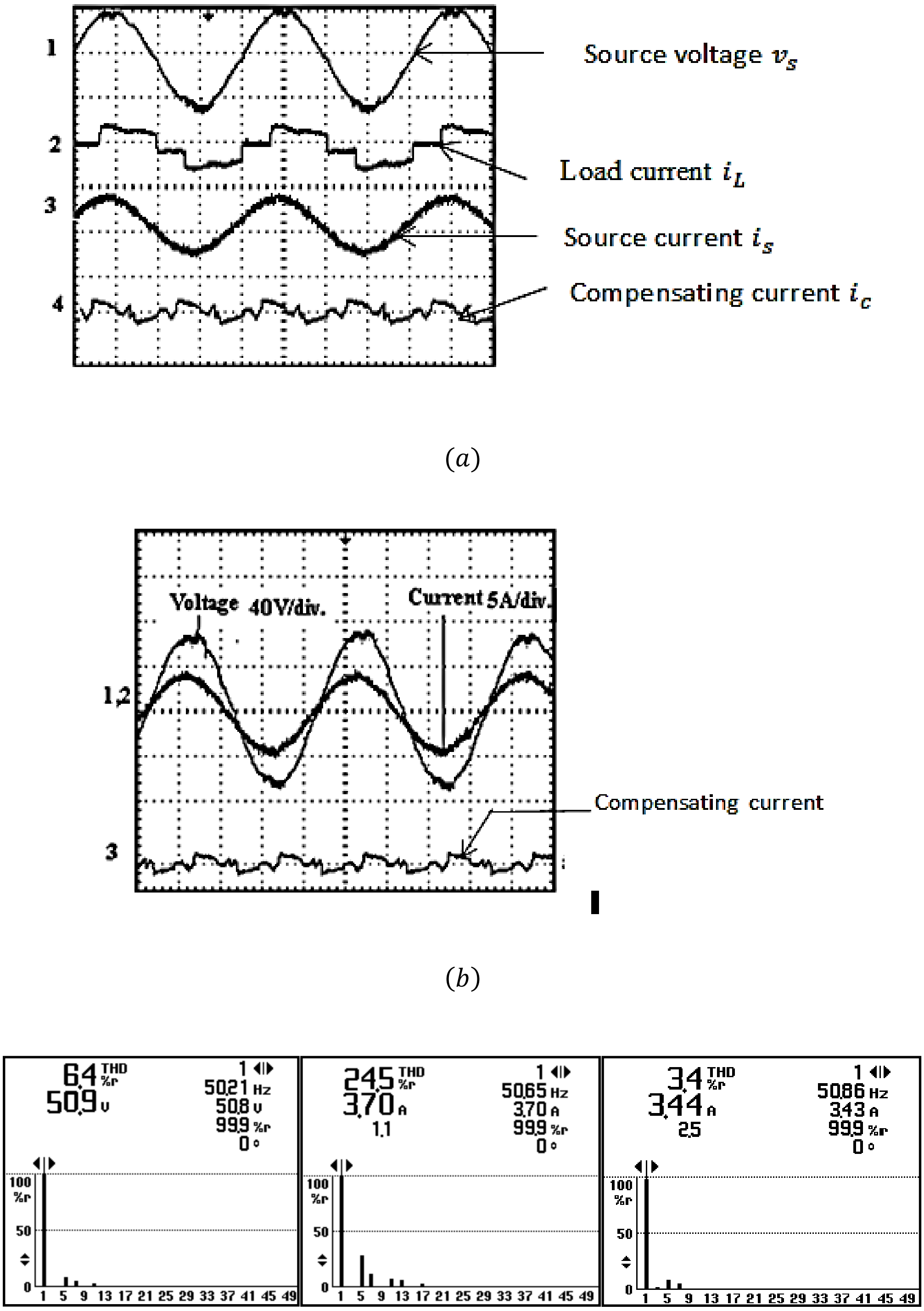

(a)

(b)

(c)

Fig. 3.27 Experimental Results for Case 2: (a) 1 - Source voltage (75 V/div), 2 - Load current (10 A/div), 3-Source current (5 A/div), 4 - Inverter compensating current (5 A/div) (b) 1, 2 - Source voltage and source current together, 3 - Inverter compensating current (c) THDs of source voltage, load current and compensated source current high series impedance is connected, which results in distorted voltage with 6.4% THD. $Fig. 3.27\ (a)$ shows the waveforms of the source voltage, load current, compensated source current, and inverter compensating current for phase a in this case. $Fig. 3.27\ (b)$ shows the source voltage and compensated source current together, and inverter compensating current. Source currents after compensation are found in phase with the respective source voltages and completely sinusoidal in shape. This ensures the compensation of both harmonics and reactive power under non-sinusoidal source voltage. The FFT of source voltage, load current, and compensating source current of phase a are carried out, and given in $Fig. 3.27\ (c)$. The THD of load current is 24.5% and that of compensated source current is 3.4%.

3.5 CONCLUSION

In the proposed work, the features of shunt active power filter have been incorporated in the inverter interfacing the FC to the grid without any additional hardware cost. Thus a common inverter with the proposed control is utilised to inject active power generated from FC to the PCC and also to operate as SAPF. The results show that the VSI not only injects active power at the PCC but also compensates load reactive power and maintains a sinusoidal current from/to grid thus proving the effectiveness of the proposed control in harmonic reduction and power factor correction. The inverter control works effectively under non-sinusoidal voltage and compensates customer as well as utility generated harmonics under unbalanced and varying load conditions. After compensation, the grid current is sinusoidal and in phase with grid voltage. The THD in the grid current is well within the IEEE 519-1992 recommended limits.

The grid-interfacing FC inverter is effectively utilised to perform different functions either individually or simultaneously: FC power transfer to the PCC, load reactive power demand, current harmonic compensation at PCC and load current imbalance. Thus, the proposed interface does not require any additional circuit for enabling the existing inverter to also perform APF function. This concept, thus, reduces the overall design cost of the system.

The designed controller for FC inverter either regulates the power flow between the FC and the grid or works as an active power filter or performs both the functions simultaneously. The results are obtained for different operating conditions with varying load demands to prove the effectiveness of the entire system. The simulation study is carried out in MATLAB/Simulink to verify the proposed control algorithm to achieve multi-objectives of power quality enhancement and FC power injection to the grid. Two different modes of operation are considered: Simultaneous power quality enhancement and FC power injection, and only power quality enhancement mode. Experimental prototype is developed and results obtained for single-phase and three-phase system in Mode 2 operation.

Chapter-4

GRID-CONNECTED PHOTOVOLTAIC SYSTEM WITH MAXIMUM POWER POINT TRACKING AND REACTIVE POWER CONTROL

Solar energy is the ultimate source of energy which is naturally replenished in a short period of time, hence called renewable energy or sustainable energy source. The first half of the chapter gives an overview of the photovoltaic technology for converting solar energy into electrical energy and the modeling of photovoltaic array required for photovoltaic studies. This second half of this chapter presents the modeling and design of a single-stage three-phase grid-connected photovoltaic system topology with maximum power point tracking and reactive power control.

4.1 INTRODUCTION

The Photovoltaic energy is particularly attractive as a renewable source for distributed generation systems due to their clean, pollution free and inexhaustible nature [77]**.** With the decrease in price of the PV modules due to massive increase in the production capability of PV modules [81], PV systems are expected to play an important role in the future and so a great deal of research work is dedicated to enhancing the performance and efficiency of PV systems [1]. In the near future, a significant penetration of PV energy into the power system is anticipated [68]. In the PV system, PV modules are connected in series and parallel to enable power generation and processing at an adequately large voltage level and efficiency [1]**.** In the distributed generation PV systems, power electronic converters are needed to realise the DC-AC power conversion, grid-interconnection and power optimisation [169]**.**

Interfacing the PV to the grid presents a quite different and challenging scenario because unlike the conventional system, the PV cannot be directly connected to the grid. A power conditioning interface between the PV and grid is required to match the characteristics of PV and the requirements of the grid connections such as voltage, frequency, active and reactive power control, harmonic minimization etc. The connection of the PV array to the grid is usually made with a voltage source inverter which include an intermediate DC-DC converter for voltage boosting [170]. The presence of a DC-DC converter allows the PV panels to operate over a wider voltage range, with a fixed inverter DC voltage and a simplified system design. On the other hand, the DC-DC converter increases the cost and decreases the conversion efficiency [96, 171]**.**

A grid-connected PV system has two control loops. The inner loop modulates the output current of the inverter to meet the waveform and phase requirement. The outer loop determines the output power of the inverter according to the maximum power point of PV panels [75, 96]. Conventionally, these two loops are realized respectively in two stages of power conversion, one is a

DC-DC converter with MPPT control and the other is a DC-AC inverter [96]**.** In single-stage grid-connected PV systems, both loops can be realized simultaneously in one power conversion stage, thus simplifying the system topology. According to [172]**,** the total power loss in a single-stage grid-connected PV system is close to a two-stage PV system, while in a single-stage one stage of boost converter can be saved. Thus from a viewpoint of efficiency, cost and system size, a single-stage grid-connected PV system is feasible if the operating voltage range is properly selected [171].

Due to the utilization of only one energy conversion stage, the single-stage grid-connected PV system is expected to be simpler, more efficient and economical than its two-stage counterpart [68]. However, since the MPPT control, synchronization with the utility voltage, output current control with harmonic reduction needs to be considered simultaneously, the complexity of the control scheme would be much increased [96]. This chapter presents the design and analysis of a single-stage three-phase PV based DG system. The PV array is interfaced to the grid through the power conditioning unit with MPPT and reactive power flow control. The proposed system consists of PV array connected to the DC-side of the VSI for interfacing to the grid. The maximum power point tracking, grid synchronisation, reactive power compensation, output current harmonic reduction is included simultaneously in the inverter control. The entire system is modeled in MATLAB/Simulink environment and simulations carried out to verify the operation and the control principle. Various simulation results are presented for the proposed PV grid-interfaced system.

4.2 DEVELOPMENT OF PHOTOVOLTAIC ARRAY MODEL

Photovoltaic model is required for the purpose of studying electronic converters for PV systems. The manufacturers of PV devices provide a set of empirical data that may be used for the design of PV model. Some manufacturers also provide $I - V$ curves obtained experimentally for different operating conditions. The PV model use in this work is adjusted with the experimental curves of Kyocera KC200GT 200 W PV module. *Table 4.1* gives the nomenclature for PV array modeling.

Table 4.1 **Nomenclature for Photovoltaic Array Modeling**

α	Diode ideality factor
β	Inverse thermal voltage
G	Solar irradiance (W/m^2)
G_n	Solar irradiance at STC (1000 W/m^2)
I	PV cell output current (A)
I_d	Current through the diode (A)
I_g	Current source in PV equivalent circuit (A)
I_0	Diode reverse saturation current (A)
I_{mp}	Current at MPP at solar insolation G and temperature T (A)
$I_{mp,n}$	Current at MPP at STC (A)

I_p	Current through R_p (A)
I_{sc}	PV module short circuit current at irradiance G and temperature T (A)
$I_{sc,n}$	Short circuit current at STC (A)
k	Boltzmann’s constant
K_V	Open circuit voltage temperature coefficient
K_I	Short circuit current temperature coefficient
N_s	Number of PV modules in series in a PV array
N_p	Number of PV modules in parallel in a PV array
P_{mp}	Power at MPP at solar insolation G and temperature T
P_{max}	Power at MPP at STC
q	Electron charge
R_s	Series resistance in equivalent circuit of PV cell
R_p	Parallel resistance in equivalent circuit of PV cell
T	$p-n$ junction temperature (K)
T_n	STC temperature (298 K)
V	PV cell output voltage
V_{mp}	Voltage at MPP at solar insolation G and temperature T
$V_{mp,n}$	Voltage at MPP at STC
V_{oc}	PV module open circuit voltage at irradiance G and temperature T
$V_{oc,n}$	Open circuit voltage at STC

Fig. 4.1 shows the equivalent circuit of a PV cell. The $I-V$ characteristic of a single-diode PV cell described by Equation 4.1 is represented by a current source I_g and a diode in parallel with the current source.

$$I = I_g - I_d - I_p = I_g - I_0\left(e^{\frac{\beta(V+R_sI)}{\alpha}} - 1\right) - \left(\frac{V+R_sI}{R_p}\right) \tag{4.1}$$

The current source models the photon generated electron-hole pairs under the influence of the built-in electric field. The diode models the diffusion of minority carriers in the depletion region.

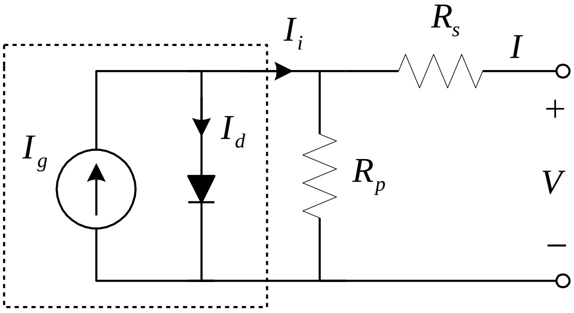

$Fig.$ 4.1 Equivalent circuit of a PV cell

where I and V are the terminal current and voltage of the PV cell, I_d is the current through the diode. The current I_d is replaced by the Shockley diode equation. α is the diode ideality factor to account for the effect of recombination in the space-charge region and depends on the PV device type. I_0 is the diode reverse saturation current, and β is the inverse thermal voltage defined by Equation 4.2.

$$\beta(T) = \frac{q}{kT} \tag{4.2}$$

Here k is the Boltzmann's constant, q is the electron charge, T is the $p - n$ junction temperature. R_s represents the structural resistance of the PV cell. R_p models the leakage current of the $p - n$ junction and depends upon the fabrication method of the PV cell. I_p is the current through R_p. R_p is generally high and hence some authors neglect it to simplify the model. The value of R_s is very low and also neglected sometimes.

The PV module is composed of a parallel connection of strings of panels to ensure adequately large power. In turn, to ensure an adequately large DC voltage, each string consists of a number of PV panels connected in series. The PV panel corresponds to series-connected PV cells. The PV module datasheets gives the following data with reference to nominal or standard test conditions (STC) of temperature (T_n = 298 K) and solar irradiance (G_n = 1 kW/m^2): open circuit voltage $V_{oc,n}$, short circuit current $I_{sc,n}$, voltage at maximum power point $V_{mp,n}$, current at the maximum power point $I_{mp,n}$, open circuit voltage temperature coefficient K_V, short circuit current temperature coefficient K_I and the maximum output power P_{max}. The light generated I_g depends on solar irradiance G and junction temperature T. In the short circuit condition I_g can be expressed as:

$$I_g = \left(I_{sc,n} + K_I(T - T_n)\right)\frac{G}{G_n} \tag{4.3}$$

Diode reverse saturation current I_0 depends only on T. In open circuit condition, I_0 can be expressed as:

$$I_0 = \frac{I_{sc,n}+K_I(T-T_n)}{e^{\frac{\beta}{\alpha}\left(V_{oc,n}+K_v(T-T_n)\right)}-1} \tag{4.4}$$

R_s and R_p can be determined by imposing two conditions with reference to the maximum power point at the STC. Evaluating Equation 4.1 at MPP, we get,

$$I_{mp} = I_g - I_0\left(e^{\frac{\beta}{\alpha}(V_{mp,n}+R_S I_{mp,n})} - 1\right) - \left(\frac{V_{mp,n}+R_S I_{mp,n}}{R_p}\right) \tag{4.5}$$

Taking the derivative of PV power with respect to terminal voltage at MPP at STC and equating to zero, $\left.\frac{\partial(IV)}{\partial V}\right|_{I_{mp,n}V_{mp,n}} = 0$

$$I_{mp,n} = V_{mp,n}\frac{\frac{\beta}{\alpha}I_0 T_n e^{\frac{\beta}{\alpha}(V_{mp,n}+R_S I_{mp,n})}+\frac{1}{R_p}}{1+\frac{\beta}{\alpha}I_0 T_n e^{\frac{\beta}{\alpha}(V_{mp,n}+R_S I_{mp,n})}+\frac{R_S}{R_p}} \tag{4.6}$$

Thus R_s and R_p is derived from Equation 4.5 and Equation 4.6. The $I - V$ characteristic of the PV device depends upon the internal characteristics of the device (R_s, R_p) and on external influences such as irradiation level G and temperature T. The $I - V$ and $P - V$ characteristic of a PV module can be determined for a given radiation level G and ambient temperature T using the following relations:

$$\Delta I = K_I(T - T_n)\left(\frac{G}{G_n}\right) + I_{sc}\left(\frac{G}{G_n} - 1\right) \tag{4.7}$$

$$\Delta V = -K_V(T - T_n) - R_s\Delta I \tag{4.8}$$

$$V_{oc} = V_{oc,n} + \Delta V \tag{4.9}$$

$$I_{sc} = I_{sc,n} + \Delta I \tag{4.10}$$

where V_{oc} indicates PV module open circuit voltage and I_{sc} the PV module short-circuit current, corresponding to G and T, respectively.

The rating of a PV module is estimated by the maximum power produced by a module at STC. The power output from a PV array, containing N_s in series and N_p in parallel PV modules, can be calculated as:

$$P_{PV} = N_s N_p FF V_{oc} I_{sc} \tag{4.11}$$

where fill factor (FF) is given by the following relation:

$$FF = \frac{V_{mp,n} I_{mp,n}}{V_{oc,n} I_{sc,n}} \tag{4.12}$$

The modelled PV array used for single-phase system study (in Chapter 5) is a 2×15 series-parallel matrix of 200 W PV module, thus having a rating of 6 kW. The PV array used for three-phase system study is a 30×30 series-parallel matrix of 200 W PV module thus having a maximum power output of 180 kW.

4.3 POWER CIRCUIT DESCRIPTION OF SINGLE-STAGE GRID-INTERFACED PHOTOVOLTAIC SYSTEM

The proposed three-phase single-stage grid-connected PV system consists of PV panels, a VSI, a controller and a filter. $Fig. 4.2$ shows a schematic diagram of a three-phase, single-stage PV system interfaced to the distribution network at the point of common coupling. The core of the PV system is a current-controlled VSI that interfaces a PV array with the distribution network. The PV array is connected in parallel to the DC-link capacitor C and the DC-side terminals of the VSI. The VSI AC-side is connected to the network, at the PCC through a three-phase LC filter and a coupling transformer. The LC filter prevents the switching voltage and current harmonics generated by the VSI from penetrating into the grid. Thus the harmonic currents injected by the PV system into the network and the voltage distortions at PCC are reasonably low. C provides a low-impedance path for the current harmonics generated by the PV system and prevents them from penetrating into the distribution network. The interface reactor connects the AC-side terminals of the VSI to the corresponding phases of the PCC via the transformer. The transformer is included in the PV system to adapt the VSI AC-side terminal voltage to the nominal PCC voltage. The transformer has a delta winding connection on low-voltage side to avoid distortions due to the triple-n harmonics of the magnetizing current. The higher voltage side has a wye winding configuration and is grounded. Also, the transformer isolates the PV system from the grid, in terms of zero sequence components of fault currents. The VSI is controlled based on the sinusoidal PWM strategy. The distribution network is supplied by a utility substation and is represented by a three-phase voltage source. Further a three-phase load is connected at the PCC. The inductance and resistance of the distribution line segment between the inverter and the PCC is represented by L_1 and R_1 respectively. L_1 and R_1 also include the leakage inductance and winding resistance of transformer respectively.

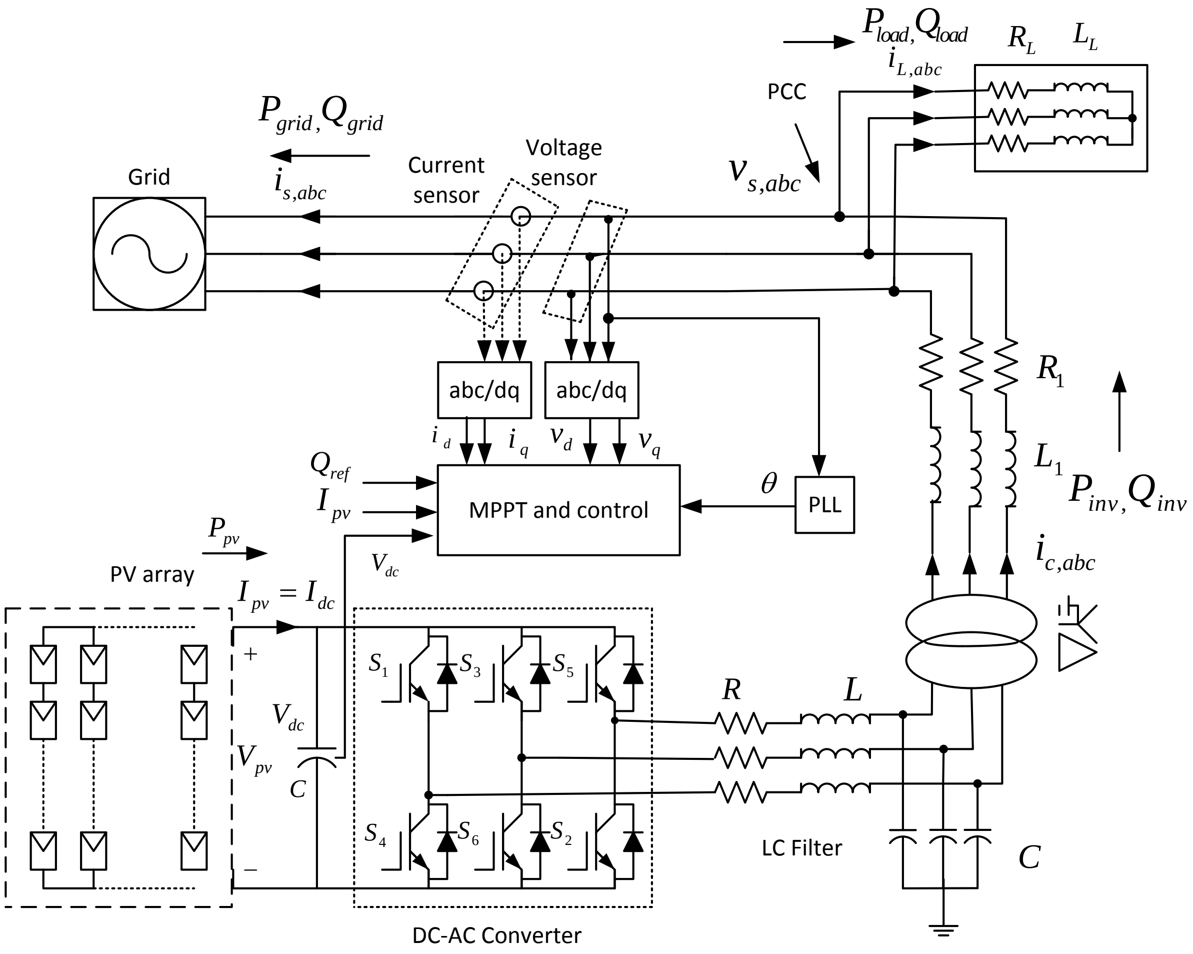

$Fig.$ 4.2 Three-phase single-stage PVDG system

4.4 GRID-INTERFACING INVERTER CONTROL DESIGN

The dynamics of the VSI AC-side current can be described by the following phasor equation:

$$L_c \frac{d\vec{\imath}}{dt} = -R_c\,\vec{\imath} + \vec{v_t} - \vec{v_s} \tag{4.13}$$

$\vec{v_t}$ the VSI AC-side terminal voltage can be controlled as:

$$\vec{v_t} = \frac{V_{dc}}{2}\vec{m} \tag{4.14}$$

where $\vec{m}$ represents the phasor corresponding to the PWM modulating signal normalised to the peak value of the triangular carrier signal. Substituting (4.14) in (4.13):

$$L_c \frac{d\vec{\imath}}{dt} = -R_c\,\vec{\imath} + \frac{V_{dc}}{2}\vec{m} - \vec{v_s} \tag{4.15}$$

4.4.1 Active and Reactive Power Flow Control

$Fig.$ 4.3 shows the active and reactive power flow control circuit. The real power and reactive power flow from the PV to the grid is controlled by regulating phase and amplitude, respectively of the inverter output voltage relative to grid voltage. This is implemented in rotating dq reference frame. The controller $k_d(s)$ and $k_q(s)$ act on the error signals $P_{ref} - P$ and $Q_{ref} - Q$ respectively to determine the d-axis and q-axis components of the VSI terminal current references $i_{d,ref}$ and $i_{q,ref}$. To regulate the d-axis and q-axis components of the VSI current i_d and i_q, two PI controllers are used which process the errors $i_{d,ref} - i_d$ and $i_{q,ref} - i_q$ to determine the reference voltage components $v_{d,ref}$ and $v_{q,ref}$. The compensator outputs are augmented by grid voltage components v_d and v_q passed through low pass filters (LPFs), as feedforward signals for improved response to start-up transients, grid voltage disturbances and imbalance. The feedforward signals are passed through low pass filters to nullify the effect of switching ripple components. $v_{d,ref}$ and $v_{q,ref}$ are divided by VSI amplification gain 0.5 V_{dc} to generate m_d and m_q to provide switching pulses to the inverter. Saturation blocks are used to protect the VSI against overcurrents and network faults. PI controllers are used with the dq control structure since they provide satisfactory behaviour when regulating DC variables. The active and reactive powers P and Q are calculated as:

$$P = \frac{3}{2}\left(v_d i_d + v_q i_q\right) \tag{4.16}$$

$$Q = \frac{3}{2}\left(v_q i_d - v_d i_q\right) \tag{4.17}$$

The desired reactive power to be delivered to the PCC determines the value of Q_{ref}, the reference for reactive power control. Regulation of v_q at zero has the effect that the expression for the PV system real power output is simplified to:

$$P = \frac{3}{2} v_d i_d \tag{4.18}$$

The above equation indicates that P is proportional to and can be controlled by i_d. P is controlled to regulate the DC-link voltage and control the power extracted from the PV array. Similarly, the expression Q is simplified to

$$Q = -\frac{3}{2} v_d i_q \tag{4.19}$$

Thus, Q can be regulated by i_q to adjust the power factor that the PV system exhibits to the distribution network

4.4.2 VSI Current Control

The current control scheme is devised to ensure that i_d and i_q rapidly track their respective reference commands $i_{d,ref}$ and $i_{q,ref}$. The current control strategy also enhances protection of the VSC against *overload and external faults. The current control schemes are designed based on the following equations which are dq-frame equivalents of Equation (5.15).*

$$L_c \frac{di_d}{dt} = -R_c i_d + L_c \omega i_q + \frac{V_{dc}}{2} m_d - v_d \tag{4.20}$$

$$L_c \frac{di_q}{dt} = -R_c i_q + L_c \omega i_d + \frac{V_{dc}}{2} m_q - v_q \tag{4.21}$$

In Equations (4.20) and (4.21) i_d and i_q are the state variables and the outputs m_d and m_q are the control inputs, and v_d and v_q are the disturbance inputs. Due to the factor $L_c\omega$, the dynamics of i_d and i_q are coupled and nonlinear. To decouple and linearize the dynamics, m_d and m_q are determined based on the following control laws:

$$m_d = \frac{2}{V_{dc}} \left(u_d - L_c \omega i_q + v_d\right) \tag{4.22}$$

$$m_q = \frac{2}{V_{dc}} \left(u_q + L_c \omega i_d + v_q\right) \tag{4.23}$$

where u_d and u_q are the two new control inputs. Substituting m_d and m_q in Equations (4.20) and (4.21), we get:

$$L_c \frac{di_d}{dt} = -R_c i_d + u_d \tag{4.24}$$

$$L_c \frac{di_q}{dt} = -R_c i_q + u_q \tag{4.25}$$

The above equations represent two, decoupled, linear, first-order systems in which i_d and i_q can be controlled by u_d and u_q respectively. The block diagram of the control scheme in Figure 4.3 shows that the control signal u_d is the output of a compensator $k_i(s)$, processing the error signal $e_d = i_{d,ref} - i_d$. Similarly u_q is the output of another compensator $k_i(s)$ processing the error signal $e_q = i_{q,ref} - i_q$. To produce m_d and m_q, the factor $2/V_{dc}$ is employed as a feedforward signal to decouple the dynamics of i_d and i_q from those of V_{dc}. The PWM modulating signals are generated by transformation of m_d and m_q into m_a, m_b and m_c.

4.4.3 DC-Link Voltage Control

Fig. E.2 (a) of *Appendix-E* shows the variations of P_{pv} as a function of V_{dc} for different levels of the solar irradiation. For a given irradiation level, $P_{pv} = 0$ for $V_{dc} = 0$ but increases with increase in V_{dc}. This continues only up to a certain voltage at which P_{pv} reaches a peak value. Beyond this voltage P_{pv} decreases with increase in V_{dc}. Thus P_{pv} can be maximised by the control of V_{dc}. This is referred to as Maximum Power Point Tracking. The DC-link voltage control as shown in $Fig.$ 4.4 is required to regulate the DC-link voltage to its reference value $V_{dc,ref}$ which in turn is determined by the MPPT scheme. It is also required for protection of DC-link capacitor and VSI switches against overvoltage stress accomplished through real power control. The DC-link voltage control scheme processes the error $V_{dc,ref} - V_{dc}$ to give the real power reference P_{ref} for real power control. Ignoring the VSI power losses, the active power P is approximately equal to the power that is drawn from VSI DC-side terminals. The difference between active power P and incoming power P_{pv} is integrated by the DC-link capacitor C and results in a voltage rise or fall. In steady state V_{dc} settles to $V_{dc,ref}$ due to the integral term of $k_v(s)$ and P becomes equal to P_{pv} as given in Equation 4.26.

$$\frac{d}{dt}\left(\frac{1}{2}CV_{dc}^{\;2}\right) \approx P_{pv} - P \tag{4.26}$$

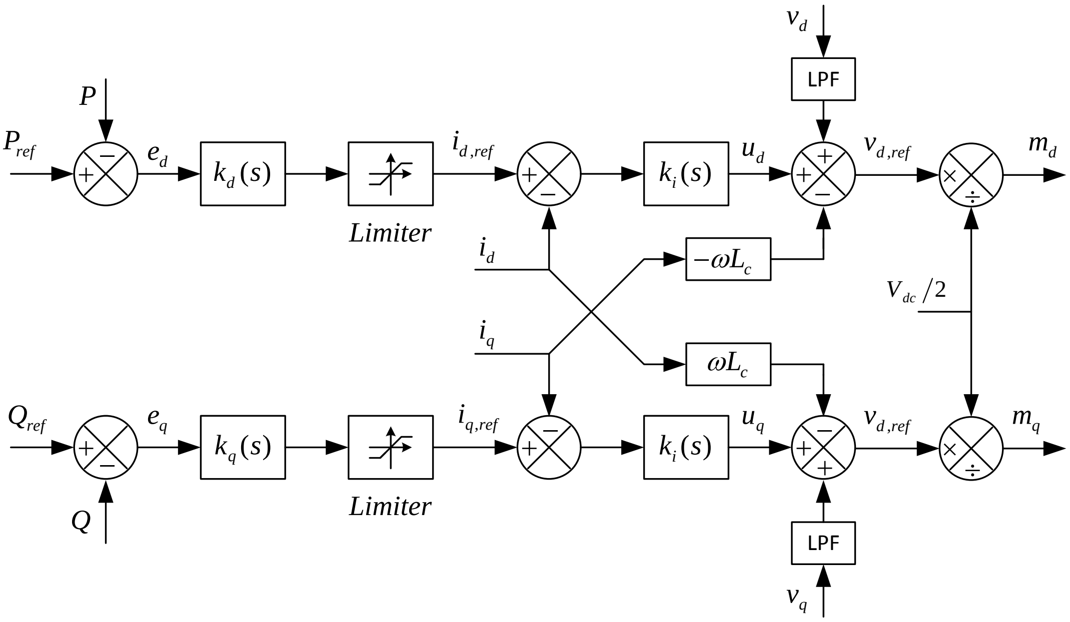

$Fig.$ 4.3 PVDG inverter control circuit

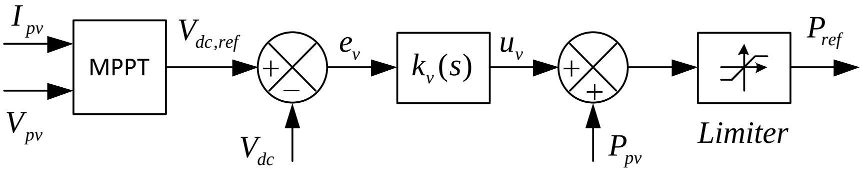

$Fig.$ 4.4 DC-link voltage control

4.4.4 Maximum Power Point Tracking Control

The task of a maximum power point tracker in a PV energy conversion system is to continuously tune the system so that it draws maximum power from the PV array regardless of weather or load conditions [90]. The two algorithms most commonly used to achieve MPP tracking are Perturb and Observe (P&O) method and the Incremental Conductance (IC) methods. The IC method has good performance under rapidly changing atmospheric conditions. The disadvantage associated with it is that four sensors are required to perform the computations. Thus the MPPT will take more time to track the maximum power point. During the tracking time, the PV power is less than the maximum power. Thus IC method results in more power loss. On the contrary, the P&O method requires only two sensors, thus reducing hardware requirement and cost. Thus, in this work, P&O method is used to control the MPPT process.

4.5 SIMULATION RESULTS AND DISCUSSIONS

To evaluate the performance of PV system and the effectiveness of its control strategy, a detailed model of 180 kW photovoltaic system is simulated in MATLAB. The various parameters used for simulation are given in *Table 4.2*. The grid is represented by a balanced three-phase voltage source. Each phase is connected with a series $R-L$ branch. An inductive load is connected at the point of common coupling. The PV array consists of N_p = 30 parallel connected strings of N_s= 30 series connected PV modules. Each module in turn is composed of 54 identical PV cells. The power circuit is developed as per $Fig.$ 4.2 and the control circuit as per $Fig.$ 4.3. Perturb and Observe control algorithm is used for the MPPT scheme. Simulation results have been presented for the PV system during start-up process and normal operating conditions with variation in solar irradiation.

$Fig.$ 4.5 shows the PV output voltage V_{pv}, PV output current I_{pv} and PV output power P_{pv} for two different solar irradiations of 1 kW/m^2 and 0.4 kW/m^2 during start-up. The junction temperature is 25°C. The PV system is started at t = 0.1 s. For solar irradiation G of 1 kW/m^2 the PV output power is 180 kW and for solar irradiation of 0.4 kW/m^2 the PV output power is 72 kW. The prestart-up DC-link voltage for G = 1 kW/m^2 is 1000V which is higher than that for G = 0.4 kW/m^2 which is 950 V.

Table 4.2 **Parameters used for PVDG System Simulation**

Parameter	Value
PV module data	
STC Temperature, T_n	25°C
STC Irradiance, G_n	1 kW/m^2
Open circuit voltage at STC, $V_{oc,n}$	32.9 V
Short circuit current at STC, $I_{sc,n}$	8.21 A
Maximum power at STC, $P_{max,n}$	200 W
Voltage at $P_{max,n}$, $V_{mp,n}$	26.3 V
Current at $P_{max,n}$, $I_{mp,n}$	7.61 A
Short circuit current temperature coefficient, K_I	3.18 mA/°C
Open circuit voltage temperature coefficient, K_V	-123 mV/°C
PV array	
Number of modules in parallel, N_p	30
Number of modules in series, N_s	30
Number of series cells in PV module, M_s	54
Others	

Boltzmanns constant, k	1.3806503×10-23 J/K
Electron charge, q	1.60217646×10-19 C
Diode ideality factor, a	1.5
Grid voltage V_s	440 (Ph-Ph Vrms)
DC-link capacitor, C_{dc}	1000µF
Filter inductance, L_f	0.3 mH
Filter Capacitance, C_f	1 µF
VSI Switching frequency	1080 Hz
Transformer ratio Y/Δ	200 V/440 V
Transformer rating	500 kW

$Fig.$ 4.6 represents the change in PV output power with change in solar irradiation. The initial solar irradiation is G = 0.5 kW/m^2 and the solar irradiation increases to 1.0 kW/m^2 at t = 0.4 s and again drops down to 0.5 kW/m^2 at t = 0.8 s. The PV DC-link voltage is maintained at 400 V. The DC-link voltage is compensated by the MPPT scheme for any variation in solar irradiation so as to maximize the output power.

$Fig.$ 4.7 shows the reference active power P_{ref} with the active power P delivered to the PCC and the reference reactive power Q_{ref} with the reactive power Q delivered to the PCC, simultaneously. The reactive power reference Q_{ref} is determined by the reactive power requirement of the load connected at the PCC. Initially the reactive power demand is 85 VAR which is changed to 60 VAR at t = 0.55 s. The change is captured in 0.05 s. The reference active power P_{ref}, and hence active power delivered to PCC, P is determined by the MPPT and hence increases with increase in solar insolation and vice-versa.

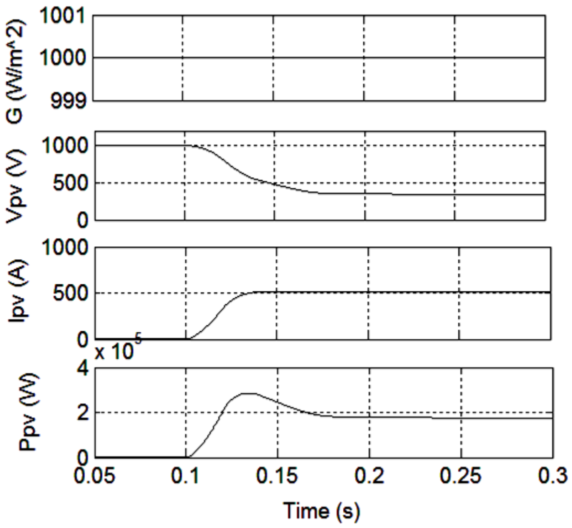

$Fig.$ 4.5 (a) PV output voltage V_{pv}, PV output current I_{pv} and PV output power P_{pv} at solar irradiation G = 1kW/m^2

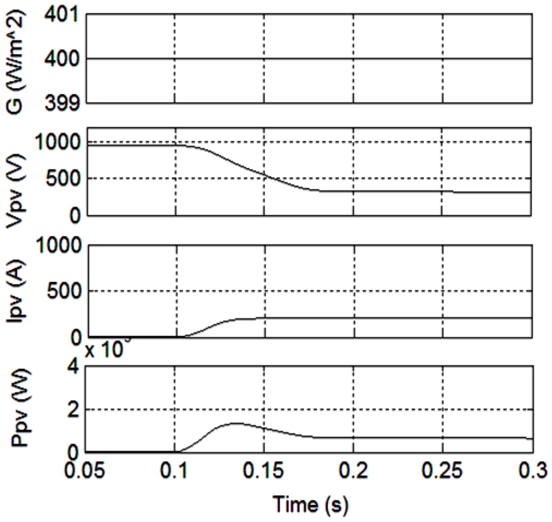

$Fig.4.5$ (b) PV output voltage V_{pv}, PV output current I_{pv} and PV output power P_{pv} at solar irradiation G = 0.4 kW/m^2

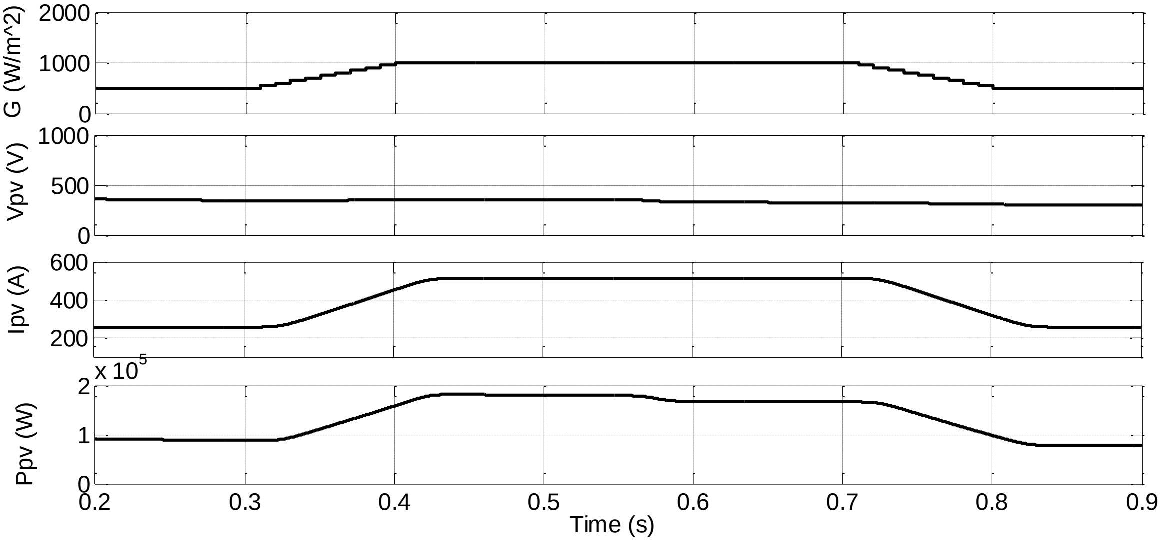

$Fig.4.6$ PV system response to change in solar irradiation: Solar irradiation G, PV voltage V_{pv}, PV current I_{pv}, PV power P_{pv}

$Fig.4.8$ shows the three-phase grid voltage and current simultaneously. Initially the reactive power demand of the load connected at PCC is provided by the grid and hence the grid voltage and current are not in phase with each other. At t = 0.1 s, when the PV system is switched on, the grid current becomes in phase with the grid voltage because the reactive power requirement of the load is now provided by the PV system and the grid needs to provide only the active power to the load if the PV power delivered to the PCC is less the load active power requirement or receive active power from the PV if the generated PV power is more that the load active power requirement.

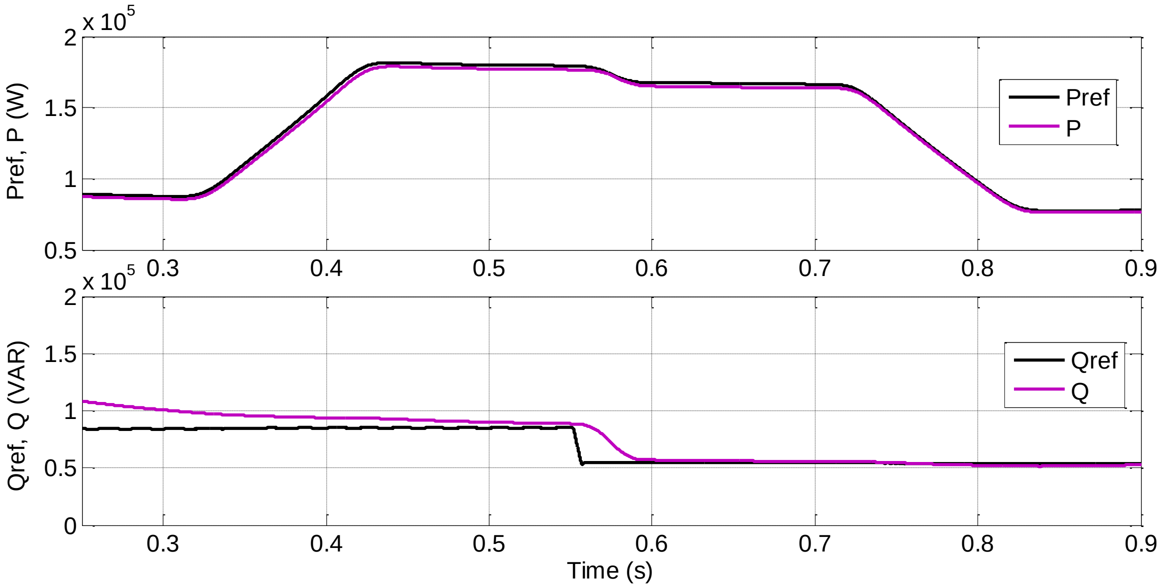

$Fig.$ 4.7 Reference and actual active power $(P_{ref},\ P)$, reference and actual reactive powers $(Q_{ref,}Q)$ delivered by PV to the PCC

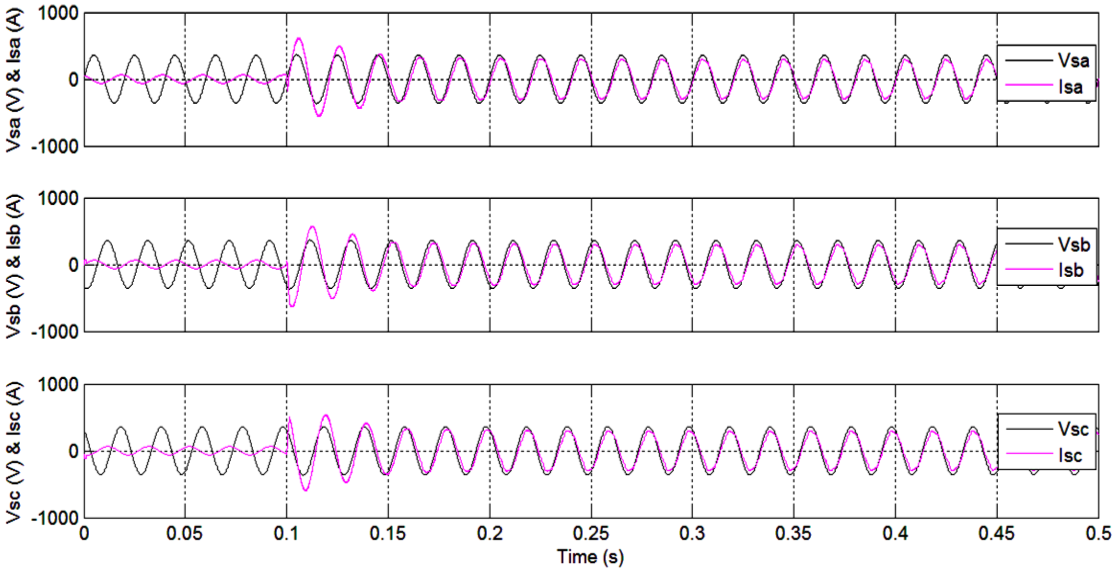

$Fig.$ 4.8 Grid current and voltage simultaneously for phase a, b and c

Grid connected PV application is not restricted to power generation alone. It has been shown that such systems have significant potential in terms of improving the grid power quality [60]. The grid-connected PV based inverter feeding active power into the grid, can also be controlled to act as APF so that it can compensate for harmonic and reactive power demand.

4.6 CONCLUSION

The substantial increase of research and development work in the area of PV systems in recent years has made the PV generators a feasible alternative energy source. The increase in PV energy usage is related to the increasing efficiency of solar cells as well as the improvements of manufacturing technology of solar panels. With the development of distributed generation systems, the renewable electricity from PV generators have become a resource of energy in great demand. The fundamental issues related to PV generation are the PV generation efficiency and issues related to grid integration. PV sources needs to be integrated with control algorithm that perform the task of ensuring maximum power point operation.

The first half of this chapter presented the modeling of PV generator which is further used for design of PVDG system. The presented PV model exhibits a non-linear voltage-current characteristic and its maximum power point varies with solar insolation and temperature. The second half of this chapter presented the modeling and control of single-stage three-phase grid-connected PV system. The power flow between the PV source and the grid is controlled by a power conditioning system which is designed to obtain the power extracted from the PV panels close to MPP and also provide reactive power flow control. The proposed system consists of PV array connected to the DC-side of the VSI for interfacing to the grid.

A two-loop control scheme is used to control the power delivered from the PV system to the utility grid. The MPPT control, the output current control and the reactive power control is realized simultaneously in one power conversion stage thus simplifying the system topology, however increasing the control complexity. The entire system is modeled in MATLAB/Simulink environment and simulations carried out to verify the operation and the control principle. Various simulation results are presented for the proposed PV grid-interfaced system.

Chapter-5

GRID-INTERACTIVE PHOTOVOLTAIC-FUEL CELL HYBRID SYSTEM WITH REACTIVE AND HARMONIC COMPENSATION OF PCC LOAD

This chapter proposes a utility-interactive hybrid distributed generation system consisting of PV and FC to realize a reliable power supply for a grid connected critical load. The proposed system ensures maximum utilization of the PV array, and necessary utilisation of FC stack resulting in optimum operational costs. The inverter control also provides harmonic compensation for any non-linear load connected at the PCC thus maintaining the grid current free of any distortions because of the load.

5.1 INTRODUCTION

Distributed Generations are rapidly increasing across the globe because they can meet the increasing power demand while complying with the environmental regulations of low emissions [164]. When, different types of energy sources are integrated into a DG system, it is called a Hybrid Distributed Generation System (HDGS) [140]. Photovoltaic power generation is the most promising renewable power generation technology but it has large variations in its output power during day and night and during varying weather conditions. Fuel Cell systems show great potential in DG source of the future due to their fast technology development, high energy efficiency, extremely low emission of pollutant gases, reusability of exhaust heat, low noise, cleanness of its energy production and flexible modular structure. However, the cost of FC is too high to justify their widespread use. Hence a PV-FC hybrid system proves to be best to provide a reliable power source for grid-connected applications than a system comprising a single resource [137-141, 143].

This chapter proposes a hybrid PV-FC DG system to realize a reliable power supply for a grid connected critical linear/non-linear load. The power conditioning unit consists of two DC-DC boost converters where one of them is fed by a PV array and the other by an FC stack. The output of the two DC-DC converters is connected to a common DC-link. The power from the DC-link is fed to the grid through the inverter. The power circuit description, the control circuit for the PV DC-DC converter which extracts maximum power from the PV array, the control circuits for the FC DC-DC converter which regulates the required FC power, the control circuit for the DC-AC converter which apart from feeding active power to the grid also provides reactive power and harmonic compensation of PCC load, the algorithm implementation of Maximum Power Point Tracking (MPPT) in PV, and MATLAB simulation results are presented.

The advantages offered by the proposed single inverter hybrid system is that in this topology only the two DC output voltages are required to match whereas in the two inverter topology both the magnitude and the phase are required to match. Further the presence of DC-DC converters ensures a stable DC-link voltage at the input of the inverter, thus eliminating the chances of injecting sub-harmonics into the grid. The DC-DC converter provides the required boosting. This topology offers independent control of active and reactive power by controlling the phase angle and modulation index or magnitude of the inverter respectively. The number of switches is reduced from 12 as in the two inverter topology to 8 switches in the proposed scheme. The MPPT implemented in the PV DC-DC converter ensures maximum utilisation of the PV array. The system is optimised to minimise the running cost by making only necessary utilisation of the FC stack. It provides a reliable power supply to the grid-connected critical load. The inverter interfacing the FC and the PV to the grid also provides active power filtering if the PCC load is non-linear thus ensuring a sinusoidal grid current in phase with the grid voltage.

5.2 POWER CIRCUIT DESCRIPTION OF THE HYBRID PV-FC-DG SYSTEM

The PV array model of 6 kW rating used for this study is a 2×15 series-parallel matrix of 0.2 kW PV module. The FC stack model used for this study has a rating of 6 kW. The power circuit topology of the proposed hybrid PV-FC DG system consists of two DC-DC boost converters. One of the converters is fed by the PV array and the other by the FC stack. The incremental conductance MPPT control algorithm is implemented in the DC-DC converter connecting the PV array to the DC-link. This ensures extraction of maximum power from the PV array under all conditions. The difference of required power and the PV power is provided by the FC and regulated through proper control of DC-DC converter connecting the FC stack to the DC-link. The outputs of the DC-DC converters are connected to a common DC-link. The power from the DC-link is fed into the grid through an inverter. An inductive filter is connected at the output of the inverter to reduce the harmonics introduced by the inverter. A step-up transformer is then used to increase the voltage level before the system is connected to the grid.

The inverter control is so designed that apart from feeding active power into the grid, the system can also provide reactive power and harmonic compensation for any non-linear/linear load connected at PCC. The inverter power angle is controlled to maintain a constant DC-link voltage to ensure that all the power transferred from the two DC-DC converters is delivered to the PCC. The reactive power requirement of the PCC load is controlled by controlling the inverter’s modulation index. Thus the active and reactive powers are controlled independently by controlling the inverter angle and the modulation index. The inverter also includes the active filtering functionality thus providing harmonic power requirement of the PCC load thus maintaining the grid current free of any distortions.

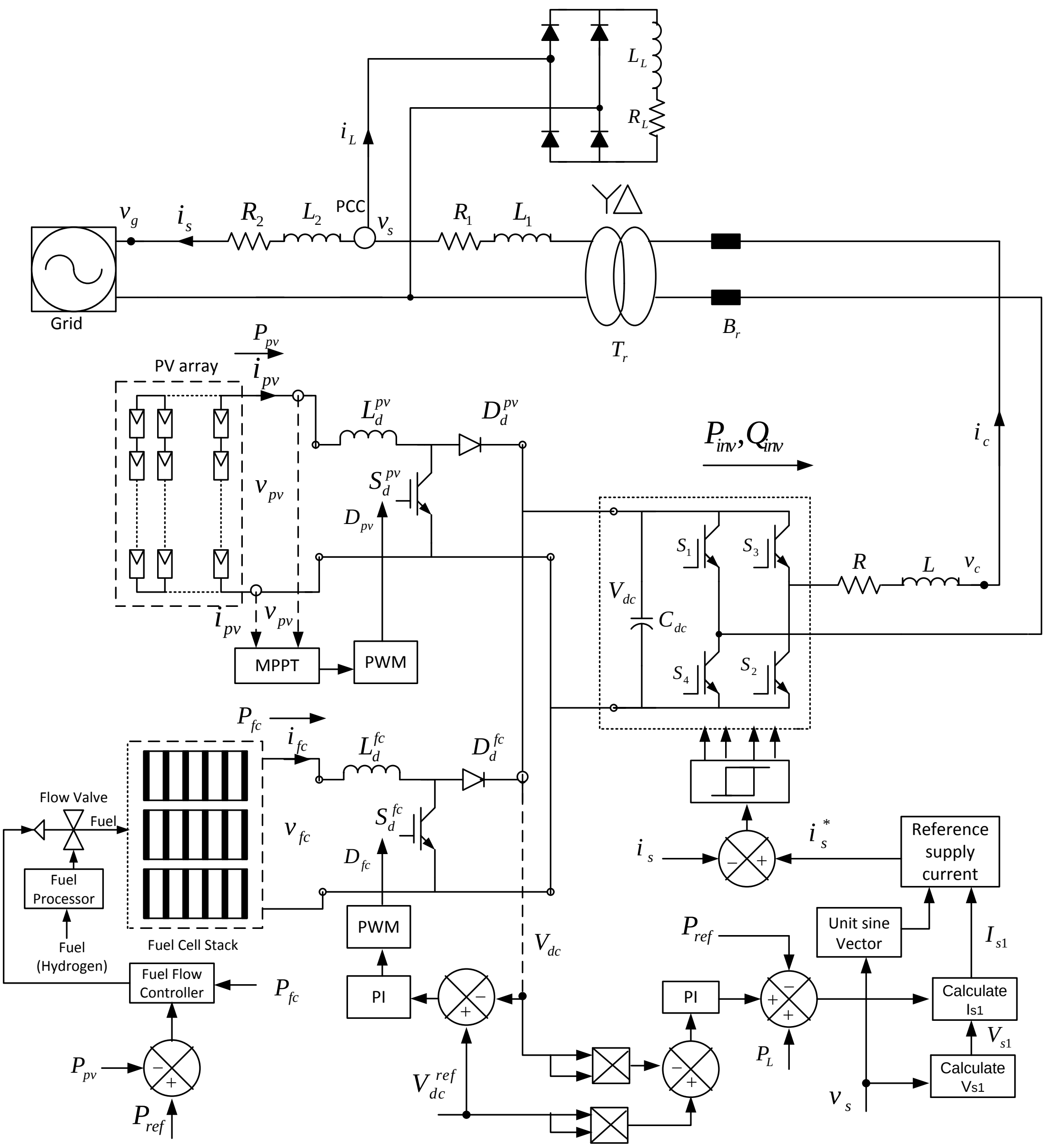

$Fig.$ 5.1 Proposed PV-FC hybrid system

5.3 CONTROL CIRCUIT DESCRIPTION

The FC generates power at variable low DC voltage. A simple DC-DC boost converter is used to boost the output voltage of the FC stack before being interfaced to the DC-link of the grid-interfacing inverter. The boost converter has higher efficiency and requires less components as compared to other DC-DC converter topologies like push pull, half bride and full bridge etc. which could possibly be used to interface the FC system to the grid.

The DC-DC converter output voltage (inverter DC-link voltage) V_{dc} is compared with a reference value $V_{dc,ref}$ and the error signal is processed through PI controller. The output of the controller is used to control the pulse width modulated pulses with the right duty ratio D_{fc} so that the output voltage follows the reference value. Similarly, a DC-DC converter connects the PV array to the DC-link. The MPPT control is implemented in the DC-DC converter to extract maximum power from the PV array under all conditions. The output of the MPPT controls the PWM pulses with the right duty ratio D_{pv} for maximum power extraction.

For PV array,

$$P_{pv} = I_{pv}V_{pv} = I_{pv}V_{dc}\left(1 - D_{pv}\right) \tag{5.1}$$

where V_{pv} and I_{pv} are PV array voltage and current, respectively.

Similarly, for FC stack,

$$P_{fc} = I_{fc}V_{fc} = I_{fc}V_{dc}\left(1 - D_{fc}\right) \tag{5.2}$$

where V_{fc} is the FC stack voltage, I_{fc} is the FC stack current. The active and reactive power transfer (P_{inv}, Q_{inv}) from DC-link voltage to PCC is expressed as:

$$P_{inv} = \frac{V_s V_c}{X_c} sin\, \delta_c = \frac{m_a V_{dc} V_s}{X_c} sin\, \delta_c \tag{5.3}$$

$$Q_{inv} = \frac{V_s}{X_c}(V_c \cos \delta_c - V_s) = \frac{V_s}{X_c}(m_a V_{dc} \cos \delta_c - V_s) \tag{5.4}$$

where V_s is the grid voltage, V_c is the inverter output voltage, X_c is the resultant impedence between AC-side of inverter and the PCC which includes the filter, transformer and line impedances, δ_c is the inverter power angle and m_a the inverter modulation index.

Thus there are four control variables D_{pv}, D_{fc}, m_a and δ_c available. m_a is strongly coupled to Q_{inv} while δ is strongly coupled to P_{inv}. Thus P_{inv} and Q_{inv} can be controlled independent of each other by controlling δ_c and m_a respectively. For a voltage source inverter, it is desirable to maintain V_{dc} constant. D_{pv} and D_{fc} can control the PV and FC power components, respectively, and there is only slight dependency between the two. The power angle δ_c directly controls the output power of the inverter. It also controls V_{dc} to a constant value by achieving a perfect power balance across the DC-link capacitor. The MPPT governs D_{pv} independent of any other variables. This ensures transfer of maximum power to DC-link under all conditions. The power deficit between P_{ref} and P_{pv} is supplied by the FC stack through proper control of D_{fc}. Once D_{fc} and D_{pv} are determined, the amount of power transfer from the boost converters to the inverter input is decided. δ_c is suitably controlled to regulate V_{dc}, thereby ensuring that all the power pumped in by the DC-DC converters to the DC-link is transferred to the PCC. Depending on the reactive power requirement of the PCC load Q_{ref}, Q_{inv} can be changed with the help of m_a [168]. $Fig.$ 5.1 shows the proposed system and the control circuit. The inverter control also includes the functionality of harmonic compensation of PCC load. *Appendix-C* gives an insight into the boost converter topology and its small signal analysis for controller design.

5.4 SIMULATION RESULTS AND DISCUSSIONS

To demonstrate the proposed HDGS scheme, a model has been built and simulated in MATLAB/ Simulink environment. Both FC stack and PV panel is of 6 kW rating. Four different modes of HDGS operation are considered.

- Mode 1 is operational only when the generated PV power is greater than the reference power and thus only PV source is operational thus saving the FC running cost. As the PV array is operated with MPPT, the inverter provides the maximum power available to the DC-link. Any extra power after fulfilling the load requirement is fed into the grid.
- Mode 2 is operational when the power generated by the PV array is less than the reference value. The difference between the reference power and the power supplied by the PV is supplied by the FC stack.
- In mode 3, only the FC stack supplies power. This mode is operational only when the PV power becomes zero during nights or less than a defined minimum value during cloudy conditions. In all these modes, apart from transferring active power from DC-link to grid, the inverter also provides the reactive and harmonic power to the PCC load.
- Mode 4 operation is further considered when both the energy sources are non-operational for any reason, the active power demand of PCC load is provided by the grid while the reactive and harmonic power of the PCC load is provided by the inverter. The parameters used for simulation are given in *Table 5.1*.

Table 5.1 **Parameters used for PV-FC-DG Hybrid System Simulation**

Parameters	**Values**	
FC rating	6 kW	
PV rating	6 kW	
DC-link capacitance	C_{dc} = 15000 μF	
Reference DC-link voltage	V_{dcref} = 100 V	
Source voltage, frequency	v_s = 230V, 50 Hz	
Source resistance	R_s = 0.1 Ω	
Source inductance	L_s = 0.15 mH	
Filter inductance	L = 5 mH	
Step-up transformer	V_n=100V/230V, P_n=15 kW	
Load parameters:		
Mode (a), (b)	t < 3.3, t > 3.7	Z_{dc_side}=10+j3.77
	3.3 < t < 3.7	Z_{dc_side}= (10+j3.77)$\parallel$(10+j0)
Mode (c)	t < 2.4, t > 2.8	Z_{dc_side}=10+j3.77
	2.4 < t < 2.8	Z_{dc_side}= (10+j3.77)$\parallel$(10+j0)
Mode (d)	t < 0.4, t > 0.8	Z_{dc_side}=10+j3.77
	0.4 < t < 0.8	Z_{dc_side}= (10+j3.77)$\parallel$(10+j0)

5.4.1 Only Photovoltaic Operation Mode $\left(\boldsymbol{P_{pv} > P_{ref,}P_{fc} = 0}\right)$

This mode is operational when PV power P_{pv} is greater than the reference power P_{ref}. Since the PV array is operated with MPPT, the inverter feeds the maximum power available to the DC-link. The remaining power after supplying the local load is fed into the grid. To study the effect of change in solar insolation, G is gradually increased from 0.7 kW/m^2 to 1.0 kW/m^2, starting at $t = 1\,s$, then decreased linearly from 1.0 kW/m^2 to 0.5 kW/m^2, starting at $t = 1.4\,s$ and finally increased to 0.5 kW/m^2 starting at $t = 2.5\,s$. Simulation results showing the transients in V_{pv}, I_{pv} and P_{pv} due to variations in G are given in $Fig. 5.2\ (a)$. With change in insolation, the current fed by the DC-DC converter into the DC-link changes with a corresponding change in the power generated by the PV array. V_{dc} also changes during change in insolation, but the control circuit restores it to its reference value of 100 V.

$Fig. 5.2\ (b)$ shows the PCC voltage V_s, PCC load current I_L, grid current I_s, inverter output current I_c and DC-link voltage V_{dc}. The reactive power and harmonic power demanded by the non-linear PCC load is supplied by the inverter, independent of P_{pv} thus maintain the grid current I_s sinusoidal. A 180-degree phase shift between V_s and I_s as can be seen in $Fig. 5.2\ (c)$ shows that extra power remaining after supplying the load is fed to the grid. $Fig. 5.2\ (d)$ shows the variation in grid, load and inverter active powers $\left(P_{grid}, P_{load} \text{ and } P_{inv}\right)$ and reactive powers $\left(Q_{grid}, Q_{load} \text{ and } Q_{inv}\right)$. The active power from PV is given to load and grid, and the reactive power of the load is provided by the inverter. Due to small fluctuations in V_{dc}, the disturbances in the reactive power appear more pronounced. This shows a strong coupling between Q_{inv} and V_{dc}. This is due to the incremental conductance algorithm employed by the MPPT technique and the power balance carried out by the inverter at the DC-link. $Fig. 5.2\ (d)$ also shows a load change at the PCC at times $t = 3.3s$ and $t = 3.7s$.

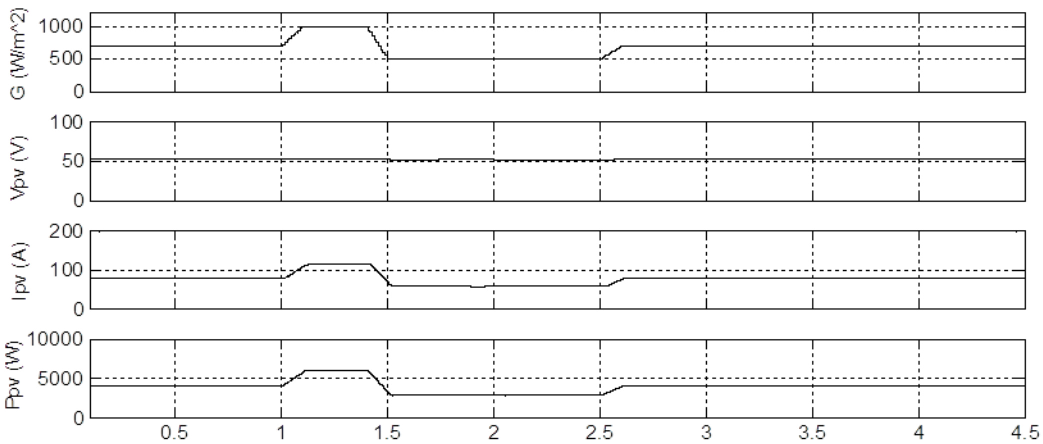

$Fig. 5.2\ (a)$ Only PV mode operation: Solar insolation G, PV output voltage V_{pv}, PV output current I_{pv} and PV output power P_{pv}

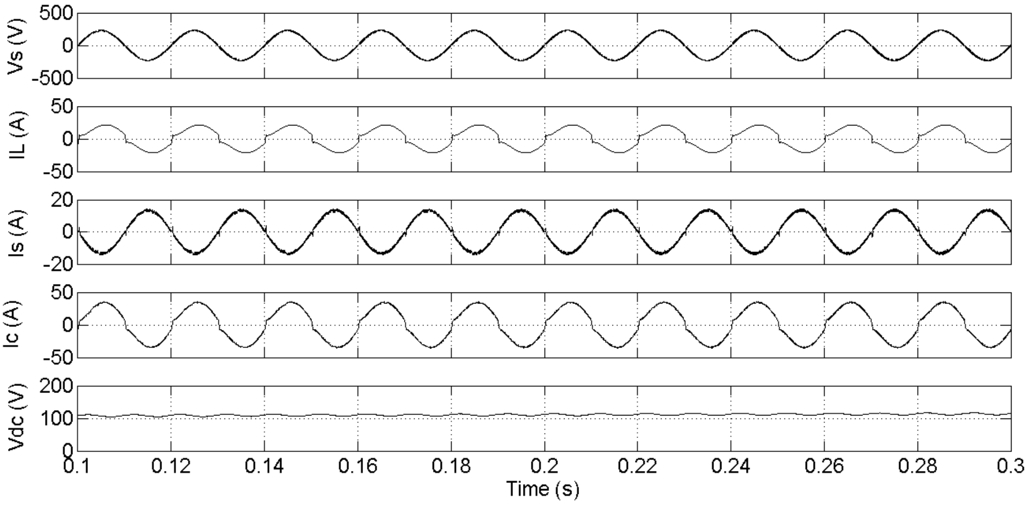

$Fig. 5.2\ (b)$ Only PV mode operation: PCC voltage V_s, Load current I_L, Grid current I_s, Inverter output current I_c and DC-link voltage V_{dc}

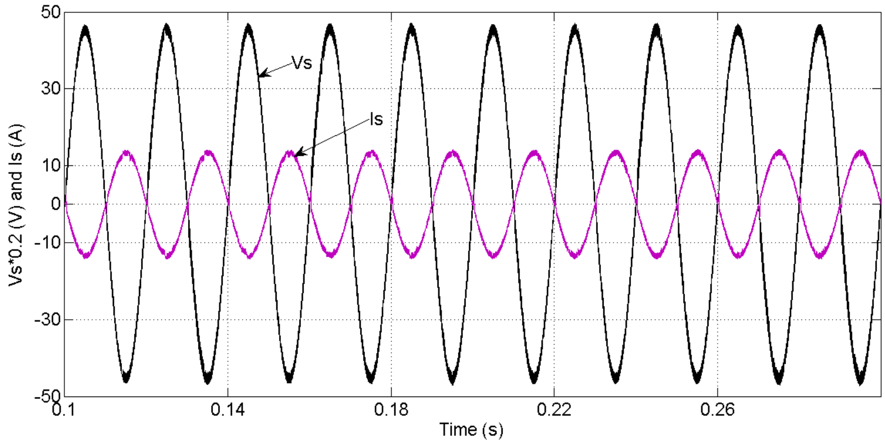

$Fig. 5.2\ (c)$ Only PV mode operation: PCC voltage V_s and grid current I_s simultaneously

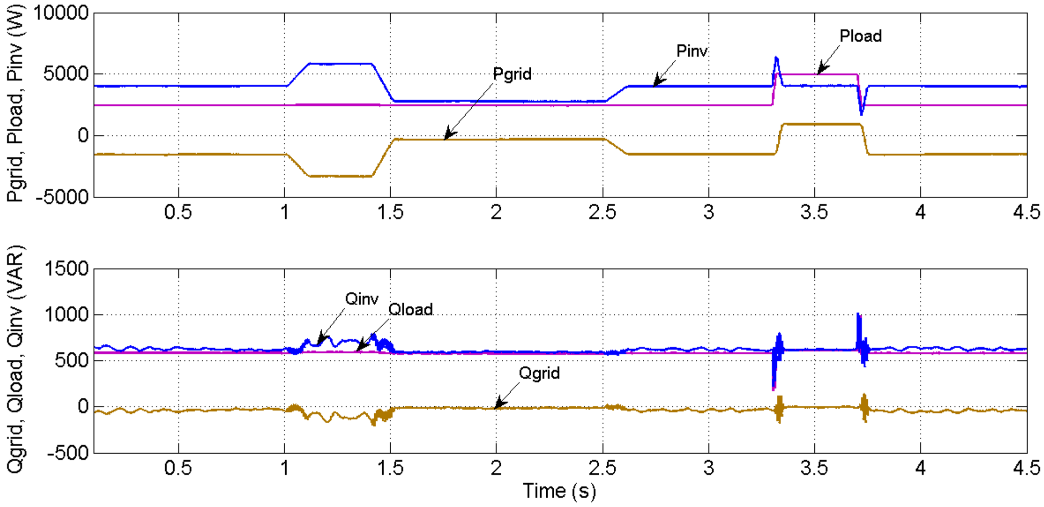

$Fig. 5.2\ (d)$ Only PV mode operation: Active powers of grid, load and inverter $(P_{grid}, P_{load}$ and $P_{inv})$, Reactive powers of grid, load and inverter $(Q_{grid}, Q_{load}$ and $Q_{inv})$

5.4.2 Photovoltaic and Fuel Cell Combination Operation Mode $\left(\boldsymbol{P_{pv} = P_{max}}, \boldsymbol{P_{fc} = P_{ref} - P_{max}}\right)$

This mode is operational when the power generated by the PV array is less than required reference power P_{ref}. The power difference between P_{ref} and P_{pv} is supplied by the FC stack. The PV array is operated with MPPT, thus freely available P_{pv} is completely utilized and the FC stack is used to meet the deficit power $\left(P_{ref} - P_{pv}\right)$. Again, the reactive power and harmonic power demanded by the load is supplied by the inverter, independent of P_{pv} and P_{fc}.

To study the transient behaviour of the HDGS P_{ref} and G are varied at different time intervals and the response shown. $Fig. 5.3\ (a)$ shows the variation in P_{ref} and solar insolation G. P_{ref} changes in a stepwise manner every 1 s. Initially, the solar insolation is maintained at 700 W/m^2. There is a gradual increase in insolation between $t = 1\ s$ and $t = 1.1\ s$ and finally reaches an insolation of 1000 W/m^2. At $t = 1.4\ s$, the insolation starts decreasing from 1.0 kW/m^2 and reaches 0.5 kW/m^2 by $t = 1.5\ s$ and is further increased to 0.7 kW/m^2 from $t = 2.5\ s$ to $t = 2.6\ s$ and maintained constant thereafter.

$Fig. 5.3\ (b)$ shows the PV output voltage V_{pv}, PV output current I_{pv}, PV DC-DC converter output voltage V_{dc} and PV DC-DC converter output current I_{dc_pv}. V_{dc} is maintained constant at 100 V. $Fig. 5.3\ (c)$ shows the FC output voltage V_{fc}, FC output current I_{fc}, FC DC-DC converter output voltage V_{dc} and FC DC-DC converter output current I_{dc_fc}. $Fig. 5.3\ (d)$ shows the variation in FC output power P_{fc} and PV output power P_{pv}. P_{pv} varies according to G tracking its maximum power point. Any deficit between P_{ref} and P_{pv} is supplied by the FC source. When P_{pv} becomes equal to P_{ref}, FC stops supplying power, $P_{fc} = 0$. $Fig. 5.3\ (e)$ shows variations in the duty ratio of PV DC-DC converter switch D_{pv} and FC DC-DC converter switch D_{fc}. The ripple in D_{pv} is due to MPPT. $Fig. 5.3\ (f)$ shows the variation in grid, load and inverter active powers $\left(P_{grid}, P_{load} \text{ and } P_{inv}\right)$ and reactive powers $\left(Q_{grid}, Q_{load} \text{ and } Q_{inv}\right)$. Whenever P_{inv} is greater than P_{load}, the remaining power $P_{inv} - P_{load}$ is given to the grid. Q_{inv} follows Q_{load} very closely. The figure also shows a load variation at times $t = 3.3s$ and $t = 3.7s$. $Fig. 5.3\ (g)$ shows the PCC voltage V_s, PCC load current I_L, grid current I_s, inverter output current I_c and DC-link voltage V_{dc} showing the inverter is again providing harmonic compensation to PCC load.

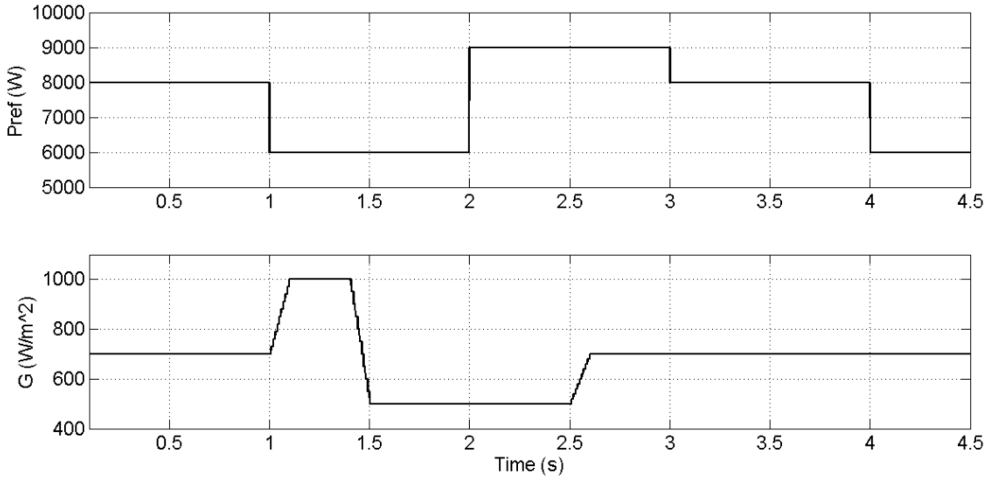

$Fig. 5.3$ (a) PV and FC combination mode operation: Reference power P_{ref} and solar insolation G

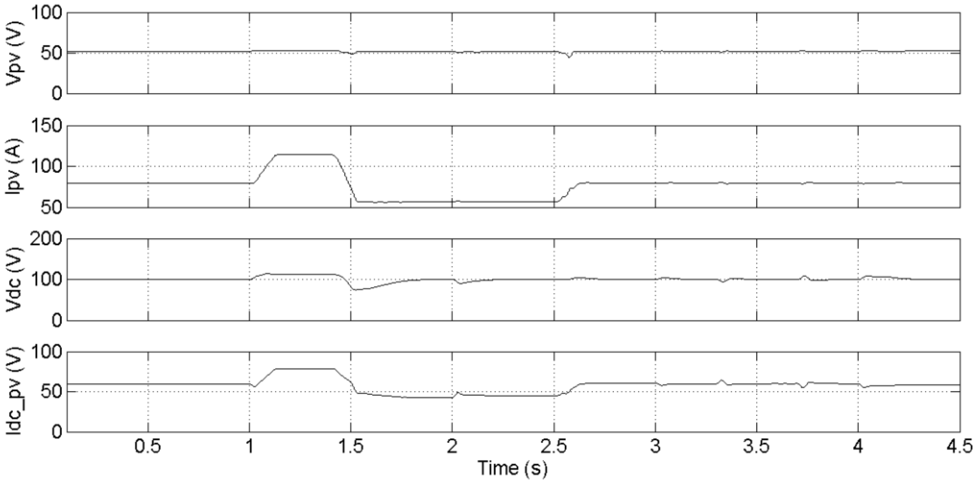

$Fig. 5.3$ (b) PV and FC combination mode operation: PV output voltage V_{pv}, PV output current I_{pv}, PV DC-DC converter output voltage V_{dc} and PV DC-DC converter output current I_{dc_pv}

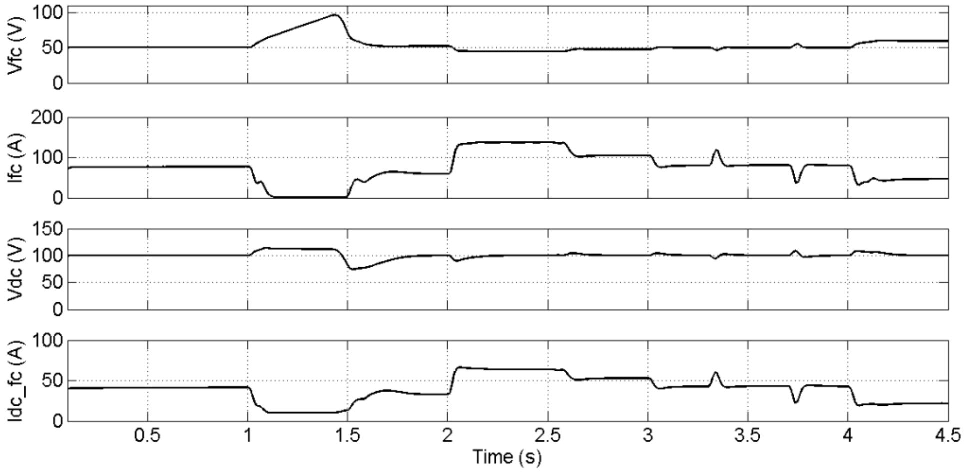

$Fig. 5.3$ (c) PV and FC combination mode operation: FC output voltage V_{fc}, FC output current I_{fc}, FC DC-DC converter output voltage V_{dc} and FC DC-DC converter output current I_{dc_fc}

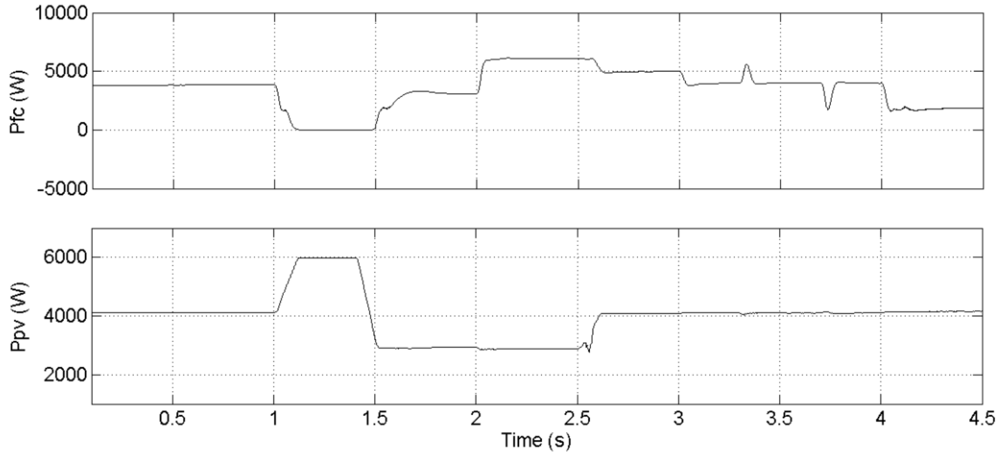

$Fig. 5.3\ (d)$ PV and FC combination mode operation: FC output power P_{fc} and PV output power P_{pv}

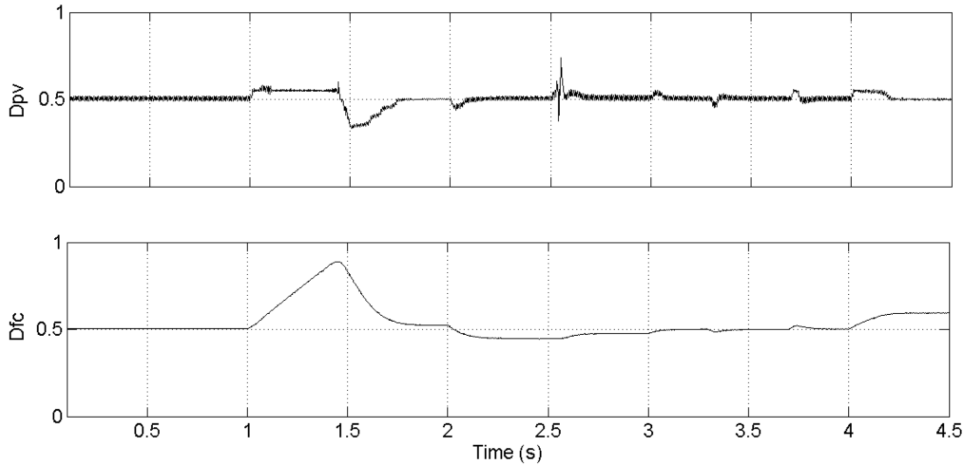

$Fig. 5.3\ (e)$ PV and FC combination mode operation: Duty ratio of PV DC-DC converter switch D_{pv} and FC DC-DC converter switch D_{fc}

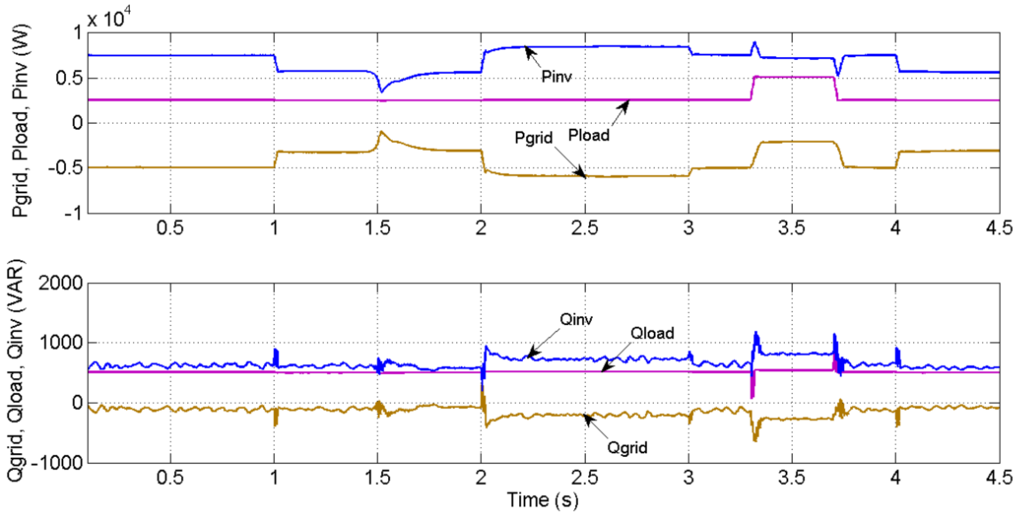

$Fig. 5.3\ (f)$ PV and FC combination mode operation: Active powers of grid, load and inverter $(P_{grid}, P_{load}$ and $P_{inv})$, Reactive powers of grid, load and inverter $(Q_{grid}, Q_{load}$ and $Q_{inv})$

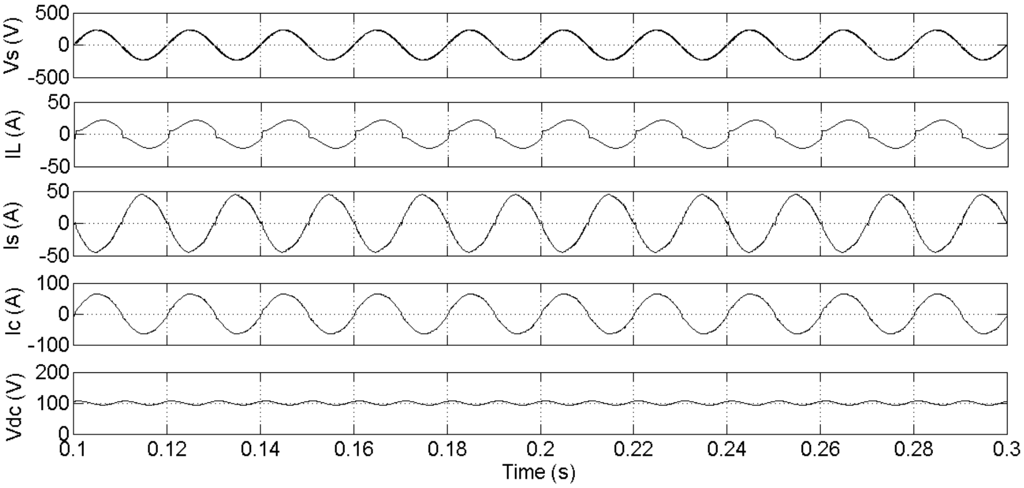

$Fig.$ 5.3 (g) PV and FC combination mode operation: PCC voltage V_s, load current I_L, grid current I_s, inverter output current I_c and DC-link voltage V_{dc}

5.4.3 Only Fuel Cell Operation Mode $\left(P_{fc} = P_{ref}, P_{pv} = 0\right)$

In this mode, only the FC stack supplies power. This mode is operational when $P_{pv} = 0$ i.e. during nights or less than a minimum defined value i.e. during cloudy conditions. The reference active power is provided by the FC and the reactive power demand of the load is provided by the inverter. Even though the FC source is capable of supplying more power, only P_{ref} is supplied because operation of the FC incurs running cost, thereby increasing the overall cost. Q_{ref} demanded by the load is supplied by the inverter and it is independent of either P_{fc} or P_{ref}. V_{dc} is maintained at 100 V.

Initially P_{ref} is 4 kW. P_{ref} is varied from one value to another in a time interval of 1 s in a stepwise manner. P_{fc} follows P_{ref} very closely highlighting the effectiveness of the control circuit. In response to the sudden change in P_{ref}, D_{fc} tries to increase abruptly to meet the new demand. This overshoot in D_{fc} causes an overshoot in V_{dc} that also gets projected in Q_{inv}. $Fig.$ 5.4 (a) shows the reference power P_{ref} and the power supplied by the FC P_{fc}. The PCC load variation can be seen projected in P_{fc}. $Fig.$ 5.4 (b) shows the variations in FC stack output voltage V_{fc}, FC stack output current I_{fc}, DC-DC converter output voltage V_{dc} and DC-DC converter output current I_{dc_fc} with change in P_{ref}. $Fig.$ 5.4 (c) shows the duty ratio of FC DC-DC converter D_{fc}. $Fig.$ 5.4 (d) shows the active powers of grid, load and inverter $\left(P_{grid}, P_{load} \text{ and } P_{inv}\right)$, and the reactive powers of grid, load and inverter $\left(Q_{grid}, Q_{load} \text{ and } Q_{inv}\right)$.

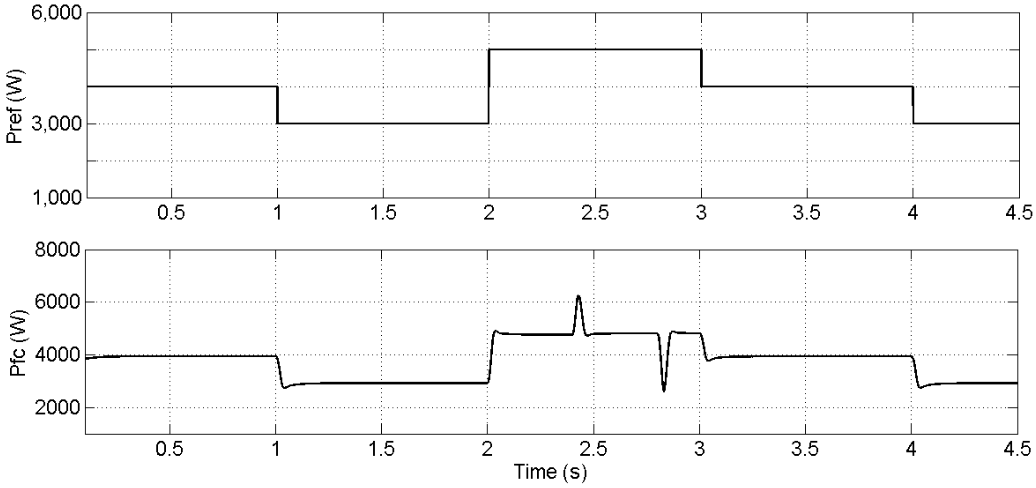

$Fig. 5.4\ (a)$ Only FC mode operation: Reference power P_{ref} and FC stack power P_{fc}

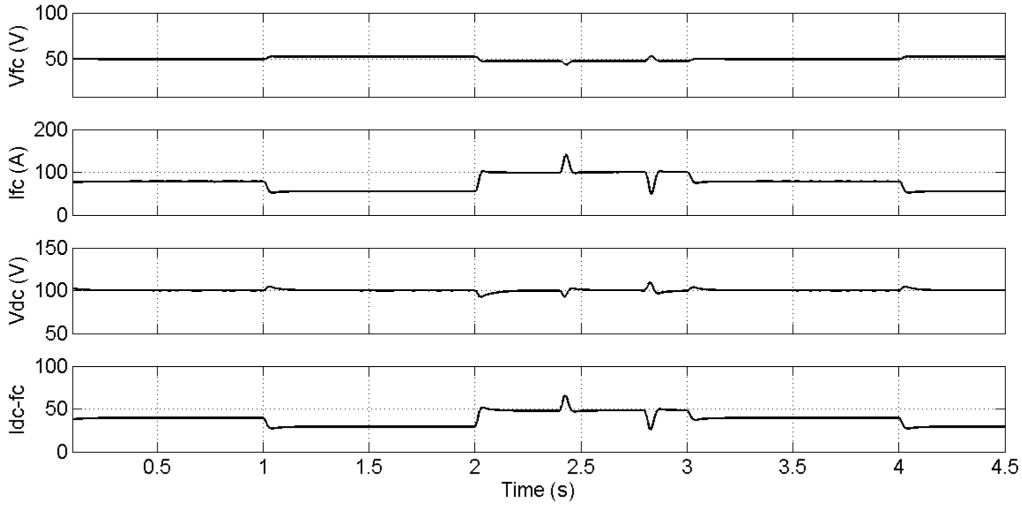

$Fig. 5.4\ (b)$ Only FC mode operation: FC stack output voltage V_{fc}, FC stack output current I_{fc}, DC-DC converter output voltage V_{dc} and DC-DC converter output current I_{dc_fc}

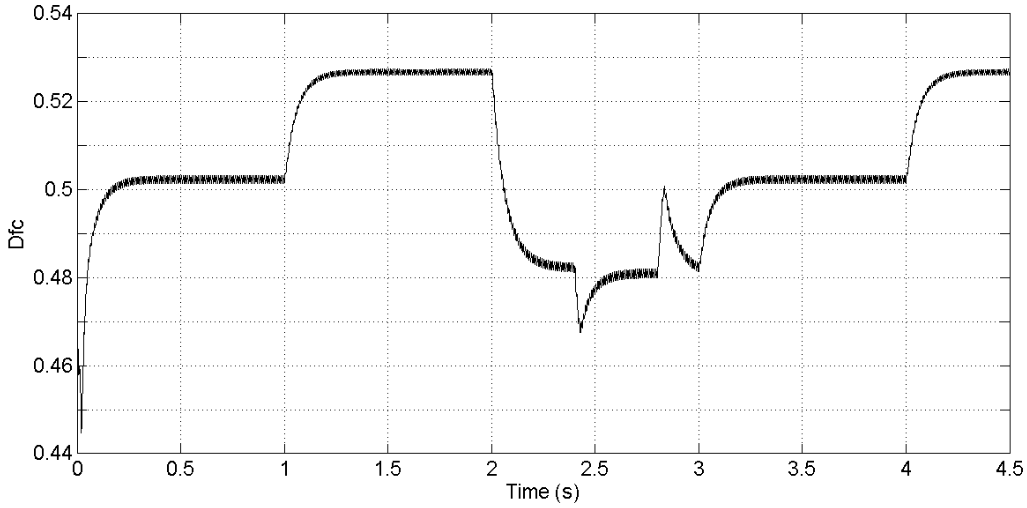

$Fig. 5.4\ (c)$ Only FC mode operation: Duty ratio of FC DC-DC converter D_{fc}

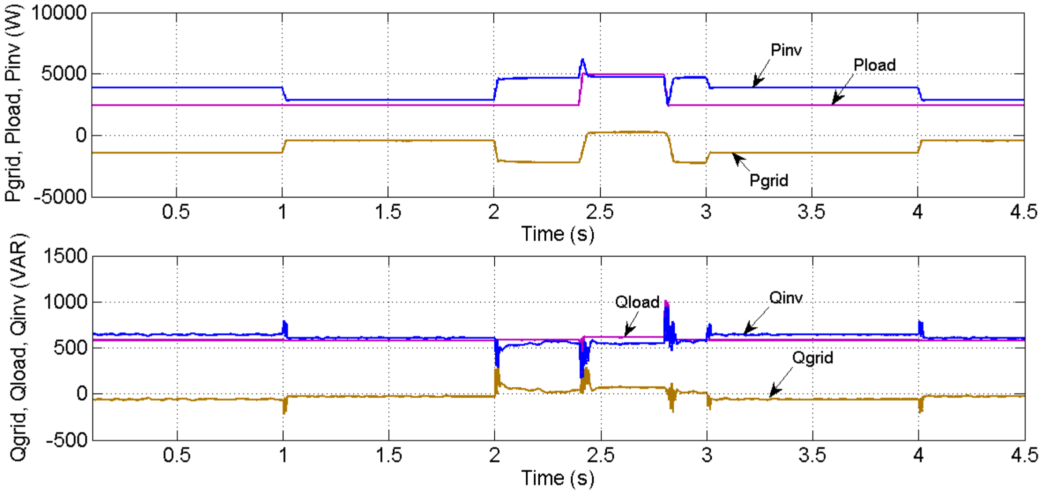

$Fig.5.4\ (d)$ Only FC mode operation: Active powers of grid, load and inverter $\left(P_{grid}, P_{load} \text{ and } P_{inv}\right)$, reactive powers of grid, load and inverter $\left(Q_{grid}, Q_{load} \text{ and } Q_{inv}\right)$

5.4.4 No supply from Photovoltaic or Fuel Cell $\left(P_{fc} = 0, P_{pv} = 0\right)$

Mode 4 operation is functional when both the energy sources are non-operational for any reason. Thus the active power demand of PCC load is provided by the grid while the reactive and harmonic power of the PCC load is provided by the inverter. Fig 5.5 (a) shows the PCC voltage V_s, load current I_L, grid current I_s, inverter output current I_c and DC-link voltage V_{dc}. It can be seen that the inverter supplies a compensating current to the PCC so that the grid current remains of good quality. $Fig.5.5\ (b)$ shows active powers of grid, load and inverter $\left(P_{grid}, P_{load} \text{ and } P_{inv}\right)$, and the reactive powers of grid, load and inverter $\left(Q_{grid}, Q_{load} \text{ and } Q_{inv}\right)$. The inverter consumes a small amount of active power from the grid to maintain the DC-link voltage and to overcome the losses associated with the inverter. The load reactive power is provided by inverter effectively. $Fig.5.5\ (c)$ shows the PCC voltage V_s and grid current I_s simultaneously. They are in phase with each other, means now the grid is supplying power to the load.

Similar to a single-phase PV-FC hybrid system a three-phase hybrid system could be designed. The DC-DC converters would remain the same. The single-phase DC-AC converter would be replaced by a three-phase converter. The control algorithm and control circuit would be similar to that given in Chapter-3 for three-phase FC system with active filter functionality. Thus a three-phase hybrid system can be designed with a single inverter and the same inverter also acts as an APF.

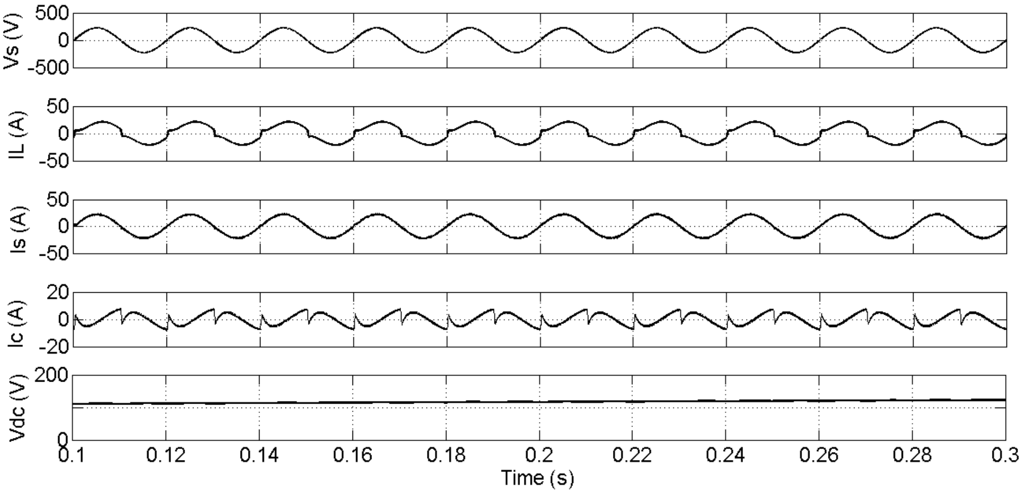

$Fig. 5.5\ (a)$ No supply from PV and FC: PCC voltage V_s, Load current I_L, Grid current I_s, Inverter output current I_c and DC-link voltage V_{dc}

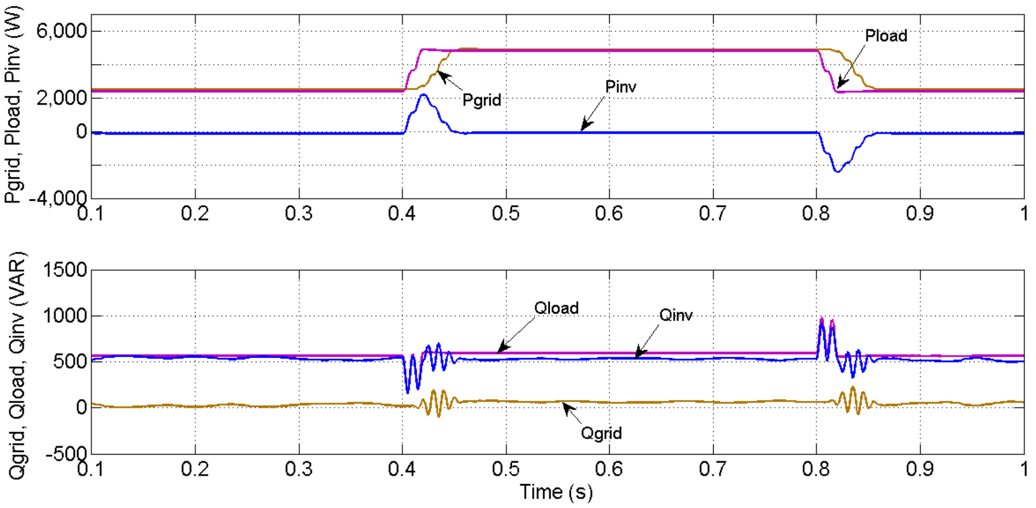

$Fig. 5.5\ (b)$ No supply from PV and FC: Active powers of grid, load and inverter $\left(P_{grid}, P_{load} \text{ and } P_{inv}\right)$, Reactive powers of grid, load and inverter $\left(Q_{grid}, Q_{load} \text{ and } Q_{inv}\right)$

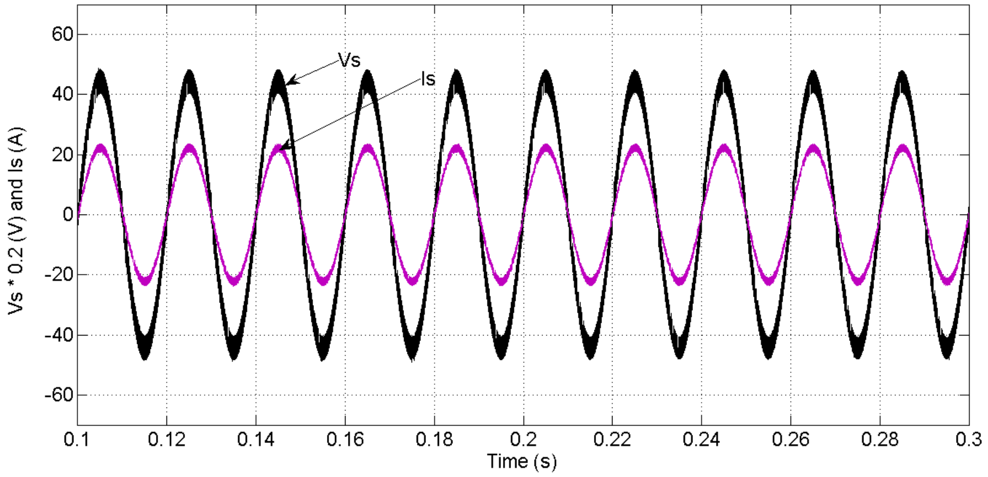

$Fig. 5.5\ (c)$ No supply from PV and FC: PCC voltage V_s and grid current I_s simultaneously

5.5 CONCLUSION (Comment [14])

In conclusion, FC is a promising technology for DG. However, considering with the performance and cost of the FC, a hybrid power system is a practical solution. It can provide higher efficiency, enhanced reliability, lower emissions, and an acceptable cost. The chapter presented a new hybrid PV-FC DG system. Instead of connecting the PV and FC sources to the grid with separate inverters, the energy sources are first connected to a common DC-link by separate DC-DC converters and then connected to the grid through a common inverter. The proposed system works flexibly, exploiting maximum solar energy and optimum energy from FC. Appropriate control schemes have been designed for the inverter incorporating the active filtering capability thus compensating for reactive and harmonic power of PCC load as well and thus maintaining the grid current of good quality.

In the proposed hybrid system, only the two DC output voltages are required to match whereas in the two inverter topology both the magnitude and the phase are required to match. The presence of DC-DC converters ensures a stable DC-link voltage at the input of the inverter. This topology offers independent control of active and reactive power by controlling the phase angle and modulation index or magnitude of the inverter respectively. The Incremental Conductance MPPT implemented in the PV DC-DC converter ensures maximum utilisation of the PV array. The system is optimised to minimise the running cost by making only necessary utilisation of the FC stack. It provides a reliable power supply to the grid-connected critical load. The inverter interfacing the FC and the PV to the grid also provides active power filtering if the PCC load is non-linear thus ensuring a sinusoidal grid current in phase with the grid voltage.

Chapter-6

CONCLUSION AND SCOPE OF FUTURE WORK

6.1 CONCLUSIONS (Comment [15])

The concept of using alternative energy sources as distributed generation is rapidly gaining universal acceptance because of its technical, economic and environmental benefits over conventional energy generation. This thesis gives an insight into photovoltaic and fuel cell distributed energy systems. FCs and PVs produce DC power which needs to be converted to single-phase or three-phase AC for grid-interface. This has led to the development of various power electronic topologies for converting the generated DC power to utility compatible AC power.

- *Conventionally, an isolated or non-isolated DC-DC converter is used before the DC-AC grid-interfacing inverter to provide the required voltage boost. In this thesis, a single-stage FC based DG system is proposed where instead of using DC-DC converter for voltage boosting, a transformer is used for making the DC-AC converter output voltage compatible with the grid voltage. The behaviour of the FC system is studied by performing mathematical analyses and simulation studies. Suitable control strategy is designed for the DC-AC converter in FC system. An attempt has been made to address the following key challenges: developing single-stage DC-AC conversion with low component count, regulation of active and reactive power to the grid, harmonic control in inverter output voltage and grid synchronisation. A dynamic circuit model for a Proton Exchange Membrane FC based on its electrochemical and thermodynamic phenomena was used for the simulation study.*
- *In the conventional two-stage PVDG system, the power electronic converter is a DC-DC-AC converter. Thus the PV voltage is first boosted to an adequately large level and the VSI interfaces the boosted voltage to the grid. In second phase of the presented work, a single-stage PVDG system is proposed. The VSI facilitates the MPPT through regulation of DC-link voltage as well as transfer of power to the grid. Due to the utilisation of only one conversion stage, the proposed single-stage PVDG system proved to be simpler, more efficient and economical than the two-stage conversion system. All the four operation, power flow control, the DC-link voltage control, the maximum power point tracking and grid synchronisation was included simultaneously in the PVDG inverter.*
- *A novel control for a grid-interfacing inverter to improve the quality of power at PCC for a single-phase and three-phase FCDG system has further been proposed. It has been shown that the grid-interfacing inverter can be effectively utilized for power conditioning without affecting its normal operation of real power transfer. The grid-interfacing inverter with the proposed approach can be utilized to inject real power generated from FC to the grid, and/or*

operate as a Shunt Active Power Filter. This approach thus eliminates the need for additional power conditioning equipment to improve the quality of power at PCC. Simulation as well as experimentation have validated the proposed approach and have shown that the grid-interfacing inverter can be utilized as a multi-function device.

It is further demonstrated that the PQ enhancement can be achieved under different scenarios. The current unbalance, current harmonics and load reactive power due to unbalanced and non-linear load connected to the PCC, are compensated effectively such that the grid side currents are always maintained as balanced and sinusoidal at unity power factor. When the power generated from FC is more than the total load power demand, the grid-interfacing inverter with the proposed control approach not only fulfils the total load active and reactive power demand with harmonic compensation but also delivers the excess generated active power to the grid at unity power factor.

- *The last part of the work presented PV- FC hybrid DG system. PV power generation has large variations in its output power and the cost of FC is too high to justify their widespread use. Hence a PV-FC hybrid system is proposed to provide a reliable power source for grid-connected applications than a system comprising a single resource.*

  Instead of connecting the PV and FC sources to the grid with separate inverters, the energy sources are first connected to a common DC-link by separate DC-DC converters and then connected to the grid through a common inverter. The proposed system works flexibly, exploiting maximum solar energy and optimum energy from FC. Appropriate control scheme have been designed for the DC-DC converters and the inverter incorporating the active filtering capability thus compensating for reactive and harmonic power of PCC load as well and thus maintaining the grid current of good quality.

  The system configuration and control strategy for power management is presented for the PVFC hybrid system. The simulation results show that the PV-FC hybrid system with proposed control and power management can achieve the desired performance. The PV-FC hybrid system thus provides higher efficiency, enhanced reliability, low emission and reduced cost. Thus the proposed hybrid system has a better potential to provide higher quality and more reliable power than a system comprising a single source.

6.2 FUTURE SCOPE OF WORK

- The simulation results of the PV system, FC system and the PV-FC hybrid system may be validated using lab experiments and on-site monitoring with actual installation of FC and PV. The practically measured data with variation in solar irradiance, ambient temperature and wind velocity should be compared with the values predicted from the simulation work.

- Studies on economic feasibility and analysis, initial investment and operating costs, payback period for all the systems and the cost of electricity generated by PV, FC and hybrid systems compared to utility rates for all three alternatives.
- Energy storage devices such as batteries and ultracapacitors can be used with FCs to improve the performance of FC under transient disturbances and also with PVs to provide uninterrupted supply.
- Multi-level inverter for integrating PV and FC to the grid combining the features of active power filter for high power applications is a potential area for future research.
- Advance control techniques like artificial neural network and fuzzy logic can be introduced into the power converter circuits to generate the converter switching signals.
- The proposed systems are grid-connected systems and cease to operate in case of grid failure. The system works well as long as the grid is present. In an event of grid failure, appropriate design will be needed. This needs to be investigated further and reported in future work.

LIST OF PUBLICATIONS FROM THE RESEARCH WORK

LIST OF CONFERENCE PAPER PUBLICATIONS

1. **Gitanjali Mehta**, S. P. Singh, and R. D. Patidar, “Grid interconnection of distributed generation system with power quality improvement features,” in proceedings of IEEE International Conference on Power Electronics and Drive Systems, PEDS-2011, 5-8 December, 2011, Singapore, 329-333.

2. **Gitanjali Mehta**, S. P. Singh, and R. D. Patidar, “Non-linear load compensation in Fuel Cell grid interfaced system using active power filter,” in proceedings of IEEE International Conference on Power Electronics and Drive Systems, PEDS-2011, 5-8 December, 2011, Singapore, pp. 197-202.

3. **Gitanjali Mehta** and S. P. Singh, “Active and Reactive Power Control of Proton Electrolyte Membrane Fuel Cell based Distributed Generation System,” in proceedings of IEEE International Conference on Power Electronics, IICPE-2010, 28-30 January, 2011, N.S.I.T. Delhi, India, pp. 1-6.

4. **Gitanjali Mehta**, R. D. Patidar and S. P. Singh, “Design, Analysis and Implementation of DSP based single-phase Shunt Active Filter Controller,” in proceedings of IEEE International Conference on Emerging Trends in Electrical and Computer Technology, ICETECT-2011, 23-24 March, 2011, Kanyakumari, India, pp. 166-173.

5. **Gitanjali Mehta** and S. P. Singh, “Grid-interfacing Fuel Cell System with active and reactive power flow control,” in proceedings of IET International Conference on Sustainable Energy and Intelligent System, SEISCON-2011, 20-22 July, 2011, DR. M. G.R. University, Chennai, India.

6. **Gitanjali Mehta** and S. P. Singh, “Improvement of power quality at PCC through grid interfacing photovoltaic system,” in proceedings of The Sixth IASTED Asian Conference on Power and Energy Systems AsiaPES 2013, 10-12 April, 2013, Phuket, Thailand.

7. **Gitanjali Mehta** and S. P. Singh, “Design and Analysis of Photovoltaic-Fuel Cell Hybrid Distributed Generation System,” in proceedings of 39th IEEE Photovoltaic Specialists Conference, 16-21 June, 2013, Florida, USA.

LIST OF JOURNAL PAPER PUBLICATIONS

1. **Gitanjali Mehta**, S. P. Singh, and R. D. Patidar, “Fuel Cell based Distributed Generation System with Power Flow and Power Quality Control,” International Journal of Power and Energy Conversion, vol. 4, no. 1, 2013, pp. 73-94.

2. **Gitanjali Mehta** and S. P. Singh, “Power quality improvement through grid integration of renewable energy sources,” IETE Journal of Research, vol. 59, no. 3, May-June 2013, pp. 210-218.

3. **Gitanjali Mehta** and S. P. Singh, “Design of single-stage three-phase grid-connected photovoltaic system with MPPT and reactive power compensation control,” International Journal of Power and Energy Conversion, vol. 5, no. 3, 2014, pp. 211-227.

4. **Gitanjali Mehta** and S. P. Singh, “Modeling, design and analysis of utility-interactive photovoltaic-fuel cell hybrid distributed generation scheme with reactive and harmonic compensation of PCC load,” accepted in Journal of Scientific and Industrial Research.

5. **Gitanjali Mehta** and S. P. Singh, “Modelling, analysis and design of Fuel Cell based distributed generation system with active and reactive power flow control,” International Review on Modelling and Simulations, vol. 5, no. 4 , Aug 2012, pp. 1750-1757.

6. **Gitanjali Mehta**, S. P. Singh and R. D. Patidar, “Active, reactive and harmonic compensation control of grid-interfaced fuel cell system,” International Journal of Emerging Electric Power Systems, vol. 13, no. 4, Oct 2012.

BIBLIOGRAPHY

[1] H. Ghoddami and A. Yazdani, "A Single-Stage Three-Phase Photovoltaic System With Enhanced Maximum Power Point Tracking Capability and Increased Power Rating," IEEE Transactions on Power Delivery, vol. 26, no. 2, pp. 1017-1029, April 2011.

[2] B. Das and B. C. Pal, "Voltage Control Performance of AWS Connected for Grid Operation," IEEE Transactions on Energy Conversion, vol. 21, no. 2, pp. 353-361, June 2006.

[3] Y.-K. Lo, H.-J. Chiu, T.-P. Lee, I. Purnama, and Wang J.-M., "Analysis and Design of a Photovoltaic System DC Connected to the Utility With a Power Factor Corrector," IEEE Transactions on Industrial Electronics, vol. 56, no. 11, pp. 4354-4362, November 2009.

[4] R. Gopinath, S. Kim, J.-H. Hahn, P. N. Enjeti, M. B. Yeary, and J. W. Howze, "Development of a low cost fuel cell inverter system with DSP control," IEEE Transactions on Power Electronics,, vol. 19, no. 5, pp. 1256-1262, September 2004.

[5] *M. Miyatake, M. Veerachary, F. Toriumi, N. Fujii, and H. Ko, "Maximum Power Point Tracking of Multiple Photovoltaic Arrays: A PSO Approach," IEEE Transactions on Aerospace and Electronic Systems, vol. 47, no. 1, pp. 367-380, January 2011.*

[6] B. K. Bose, "Global Energy Scenario and Impact of Power Electronics in 21st Century," IEEE Transactions on Industrial Electronics, vol. 60, no. 7, pp. 2638-2651, July 2013.

[7] J.-W. Jung and A. Keyhani, "Control of a Fuel Cell Based Z-Source Converter," IEEE Transactions on Energy Conversion, vol. 22, no. 2, pp. 467-476, June 2007.

[8] M. Singh, V. Khadkikar, A. Chandra, and R. K. Varma, "Grid Interconnection of Renewable Energy Sources at the Distribution Level With Power-Quality Improvement Features," IEEE Transactions on Power Delivery, vol. 26, no. 1, pp. 307-315, January 2011.

[9] B. Kroposki, C. Pink, R. DeBlasio, H. Thomas, M. Simoes, and P. K. Sen, "Benefits of Power Electronic Interfaces for Distributed Energy Systems," IEEE Transactions on Energy Conversion, vol. 25, no. 3, pp. 901-908, September 2010.

[10] F. Blaabjerg, Z. Chen, and S. B. Kjaer, "Power electronics as efficient interface in dispersed power generation systems," IEEE Transactions on Power Electronics, vol. 19, no. 5, pp. 1184-1194, September 2004.

[11] G. Mehta, S. P. Singh, and R. D. Patidar, "Grid interconnection of distributed generation system with power quality improvement features," in proceedings of IEEE International Conference on Power Electronics and Drive Systems, PEDS-2011, pp. 329-333, 2011.

[12] A. Kirubakaran, S. Jain, and R. K. Nema, "A review on fuel cell technologies and power electronic interface," Renewable and Sustainable Energy Reviews, vol. 13, pp. 2430-2440, 2009.

[13] http://www.aaenvironment.com/DG.htm.

[14] G. S. Reddy and R. K. Singh, "Distributed generation based Dynamic Voltage Restorer," in *IET-UK International Conference on Information and Communication Technology in Electrical Sciences* 2007, pp. 262-266.

[15] G. S. Reddy and R. K. Singh, "Modeling and control of a distributed generation system," in *IET-UK International Conference on Information and Communication Technology in Electrical Sciences* 2007, pp. 256-261.

[16] W. Kramer, S. Chakraborty, B. Kroposki, and H. Thomas, "Advanced power electronic interfaces for distributed energy systems Part 1: Systems and Topologies," Technical Report NREL/TP-581-42672, March 2008.

[17] E. M. Stewart, R. Tumilty, J. Fletcher, A. Lutz, G. Ault, and J. McDonald, "Analysis of a Distributed Grid-Connected Fuel Cell During Fault Conditions," IEEE Transactions on Power Systems, vol. 25, no. 1, pp. 497-505, February 2010.

[18] R. A. Shayani and M. A. G. Oliveira, "Photovoltaic Generation Penetration Limits in Radial Distribution Systems," IEEE Transactions on Power Systems, vol. 26, no. 3, pp. 1625-1631, August 2011.

[19] http://en.wikipedia.org/wiki/Electricity_sector_in_India.

[20] http://www.indianmirror.com/indian-industries/2012/power-2012.html.

[21] D. H. Kokate, V. V. Kulkarni, and P. H. Kokate, "An overview of electricity sector and its linkages with social development in India," Indian Streams Research Journal, vol. 3, no. 1, February 2013.

[22] B. Singh and S. N. Singh, "Development of grid connection requirements for wind power generators in India," Renewable and Sustainable Energy Reviews, vol. 15, pp. 1669-1674, 2011.

[23] S. N. Dalvi and M. V. Jadhav, "A Review: Research Opportunities And Challenges In Fuel Cell For India," Indian Streams Research Journal, vol. 2, no. 9, October 2012.

[24] S. Jain, J. Jiang, X. Huang, and S. Stevandic, "Modeling of Fuel-Cell-Based Power Supply System for Grid Interface," IEEE Transactions on Industry Applications, vol. 48, no. 4, pp. 1142-1153, July/August 2012.

[25] A. Kirubakaran, S. Jain, and R. K. Nema, "DSP-Controlled Power Electronic Interface for Fuel-Cell-Based Distributed Generation," IEEE Transactions on Power Electronics, vol. 26, no. 12, pp. 3853-3864, December 2011.

[26] A. Kirubakaran, S. Jain, and R. K. Nema, "A two-stage power electronic interface for fuel cell-based power supply system," International Journal of Power Electronics vol. 3, no. 2, pp. 111-133, 2011.

[27] A. Cruden, T. Houghton, S. Gair, M. Duerr, G. D. Agnew, E. M. Stewart, and A. Lutz, "Fuel cells as distributed generation," in *Proceedings of the Institution of Mechanical Engineers, Part A: Journal of Power and Energy*, 2008, pp. 707-720.

[28] C. Wang, M. H. Nehrir, and H. Gao, "Control of PEM fuel cell distributed generation systems," IEEE Transactions on Energy Conversion, vol. 21, no. 2, pp. 586-595, June 2006.

[29] M. A. R. S. Al-Baghdadi, "A simple mathematical model of performance for proton exchange membrane fuel cells," International Journal of Sustainable Energy, vol. 26, no. 2, pp. 79-90, 2007.

[30] M. H. Nehrir, C. Wang, and S. R. Shaw, "Fuel cells: promising devices for distributed generation," IEEE Power and Energy Magazine, vol. 4, no. 1, pp. 47-53, January/February 2006.

[31] S. Chakraborty, B. Kroposki, and W. Kramer, "Advanced power electronic interfaces for distributed energy systems Part 2: Modeling, development and experimental evaluation of advanced control functions for single-phase utility connected inverter," Technical report NREL/TP-550-44313, November 2008.

[32] S. Pasricha, M. Keppler, S. R. Shaw, and M. H. Nehrir, "Comparison and Identification of Static Electrical Terminal Fuel Cell Models," IEEE Transactions on Energy Conversion, vol. 22, no. 3, pp. 746-754, September 2007.

[33] J. M. Correa, F. A. Farret, L. N. Canha, and M. G. Simoes, "An electrochemical-based fuel-cell model suitable for electrical engineering automation approach," IEEE Transactions on Industrial Electronics, vol. 51, no. 5, pp. 1103-1112, October 2004.

[34] M. Y. El-Sharkh, A. Rahman, M. S. Alam, A. A. Sakla, P. C. Byrne, and T. Thomas, "Analysis of active and reactive power control of a stand-alone PEM fuel cell power plant," IEEE Transactions on Power Systems, vol. 19, no. 4, pp. 2022-2028, November 2004.

[35] P. Gomaton and W. Jewell, "Fuel parameter and quality constraints for fuel cell distributed generators," in *IEEE PES Transmission and Distribution Conference and Exposition* 2003, pp. 409-412

[36] S. V. Puranik, A. Keyhani, and F. Khorrami, "Neural Network Modeling of Proton Exchange Membrane Fuel Cell," IEEE Transactions on Energy Conversion, vol. 25, no. 2, pp. 474-483, June 2010.

[37] J. M. Correa, F. A. Farret, V. A. Popov, and M. G. Simoes, "Sensitivity analysis of the modeling parameters used in Simulation of proton exchange membrane fuel cells," IEEE Transactions on Energy Conversion, vol. 20, no. 1, pp. 211-218, March 2005.

[38] www.intechopen.com.

[39] P. Pany, R. K. Singh, and R. K. Tripathi, "Power management of fuel cell and battery fed DC motor drive for electric vehicle application," in *Proceedings of International Conference on Advances in Engineering, Science and Management*, 2012, pp. 363-368.

[40] J. Jia, G. Wang, Y. T. Cham, Y. Wang, and M. Han, "Electrical Characteristic Study of a Hybrid PEMFC and Ultracapacitor System," IEEE Transactions on Industrial Electronics, vol. 57, no. 6, pp. 1945-1953, June 2010.

[41] X. Yu, M. R. Starke, L. M. Tolbert, and B. Ozpineci, "Fuel cell power conditioning for electric power applications: a summary," IET Electric Power Applications, vol. 1, no. 5, pp. 643-656, 2007.

[42] M. Tanrioven and M. S. Alam, "Modeling, Control, and Power Quality Evaluation of a PEM Fuel Cell-Based Power Supply System for Residential Use," IEEE Transactions on Industry Applications, vol. 42, no. 6, pp. 1582-1589, November/December 2006.

[43] A. Prabha, P. Enjeti, and I. J. Pitel, "An advanced fuel cell simulator," in *Applied Power Electronics Conference and Exposition, 2004. APEC '04. Nineteenth Annual IEEE*, 2004, pp. 1554-1558 Vol.3.

[44] M. Soltani and S. M. T. Bathaee, "A new dynamic model considering effects of temperature, pressure and internal resistance for PEM fuel cell power modules," in *Proceedings of Third International Conference on Electric Utility Deregulation and Restructuring and Power Technologies*, 2008, pp. 2757-2762.

[45] W. Caisheng, M. H. Nehrir, and S. Shaw, "Dynamic models and model validation for PEM fuel cells using electrical circuits," in *Power Engineering Society General Meeting, 2005. IEEE*, 2005, p. 2115 Vol. 3.

[46] G. Fontes, C. Turpin, and S. Astier, "A Large-Signal and Dynamic Circuit Model of a PEM Fuel Cell: Description, Parameter Identification, and Exploitation," IEEE Transactions on Industrial Electronics, vol. 57, no. 6, pp. 1874-1881, June 2010.

[47] A. J. D. Real, A. Arce, and C. Bordons, "Development and experimental validation of a PEM fuel cell dynamic model," Journal of Power Sources, vol. 173, pp. 310-324, 2007.

[48] N. M. Souleman, O. Tremblay, and L. A. Dessaint, "A generic fuel cell model for the simulation of Fuel Cell Power Systems," in *IEEE Power & Energy Society General Meeting*, 2009, pp. 1-8.

[49] A. Prabha, E. Prasad, and I. J. Pitel, "An advanced fuel cell simulator," in *in Proceedings of Applied Power Electronics Conference and Exposition*, 2004, pp. 1554-1558.

[50] C. Wang, M. H. Nehrir, and S. R. Shaw, "Dynamic Models and Model Validation for PEM Fuel Cells Using Electrical Circuits," IEEE Transactions on Energy Conversion, vol. 20, no. 2, pp. 442-451, June 2005.

[51] K. Sedghisigarchi and A. Feliachi, "Dynamic and transient analysis of power distribution systems with fuel cells-part I: fuel-cell dynamic model," IEEE Transactions on Energy Conversion, vol. 19, no. 2, pp. 423-428, June 2004.

[52] J. M. Carrasco, L. G. Franquelo, J. T. Bialasiewicz, E. Galvan, R. C. P. Guisado, M. A. M. Prats, J. I. Leon, and N. Moreno-Alfonso, "Power-Electronic Systems for the Grid Integration of Renewable Energy Sources: A Survey," IEEE Transactions on Industrial Electronics, vol. 53, no. 4, pp. 1002-1016, August 2006.

[53] X. Huang, Z. Zhang, and J. Jiang, "Fuel Cell Technology for Distributed Generation: An Overview," in *Proceedings of IEEE International Symposium on Industrial Electronics*, 2006, pp. 1613-1618.

[54] J. Wang, F. Z. Peng, J. Anderson, A. Joseph, and R. Buffenbarger, "Low cost fuel cell converter system for residential power generation," IEEE Transactions on Power Electronics, vol. 19, no. 5, pp. 1315-1322, September 2004.

[55] C. J. Hatziadoniu, A. A. Lobo, F. Pourboghrat, and M. Daneshdoost, "A simplified dynamic model of grid-connected fuel-cell generators," IEEE Transactions on Power Delivery, vol. 17, no. 2, pp. 467-473, April 2002.

[56] K. Sedghisigarchi and A. Feliachi, "Dynamic and transient analysis of power distribution systems with fuel cells-part II: control and stability enhancement," IEEE Transactions on Energy Conversion, vol. 19, no. 2, pp. 429-434, June 2004.

[57] M. Dai, M. N. Marwali, J.-W. Jung, and A. Keyhani, "Power Flow Control of a Single Distributed Generation Unit," IEEE Transactions on Power Electronics, vol. 23, no. 1, pp. 343-352, January 2008.

[58] S.-Y. Park, C.-L. Chen, and J.-S. J. Lai, "A Wide-Range Active and Reactive Power Flow Controller for a Solid Oxide Fuel Cell Power Conditioning System," IEEE Transactions on Power Electronics, vol. 23, no. 6, pp. 2703-2709, November 2008.

[59] J. T. Bialasiewicz, "Renewable Energy Systems With Photovoltaic Power Generators: Operation and Modeling," IEEE Transactions on Industrial Electronics, vol. 55, no. 7, pp. 2752-2758, July 2008.

[60] H. Patel and V. Agarwal, "Investigations into the performance of photovoltaics-based active filter configurations and their control schemes under uniform and non-uniform radiation conditions," IET Renewable Power Generation vol. 4, no. 1, pp. 12-22, 2010.

[61] C. Hua, J. Lin, and C. Shen, "Implementation of a DSP-controlled photovoltaic system with peak power tracking," IEEE Transactions on Industrial Electronics, vol. 45, no. 1, pp. 99-107, February 1998.

[62] N. A. Rahim and J. Selvaraj, "Multistring Five-Level Inverter With Novel PWM Control Scheme for PV Application," IEEE Transactions on Industrial Electronics, vol. 57, no. 6, pp. 2111-2123, June 2010.

[63] M. H. Rashid, "Power Electronics Handbook," Academic Press, 2001.

[64] G. Esmaili, "Application of advanced power electronics in renewable energy sources and hybrid generating systems," Ph. D. Dissertation, The Ohio State University 2006.

[65] www.sunelco.com.

[66] M. Milosevic, "On the Control of Distributed Generation in Power Systems," Ph. D. Dissertation, Swiss Federal Institute of Technology, Zurich, 2007.

[67] M. G. Villalva, J. R. Gazoli, and E. R. Filho, "Comprehensive Approach to Modeling and Simulation of Photovoltaic Arrays," IEEE Transactions on Power Electronics, vol. 24, no. 5, pp. 1198-1208, 2009.

[68] A. Yazdani, A. R. D. Fazio, H. Ghoddami, M. Russo, M. Kazerani, J. Jatskevich, K. Strunz, S. Leva, and J. A. Martinez, "Modeling Guidelines and a Benchmark for Power System Simulation Studies of Three-Phase Single-Stage Photovoltaic Systems," IEEE Transactions on Power Delivery, vol. 26, no. 2, pp. 1247-1264, April 2011.

[69] W. Xiao, W. G. Dunford, P. R. Palmer, and A. Capel, "Regulation of Photovoltaic Voltage," IEEE Transactions on Industrial Electronics, vol. 54, no. 3, pp. 1365-1374, June 2007.

[70] D. S. H. Chan and J. C. H. Phang, "Analytical methods for the extraction of solar-cell single- and double-diode model parameters from I-V characteristics," Electron Devices, IEEE Transactions on, vol. 34, no. 2, pp. 286-293, 1987.

[71] J. A. Gow and C. D. Manning, "Development of a photovoltaic array model for use in power-electronics simulation studies," IEE Proceedings - Electric Power Applications, vol. 146, no. 2, pp. 193-200, March 1999.

[72] Y. J. Wang and P. C. Hsu, "Modelling of solar cells and modules using piecewise linear parallel branches," Renewable Power Generation, IET, vol. 5, no. 3, pp. 215-222, 2011.

[73] K. Nishioka, N. Sakitani, Y. Uraoka, and T. Fuyuki, "Analysis of multicrystalline silicon solar cells by modified 3-diode equivalent circuit model taking leakage current through periphery into consideration," Solar Energy Materials and Solar Cells, vol. 91, pp. 1222-1227, 2007.

[74] C. Carrero, J. Amador, and S. Arnaltes, "A single procedure for helping PV designers to select silicon PV modules and evaluate the loss resistances," Renewable Energy, vol. 32, no. 15, pp. 2579-2589, 2007.

[75] S.-K. Kim, J.-H. Jeon, C.-H. Cho, E.-S. Kim, and J.-B. Ahn, "Modeling and simulation of a grid-connected PV generation system for electromagnetic transient analysis," Solar Energy, vol. 83, pp. 664-678, 2009.

[76] M. Cacciato, A. Consoli, R. Attanasio, and F. Gennaro, "Soft-Switching Converter With HF Transformer for Grid-Connected Photovoltaic Systems," IEEE Transactions on Industrial Electronics, vol. 57, no. 5, pp. 1678-1686, May 2010.

[77] Y.-C. Kuo, T.-J. Liang, and J.-F. Chen, "Novel maximum-power-point-tracking controller for photovoltaic energy conversion system," IEEE Transactions on Industrial Electronics, vol. 48, no. 3, pp. 594-601, June 2001.

[78] W. Xiao, N. Ozog, and W. G. Dunford, "Topology Study of Photovoltaic Interface for Maximum Power Point Tracking," IEEE Transactions on Industrial Electronics, vol. 54, no. 3, pp. 1696-1704, June 2007.

[79] *M. Veerachary, T. Senjyu, and K. Uezato, "Neural-network-based maximum-power-point tracking of coupled-inductor interleaved-boost-converter-supplied PV system using fuzzy*

controller," IEEE Transactions on Industrial Electronics, vol. 50, no. 4, pp. 749-758, August 2003.

[80] M. C. Cavalcanti, G. M. S. Azevedo, B. A. Amaral, and F. A. S. Neves, "Unified Power Quality Conditioner in a Grid Connected Photovoltaic System," Electric Power Quality and Utilisation Journal, vol. 12, no. 2, pp. 59-69, 2006.

[81] S. B. Kjaer, J. K. Pedersen, and F. Blaabjerg, "A review of single-phase grid-connected inverters for photovoltaic modules," IEEE Transactions on Industry Applications, vol. 41, no. 5, pp. 1292-1306, September/October 2005.

[82] E. Roman, R. Alonso, P. Ibanez, S. Elorduizapatarietxe, and D. Goitia, "Intelligent PV Module for Grid-Connected PV Systems," IEEE Transactions on Industrial Electronics, vol. 53, no. 4, pp. 1066-1073, August 2006.

[83] L. Zhang, K. Sun, Y. Xing, L. Feng, and H. Ge, "A Modular Grid-Connected Photovoltaic Generation System Based on DC Bus," IEEE Transactions on Power Electronics, vol. 26, no. 2, pp. 523-531, February 2011.

[84] T. Esram and P. L. Chapman, "Comparison of Photovoltaic Array Maximum Power Point Tracking Techniques," IEEE Transactions on Energy Conversion, vol. 22, no. 2, pp. 439-449, June 2007.

[85] *D. Sera, L. Mathe, T. Kerekes, S. V. Spataru, and R. Teodorescu, "On the Perturb-and-Observe and Incremental Conductance MPPT Methods for PV Systems," IEEE Journal of Photovoltaics, vol. 3, no. 3, pp. 1070-1078, July 2013.*

[86] D. P. Hohm and M. E. Ropp, "Comparative Study of Maximum Power Point Tracking Algorithms," Progress in Photovoltaics: Research and Applications, vol. 11, pp. 47-62, 2003.

[87] *M. A. G. de Brito, L. Galotto, L. P. Sampaio, G. de Azevedo e Melo, and C. A. Canesin, "Evaluation of the Main MPPT Techniques for Photovoltaic Applications," IEEE Transactions on Industrial Electronics, vol. 60, no. 3, pp. 1156-1167, March 2013.*

[88] N. Femia, G. Petrone, G. Spagnuolo, and M. Vitelli, "Optimization of perturb and observe maximum power point tracking method," IEEE Transactions on Power Electronics, vol. 20, no. 4, pp. 963-973, July 2005.

[89] K. H. Hussein, I. Muta, T. Hoshino, and M. Osakada, "Maximum photovoltaic power tracking: an algorithm for rapidly changing atmospheric conditions," IEE Proceedings - Generation, Transmission and Distribution,, vol. 142, no. 1, pp. 59-64, January 1995.

[90] E. V. Solodovnik, S. Liu, and R. A. Dougal, "Power controller design for maximum power tracking in solar installations," IEEE Transactions on Power Electronics, vol. 19, no. 5, pp. 1295-1304, September 2004.

[91] A. Safari and S. Mekhilef, "Simulation and Hardware Implementation of Incremental Conductance MPPT With Direct Control Method Using Cuk Converter," IEEE Transactions on Industrial Electronics, vol. 58, no. 4, pp. 1154-1161, April 2011.

[92] *M. A. Elgendy, B. Zahawi, and D. J. Atkinson, "Assessment of the Incremental Conductance Maximum Power Point Tracking Algorithm," IEEE Transactions on Sustainable Energy, vol. 4, no. 1, pp. 108-117, January 2013.*

[93] M. A. S. Masoum, H. Dehbonei, and E. F. Fuchs, "Theoretical and experimental analyses of photovoltaic systems with voltage- and current-based maximum power-point tracking," IEEE Transactions on Energy Conversion, vol. 17, no. 4, pp. 514-522, December 2002.

[94] S. Jain and V. Agarwal, "Comparison of the performance of maximum power point tracking schemes applied to single-stage grid-connected photovoltaic systems," IET Renewable Power Generation, vol. 1, no. 5, pp. 753-762, 2007.

[95] D. Casadei, G. Grandi, and C. Rossi, "Single-phase single-stage photovoltaic generation system based on a ripple correlation control maximum power point tracking," IEEE Transactions on Energy Conversion, vol. 21, no. 2, pp. 562-568, June 2006.

[96] W. Libo, Z. Zhengming, and L. Jianzheng, "A Single-Stage Three-Phase Grid-Connected Photovoltaic System With Modified MPPT Method and Reactive Power Compensation," IEEE Transactions on Energy Conversion, vol. 22, no. 4, pp. 881-886, December 2007.

[97] A. Yazdani and P. P. Dash, "A Control Methodology and Characterization of Dynamics for a Photovoltaic (PV) System Interfaced With a Distribution Network," IEEE Transactions on Power Delivery, vol. 24, no. 3, pp. 1538-1551, July 2009.

[98] D. Chanda, N. K. Kishore, and A. K. Sinha, "A wavelet multiresolution analysis for location of faults on transmission lines," International Journal of Electrical Power & Energy Systems, vol. 25, no. 1, pp. 59-69, 2003.

[99] M. E. Ropp and S. Gonzalez, "Development of a MATLAB/Simulink Model of a Single-Phase Grid-Connected Photovoltaic System," IEEE Transactions on Energy Conversion, vol. 24, no. 1, pp. 195-202, March 2009.

[100] F. Blaabjerg, R. Teodorescu, M. Liserre, and A. V. Timbus, "Overview of Control and Grid Synchronization for Distributed Power Generation Systems," IEEE Transactions on Industrial Electronics, vol. 53, no. 5, pp. 1398-1409, October 2006.

[101] C. H. da Silva, R. R. Pereira, L. E. B. da Silva, G. Lambert-Torres, B. K. Bose, and A. Se Un, "A Digital PLL Scheme for Three-Phase System Using Modified Synchronous Reference Frame," IEEE Transactions on Industrial Electronics, vol. 57, no. 11, pp. 3814-3821, 2010.

[102] D. Yazdani, A. Bakhshai, G. Joos, and M. Mojiri, "A Nonlinear Adaptive Synchronization Techniquefor Grid-Connected Distributed Energy Sources," IEEE Transactions on Power Electronics, vol. 23, no. 4, pp. 2181-2186, July 2008.

[103] A. Bhattacharya and C. Chakraborty, "A Shunt Active Power Filter With Enhanced Performance Using ANN-Based Predictive and Adaptive Controllers," IEEE Transactions on Industrial Electronics, vol. 58, no. 2, pp. 421-428, February 2011.

[104] A. Bhattacharya, C. Chakraborty, and S. Bhattacharya, "Shunt compensation reviewing traditional methods of reference current generation," IEEE Industrial Electronics Magazine, vol. 3, no. 3, pp. 38-49, September 2009.

[105] S. Rahmani, N. Mendalek, and K. Al-Haddad, "Experimental Design of a Nonlinear Control Technique for Three-Phase Shunt Active Power Filter," IEEE Transactions on Industrial Electronics, vol. 57, no. 10, pp. 4231-4231, October 2010.

[106] B. Singh and V. Verma, "An indirect current control of hybrid power filter for varying loads," IEEE Transactions on Power Delivery, vol. 21, no. 1, pp. 178-184, January 2006.

[107] L. H. Tey, P. L. So, and Y. C. Chu, "Improvement of power quality using adaptive shunt active filter," IEEE Transactions on Power Delivery, vol. 20, no. 2, pp. 1558-1568, April 2005.

[108] D. Yazdani, A. Bakhshai, G. Joos, and M. Mojiri, "A Real-Time Extraction of Harmonic and Reactive Current in a Nonlinear Load for Grid-Connected Converters," IEEE Transactions on Industrial Electronics vol. 56, no. 6, pp. 2185-2189, June 2009.

[109] S. Rahmani, A. Hamadi, N. Mendalek, and K. Al-Haddad, "A New Control Technique for Three-Phase Shunt Hybrid Power Filter," IEEE Transactions on Industrial Electronics, vol. 56, no. 8, pp. 2904-2915, August 2009.

[110] S. K. Jain, P. Agarwal, and H. O. Gupta, "A control algorithm for compensation of customer-generated harmonics and reactive power," IEEE Transactions on Power Delivery, vol. 19, no. 1, pp. 357-366, January 2004.

[111] S. Kim and P. N. Enjeti, "A new hybrid active power filter (APF) topology," IEEE Transactions on Power Electronics, vol. 17, no. 1, pp. 48-54, January 2002.

[112] B. Singh, K. Al-Haddad, and A. Chandra, "A review of active filters for power quality improvement," IEEE Transactions on Industrial Electronics, vol. 46, no. 5, pp. 960-971, October 1999.

[113] S. George and V. Agarwal, "A DSP Based Optimal Algorithm for Shunt Active Filter Under Nonsinusoidal Supply and Unbalanced Load Conditions," IEEE Transactions on Power Electronics, vol. 22, no. 2, pp. 593-601, March 2007.

[114] V. Khadkikar, A. Chandra, and B. N. Singh, "Generalised single-phase p-q theory for active power filtering: simulation and DSP-based experimental investigation," IET Power Electronics, vol. 2, no. 1, pp. 67-78, 2009.

[115] N. Gupta, S. P. Singh, and R. C. Bansal, "A Digital Signal Processor Based Performance Evaluation of Three-phase Four-wire Shunt Active Filter for Harmonic Elimination, Reactive Power Compensation, and Balancing of Non-linear Loads under Non-ideal Mains Voltages," Electric Power Components and Systems, vol. 40, no. 10, pp. 1119-1148, 2012.

[116] K. M. Tsang and W. L. Chan, "Design of single-phase active power filter using analogue cascade controller," IEE Proceedings - Electric Power Applications, vol. 153, no. 5, pp. 735-741, September 2006.

[117] C. Qiao, K. M. Smedley, and F. Maddaleno, "A single-phase active power filter with one-cycle control under unipolar operation," IEEE Transactions on Circuits and Systems-I: Regular Papers, vol. 51, no. 8, pp. 1623-1630, August 2004.

[118] B. N. Singh, B. Singh, A. Chandra, and K. Al-Haddad, "Design and digital implementation of active filter with power balance theory," IEE Proceedings - Electric Power Applications, vol. 152, no. 5, pp. 1149-1160, September 2005.

[119] P. Kumar and A. Mahajan, "Soft Computing Techniques for the Control of an Active Power Filter," IEEE Transactions on Power Delivery, vol. 24, no. 1, pp. 452-461, January 2009.

[120] R. I. Bojoi, L. R. Limongi, D. Roiu, and A. Tenconi, "Enhanced Power Quality Control Strategy for Single-Phase Inverters in Distributed Generation Systems," IEEE Transactions on Power Electronics, vol. 26, no. 3, pp. 798-806, March 2011.

[121] H. Li, F. Zhuo, Z. Wang, W. Lei, and L. Wu, "A novel time-domain current-detection algorithm for shunt active power filters," IEEE Transactions on Power Systems, vol. 20, no. 2, pp. 644-651, May 2005.

[122] G. W. Chang and T.-C. Shee, "A novel reference compensation current strategy for shunt active power filter control," Power Delivery, IEEE Transactions on, vol. 19, no. 4, pp. 1751-1758, October 2004.

[123] G. W. Chang, C.-M. Yeh, and W.-C. Chen, "Meeting IEEE-519 current harmonics and power factor constraints with a three-phase three-wire active power filter under distorted source voltages," IEEE Transactions on Power Delivery, vol. 21, no. 3, pp. 1648-1654, July 2006.

[124] M. Kale and E. Özdemir, "Harmonic and reactive power compensation with shunt active power filter under non-ideal mains voltage," Electric Power Systems Research, vol. 74, pp. 363-370, 2005.

[125] M. Cirrincione, M. Pucci, and G. Vitale, "A Single-Phase DG Generation Unit With Shunt Active Power Filter Capability by Adaptive Neural Filtering," IEEE Transactions on Industrial Electronics, vol. 55, no. 5, pp. 2093-2110, May 2008.

[126] T.-F. Wu, H.-S. Nien, C.-L. Shen, and T.-M. Chen, "A single-phase inverter system for PV power injection and active power filtering with nonlinear inductor consideration," IEEE Transactions on Industry Applications, vol. 41, no. 4, pp. 1075-1083, July/August 2005.

[127] R. A. Mastromauro, M. Liserre, T. Kerekes, and A. Dell'Aquila, "A Single-Phase Voltage-Controlled Grid-Connected Photovoltaic System With Power Quality Conditioner Functionality," IEEE Transactions on Industrial Electronics, vol. 56, no. 11, pp. 4436-4444, November 2009.

[128] N. Sung, J. Lee, B. Kim, M. Park, and I. Yu, "Novel concept of a PV power generation system adding the function of shunt active filter," in *IEEE/PES Transmission and Distribution Conference and Exhibition, Asia Pacific.*, 2002, pp. 1658-1663.

[129] M. F. Schonardie and D. C. Martins, "Three-phase grid-connected photovoltaic system with active and reactive power control using dq0 transformation," in *IEEE Power Electronics Specialists Conference, 2008*, 2008, pp. 1202-1207.

[130] C. J. Gajanayake, D. M. Vilathgamuwa, P. C. Loh, R. Teodorescu, and F. Blaabjerg, "Z-Source-Inverter-Based Flexible Distributed Generation System Solution for Grid Power Quality Improvement," IEEE Transactions on Energy Conversion, vol. 24, no. 3, pp. 695-704, September 2009.

[131] H. Tao, J. L. Duarte, and M. A. M. Hendrix, "Line-Interactive UPS Using a Fuel Cell as the Primary Source," IEEE Transactions on Industrial Electronics, vol. 55, no. 8, pp. 3012-3021, August 2008.

[132] M. Park, H.-R. Seo, D.-H. Lee, and I.-K. Yu, "Characteristics analysis of a PV-AF-SPE system under several irradiation conditions," Renewable Energy, vol. 34, pp. 499-503, 2009.

[133] R. K. Varma, V. Khadkikar, and R. Seethapathy, "Nighttime Application of PV Solar Farm as STATCOM to Regulate Grid Voltage," IEEE Transactions on Energy Conversion, vol. 24, no. 4, pp. 983-985, December 2009.

[134] R. C. Bansal, "Automatic Reactive-Power Control of Isolated Wind - Diesel Hybrid Power Systems," IEEE Transactions on Industrial Electronics, vol. 53, no. 4, pp. 1116-1126, August 2006.

[135] R. T. Jagaduri and G. Radman, "Modeling and control of distributed generation systems including PEM fuel cell and gas turbine," Electric Power Systems Research, vol. 77, pp. 83-92, 2007.

[136] A. Hajizadeh and M. A. Golkar, "Fuzzy neural control of a hybrid fuel cell/battery distributed power generation system," IET Renewable Power Generation, vol. 3, no. 4, pp. 402-414, 2009.

[137] S. Rahman and K. S. Tam, "A feasibility study of photovoltaic-fuel cell hybrid energy system," IEEE Transactions on Energy Conversion, vol. 3, no. 1, pp. 50-55, March 1988.

[138] K.-S. Tam and S. Rahman, "System performance improvement provided by a power conditioning subsystem for central station photovoltaic-fuel cell power plant," IEEE Transactions on Energy Conversion, vol. 3, no. 1, pp. 64-70, March 1988.

[139] K. Ro and S. Rahman, "Two-loop controller for maximizing performance of a grid-connected photovoltaic-fuel cell hybrid power plant," IEEE Transactions on Energy Conversion, vol. 13, no. 3, pp. 276-281, September 1998.

[140] K. N. Reddy and V. Agarwal, "Utility-Interactive Hybrid Distributed Generation Scheme With Compensation Feature," IEEE Transactions on Energy Conversion, vol. 22, no. 3, pp. 666-673, September 2007.

[141] L. N. Khanh, S. J.-J., K. Y.-S., and D.-J. Won, "Power-Management Strategies for a Grid-Connected PV-FC Hybrid System," IEEE Transactions on Power Delivery, vol. 25, no. 3, pp. 1874-1882, July 2010.

[142] F. Shahnia, R. Majumder, A. Ghosh, G. Ledwich, and F. Zare, "Operation and control of a hybrid microgrid containing unbalanced and nonlinear loads," Electric Power Systems Research, vol. 80, pp. 954-965, 2010.

[143] S. Jain and V. Agarwal, "An Integrated Hybrid Power Supply for Distributed Generation Applications Fed by Nonconventional Energy Sources," IEEE Transactions on Energy Conversion, vol. 23, no. 2, pp. 622-631, June 2008.

[144] G. Mehta and S. P. Singh, "Modelling, analysis and design of Fuel Cell based distributed generation system with active and reactive power flow control," International Review on Modelling and Simulations vol. 5, no. 4, pp. 1750-1757, August 2012.

[145] S. Puranik, "Control of Fuel Cell based green energy systems for distributed generation applications," Ph. D. Dissertation, The Ohio State University, 2009.

[146] G. Mehta, S. P. Singh, and R. D. Patidar, "Non-linear load compensation in Fuel Cell grid interfaced system using active power filter," in proceedings of IEEE International Conference on Power Electronics and Drive Systems, Singapore, pp. 197-202, December 2011.

[147] S. V. Puranik, A. Keyhani, and F. Khorrami, "State-Space Modeling of Proton Exchange Membrane Fuel Cell," IEEE Transactions on Energy Conversion, vol. 25, no. 3, pp. 804-813, September 2010.

[148] J. Kim, I. Lee, Y. Tak, and B. H. CHo, "State-of-health diagnosis based on hamming neural network using output voltage pattern recognition for a PEM fuel cell," International Journal of Hydrogen Energy, vol. 37, no. 5, pp. 4280-4289, March 2012.

[149] IEEE Std. 519-1992, “IEEE Recommended Practices and Requirements for Harmonic Control in Power System”, 1993.

[150] M. Prodanovic and T. C. Green, "Control and filter design of three-phase inverters for high power quality grid connection," IEEE Transactions on Power Electronics, vol. 18, no. 1, pp. 373-380, January 2003.

[151] T.-I. Choi and K. Y. Lee, "Interface of a fuel cell distributed generator with distribution system network," in *IEEE Power & Energy Society General Meeting*, 2009, pp. 1-8.

[152] G. Mehta, R. D. Patidar, and S. P. Singh, "Design, Analysis and Implementation of DSP based single-phase Shunt Active Filter Controller," in proceedings of IEEE International Conference on Emerging Trends in Electrical and Computer Technology, ICETECT-2011, vol. Kanyakumari, India, pp. 166-173, 2011.

[153] R. D. Patidar, "Modeling, Control and Application of Active Power Filters to Improve Power Quality " Ph. D. Thesis, Indian Institute of Technology, Roorkee, India, 2010.

[154] A. Chandra, B. Singh, B. N. Singh, and K. Al-Haddad, "An improved control algorithm of shunt active filter for voltage regulation, harmonic elimination, power-factor correction, and balancing of nonlinear loads," IEEE Transactions on Power Electronics, vol. 15, no. 3, pp. 495-507, May 2000.

[155] R. D. Patidar and S. P. Singh, "Digital Signal Processor Based Shunt Active Filter Controller for Customer-generated Harmonics and Reactive Power Compensation," Electric Power Components and Systems, vol. 38, no. 8, pp. 937-959, 2010.

[156] W. Xu and Y. Liu, "A method for determining customer and utility harmonic contributions at the point of common coupling," IEEE Transactions on Power Delivery, vol. 15, no. 2, pp. 804-811, April 2000.

[157] B. Singh, K. Al-Haddad, and A. Chandra, "A new control approach to three-phase active filter for harmonics and reactive power compensation," IEEE Transactions on Power Systems, vol. 13, no. 1, pp. 133-138, February 1998.

[158] L. P. Kunjumuhammed and M. K. Mishra, "A control algorithm for single-phase active power filter under non-stiff voltage source," IEEE Transactions on Power Electronics, vol. 21, no. 3, pp. 822-825, May 2006.

[159] A. Chaoui, J. P. Gaubert, F. Krim, and G. Champenois, "PI Controlled Three-phase Shunt Active Power Filter for Power Quality Improvement," Electric Power Components and Systems, vol. 35, no. 12, pp. 1331-1344, 2007.

[160] J. F. Petit, G. Robles, and H. Amaris, "Current Reference Control for Shunt Active Power Filters Under Nonsinusoidal Voltage Conditions," IEEE Transactions on Power Delivery, vol. 22, no. 4, pp. 2254-2261, October 2007.

[161] J. H. R. Enslin and P. J. M. Heskes, "Harmonic interaction between a large number of distributed power inverters and the distribution network," IEEE Transactions on Power Electronics, vol. 19, no. 6, pp. 1586-1593, November 2004.

[162] J. P. Pinto, R. Pregitzer, L. F. C. Monteiro, and J. L. Afonso, "3-phase 4-wire shunt active power filter with renewable energy interface," IEEE Renewable Energy and Power Quality Conference, Spain, 2007.

[163] T.-F. Wu, H.-S. Nien, H.-M. Hsieh, and C.-L. Shen, "PV Power Injection and Active Power Filtering With Amplitude-Clamping and Amplitude-Scaling Algorithms," IEEE Transactions on Industry Applications, vol. 43, no. 3, pp. 731-741, May/June 2007.

[164] G. Mehta, S. P. Singh, and R. D. Patidar, "Fuel Cell based Distributed Generation System with Power Flow and Power Quality Control," International Journal of Power and Energy Conversion, vol. 4, no. 1, pp. 73-94, 2013.

[165] M. P. Kazmierkowski and L. Malesani, "Current control techniques for three-phase voltage-source PWM converters: a survey," IEEE Transactions on Industrial Electronics, vol. 45, no. 5, pp. 691-703, October 1998.

[166] G. Mehta and S. P. Singh, "Power quality improvement through grid integration of renewable energy sources," IETE Journal of Research, vol. 59, no. 3, pp. 210-218, 2013.

[167] R. D. Patidar and S. P. Singh, "Active and Reactive Power Control and Quality Management in DG-grid interfaced systems," Journal of Engineering and Applied Sciences, vol. 4, no. 3, pp. 81-90, May 2009.

[168] G. Mehta and S. P. Singh, "Design and Analysis of Photovoltaic-Fuel Cell Hybrid Distributed Generation System," in proceedings of 39th IEEE Photovoltaic Specialists Conference, Florida, USA, 2013.

[169] B. Yang, W. Li, Y. Zhao, and X. He, "Design and Analysis of a Grid-Connected Photovoltaic Power System," IEEE Transactions on Power Electronics, vol. 25, no. 4, pp. 992-1000, April 2010.

[170] G. Grandi, C. Rossi, D. Ostojic, and D. Casadei, "A New Multilevel Conversion Structure for Grid-Connected PV Applications," IEEE Transactions on Industrial Electronics, vol. 56, no. 11, pp. 4416-4426, November 2009.

[171] Y.-C. Kuo, T.-J. Liang, and J.-F. Chen, "A high-efficiency single-phase three-wire photovoltaic energy conversion system," IEEE Transactions on Industrial Electronics, vol. 50, no. 1, pp. 116-122, February 2003.

[172] T.-F. Wu, C.-H. Chang, L.-C. Lin, and Kuo C.-L., "Power Loss Comparison of Single- and Two-Stage Grid-Connected Photovoltaic Systems," IEEE Transactions on Energy Conversion, vol. 26, no. 2, pp. 707-715, June 2011.

[173] C. Wang, "Modeling and Control of Hybrid Wind/Photovoltaic/Fuel Cell Distributed Generation Systems," Ph. D. Dissertation, Montana State University, Bozeman, Montana, 2006, 2006.

[174] "eZdsp™ F2812 Technical Reference, Spectrum Digital, Inc.," http://c2000.spectrumdigital.com/ezf2812/docs/ezf2812_techref.pdf.

[175] P. Molin, "Evaluation of a DSP for power electronic applications," Industrial Electrical Engineering and Automation, pp. 1-57, 2008.

Appendix-A

MODELING OF VSI CONNECTED TO THE GRID

A.1 CIRCUIT TOPOLOGY

In a single-stage FC system, the transfer of energy from the FC to the grid is achieved by a DC-AC converter. $Fig. A.1$ shows the circuit of a three-phase PWM VSI connected to AC bus. The VSI is used to convert the power from a DC voltage to three-phase AC output voltages with 120° phase displacement to each other. The VSI has three arms, one for each phase. Each arm has two power electronic switches - the upper and the lower. The output of each phase with respect to the negative point on the DC-side $v_{an'}$ depends on how the switches in arm a are controlled and on the value of the DC voltage. The output obtained is either positive or a zero value. The corresponding output with respect to the neutral point n on the DC bus v_{an} is either positive or negative. Thus the DC is converted to AC [173].

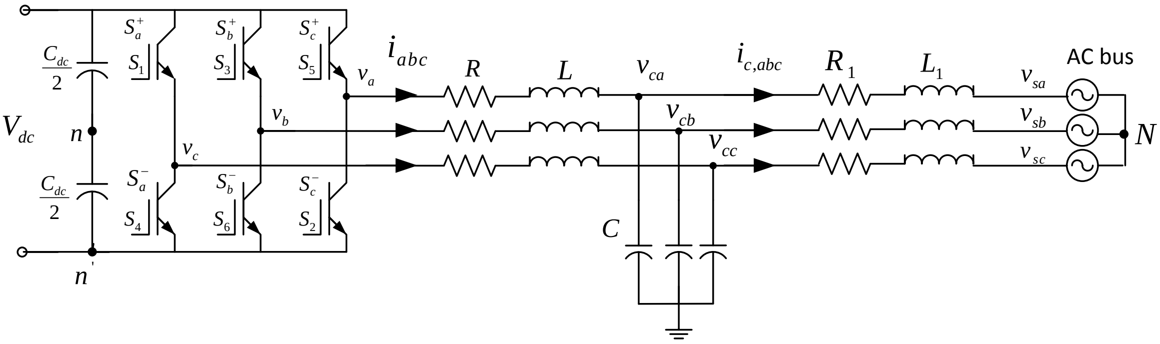

$Fig. A.1$ Three-phase DC-AC voltage source inverter

Sinusoidal pulse-width modulation scheme is one of the modulation schemes used to generate appropriate switching pulses to the six switches of the VSI to control the magnitude, phase angle and frequency of the AC output voltage. In this scheme, three balanced sinusoidal control voltages called carrier signals v_a^c, v_b^c and v_c^c are compared with the same triangular voltage v_{tri} with a switching frequency f_s much higher than the carrier signal frequency f_1. The frequency modulation ratio is defined as $m_f = f_s/f_1$ and the amplitude modulation ratio is defined as $m_a = V^c/V_{tri}$ where V^c is the peak value of the control signal for each phase and V_{tri} is the peak value of the triangular voltage.

For phase a, when the control voltage v_a^c is larger than the triangular signal v_{tri}, the upper switch S_a^+ is on and the lower switch S_a^- is off. Thus the output voltage of phase a with respect to the negative terminal of the DC bus $v_{an'}$ is equal to V_{dc}. Thus, $v_{an'} = V_{dc}$ when $v_a^c > v_{tri}$ and $v_{an'} = 0$

when $v_a^c < v_{tri}$. The output voltages of other two phases are modulated similar to phase a. The switching pulse for S_a^+ has the same wave shape as $v_{an'}$ and the switching pulse for S_a^- is inverse of S_a^+. The DC component and the harmonics of multiples of three of the fundamental frequency are cancelled out in the line to line voltages.

The switching frequency f_s is first determined depending upon the switching properties of the power electronic switches used in the inverter. For linear modulation, the rms value of the line-to-line voltage at fundamental frequency f_1 is :

$$V_{L-L} = \frac{\sqrt{3}}{2\sqrt{2}} m_a V_{dc} \quad (m_a \leq 1) \tag{A.1}$$

Though some harmonics are cancelled out in the line-to-line voltage, the voltage is still pulsating, not sinusoidal. To further reduce the harmonics in the output, an output filter is normally needed.

A.2 STATE-SPACE REPRESENTATION OF THREE-PHASE VSI

Taking the neutral point N as the common potential reference point, defining the following switching functions:

$$\begin{aligned} d_1^* &= \begin{cases} 1 & S_a^+ \ on \\ -1 & S_a^- \ off \end{cases} \\ d_2^* &= \begin{cases} 1 & S_b^+ \ on \\ -1 & S_b^- \ off \end{cases} \\ d_3^* &= \begin{cases} 1 & S_c^+ \ on \\ -1 & S_c^- \ off \end{cases} \end{aligned} \tag{A.2}$$

the inverter output voltages between each phase and its imaginary neutral point n (v_{an}, v_{bn} and v_{cn}) can be expressed as:

$$\begin{aligned} v_{an} &= \frac{d_1^*}{2} V_{dc} \\ v_{bn} &= \frac{d_2^*}{2} V_{dc} \\ v_{cn} &= \frac{d_3^*}{2} V_{dc} \end{aligned} \tag{A.3}$$

where V_{dc} is the DC bus voltage.

The output phase potentials of the inverter v_a, v_b and v_c can be obtained as:

$$\begin{aligned} v_a &= v_{an} + v_n \\ v_b &= v_{bn} + v_n \\ v_c &= v_{cn} + v_n \end{aligned} \tag{A.4}$$

where v_n is the voltage between the point n and the common reference neutral point N. Since $i_a + i_b + i_c = 0$ and $v_{sa} + v_{sb} + v_{sc} = 0$ and $v_a + v_b + v_c = 0$. That is, $v_{an} + v_{bn} + v_{cn} + 3v_n = 0$. Therefore v_n is obtained as:

$$v_n = -\frac{V_{dc}}{6} \sum_{k=1}^{3} d_k^* \tag{A.5}$$

The following dynamic equations is obtained for the circuit shown:

$$R_1 i_{ca} + L_1 \frac{di_{ca}}{dt} = v_{ca} - v_{sa}$$
$$R_1 i_{cb} + L_1 \frac{di_{cb}}{dt} = v_{cb} - v_{sb} \qquad \text{(A.6)}$$
$$R_1 i_{cc} + L_1 \frac{di_{cc}}{dt} = v_{cc} - v_{sc}$$

A.3 IDEAL MODEL OF THREE-PHASE VSI

$Fig. A.2$ shows the ideal model for a three-phase VSI used for long time simulation studies. The load current of the input DC voltage source I_{dc} is determined by the power consumed at the AC-side. The other three input quantities are the desired output AC frequency f, AC voltage amplitude index (similar to the modulation index in a real VSI control) m, and the initial phase of the three-phase AC output voltages $\emptyset_0$.The "abc signal formation" block gives the base signals for the three phases $v_a(t)$, $v_b(t)$ and $v_c(t)$.

$$v_a(t) = m\sin(2\pi f t + \emptyset_0)$$
$$v_b(t) = m\sin(2\pi f t + 2\pi/3 + \emptyset_0) \qquad \text{(A.9)}$$
$$v_c(t) = m\sin(2\pi f t + 4\pi/3 + \emptyset_0)$$

The output voltage values $V_a(t)$, $V_b(t)$ and $V_c(t)$ are calculated by multiplying the base signal values by the possible peak of the output AC, which is 0.5 V_{dc}. For example, $V_a(t) = 0.5\, V_{dc} \times v_a(t)$. Then $V_a(t)$, $V_b(t)$ and $V_c(t)$ are used to control the three controlled voltage sources, which are the AC output voltages of the inverter model. The AC power is calculated as:

$$P_{ac} = I_a(t) \times V_a(t) + I_b(t) \times V_b(t) + I_c(t) \times V_c(t) \qquad \text{(A.10)}$$

The ideal model is capable of simulating a VSI with good accuracy at large time scale.

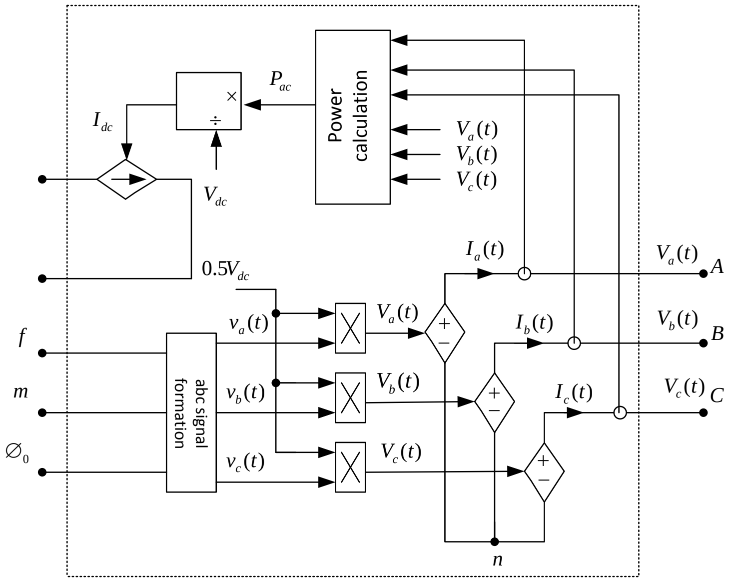

$Fig. A.2$ Ideal model for three-phase VSI

Appendix-B

DESIGN OF APF PARAMETERS

The desired compensation current waveform is obtained by controlling the switching of the IGBTs in the VSI. The switching ripple i_{sw} of the compensation current is determined by the available driving voltage across the interfacing inductor, the size of the interfacing inductor and switching frequency. In the proposed scheme, the driving voltage is the DC-bus voltage V_{dc}. The bipolar DC-bus voltage across the interfacing inductor determines the peak-to-peak switching ripple $\Delta I_{sw,p-p}$ [153].

A controllable voltage source $v_c(t)$ is applied to the interfacing inductor L_c terminal to establish the compensation current $i_c(t)$ as illustrated by $Fig.B.1$.

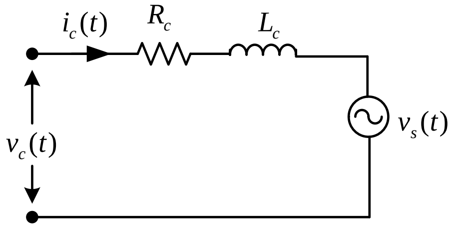

$Fig.B.1$ Equivalent circuit of SAPF

Therefore i_c in the interfacing inductor is determined by v_c, the source voltage v_s, the interfacing inductor resistor R_c and the interfacing inductor L_c, as given by:

$$v_c(t) = v_s(t) + Ri_c(t) + L_c\frac{di_c(t)}{dt} \tag{B.1}$$

The terminal voltage and the compensation current can be expressed in terms of their DC and the switching ripple components as

$$v_c(t) = V_c + v_{sw}(t) \tag{B.2}$$

$$i_c(t) = I_c + i_{sw}(t) \tag{B.3}$$

where $v_{sw}(t)$ and $i_{sw}(t)$ are the ripple components in v_c and i_c respectively. From the above equations:

$$V_c + v_{sw}(t) = v_s + R[I_c + i_{sw}(t)] + L\frac{di_{sw}(t)}{dt} \tag{B.4}$$

where $V_c = RI_c$ and

$$v_{sw}(t) = v_s + Ri_{sw}(t) + L\frac{di_{sw}(t)}{dt} \tag{B.5}$$

We know that the ripple current is high frequency component and primarily determined by the interfacing inductor L. Therefore, v_s and R are assumed to have negligible effects. From above equation:

$$v_{sw}(t) \cong L\frac{di_{sw}(t)}{dt} \tag{B.6}$$

$Fig. B.2$ shows the voltage ripple $v_{sw}(t)$ and the resulting ripple current $i_{sw}(t)$ using the above equation. It is assumed that the voltage ripple $v_{sw}(t)$ is represented by the bipolar DC-bus voltage (V_{dc} or $-V_{dc}$)

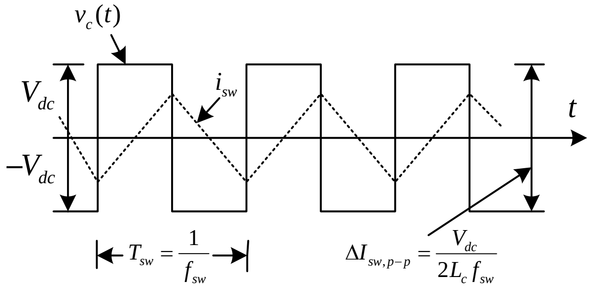

$Fig. B.2$ Switching ripple of the compensation current

From the above equation the peak-to-peak switching ripple can be calculated as:

$$\frac{di_{sw}(t)}{dt} = \frac{v_{sw}(t)}{L} \tag{B.7}$$

$$\Delta I_{sw,p-p} = \frac{1}{L}\int_0^{T_{sw}/2} v_{sw}(t)dt \tag{B.8}$$

$$\Delta I_{sw,p-p} = \frac{V_{dc}T_{sw}}{2L} = \frac{V_{dc}}{2Lf_{sw}} \tag{B.9}$$

From the above equation, the minimum interfacing inductor L_{min} can be derived as:

$$L_{min} = \frac{V_{dc}}{2\Delta I_{sw,p-p} f_{sw,max}} \tag{B.10}$$

where $f_{sw,max}$ is maximum frequency of switching ripple and $\Delta I_{sw,p-p}$ is the peak-to-peak switching ripple of compensation current.

This VSI uses DC-link capacitor as the supply and switches at high-frequency to generate a compensation current that follows the estimated current reference. Thus, the voltage across the DC-bus capacitor V_{dc} must kept to a value that is higher than the amplitude of the source voltage ($> 2V_s$)

The DC-bus capacitor C_{dc} is used as a temporally energy storage element in the proposed SAPF. During steady state condition, the reactive and harmonic load currents will charge and discharge the DC-bus capacitor during the source voltage period. The size determination of the DC-link capacitor is based on the energy balance principle. Using this concept, the following equations can be derived:

$$\frac{1}{2}C_{dc}\left({V_{dc,ref}}^2 - {V_{dc}}^2\right) = \frac{1}{2}\cdot\sqrt{2}V_s \cdot I_c \cdot \frac{T}{2} \tag{B.11}$$

$V_{dc,ref}$ is the DC-bus voltage reference, V_s is the rms value of the source voltage, I_c is the rms value of harmonic and reactive load current (compensating current of APF) and T is the period of source voltage. The size of DC-link capacitor is determined by

$$C_{dc} \geq \frac{\sqrt{2}V_S \cdot I_C \cdot T/2}{{V_{dc,ref}}^2 - {V_{dc}}^2} \tag{B.12}$$

Appendix-C

BOOST CONVERTER WITH CONTROLLER DESIGN

C.1 *CIRCUIT OF A BOOST CONVERTER (Comment [17])*

The circuit diagram of a boost DC-DC converter is shown in $Fig. C.1\,(a)$. $Fig. C.1\,(b)$ shows the steady state inductor voltage and current waveforms for continuous conduction operation mode of the circuit i.e when inductor current flows continuously. With positive switching pulse, switch S_d is on and diode D_d is off. Thus the voltage across the inductor v_{L_d} is same as the input voltage $V_{d,in}$ and the inductor current i_{L_d} increases with a slope $V_{d,in}/L_d$. With negative switching pulse, switch S_d is off and diode D_d is on. Thus the inductor voltage becomes $\left(V_{d,in} - V_{d,out}\right)$ and the inductor current decreases with a slope of $\left(V_{d,out} - V_{d,in}\right)/L_d$. In steady state the average value of inductor current i_{L_d} is constant in one switching period T_s. The inductor voltage can be written as $v_{L_d} = L_d\left(di_{L_d}/dt\right)$. The integral of the inductor voltage v_{L_d} over one switching period is zero in steady state [173]. Hence:

$$V_{d,in}.t_{on} + \left(V_{d,in} - V_{d,out}\right).t_{off} = 0 \tag{C.1}$$

From the above equation, the output voltage V_{out} can be written as

$$V_{d,out} = V_{d,in}/(1 - D) \tag{C.2}$$

Where $D = t_{on}/T_s$ is the duty ratio of the switching pulse.

The values of inductor L_d and capacitor C_d are selected according to the rated voltage, current ripple, voltage ripple and switching frequency of the boost converter.

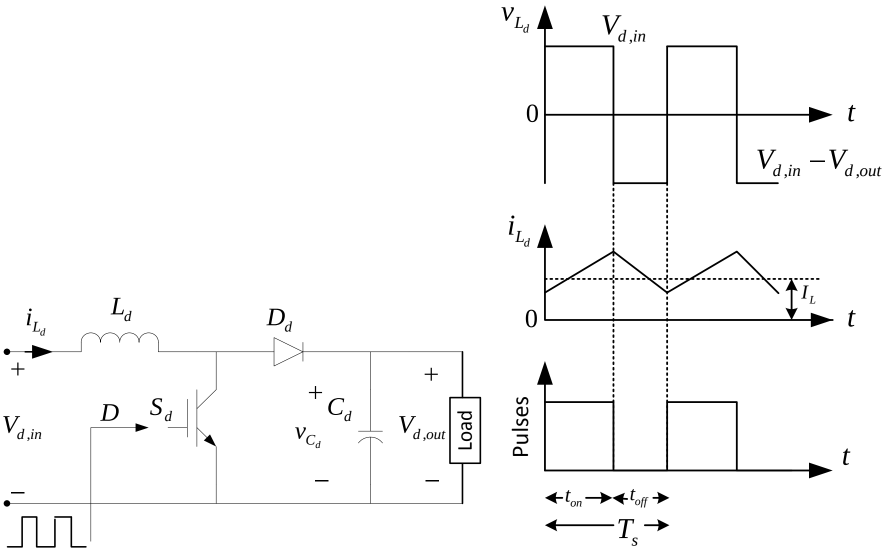

(a) (b)

$Fig. C.1\,(a)$ DC-DC boost converter (b) Inductor current and voltage waveforms in continuous conduction mode

C.2 STATE-SPACE MODEL OF BOOST CONVERTER (Comment [18])

Taking $x_1 = i_{L_d}$ and $x_2 = v_{C_d}$ as state variables. Let $x = X + \tilde{x}$, $d = D + \tilde{d}$, $v_{d,in} = V_{d,in} + \tilde{v}_{d,in}$ and $v_{d,out} = V_{d,out} + \tilde{v}_{d,out}$. The symbol "~" denotes small perturbation signals and state variable X denotes the system operating point.

When switch S_d is on and diode D_d is off, the state-space equation of the circuit can be written as:

$$\dot{x} = A_1 x + B_1 v_{d,in}$$

$$v_{d,out} = C_1^T x \tag{C.3}$$

where $x = [x_1 \quad x_2]^T$, $A_1 = \begin{bmatrix} 0 & 0 \\ 0 & -1/RC_d \end{bmatrix}$, $B_1 = \begin{bmatrix} 1/L_d \\ 0 \end{bmatrix}$ and $C_1^T = [0 \quad 1]$. The symbol "T" represents the transpose operation of matrix.

When switch S_d is off and diode D_d is on, the state-space equation of the circuit can be written as:

$$\dot{x} = A_2 x + B_2 v_{d,in}$$

$$v_{d,out} = C_2^T x \tag{C.4}$$

where, $A_2 = \begin{bmatrix} 0 & -1/L_d \\ 1/C_d & -1/RC_d \end{bmatrix}$, $B_2 = \begin{bmatrix} 1/L_d \\ 0 \end{bmatrix}$ and $C_2^T = [0 \quad 1]$.

Hence, the average state-space model of the circuit at the operating point is:

$$\dot{x} = Ax + Bv_{d,in}$$

$$v_{d,out} = C^T x \tag{C.5}$$

where $A = A_1 d + A_2(1-d) = \begin{bmatrix} 0 & -(1-d)/L_d \\ (1-d)/C_d & -1/RC_d \end{bmatrix}$

$B = B_1 d + B_2(1-d) = \begin{bmatrix} 1/L_d \\ 0 \end{bmatrix}$, $C^T = [C_1 d + C_2(1-d)]^T = [0 \quad 1]$

The small signal model for the DC-DC boost converter can be written as:

$$\dot{\tilde{x}} = A_d \tilde{x} + B_d \tilde{d} + B_v \tilde{v}_{d,in}$$

$$\tilde{v}_{d,out} = C^T \tilde{x} \tag{C.6}$$

where $\tilde{x} = [\tilde{x}_1 \quad \tilde{x}_2]^T$, $A_d = \begin{bmatrix} 0 & -(1-D)/L_d \\ (1-D)/C_d & -1/RC_d \end{bmatrix}$, $B_d = \begin{bmatrix} X_2/L_d \\ -X_1/C_d \end{bmatrix}$ and $B_v = \begin{bmatrix} 1/L_d \\ 0 \end{bmatrix}$

X_1 and X_2 are the steady state values of x_1 and x_2 respectively. Considering only the perturbation of duty ratio $\tilde{d}$ i.e. $\tilde{v}_{d,in} = 0$, the transfer function $T_{vd}(s)$ can be obtained as:

$$T_{vd}(s) = \frac{\tilde{v}_{d,out}(s)}{\tilde{d}(s)} = C^T[sI - A_d]^{-1}B_d = \frac{[-X_1 s/C_d] + [(1-D)X_2/L_d C_d]}{s[s + (1/RC_d)] + [(1-D)^2/L_d C_d]} \tag{C.7}$$

The developed transfer function is used for the controller design.

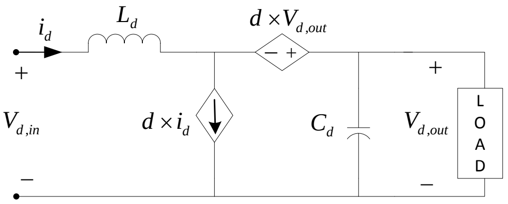

$Fig. C.2$ Average model for DC-DC boost converter

Appendix-D

DETAILS OF EXPERIMENTATION (Comment [5])

A single-phase and three-phase inverter *experimental (Comment [5])* platform is developed to test the control for the utility connected APF inverter. The *experimental (Comment [5])* setup consists of inverter power and control circuits, sinusoidal/non-sinusoidal supply source, DC voltage source, DC-link capacitor, filter inductors, linear/non-linear load bank etc. The integrated power electronic modules with IGBTs are used for the power circuit whereas a DSP-based controller is used to implement the control objectives. The same platform can be extended for integration of the distributed energy into the utility.

D.1 Inverter Power Circuit

In the *experimentation (Comment [5])*, a Semikron make SKAI module was used. The module consists of six 1200V, 45 A IGBTs of type APT25GP120BDF1 arranged in a three-phase bridge format. Three inductors of 2.75 mH are connected to each of the three phases on the inverter AC-side. An electrolytic capacitor of 1600 µF, 1200 V is connected on the DC-side of inverter module. The non-linear load is full bridge diode rectifier module SKB60/08 (Semikron) of 1200V, 25 A.

External current sensors LA-25NP (LEM) are used to sense the AC current signals from the inverter power circuit. LA-25NP provides five selectable current measurement ranges (5/6/8/12/25 A). The supply voltage requirement is ± 15 V.

External voltage sensors LV25-P (LEM) is used to sense the AC voltages and the DC-link voltage. The supply voltage ranges from ± 12V to ± 15V. Both the sensors provide galvanic isolation between the high voltage power circuit and the low voltage control circuit with isolation capability of about 2.5 kV rms at 50 Hz. Further details can be obtained from the attached datasheet.

The signals from the current and voltage sensors are passed through signal conditioner before being applied to ADC of the DSP. The signal conditioner converts these bipolar signals (in the range of ± 1.5 V) into the unipolar signals (in the range of 0-3V) by providing a shift of 1.5 V DC in the AC signals, thus making it compatible with the analog channels of the DSP.

The switching signals obtained from the DSP are not suitable to drive the IGBTs of the inverter. Isolation and amplifier circuit using Photocoupler TLP250 (Toshiba) is used between the DSP output switching signals and the inverter module in order to make the generated switching pulses compatible to the IGBT switches of the VSI.

D.2 Inverter Control Circuit

The inverter control is designed with Spectrum Digital eZdspF2812 [174, 175] evaluation module. This module contains the TMS320F2812 DSP by Texas Instruments. To simplify code development and shorten debugging time a C2000 Tools Code Composer Studio (Texas Instruments) driver is provided with the eZdsp module. The inputs to the control board are voltage and current measurement signals from the external sensors. Thus the instantaneous values of source voltages, DC-bus capacitor voltage, and linear/nonlinear load currents are the inputs to the controller.

D.3 OVERVIEW OF THE eZdspTM F2812

The eZdspTM F2812 is an excellent platform to develop and run software for the TMS320F2812 processor. The eZdspTM F2812 allows full speed verification of F2812 code. To simplify code development and shorten debugging time, a C2000 Tools Code Composer driver is provided. In addition, an onboard JTAG connector provides interface to emulators, operating with other debuggers to provide assembly language and 'C' high level language debug.

D.3.1 Key Features of the eZdspTM F2812

The eZdspTM F2812 has the following features:

- TMS320F2812 Digital Signal Processor
- 150 MIPS operating speed
- 18K words on-chip RAM
- 128K words on-chip Flash memory
- 64K words off-chip SRAM memory
- 30 MHz. clock
- 2 Expansion Connectors (analog, I/O)
- Onboard IEEE 1149.1 JTAG Controller
- 5-volt only operation with supplied AC adapter
- TI F28xx Code Composer Studio tools driver
- On board IEEE 1149.1 JTAG emulation connector

D.3.2 Functional Overview of the eZdspTM F2812

$Fig. D.1$ shows a block diagram of the basic configuration for the eZdspTM F2812. The major interfaces of the eZdsp are the JTAG interface and the expansion interface.

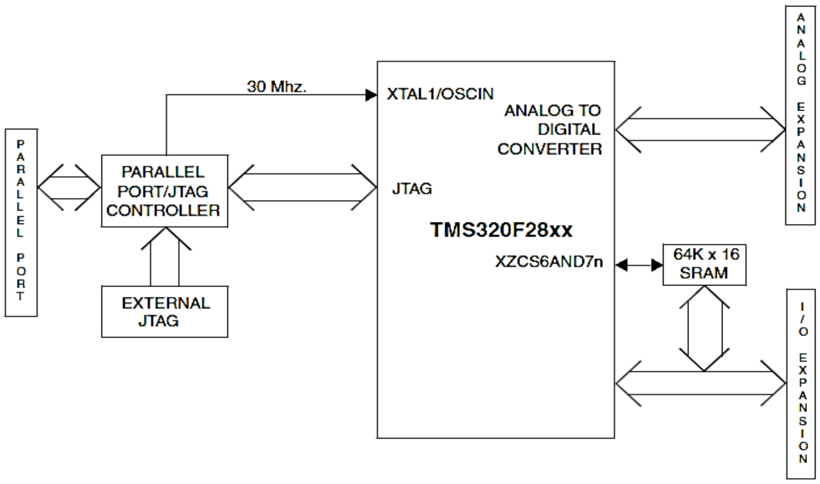

Fig. D. 1 Block diagram of eZdsp$^{\text{TM}}$F2812

The eZdsp$^{\text{TM}}$ F2812 consists of four major blocks of logic:

- Analog Interface Connector
- I/O Interface Connector
- JTAG Interface
- Parallel Port JTAG Controller Interface

The eZdsp$^{\text{TM}}$F2812 is a 5.25 x 3.0 inch, multi-layered printed circuit board, powered by an external 5-Volt only power supply. *Fig. D.* 2 shows the layout of eZdsp$^{\text{TM}}$F2812.

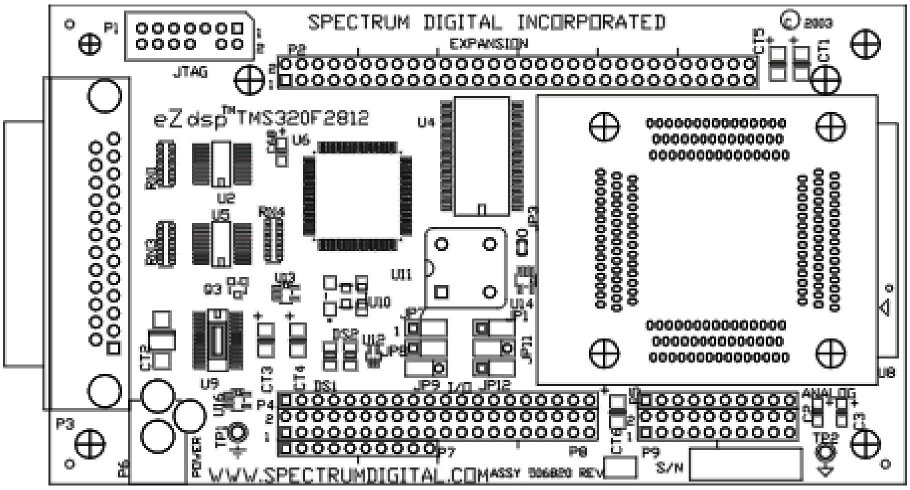

Fig. D. 2 Layout of eZdsp$^{\text{TM}}$F2812 PCB

Appendix-E

PHOTOVOLTAIC MODELING AND MPPT ALGORITHMS

E.1 PHOTOVOLTAIC MODELING

$Fig. E.1\,(a)$ shows the $I-V$ and $Fig. E.1\,(b)$ the $P-V$ curve of the modeled PV device (based on KC200GT module) at STC highlighting the three main points: short circuit $(0, I_{sc,n})$, maximum power point $(V_{mp,n}, I_{mp,n})$ and open circuit $(V_{oc,n}, 0)$.

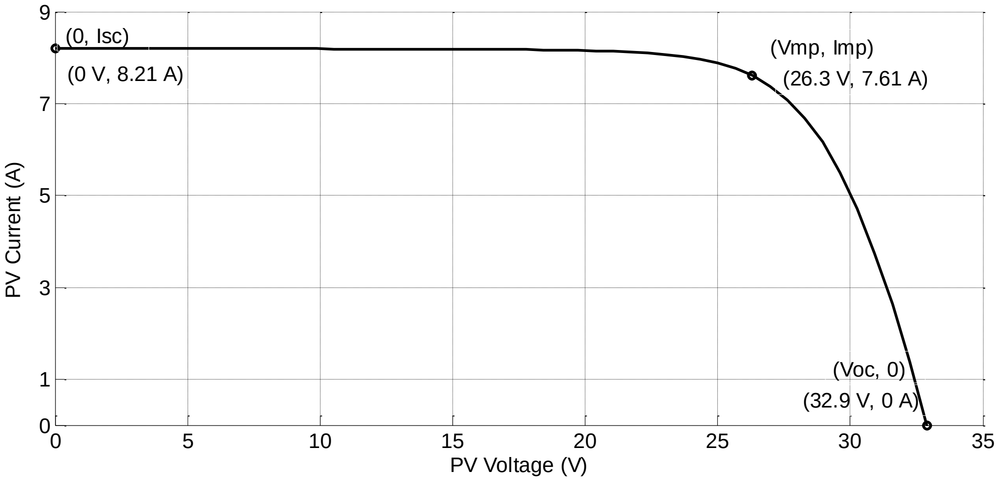

$Fig. E.1\,(a)$ $I-V$ characteristic of PV Module at STC (based on Kyocera KC200GT 200W PV module)

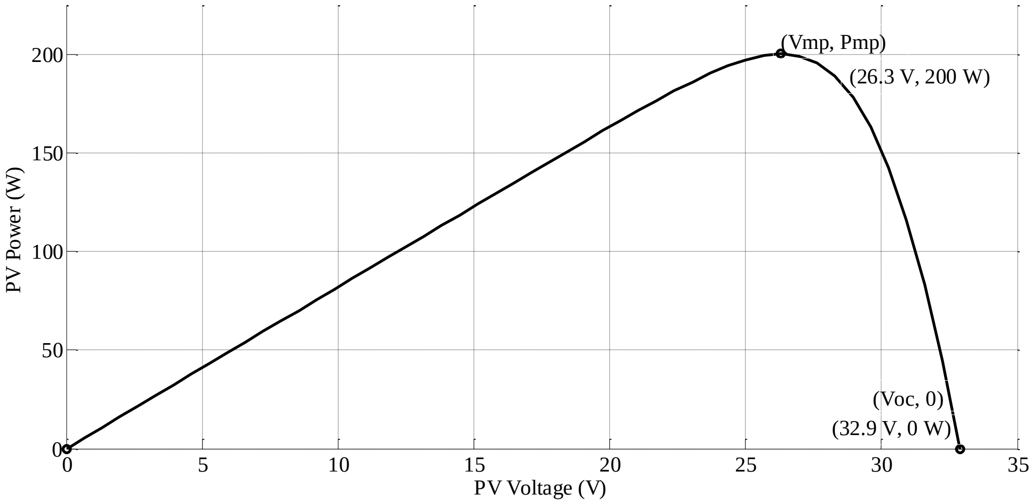

$Fig. E.1\ (b)$ $P-V$ characteristic of PV Module at STC (based on Kyocera KC200GT 200W PV module)

$Fig.E.2\ (a)$ shows the $I-V$ characteristic of PV module at different irradiance levels with constant cell temperature of 25 °C and $Fig.E.2\ (b)$ the $I-V$ characteristic of PV module at different cell temperatures with constant solar irradiation of 1 kW/m^2. $Fig.E.2\ (a)$ shows that the open circuit voltage increases logarithmically with irradiance while the short circuit current is a linear function of the irradiance. $Fig.E.2\ (b)$ shows that with increasing cell temperature there is linear decrease of the open circuit voltage, the cell being thus less efficient. The short circuit current slightly increases with cell temperature.

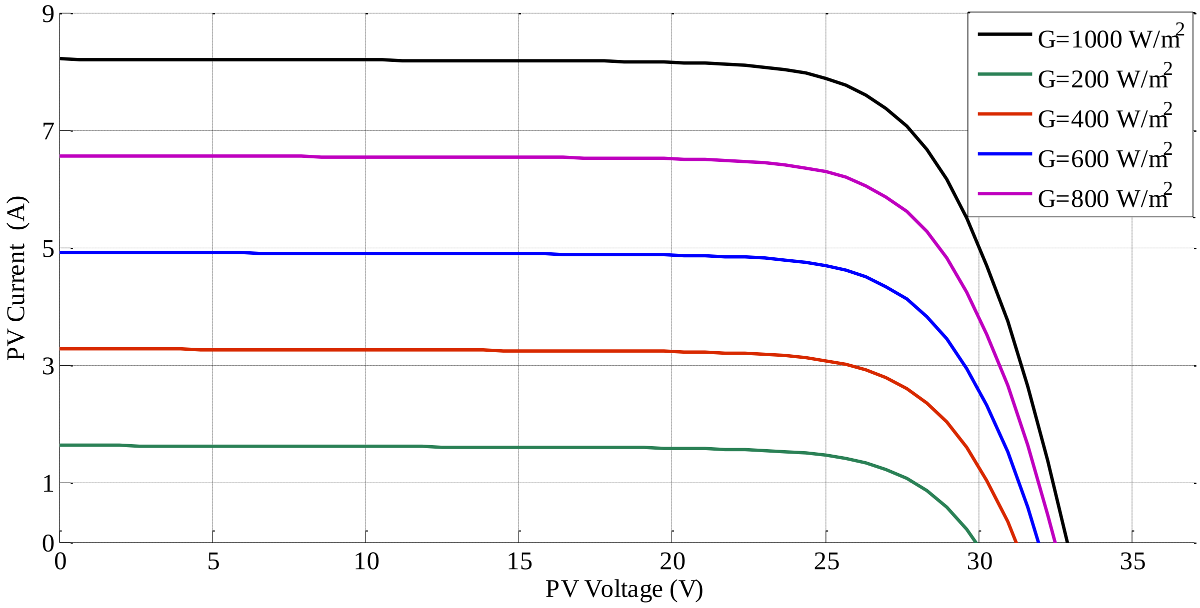

(a)

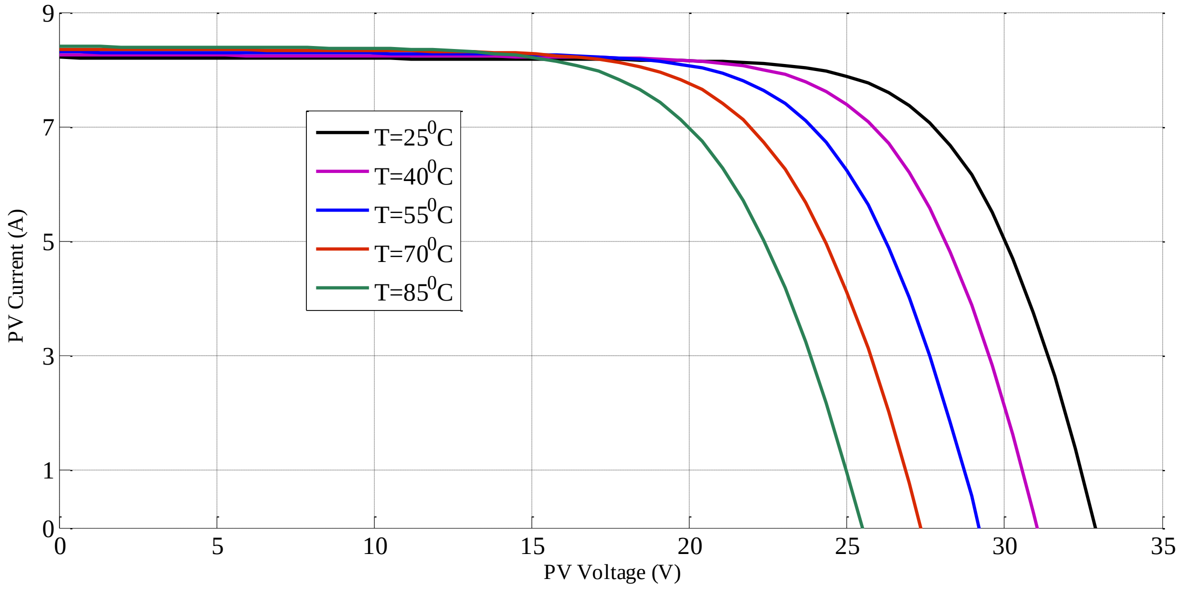

(b)

$Fig.E.2$ $I-V$ characteristic of Photovoltaic Module (based on Kyocera KC200GT PV module) at (a) different irradiance levels G (T = 25°C) (b) different cell temperatures T (G = 1 kW/m^2)

$Fig.E.3$ (a) shows the $P-V$ characteristic of PV module at different irradiance levels with constant cell temperature of 25 °C and $Fig.E.3$ (b) the $P-V$ characteristic of PV module at different cell temperatures with constant solar irradiation of 1 kW/m^2.

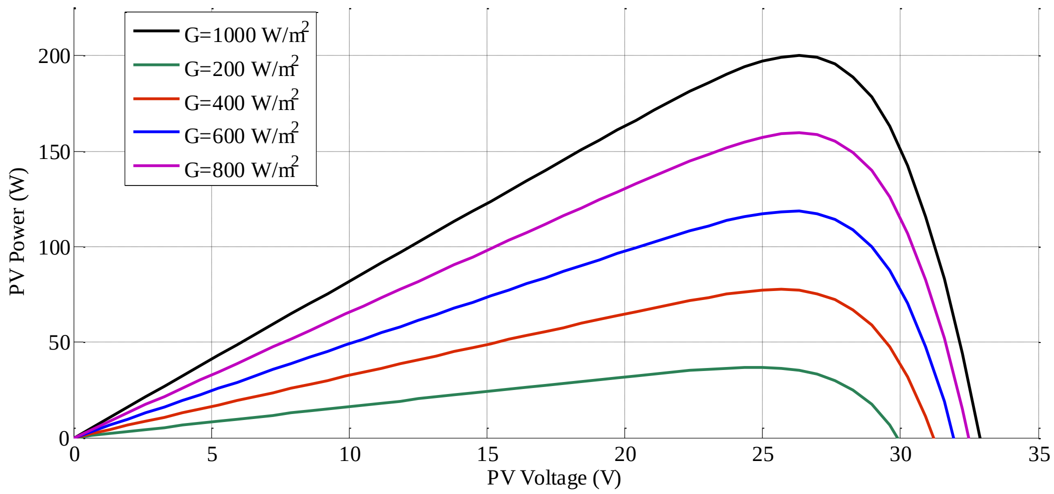

(a)

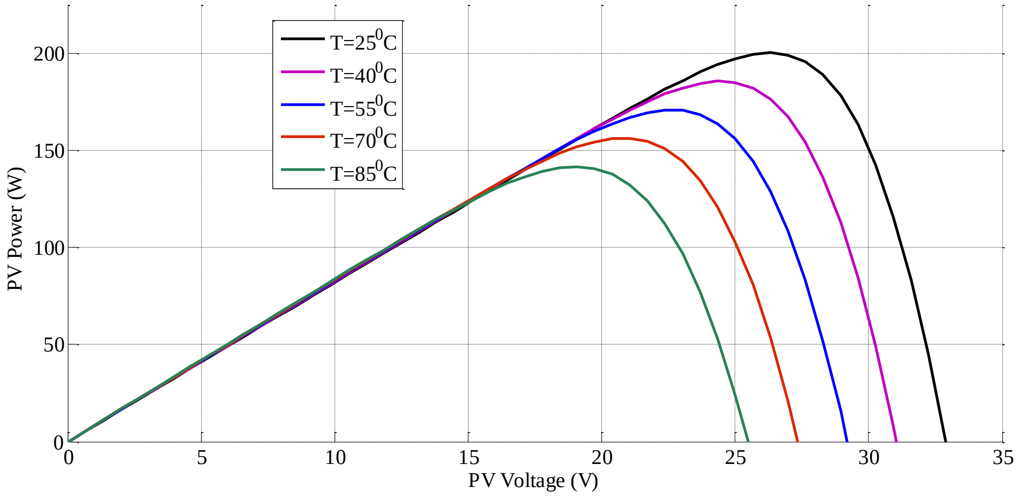

(b)

$Fig.E.3$ $P-V$ characteristic of Photovoltaic Module (based on Kyocera KC200GT PV module) at (a) different irradiance levels G (T = 25°C) (b) different cell temperatures T (G = 1 kW/m^2)

E.2 MPPT Algorithms

- **Perturb and Observe MPPT control algorithm**

$Fig. E.4$ shows the flowchart for the Perturb and Observe MPPT algorithm. In this method, periodic incremental or decremental perturbations are imposed on the PV system output voltage V_{pv} and the resulting power output P_{pv} is compared with the value in the last perturbation cycle. If the changes in the power and voltage are of the same polarity, i.e. if dP_{pv}/dV_{pv} is greater than zero, then the MPPT scheme continues to change the voltage in the same direction as that in the last cycle otherwise the voltage is changed in the opposite direction for the next cycle [66, 84, 88]**.**

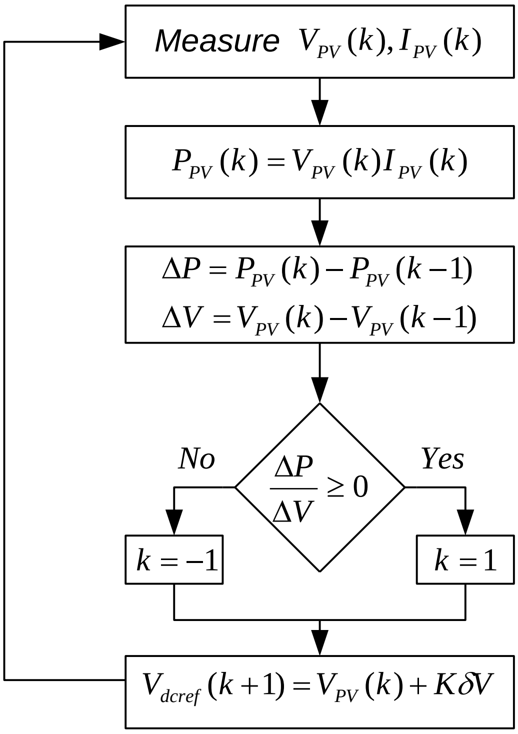

$Fig. E.4$ Perturb and Observe MPPT algorithm

- **Incremental Conductance MPPT control algorithm**

The Incremental Conductance (IC) MPPT control algorithm is based on the observation that the following equation holds at the MPP: $(\Delta i_{pv}/\Delta v_{pv}) + (i_{pv}/v_{pv}) = 0$. $(\Delta i_{pv}/\Delta v_{pv}) + (i_{pv}/v_{pv})$ is negative when the operating point on the $P - V$ plane is on the right-hand side of the MPP, and is positive when the operating point is on the left-hand side of the MPP. The MPP can thus be tracked by trying to regulate the difference between instantaneous conductance i_{pv}/v_{pv} and incremental conductance $\Delta i_{pv}/\Delta v_{pv}$ at zero, by properly shifting the PV terminal voltage v_{pv}. The algorithm is described by the flowchart given in $Fig. E. 5$. If $(\Delta i_{pv}/\Delta v_{pv}) + (i_{pv}/v_{pv})$ is positive and larger than a small value ε, the operating point is on the left-hand side of the MPP, and v_{pv} is increased by one step. If $(\Delta i_{pv}/\Delta v_{pv}) + (i_{pv}/v_{pv})$ is negative and larger in absolute value than ε, then the operating point is on the right-hand side of the MPP, and v_{pv} is decreased by one step. When the absolute value of $(\Delta i_{pv}/\Delta v_{pv}) + (i_{pv}/v_{pv})$ becomes smaller than ε, the MPP is considered to have reached and the voltage is kept unchanged, unless a new change is detected in i_{pv}. If so, the algorithm changes v_{pv} in an appropriate direction and the search for the new MPP begins. The IC method offers satisfactory performance under rapidly changing atmospheric conditions. The IC algorithm requires measurement of both v_{pv} and i_{pv}. The magnitude of the voltage increment step δV determines the algorithm tracking speed [66, 68, 84, 90].

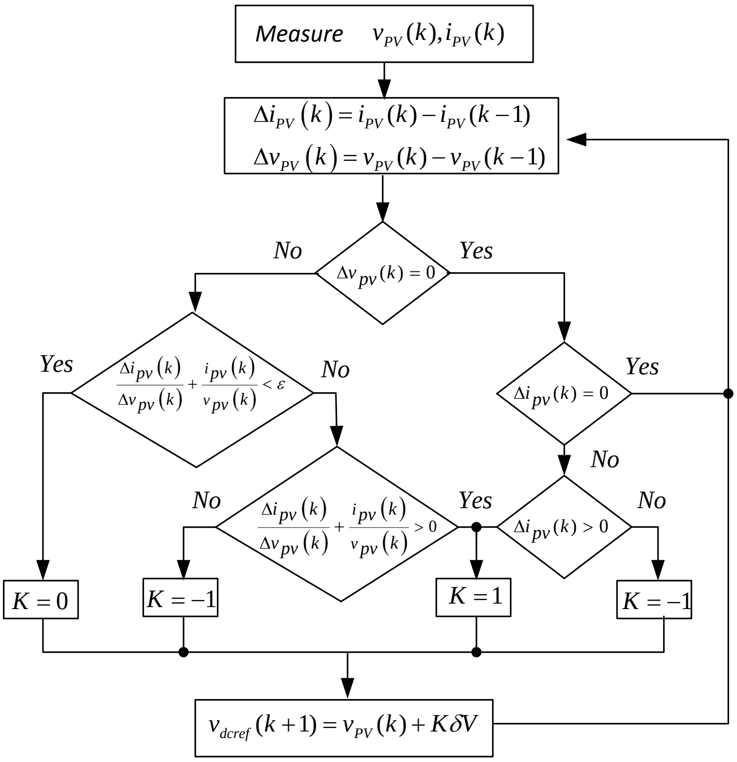

$Fig. E. 5$ Incremental Conductance MPPT algorithm